1-1-2011

Measurement of Trace Environmental Contaminants Using Cavity Ringdown Spectroscopy

Susan Theresa Scherrer

MEASUREMENT OF TRACE ENVIRONMENTAL CONTAMINANTS

USING CAVITY RINGDOWN SPECTROSCOPY

By

Susan Theresa Scherrer

A Dissertation
Submitted to the Faculty of
Mississippi State University
in Partial Fulfillment of the Requirements
for the Degree of Doctor of Philosophy
in Chemistry
in the Department of Chemistry

Mississippi State, Mississippi

December 2011

MEASUREMENT OF TRACE ENVIRONMENTAL CONTAMINANTS

USING CAVITY RINGDOWN SPECTROSCOPY

By

Susan Theresa Scherrer

Approved:

Stephen C. Foster Associate Professor of Chemistry (Director of Dissertation and Graduate Coordinator)	Chuji Wang Associate Professor of Physics (Co-Director of Dissertation)
Svein Saebo Professor of Chemistry (Committee Member)	Steven Gwaltney Associate Professor of Chemistry (Committee Member)
David L. Monts Professor of Physics (Committee Member)	Gary L. Myers Professor and Dean College of Arts & Sciences

Name: Susan Theresa Scherrer

Date of Degree: December 9, 2011

Institution: Mississippi State University

Major Field: Chemistry

Major Professor: Dr. Stephen C. Foster, Dr. Chuji Wang

Title of Study: MEASUREMENT OF TRACE ENVIRONMENTAL CONTAMINANTS USING CAVITY RINGDOWN SPECTROSCOPY

Pages in Study: 247

Candidate for Degree of Doctor of Philosophy

Environmental contamination has become a significant threat to the health and well-being of mankind as well as to the environment, prompting the establishment and implementation of stringent environmental regulations. The ability to accurately detect and quantify contaminants, such as mercury (Hg), uranium (U), and volatile organic compounds (VOCs), in real-time, *in situ* is of significant importance to monitoring and remediation efforts. In an effort to develop a real-time, fast-response detector that is portable, highly sensitive, and cost efficient, this research explored the feasibility of utilizing cavity ringdown spectroscopy (CRDS) in conjunction with various plasma sources and vacuum cavities to accurately detect trace quantities of contaminants.

The feasibility of detecting Hg with a low power, low temperature candle-shaped microwave-induced plasma (MIP) and a copper surfatron microwave cavity with various plasma discharge tube configurations in conjunction with cavity ringdown spectroscopy (MIP-CRDS) is discussed. Detection limits were on the order of 221 ppt Hg in the vapor phase for the candle-shaped MIP and improved by a factor of 10 with the tube-shaped plasma. The ability to detect elemental Hg naturally-evaporating from contaminated soils

and solutions was evaluated, and 10's of ppt were consistently obtained. Additionally, the fine structure of the Hg 253.65 nm transition was observed with each iteration of this approach.

The potential of effectively generating uranium atoms and ions with a low-power, low-flow rate microwave-induced plasma was evaluated. Uranium emission spectra covering 320 – 430 nm were obtained, labeled, and compared to the available literature values. Calibration curves were generated, and the detection limits were determined to be ~0.4 ppm. The feasibility of measuring U incorporating diode laser-plasma-CRDS was explored. The preliminary studies clearly show the ability to detect U vapor with this technique and sub-ppm detection limits were obtained.

A continuous wave cavity ringdown spectroscopy system (CW-CRDS) incorporating commercially available telecommunications diode lasers was constructed, and the overall sensitivity of this system was evaluated by utilizing the absorption of the asymmetric C-H stretch overtones of several VOCs, including benzene, chlorobenzene, 1,2-dichlorobenzene, toluene, and acetone. Detection limits are determined to be in the ppb's for each of the organics examined.

DEDICATION

To Bryan and Mary Alexandra “Alex”

ACKNOWLEDGEMENTS

I would like to express my sincerest appreciation to my major advisors, Drs. Stephen C. Foster and Chuji Wang, for their encouragement, support, and guidance during this research. The knowledge and experience I have gained from this experience will serve as my foundation for all future work.

I would also like to thank my committee members, Drs. Svein Saebo, Steven Gwaltney, and David L. Monts, for serving on my committee and assisting in my educational experience.

A special thank you goes out to the people in the Department of Chemistry and ICET who generously donated their time and talents. Your help and advice has been invaluable, and your friendship has made my time here much more pleasant.

Additionally, I would like to thank my family and friends, who have not only helped me maintain my sanity through this process, but given me the love and encouragement to pursue my dreams.

TABLE OF CONTENTS

LIST OF TABLES

LIST OF FIGURES

CHAPTER I

INTRODUCTION

1.1 Introduction

Cavity ringdown spectroscopy (CRDS) is a powerful, laser absorption spectroscopic technique. Since the inception of the CRDS-principle two decades ago,[1] this technique has rapidly matured from the initial two-mirror high-finesse optical resonator cavity for measurements of vapor phase species to incorporate various cavity configurations[2, 3] and laser sources[4, 5, 6] as well as liquid[7, 8, 9, 10]and, in principle, solid samples. Extremely long effective pathlengths, high sensitivity, absolute absorption measurement capabilities, and relative insensitivity to laser power fluctuations are key characteristics attributed to this field of study. Adaptability to a plethora of experimental environments, coupled with a wide range of diagnostic applications to which this technique can be utilized, has led to an explosion of research efforts implementing CRDS.[11, 12, 13] The goal of many research projects incorporating CRDS is to develop a system which offers highly sensitive, fast-response measurements of a particular species of interest. The research presented in this dissertation focuses on the detection of multiple environmental contaminants, namely, mercury, uranium, and specific volatile organic compounds (VOC's), while predominantly employing the cavity ringdown spectroscopic technique. As such, this dissertation will be divided into three sections after the introduction of the CRDS technique. The first section will emphasize mercury-related CRDS studies. The next element examined in detail was uranium, and the

material presented in the second section will describe research efforts to generate and detect uranium atoms/ions from solution samples. The final portion will address VOC measurements made with a vacuum-CRDS system.

1.2 Mercury

1.2.1 Motivation

The unique properties of mercury have simultaneously fascinated and plagued mankind for thousands of years.[14] Mercury, which exists in the elemental form or bound to organic and/or inorganic compounds in the environment,[15] is the only naturally-occurring metallic element that is a liquid at room temperature. In the elemental form, mercury can be present as a liquid or a vapor, and it can also bind to atoms, ions, and molecules to form organic and inorganic molecules. All forms of mercury are neurologically toxic.[16] Due to the toxicity of mercury and mercury-containing compounds, mercury released into the environment from natural sources, such as volcanic eruptions, weathering and erosion of rocks and soil, and vaporization from the oceans, as well as from anthropogenic sources, such as manufacturing industries, mining, and the incineration of coal, medical waste, and other mercury-containing materials, has become a serious concern.[17] Mercury released into the environment from anthropogenic as well as natural sources is becoming a serious health threat to humans. Humans are exposed to mercury and mercury-containing compounds in different ways, and the severity of mercury's toxic effects is dependent upon the form and concentration to which the individual was exposed as well as the route of exposure.[18] Mercury and mercury-containing compounds have been proven to cause extensive, irreversible damage and degradation to numerous biological systems and organs, especially in humans and the

developing fetus. The main effects of mercury exposure, even at very low levels, include neurological, renal, cardiovascular, and immunological deterioration; additionally, chronic exposure has been linked to severe degradation and/or damage to the brain, spinal cord, kidneys, liver, and developing fetus.[19]

Environmental contamination has become a significant health threat, prompting the establishment and implementation of environmental and health standards by the US EPA.[15] Upon entering the environment, mercury can be widely disseminated among the soil, groundwater, atmosphere, oceans, natural ice, and living organisms, including plants and animals.[20] Once airborne, mercury is widely disseminated and may be transported great distances over several months (years) prior to being deposited by precipitation in aquatic or terrestrial ecosystems. Once mercury enters the water, either directly via precipitation or through run-off, biological processes transform mercury into the more toxic form methylmercury, and other organic-Hg compounds, and the potential for bioaccumulation is greatly enhanced.[21] The primary exposure pathway to organic mercury compounds for humans is through the consumption of predatory fish, such as shark, tuna, and swordfish, in which the accumulated mercury can be well above the maximum allowed dosage as reported by the EPA. Accidental exposure to elemental mercury via prolonged exposure from, for instance, a broken light bulb or thermometer or even from dental fillings constitutes a large portion of reported mercury incidents. Mercury concentrations in the atmosphere are typically 3 to 250 parts per billion by volume (ppbv). According to data obtained from the Center for Disease Control, the time-weighted average (TWA), permissible exposure limit (PEL) set by the Occupational Safety and Health Administration[22] (OSHA) for mercury vapor exposure is 0.1 mg/m^3, and the recommended exposure limit (REL) set by the National Institute of Occupational

Safety and Health[23] (NIOSH) is 0.05 mg/m^3 with a 0.1 mg/m^3 ceiling for a 10 hr work day and a 40 hr week.

There are many on-going research efforts targeting the detection and monitoring of environmental mercury. To date, the majority of mercury emission surveys utilize cold vapor atomic absorption spectroscopy (CVAAS),[24, 25, 26] inductively coupled plasma-mass spectrometry (ICP-MS),[27, 28, 29, 30] atomic fluorescence spectroscopy (AFS),[31] differential optical absorption spectroscopy (DOAS),[32 33, 34, 35] plasma cavity ringdown spectroscopy (P-CRDS),[36, 37, 38, 39, 40, 41] cold vapor cavity ringdown spectroscopy (CV-CRDS),[38] and/or laser atomic absorption spectroscopy (LAAS).[42] Additionally, there are several types of mercury analyzers and/or monitors currently on the market.[43, 44] Each system presents advantages and limitations, depending on the specific application. For example, the cold vapor approach, which can routinely yield mercury detection limits of 0.2 ppb, requires a sample-preconcentration step prior to mercury detection and cannot measure naturally occurring mercury in the air, thus, hindering real-time and dynamic behavior analysis. Typical mercury detection limits with ICP-MS are ~ 0.1 - 10 parts per trillion by volume (pptv); however, the sample must first be injected into a plasma and atomized before the mercury can be detected by the mass spectrometer, and the instrumentation is very bulky and expensive. There are several critical limitations shared by the majority of the commercially available mercury monitors; specifically, they require either complicated and time-consuming sample collection and preparation or the instruments are not field deployable and, therefore, do not offer real-time analysis. The ability to detect and monitor mercury in real-time with a portable, sensitive mercury analyzer would be a very useful diagnostic approach to determine the presence of Hg emissions and contamination.

1.2.2 Objective and Scope

In an effort to develop a real-time, fast-response mercury detector that is portable, highly sensitive, and cost efficient, this research explored the feasibility of utilizing Cavity Ringdown Spectroscopy (CRDS) in conjunction with various plasma sources (plasma-CRDS) to accurately detect trace quantities of mercury. The first successful demonstration of plasma-CRDS implementing a low-cost, compact microwave-induced plasma (MIP) as the plasma source for measurements of elemental mercury and its stable isotopes under atmospheric conditions resulted from this research effort,[45] and the details will be the topic of Chapter III. Utilizing this MIP-CRDS system, detection limits of 221 pptv, orders of magnitude below the maximum exposure limit, were readily and reproducibly obtained. This plasma is referred to as the candle-shaped plasma in the text because of the distinct shape generated with this atomization source, which closely resembled the flame-portion of a burning candle and is described and depicted in Figure 3.2. Due to the presence of spectral interference generated by the candle-shaped plasma, efforts turned to experimentally improving the existing instrument configuration and sensitivity by systematically incorporating alternate plasma sources, which will be the subject of Chapter IV, and a compact diode laser[46, 47] as the light source to, ultimately, yield diode laser MIP-CRDS for mercury detection. During the course of this research, the ability to detect elemental mercury naturally evaporating from contaminated soil samples as well as mercury-spiked solutions under atmospheric conditions was explored; the preliminary results, which will be the topic of Chapter V, are given.

1.3 Uranium

1.3.1 Motivation

Uranium, the first element discovered to be radioactive,[48] is of much interest in several areas of research. When considering the most stable isotopes of radioactive elements, uranium is the heaviest naturally-occurring element; however, when considering the atomic mass of naturally-occurring elements, uranium is the third heaviest.[49, 50, 51, 52] Uranium, which is found in low concentrations in rocks, soil, and water,[49] possesses a relatively unique combination of characteristics. For instance, uranium readily bonds with other elements and compounds,[53] especially compounds with oxygen, and undergoes chain reactions and nuclear fission; for this reason, uranium is oftentimes encountered in nuclear production facilities. Additionally, uranium, a member of the actinide family, easily combines with active species during the atomization process to form oxides at atmospheric pressure in hot sources and to form carbides in graphite furnaces.[54] Because uranium has a relatively low ionization potential (~ 6.08 eV), introduction of uranium into a high-power plasma source, such as an inductively coupled plasma (ICP), results in almost complete ionization.[55] While the ionization efficiency is high,[56, 57] the atomization efficiency is relatively poor for U in a high-power plasma source. Unfortunately, low-power sources, such as flames or graphite furnaces, typically cannot sufficiently atomize U,[58] which prevents acceptable uranium detection using atomic emission or absorption methods with a flame or furnace as the atomization source. Uranium atoms (U I) and ions (U II) give rise to over 300,000 spectral lines.[59] Utilizing a 27 MHz ICP, the initial detection limit of U at 385.957 nm was reported by Winge *et al* to be 250 ng/mL;[60] this detection limit was subsequently improved by Boumans and Vrakking[61] by over an order of magnitude to 16 ng/mL by implementing a 50 MHz ICP

and taking into consideration effects of source characteristics, noise, and spectral bandwidth of each transition line.

The research presented in Chapters VI and VII is a continuation of research conducted in our laboratory and in conjunction with personnel at Los Alamos National Laboratory (LANL) to systematically design and develop new and/or improved sources for atomic emission and absorption measurements of multiple species of environmental concern, especially uranium. Once the operational efficiency of each atomization/ ionization source was established, the technique was combined with the highly sensitive cavity ringdown spectroscopic technique to further enhance the detection limits.

1.3.2 Objective and Scope

In an effort to move towards a field-deployable plasma-CRDS spectrometer for real time, *in situ* measurements of uranium, sequential investigations have been undertaken in this laboratory. In the initial phase of this multi-level research effort, a specifically designed ICP, which was used as the atomization source, was used in conjunction with cavity ringdown spectroscopy to obtain sensitive elemental and isotopic measurements of multiple species.[62] However, an ICP is bulky and requires higher plasma powers and gas flow rates than one would desire in a field-portable instrument. Once the feasibility of detecting uranium with the ICP-CRDS technique had been established,[63] the research effort examined the potential of incorporating a low-power, low-flow rate microwave-induced plasma (MIP) to efficiently atomize uranium from solutions in lieu of the ICP. The physical footprint of the MIP is significantly more compact, and the MIP does not require external cooling or additional electronics to operate.

Unfortunately, at the time of this research, there were very limited references covering uranium measurements obtained while utilizing an MIP, and, of the literature values available, the uranium measurements were obtained while utilizing a high-power MIP. Therefore, the capability and efficiency of generating uranium atoms and ions with a low-power MIP source[64] prior to evaluation with the combined plasma-CRDS approach for uranium detection had to be investigated.[65] The research presented in Chapter VI examined the ability of this low-power MIP to effectively serve as a viable atomization source for uranium. In order to fully evaluate this MIP for U atomization, multiple experimental parameters were explored and optimized to enhance the atomization prior to implementation of the MIP-CRDS technique for U detection and analysis. Utilizing the candle-shaped MIP as the atomization source, the emission spectra of several elements, including uranium, were successfully acquired. While uranium emission spectra and detection limits obtained with the MIP are the primary subjects of Chapter VI, the capability to atomize and detect additional elements will be briefly included.

In addition to reducing the size of the atomization source, the next limitation to portability is the very large, expensive laser system which was employed for the ICP-CRDS studies of uranium. In an effort to address this aspect, a continuous wave (CW) diode laser operating at 409 nm was employed to test the feasibility of detecting uranium with diode laser-ICP-CRDS. An in-depth characterization of the diode laser was conducted. The operational parameters of the ICP and the beam position in the plasma were optimized for U detection. The preliminary uranium measurements obtained with this system will be the subject of Chapter VII.

1.4 Volatile Organic Compounds

1.4.1 Motivation

Real-time quantification of emission by-products, pollutants, atmospheric constituents, and reaction intermediates is an important aspect of many environmental efforts. Many of these species are classified as volatile organic compounds (VOC's). Volatile organic compounds are a principal component in atmospheric reactions that form ozone and other photochemical oxidants and are prevalent in the Earth's atmosphere. Sources of VOC emissions are extremely diverse, including natural as well as anthropogenic sources, such as automobiles, chemical manufacturing facilities, dry cleaners, paint shops, and other commercial and residential sources that use solvents and paint. By definition, VOC's contain at least one carbon atom, and they readily vaporize at room temperature and pressure and enter the atmosphere. Measurement of trace levels of volatile species and pollutants can be time-consuming, expensive, and require a trained technician. The ability to incorporate compact, low cost diode lasers for high sensitivity measurements exponentially increases the potential applications to which this technique can be utilized. These features allow the systems to be implemented in numerous field-deployable scenarios while offering the advantage of real-time, *in situ* detection. This would be especially advantageous for atmospheric and emissions studies,[66, 67] monitoring various manufacturing processes, and detecting the presence of disease biomarkers in exhaled breath[4, 68] as well as the presence of explosives[69, 70, 71] or contaminants in the environment,[72] just to name a few. This research further explored the use of diode laser-CRDS to generate highly sensitive measurements of specific VOC's.[73]

1.4.2 Objective and Scope

All of the VOC's investigated in this research, benzene, chlorobenzene, 1,2-dichlorobenzene, methylbenzene (toluene), and 2-propanone (acetone), contain multiple C-H bonds. The fundamental asymmetric C-H stretch for the compounds examined in this research is observed between 3000 and 3150 cm^{-1}, and the absorption lines associated with the fundamental transitions for a molecule, which typically occur in the mid-infrared region of the electromagnetic spectrum, are relatively strong; however, during the experimental data acquisition, this frequency range could not be directly probed with the room-temperature diode lasers that were commercially available. Therefore, to use readily available room-temperature diodes, the first overtone of the asymmetric C-H stretch was examined. The energy necessary to excite the first overtone of benzene, substituted-benzene derivates, and acetone is approximately 6000 cm^{-1} (or 1667 nm); and this region could be efficiently accessed with diode lasers which were commercially available at that time, thus allowing the first vibrational asymmetric C-H stretch overtone of many organic compounds to be examined with readily available, relatively low-cost diode lasers. The results of this research will be the subject of Chapter VIII.

1.5 Organization of Dissertation

As previously mentioned, this dissertation will be divided into three dominant research topics. Chapter II will present the fundamentals of CRDS and the adaptations which were utilized in this research. Chapters III – V, respectively, will describe the efforts pertaining to mercury detection implementing a candle-shaped MIP, alternate plasma discharge tube configurations, and mercury naturally evaporating from contaminated soils and samples. Research progress related to uranium atomization and UV-diode laser-CRDS will be presented in Chapters VI and VII, respectively. VOC

absorption cross-section measurements using NIR-diode laser-CRDS will be the topic of Chapter VIII, followed by a conclusion and future direction.

CHAPTER II

CAVITY RINGDOWN SPECTROSCOPY FUNDAMENTALS AND EXPERIMENTAL CONFIGURATIONS IMPLEMENTED IN THIS RESEARCH

2.1 Introduction

The fundamental principle behind the implementation of cavity ringdown spectroscopy (CRDS) is an application of the Beer-Lambert Law, in that higher detection sensitivities can be realized by effectively increasing the absorption pathlength through the sample of interest. One highly efficient method to accomplish this is to inject a pulse of monochromatic radiation into a stable optical cavity.[74] This simplistic, yet ingenious, approach has put into motion an entirely new high sensitivity laser absorption technology from which many derivations of the initial platform have emerged. Although a relatively new spectroscopic technique, CRDS has rapidly matured and diversified to incorporate a wide range of applications in a host of experimental conditions.[11, 12] CRDS is versatile enough to be implemented in spectroscopic studies of molecules, atoms, ions, and isotopes, utilizing both pulsed and CW light sources, in a plethora of experimental conditions and environments.[13] The CRDS technique has also implemented novel cavity designs,[3] electronics,[46] and light sources[39, 75, 76, 77] to allow for the detection of species in vapor and solution phases. CRDS has been employed with plasmas[78] and flames,[79] reaction cells,[80, 81] and vacuum chambers,[82, 83] under ambient conditions,[84] in supersonic beams,[85] and in conjunction with other analytical techniques, such as High Performance

Liquid Chromatography (HPLC),[86, 87] Gas Chromatography (GC),[88] and Fluorescence Spectroscopy.[89] The CRDS technique has expanded into the detection and monitoring of trace species of environmental concern, yielding high sensitivity elemental and isotopic measurements, examining potential medical applications,[68, 90, 91] such as breath gas analysis as well as skin diagnostics, and sensor development utilizing fiber-CRDS,[68, 92, 93, 94] and the list will continue to expand as the relevant technologies come of age. As basic as well as specialized R & D in optics, electronics, and laser technology continues to make significant strides, CRDS will continue to expand into applications and chemical species detection which were previously unobtainable in its infancy. This chapter will focus on the CRDS-principle and the modifications to the technique which were implemented in the research undertaken for this dissertation as well as a brief description of additional forms utilized in our lab that were preliminary, proof-of-concept studies but were out of the scope of the dissertation efforts, and therefore, will not be presented in detail herein.

2.2 CRDS Principle

2.2.1 Beer-Lambert Law and CRDS

Cavity ringdown spectroscopy is an application of the fundamental Beer-Lambert Law, in which the detection sensitivity can be proportionately increased by increasing the interaction pathlength of the light with the sample species of interest. Simply stated,

$$A = \sigma n l \quad , \qquad \text{Eq 2.1}$$

in which the absorbance of the light, A, is a product of the sample pathlength, l, the concentration of the species, n, and the wavelength-dependent absorption cross-section, σ. Because the absorption cross-section for a particular atom or molecule is a constant at

a specific wavelength and experimental conditions, one must either increase the concentration of the sample, which can be costly, time-consuming, and sometimes impractical, or increase the sample pathlength in order to increase the absorbance. In environmental monitoring and ultra-sensitive detection schemes, increasing the sample concentration is often counterproductive, especially in most field deployable, real-time, and *in situ* applications. Various experimental approaches have been successfully implemented to effectively and efficiently increase the absorption pathlength. The most straightforward approach is to make extremely long sample chambers; however, this is probably one of the least cost-efficient approaches as additional experimental considerations become necessary to 'control' the light in the sample chamber and much more space would be required to accomplish this, i.e., practicality and financial constraints limit the absorption pathlength under normal laboratory circumstances. Another approach is to direct the light in a multi-pass configuration, in which the light pulse repeatedly crosses the sample chamber, making as many mirror encounters as is physically possible, thereby increasing the pathlength. While this approach readily increases the absorption pathlength, much longer pathlengths than can be efficiently generated in this manner are necessary to achieve very low detection limits for trace monitoring of species; additionally, these types of direct absorption techniques are further constrained by the operational limitations of the light source: for example, intensity fluctuations or drift in the spatial orientation of the laser. One technique which has proven highly adept at significantly increasing the absorption pathlength while being relatively unaffected by laser intensity fluctuations is Cavity Ringdown Spectroscopy (CRDS). While there are other cavity enhanced spectroscopic techniques, for example, Integrated Cavity Output Spectroscopy (ICOS), Cavity Enhanced Absorption

Spectroscopy (CEAS), and Cavity Leak-Out Spectroscopy (CALOS), they are predominantly variants of the CRDS technique and, therefore, only the CRDS methodology will be presented here.

The CRDS principle has been described in detail in several excellent review articles, and the explanation presented here will begin with the simplest scenario and extend into more complex variations and applications as are pertinent to the research undertaken in the course of the studies presented herein. The most basic ringdown cavity, as shown in Figure 2.1, consists of two ultra-high reflectivity mirrors, separated by a distance *d*. When a laser pulse is incident on the back side of the first cavity mirror, the majority of the pulse is reflected off the mirror, away from the cavity. A small percentage, based on the finite reflectivity of the mirror, is injected into the cavity, and this quantity is referred to as *Io*. This laser pulse will propagate through the cavity to the second high reflectivity mirror. This time, the majority of the beam will be reflected back through the cavity, while a fractional amount is transmitted through the mirror. The pulse will continue to "ring" back and forth through the optical cavity, experiencing a decrease in *I* with each mirror encounter, such that after *n* round trips through the cavity, the intensity will be equivalent to $I = I_0 R^{2n}$, where *R* is the average reflectivity of the mirrors. Assuming the cavity is configured such that the light pulse does not temporally overlap itself in the cavity, a series of discrete intensity pulses, as shown in Figure 2.2, will be detected by a photomultiplier tube (PMT) or photodiode (PD) placed directly behind the second mirror.

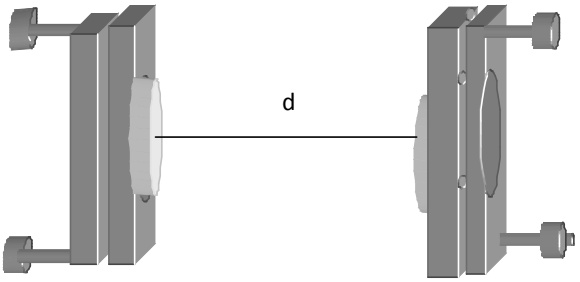

Figure 2.1 Traditional ringdown cavity.

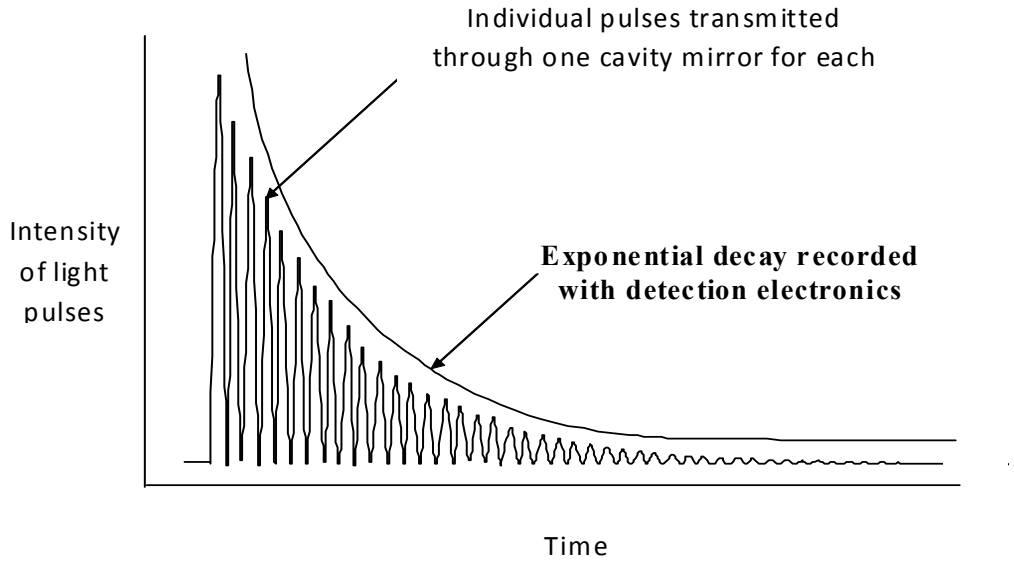

Figure 2.2 Smooth exponential decay curve as observed by detector.

The decay curve is a function of the individual light intensity pulses transmitted through the ringdown cavity with each mirror encounter. Unless the detection electronics are fast, the individual pulses will not be observed, rather a smooth exponential decay curve will be recorded.

The injected pulse travels many (up to tens of thousands) round trips in the cavity, thereby proportionately increasing the overlap between the laser light pulse and the vaporous sample. However, due to the response time of the detection electronics, as well as the physical length of the pulses, which are not usually separated in time, the intensity pulses transmitted through the second high reflectivity mirror typically appear as a

continuous exponential decay. The experimental parameters can generally be modified to produce or simulate a single-exponential decay. This decay signal is then fit to a first-order exponential decay from which the ringdown decay time constant is determined. As previously mentioned, a big advantage of the ringdown technique is that the rate of decay of the light intensity from the optical cavity, as opposed to the change in the light intensity, is measured. Therefore, fluctuations in the input laser intensity, which can vary by 10 % of the total laser intensity with the pulsed laser sources utilized in this research, do not necessarily affect the measurements or the overall system stability.

In the simplest scenario, one can assume the dominant losses are attributed to the finite mirror reflectivity and sample absorption. The ringdown time (τ), or the time required for the amplitude of the intensity to fall to *1/e* of its initial value, is equivalent to

$$\tau = \frac{d}{c\left[\left|\ln R\right| + \alpha l_s\right]}, \qquad \text{Eq 2.2}$$

where d is the cavity length, c is the speed of light, R is the mirror reflectivity, α is the Beer's Law absorption coefficient, and l_s is the single-pass pathlength through the sample; for a gas filling the entire cavity, $l_s = d$. If no sample is present in the cavity or if the laser frequency is off-resonance with a spectral transition, such that $\alpha = 0$, then the reflectivity of the mirrors can be calculated. Once the mirror reflectivity has been obtained, the number of round trips completed for the intensity to fall to *1/e* of the initial value can be determined.

Furthermore, once the ringdown times have been determined at a particular wavelength and temperature in the presence and absence of an absorbing sample, the absorption cross-section for a molecule, σ, can then be obtained at the given experimental

conditions if the concentration of the sample in the ringdown cavity is known. The correlation between τ and σ can be identified by examining the following relationship:

$$\frac{1}{\tau} = \frac{1}{\tau_{\circ}} + c\,\sigma\,n \ , \qquad \text{Eq 2.3}$$

where $\tau_{\circ}$ is the ringdown time when no absorbing species is present in the ringdown cavity, $\frac{d}{c\left|\ln R\right|}$, and $\sigma n = \alpha$, where σ is the wavelength-dependent absorption cross-section of a molecule at the transition frequency ν, and n is the concentration of the sample in the ringdown cavity. Therefore, the absorption cross-section of a molecule can be accurately determined for each wavelength examined if the ringdown times with and without an absorbing species present as well as the concentration of sample being probed are known. From this analysis, one can see that an absolute measure of the absorption cross-section has been made. This self-calibrating feature is extremely beneficial to the ringdown technique. Moreover, once the cross-section has been determined for a particular wavelength, differing concentrations of the sample at the given gas conditions can be measured by evaluating the change in ringdown time due the presence of the sample.

2.2.2 Plasma-CRDS

When implementing an atomization source in conjunction with the CRDS technique, the plasma is generally located in center of the ringdown cavity (RDC). The fundamental principle is still the same as in CRDS; however, there are additional optical losses resulting from the presence of the plasma which must be taken into consideration in order to obtain the high sensitivity and absolute concentration measurement. Losses incurred from inserting an atomization source in the cavity include scattering due to the

high temperature, plasma movement and flow rates, presence of a sample or background solution, and absorbance due to the generation of ions or radicals that absorb the light at the wavelength of interest. Therefore, the ringdown equation must be slightly modified to incorporate these attributes, such that the observed ringdown time for a plasma-CRDS experiment can be expressed as

$$\tau = \frac{d}{c\left(\left|\ln R\right| + \beta_{plasma} l_s + \beta_{air}\left(d - l_s\right) + \alpha l_s\right)} \quad , \qquad \text{Eq 2.4}$$

where β_{plasma} and β_{air} are the broadband scattering coefficients in the plasma and open air of the cavity, respectively. Experimentally, one finds that β_{plasma} and β_{air} vary slowly as a function of wavelength at a given set of experimental parameters, such that they can be incorporated into an effective reflectivity R_{eff} for the particular system. By doing so, the ringdown time can be determined by

$$\tau = \frac{d}{c\left(\left|\ln R_{eff}\right| + \alpha l_s\right)}. \qquad \text{Eq 2.5}$$

R_{eff} is calculated by measuring the ringdown time with no absorbing species in the plasma. Once the effective ringdown time with no analyte present (τ_0) is known, the ringdown time with an absorbing species present (τ) may be found. From here, the concentration of the analyte can be readily determined using Equation 2.3.

The absorbance for a plasma is a little more complicated than encountered with an open-air cavity-filled direct absorption measurement. This is because the analyte is not necessarily homogenously distributed throughout the plasma, which implies the density is position dependent, and the absorption cross-section is actually a function of frequency. Therefore, the absorbance can be more accurately expressed with the following:

$$Absorbance = 2\int_{-\infty}^{\infty}\int_{0}^{\frac{1}{2}}\sigma(\nu)n(r)dr\,d\nu \quad , \qquad \text{Eq 2.6}$$

where $\sigma(\nu)$ is the absorption cross-section for the given transition line, ν is the laser frequency, $n(r)$ is the concentration of the absorbing analyte and is often referred to as the radial density, and r indicates the position in the plasma being probed with the laser beam.[95] The radial density can be obtained through an Abel inversion for the conversion of the lateral measurements. The lineshape of the transition line is affected by linewidth broadening mechanisms under atmospheric plasma conditions, resulting in a Voigt profile, and the absorption cross-section is determined from the following expression:[63, 96, 97]

$$\sigma_{ij}(\nu) = \frac{g_j}{g_i}\frac{\lambda^4}{4\pi^2 c}\frac{A_{ij}}{\Delta\lambda_D}\nu(a,0)(\pi\ln 2)^{\frac{1}{2}} \quad , \qquad \text{Eq 2.7}$$

where g_j and g_i are the upper and lower state degeneracies for the absorption, respectively, λ is the wavelength of the transition line being probed, c is the speed of light, A_{ij} is the Einstein coefficient for spontaneous emission, $\Delta\lambda_D$ [97, 98] is the Gaussian component due to Doppler broadening, and $\nu(a,0)$ is the Voigt function of the broadened linewidth, with a being the rate of the Lorentzian and Gaussian components. The Einstein coefficients are well documented for most atomic and ionic transitions. $\Delta\lambda_D$ is equivalent to $\lambda_0\sqrt{\frac{kT}{mc^2}}$, where λ_0 is the central wavelength of the transition line, k is the Boltzmann constant, T is the kinetic temperature of the plasma gas, m is the atomic mass, and c is the speed of light. In practice, the plasmas utilized in this research displayed inhomogeneities in characteristics such as electron density and temperature distribution through the plasma. Therefore, the lineshape is a function of the position in the plasma, and the absorption cross-section, which is also position-dependent, is a function of the

laser frequency.[99, 100] When conducting these experiments, the absorption cross-sections reported are generally an average value obtained from the spatially averaged, integrated lineshape along the particular position probed. Taking this into consideration, the line-of-sight average cross-section for plasma-CRDS can be found by coupling Equations 2.5 and 2.6 to yield

$$\sigma(\nu)n(x)l = \frac{d}{c}\left(\frac{1}{\tau}-\frac{1}{\tau_0}\right) , \qquad \text{Eq 2.8}$$

which closely resembles Equation 2.3. In Equation 2.8, τ_0 includes all background losses observed in the absence of an analyte. For plasmas which are cylindrical in shape, the line-of sight measurements at each cross-section of the plasma examined can be converted to a point measurement through Abel inversion, such that

$$i(r) = -\frac{1}{\pi}\int_{r}^{R_0}\frac{I'(x)}{\sqrt{x^2-r^2}}dx , \qquad \text{Eq 2.9}$$

where *i(r)* is the converted signal intensity at the radial location (*r*) of the plasma section examined, R_0 is the center of the plasma, such that r = 0, *x* is the distance between the laser beam and the center point of the section of plasma being probed, and $I'(x)$ is the derivative of $I(x)$, the absorption signal intensity being measured at the particular point in the plasma.[63, 101] Due to discrepancies in tubing characteristics, e. g., inhomogeneities, deformities, etc., flow rates through the plasma, temperature variance, etc., even cylindrical plasmas are not always perfectly symmetric. For analytical applications addressing sensitivity and reproducibility, as pursued in this research, the line-of-sight measurements are extremely reproducible and highly applicable. Even when a plasma is incorporated as the atomization source, one can clearly see from Equation 2.8 that this is still a self-calibrating, absolute absorption technique.

2.3 Sensitivity

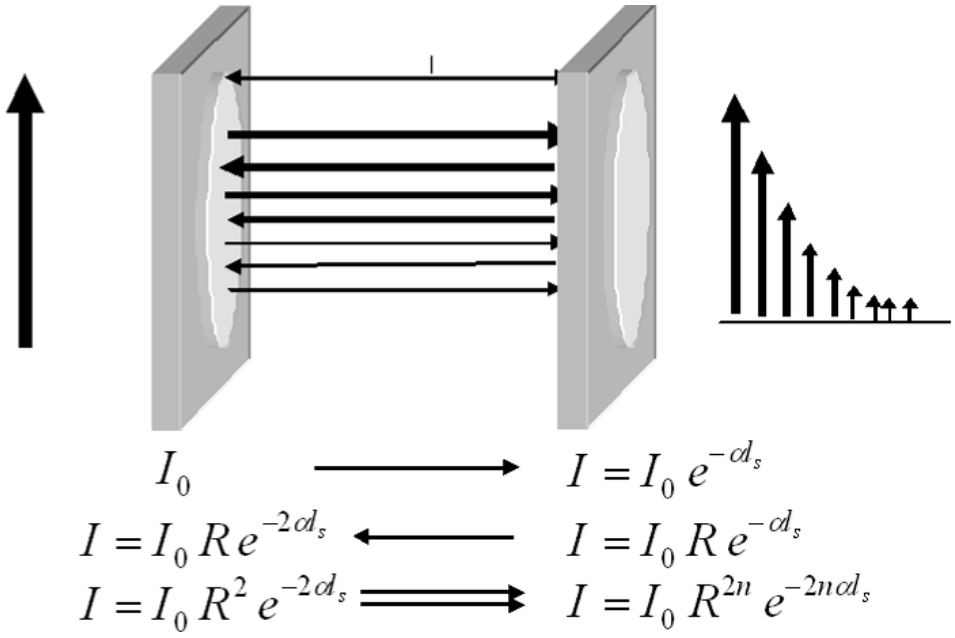

Figure 2.3 Propagation of light in a high finesse optical cavity.

Each mirror encounter and sample transversal, if one is present in the optical cavity, reduces the intensity of the incident beam such that the intensity after n round-trips through the cavity is given by $I = I_0 R^{2n} e^{-2n\alpha l}$.

CRDS is a highly sensitive absorption technique. In order to better appreciate the ringdown phenomenon and the significant improvement in detection sensitivity, as compared with CRDS's predecessors, a brief description and corresponding pictorial will be provided. Figure 2.3 displays the basic optical configuration employed in the most straightforward application of CRDS along with the first few passes (or rings) of the laser pulse in the cavity. For clarification, the sample pathlength (l_s) will be a subset of the cavity length (d) to more effectively describe the enhancement in the interaction of the light with the sample species as opposed to conventional absorption spectroscopy. With conventional absorption spectroscopy, the incident beam is injected into the sample cell and the difference in intensity before and after the sample interaction is recorded as a

ratio of the two values. The ratio is then plotted as a logarithmic function from which the concentration of the absorbing species can be extracted for a known absorption cross-section. Figure 2.4a portrays a typical, single-pass absorption configuration with a 1 cm sample cell. Clearly, the sensitivity of this approach is severely limited by the length of the sample chamber, and laser intensity fluctuations can greatly affect the measurements. Multi-passing the laser light through the sample cell, as shown in Figure 2.4b, offers the advantage of effectively enhancing the sample pathlength while providing the opportunity to have multiple interactions with the sample; unfortunately, this approach, which also measures the change in intensity as a function of sample interaction, is still influenced by power fluctuations and physical limitations.

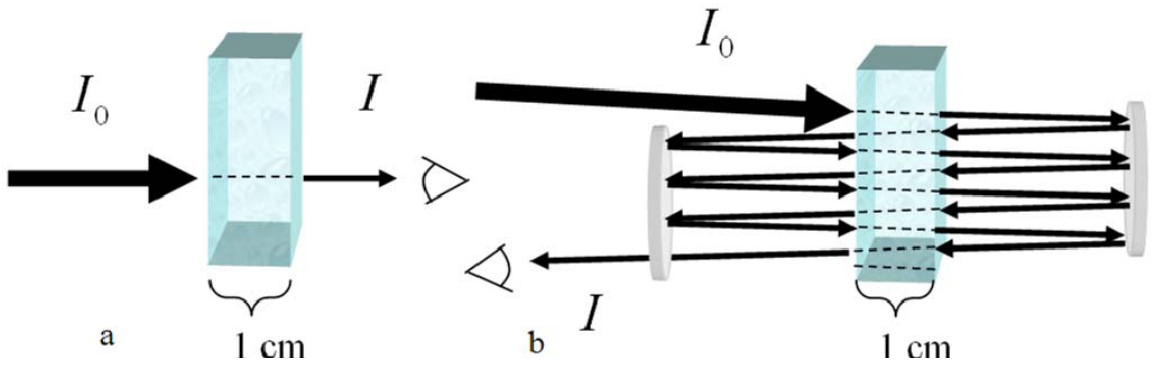

Figure 2.4 Conventional single pass (a) and Multipass (b) absorption spectroscopy through 1 cm sample cell.

By multi-passing the laser through the sample (b), the interaction between the species of interest and the light is enhanced.

In the aforementioned approaches, the laser light is directed through a sample cell, either in a direct single pass or multipassing across the cell. Assuming all scattering and absorption due to the cell and blank/background interference are taken into consideration and assuming homogeneity of the sample in the cell, the changes in light intensity as

measured by the PMT or PD will be due to absorption by the sample. For very weak or forbidden absorbance transitions (i.e., small absorption cross-sections and low probabilities) or low sample concentrations, the change in intensity due to absorption can be difficult to accurately detect through such limited sample interaction and can often be lost in laser intensity fluctuations. Therefore, the ability to "trap" a laser pulse in an optical cavity to allow numerous reverberations through the sample would significantly increase the sample pathlength, which, according to Beer's Law, proportionally increases the absorbance. This is one of the fundamental advantages of the cavity ringdown technique. A second noteworthy attribute of this approach is that CRDS is (theoretically) not influenced by laser intensity fluctuations since the time decay, and not the change in intensity, is recorded. Additional important characteristics associated with this technique, as previously described, are that CRDS is an absolute absorption and self-calibrating technique.

Typical absorptions measured with single-pass absorption spectroscopy[102] are on the order of $10^{-3} - 10^{-4}$. Multipass cells fare slightly better with detection limits in the $10^{-6} - 10^{-7}$ range. CRDS, however, can readily, accurately, and reproducibly detect $10^{-8} - 10^{-10}$ levels because of the enhanced absorption pathlength.[103] For example, a 1 m ringdown cavity comprised of two ultra-high reflectivity mirrors (99.99 %) will generate a background ringdown time of 33.4 μs; this is equivalent to a 10 km pathlength traveled by the light pulse during the first time constant. As compared to a 1 cm single-pass sample cell, this is a 6-x improvement in detection sensitivity, which is generally discussed in terms of the detection limit. The detection limit is determined by the minimum detectable absorbance measured by the system:

$$A = \sigma n l_s = (1-R)\frac{\Delta\tau}{\tau} \quad \text{Eq 2.10}$$

$$A_{\min} = (1-R)\frac{3\sigma_\tau}{\tau_0} \quad \text{Eq 2.11}$$

where $\Delta\tau$ is the difference between τ and τ_0, the ringdown times with and without an analyte present in the cavity, respectively.[78, 103, 104] In order to determine the minimum detectable absorbance based on the 3σ criterion for analytical accuracy, $\Delta\tau$ is replaced with $3\sigma_\tau$, or three times the standard deviation of the measured ringdown time, and τ is replaced with τ_0, as given in Equation 2.10b. Based on this evaluation, higher mirror reflectivities and more stable baselines will generate better detection limits. Clearly, the physical parameters, such as mirror reflectivity, cavity length, and sample pathlength, as well as the ringdown baseline noise significantly affect the overall system stability and detection limits. These experimental features, in conjunction with any effects due to optical alignment of the ringdown system, can be grouped into the expression $\frac{\sigma_\tau}{\bar{\tau}}$, or the ringdown baseline noise. A typical pulsed laser CRDS system generates baseline noise on the order of 0.3 – 0.5 % when 100 pulses are averaged. Continuous wave (CW) CRDS systems can experience baseline noise on the order of 0.05 – 0.1 % with single shot measurements, as will be discussed in the respective chapters.

2.4 Experimental Systems

2.4.1 Cavity Design and Considerations

As previously stated, a typical RDC consists of two highly reflective mirrors. However, there are additional factors which must be taken into consideration when designing a stable ringdown cavity. For example, the mirrors utilized must be of the proper shape, spacing, and coating for the desired wavelength region. In the initial

studies introducing the CRDS technique, two 1 m radius, 1" optics, spaced 1 m apart and coated for maximum reflection in the lower 600 nm range for studies of very weak atmospheric oxygen absorption, were employed. Since the inception of the ringdown technique, the optics have varied in size and shape to incorporate 0.5 " diameter mirrors to highly polished prisms to fibers with gratings inscribed in them to fiber loops. Ringdown cavities can be as small as 20 cm or larger than 2 m with standard optics, and ringdown cavities comprised of fiber loops can easily be several meters long. The coatings used in the various experiments are optimized for maximum reflectivity at the wavelength of interest. Typical reflectivities for ultraviolet (UV) and visible (Vis) transitions are > 99.99 %. The higher the mirror reflectivity, the longer the ringdown time will be, which leads to better baseline stabilities and better detection limits.

Two additional considerations which must be factored into the design are the pulse width of the laser and the mirror spacing. First and foremost, a typical ringdown cavity is a high-finesse etalon.[74, 105, 106] Therefore, the cavity will possess a discrete mode structure that is a function of the cavity design. For a ringdown cavity constructed from two concave mirrors with radius 1 (R_1) and radius 2 (R_2), stable cavity mode frequencies can be found by the following**Error! Bookmark not defined.**:[12, 96, 107, 108]

$$\nu = \frac{c}{2L}\left[n + (1+m+l)\frac{\cos^{-1}\sqrt{g_1 g_2}}{\pi}\right], \qquad \text{Eq 2.12}$$

where L is the distance between the mirror surfaces, and g_1 and g_2 are dimensionless quantities that are used to determine whether a cavity is stable: $g_1 = 1 - \frac{L}{R_1}$ and $g_2 = 1 - \frac{L}{R_2}$. A stable cavity will fit the following criteria: $0 < g_1 g_2 < 1$. The cavity modes are designated with n, l, and m, where n is the longitudinal mode and

is equal to $\approx \frac{2L}{\lambda}$, and l and m represent the transverse modes. Depending on the alignment of the cavity, one can preferentially excite the TEM_{00} mode, the lowest order mode, where l and m are both equal to 0. This is especially important in diode laser-CRDS because the different modes generate different ringdown times, and TEM_{00} excitation produces the longest and most stable ringdown times. When plane parallel mirrors are implemented, such that R_1 and R_2 are infinite, the Fabry-Perot etalon frequency transmissions are evident:

$$\nu = \frac{nc}{2L} \quad . \qquad \text{Eq 2.13}$$

Other higher order cavity modes can simultaneously be present. In general, the linewidth of a pulsed laser source is often longer than the frequency spacing and, therefore, will excite multiple cavity modes. For example, the linewidths of the pulsed lasers utilized in the research presented here are 0.08 cm^{-1} for the Nd:YAG-pumped dye laser at 380 nm and < 0.075 cm^{-1} for the Optical Parametric Oscillator (OPO) at 500 nm. For a 56.2 cm cavity, the frequency spacing for the TEM_{00} mode is 267 MHz (0.0089 cm^{-1}). As can be clearly seen in Figure 2.5, multiple modes will be excited with each laser pulse from a pulsed laser system. Because various modes are simultaneously excited, pulsed-CRDS work is usually reported as average values with typical stabilities on the order of 0.3 to 0.5 %. However, for a narrow linewidth continuous wave (CW) laser, only the frequencies which correspond to stable cavity modes are injected into the cavity. For the diode lasers utilized in this research, the typical laser linewidth was 20 – 30 MHz. For the previously mentioned cavity, the effect of injecting a 20 – 30 MHz linewidth pulse does not ensure excitation of a cavity mode, as shown by the dashed line in Figure 2.5. Therefore, by properly aligning the cavity, mode-matching the input laser beam to

the lowest order mode, and tuning the laser into resonance with the cavity mode, preferential excitation can be observed. Different cavity modes yield different ringdown times. For pulsed systems, this is somewhat unavoidable; proper alignment can minimize the effect, but not eliminate it. CW diode laser systems can achieve single-mode excitation and the resulting stabilities are on the order of 0.05 – 0.1 %.

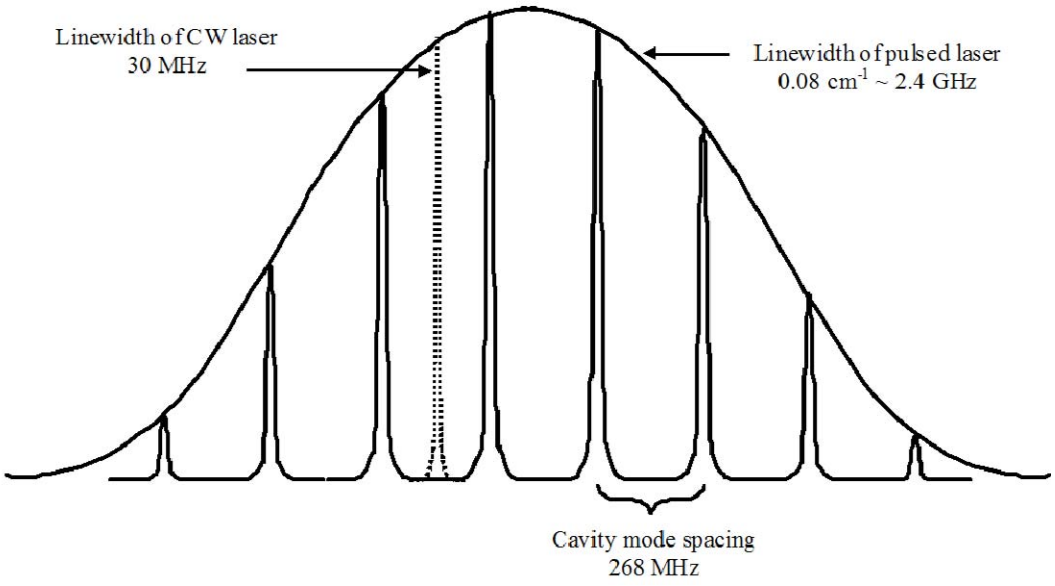

Figure 2.5 Laser linewidth vs cavity mode spacing.

For pulsed laser sources with GHz linewidth, multiple cavity modes are simultaneously excited. For narrow linewidth lasers, the laser or the cavity modes must be manipulated in order to ensure overlap.

An additional feature utilized in some of this research which affects the cavity design is the implementation of an atomization source for plasma-CRDS studies. Although various plasma configurations were explored, the basic premise remains the same: an atmospheric pressure plasma source is positioned directly in the center of the ringdown cavity to allow the sample pathlength to be drastically lengthened. As research

has shown, the position of the plasma inside the ringdown cavity is a critical parameter. Plasmas are not completely homogeneous,[109] and differences in flow rates/patterns, density distribution, and reactions of the sample in the plasma at various positions can generate drastic differences in baseline stabilities and detection limits. The ICP and the two MIP plasma sources, and their various configurations, which were employed in various phases of this research, were mounted on homemade 2-D adjustable mounts. The larger mount, utilized for the plasma torch studies, gave us +/- 0.5 mm resolution in the vertical and lateral axial directions and proved to be ideal for studies of plasma diagnostics and the analytical merit of the system with respect to the effects of laser beam position in the plasma, which will be the subject of Chapter III. For another line of research, discussed in detail in Chapter IV, we placed the compact microwave cavity on a large micrometer mount, which was affixed to a lab jack, to allow accurate and reproducible positioning of the plasma discharge tubes, such that the injected laser pulse readily traversed through specific parts of the plasma jet and sometimes through the plasma tube 'arms' when the plasma was generated in alternate plasma discharge tube configurations.

Another cavity configuration explored in this research consisted of a vacuum chamber which incorporated the ringdown mirrors as part of the vacuum seal. A 56.2 cm long stainless steel vacuum chamber was constructed to measure absorption cross-sections of volatile organic compounds (VOC's) in the near infrared (NIR) with readily available telecommunications diode lasers for proof-of-concept studies by the author for her master's thesis research. This vacuum chamber was then slightly modified and used to further the work on measuring VOC's with this technique. The ringdown mirrors were mounted in vacuum flanges which were secured in Gimble mounts affixed to the vacuum

chamber via flexible bellows at either end of the cavity, and the ringdown mirrors were seated on perfluorinated O-rings to form a seal between atmospheric and vacuum pressures. Significant attention was directed towards stabilizing the ringdown cavity from the vibrations induced by the pumping mechanism, torque on the cavity when operating the pump valve, and changes in the mirror's position when the vacuum chamber was pumped down or taken to atmospheric pressure, due to the constricting and expanding of the bellows. The vibrations were dampened by weighing down the diffusion/ mechanical pumps' cart and adding additional brackets almost everywhere two flanges were joined. This drastically improved the frequency-comb jitter observed on the oscilloscope. It was also determined that the valve separating the vacuum chamber and the pumping mechanism could not be opened/closed without introducing strain on the cavity; this issue was remedied by inserting a 2" I.D., 18" long flexible metal bellows between the cavity and the valve. With this configuration, the valve extended beyond the optics table. 0.25 " stainless steel L-brackets were attached to the optics table and the stabilizers for the valve were clamped to the L-brackets. This approach was extended to the flanges connecting the bellows, valve, and liquid nitrogen-cooled trap, which also helped reduce the vibrations from the pumping system. Tackling the stabilization of the ringdown mirrors as a function of pressure in the chamber was part physics and part technique. The base of the Gimble mounts were securely fastened to home-made aluminum blocks which were, in turn, bolted to the optics table; this modification from the standard optics posts significantly reduced drastic changes in alignment due to changes in the pressure in the cavity. The positioning of the blocks was critical to obtaining reproducible and stable ringdown times. Once the optimal position was

determined, the system was locked down, and stable, reproducible ringdown times were readily obtained with the proper alignment of the laser in the ringdown cavity.

2.4.2 Laser Sources

CRDS can be successfully implemented with both pulsed and CW lasers and over a wide range of wavelengths.[69, 110, 111] In this research, pulsed lasers and various CW lasers have been employed in CRDS studies, spanning from the UV into the NIR. The pulsed lasers consist of a Radiant NarrowScan dye laser pumped by a Continuum Nd:YAG laser (Powerlite 8020) and a SpectraPhysics Optical Parametric Oscillator (OPO) laser (MOPO-HF) pumped by a QuantaRay Nd:YAG laser (Pro-290-10). The CW lasers include telecommunications distributed feedback (DFB) diode lasers (Thorlabs), an external cavity tunable diode laser (ECDL) from Newport (Model 2010A), two blue diode lasers (Toptica, Inc. and CrystaLaser), and a visible diode laser manufactured by Newport. Output powers varied from 100 mW for the OPO system at 266 nm to 2 mW for the diode lasers at 1650 nm. Telecommunications diode lasers have been increasingly implemented in CRDS studies because of their relatively low cost and size, as well as their high resolution and narrow linewidth. Laser linewidth is a critical parameter in absorption spectroscopy. For instance, if the linewidth of the laser is large, as compared to the transition linewidth, isotopic shifts and hyperfine structures of an atomic transition can be averaged in and, therefore, not observed. Also, large linewidths can cause the absorption to be inaccurately detected, generally, undermeasured. For the lasers utilized in this research, the dual grating Radiant NarrowScan has an output linewidth of 0.08 cm^{-1} at 590 nm and 0.03 cm^{-1} at 570 nm, the OPO has a linewidth of 0.075 cm^{-1} at 500 nm, and the diode lasers were typically in the kHz to MHz range,

where 1 cm^{-1} = 30 GHz; clearly offering very high resolution capabilities. Typical atomic transition linewidths are relatively narrow, and even under high temperature plasma conditions, a transition linewidth is still only ~0.4 cm^{-1}. Clearly, high resolution spectroscopy can only be achieved with narrow linewidths for accurate detection and measurement.

When implementing laser sources, the particular wavelength of the transition must be accessible by the laser and the corresponding optics. For the studies reported in this research utilizing the CW lasers, commercially available telecommunications diode lasers operating at 1550 and at 1650 nm were implemented to study the asymmetric C-H stretching overtone of multiple volatile organic compounds (VOC's). The blue diode was used to excite the 409 nm line of uranium. The red diode was employed to study the 680 nm Sr line. The NIR diode was used in the fiber studies for pressure sensors. The MOPO-HF system can generate wavelengths from ~ 225 nm into the mid-IR without the use of dyes, but this system can be somewhat temperamental, especially when operating at the 'edge' of the nonlinear crystals, such as the deep UV wavelengths and the UV-VIS transition region. We utilized the MOPO-HF system for preliminary Hg (254 and 405 nm) and acetone and isoprene (260-275 nm) measurements. For plasma-CRDS, the majority of the atomic transitions studies presented herein are in the UV, which was generated by frequency doubling the output of the pulsed dye laser with an INRAD AutoTracker or the signal portion of the OPO. When obtaining UV wavelengths with the pulsed dye laser, dye solutions had to be carefully prepared to generate the desired wavelengths. The dyes can be messy, carcinogenic, and mutenagenic, and some have fairly short lifetimes. This technique was explored for studies of Hg at 254 nm, OH at 308 nm, and U at 409 nm.

In some studies, a 0.5 m Princeton Instruments/Acton triple grating spectrometer was simultaneously incorporated to record the emission spectra while the CRDS spectra were being obtained. This greatly aided in plasma diagnostic studies as well as in determining the behavior/best positions to observe the atoms/ions in the plasma for ringdown measurements. A Burleigh deep UV wavemeter (WA-5500) was also used in multiple studies to monitor the laser wavelength during the ringdown acquisitions. This was especially useful as the dyes degraded from usage and with the implementation of a new dye, as well as for the blue diode laser studies because the blue diode readily mode hopped to different frequencies.

2.4.3 Electronics

The electronic controls implemented in CRDS are ultimately an artifact of the laser source utilized. For pulsed-CRDS, where the bandwidth of the laser is multiple times larger than the free spectral range (FSR) of the ringdown cavity, laser light injected into the cavity will excite several cavity modes simultaneously, thereby, circumventing the need for additional electronic parts to achieve efficient cavity excitation, and the pulse effectively controls the shut off of the input laser radiation to allow the ringdown event to occur. In most of our experiments, we incorporated a mode-matching telescope to image the beam into the cavity to reduce the number of extraneous cavity modes excited. Figures 2.6 and 2.7 portray the experimental setups employed for each pulsed-CRDS system explored in this research. When narrow linewidth diode lasers were used, additional electronic controls were needed to tune the laser into resonance with a cavity mode in order to excite specific cavity modes. Overlap between the input laser pulse and the cavity mode can be achieved by modulating the laser current to change the laser

frequency, modulating the ringdown cavity to change the cavity mode spacing, or a combination of the two. Figures 2.8 and 2.9 display the setups implemented in the various diode laser studies. By specifically designing the ringdown cavity mirror spacing and tuning the laser across one particular mode, preferential excitation of that one mode can be obtained. In our research, we mode-matched the input beam to the cavity's TEM_{00} modes, and excitation of these modes generated a very stable and reproducible comb-like transmission spectrum as the laser frequency was modulated. By properly aligning the cavity, the comb-like transmission spectrum was maximized such that any other higher order modes present were insignificant. We explored current modulation to change the laser frequency to achieve this. The additional electronics are necessary to not only obtain the overlap but to rapidly shut off the excitation to allow the ringdown event to take place and be recorded.

Once sufficient laser intensity builds up in the ringdown cavity causing the threshold electronics to be triggered, the laser wavelength is rapidly changed out of resonance, which effectively shuts off the cavity excitation. The detector output was sent to a Stanford Research Systems, Inc., digital delay/pulse generator, which was used to set the threshold trigger level, and then displayed on a Tektronics TDS 430A digital oscilloscope. In some of the experiments, a secondary scope, Tektronics TDS 3012, was employed to display the mode patterns excited in the cavity, while the 430A was used to observe the single exponential ringdown waveforms. For diode lasers in which the current and frequency are independent of one another, effectively shutting off the cavity excitation is relatively straight-forward: once the trigger threshold pre-set on the pulse generator is reached, the pulse generator rapidly decreased the current while the function generator maintained the frequency. When the current is below the manufacturer's set-

point, the laser is effectively off, thereby allowing a 'pulse' of CW light to be injected into the ringdown cavity. For diode lasers in which the current and frequency are not independent of one another, a little more involved process was implemented, in which the output of the function generator is coupled with the output pulse from the pulse generator, via a Mini-Circuits ZFRSSC-2050 signal combiner, to rapidly change the laser current, as illustrated in Figure 2.10.

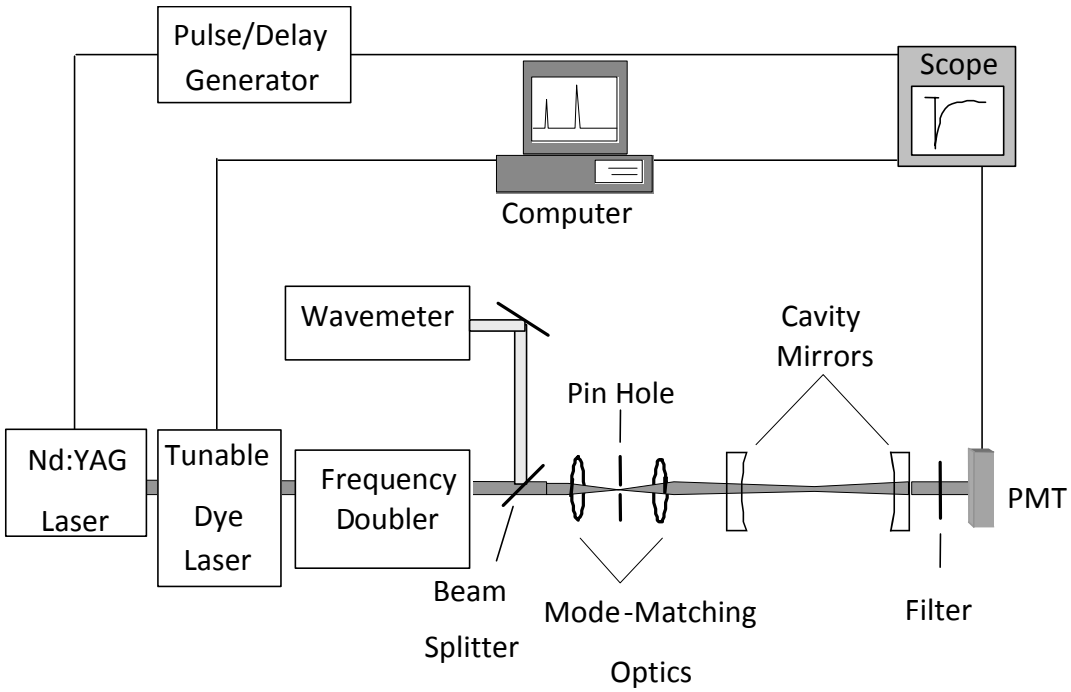

Figure 2.6 Experimental configuration utilized with pulsed-CRDS using the frequency-doubled output of a dye laser pumped by a Nd:YAG laser.

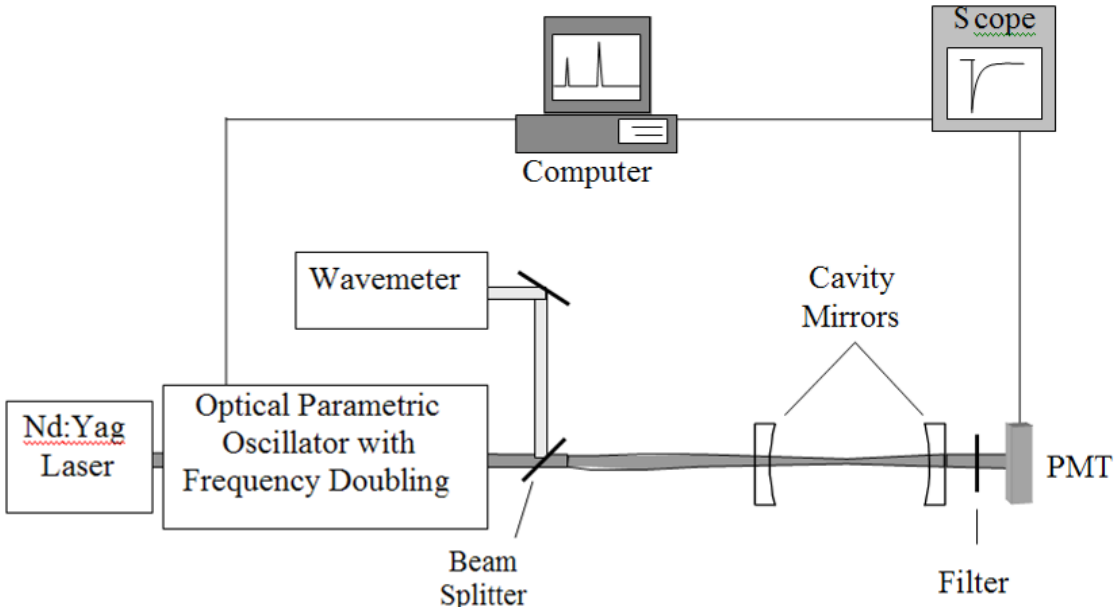

Figure 2.7 Experimental configuration utilized with MOPO-CRDS.

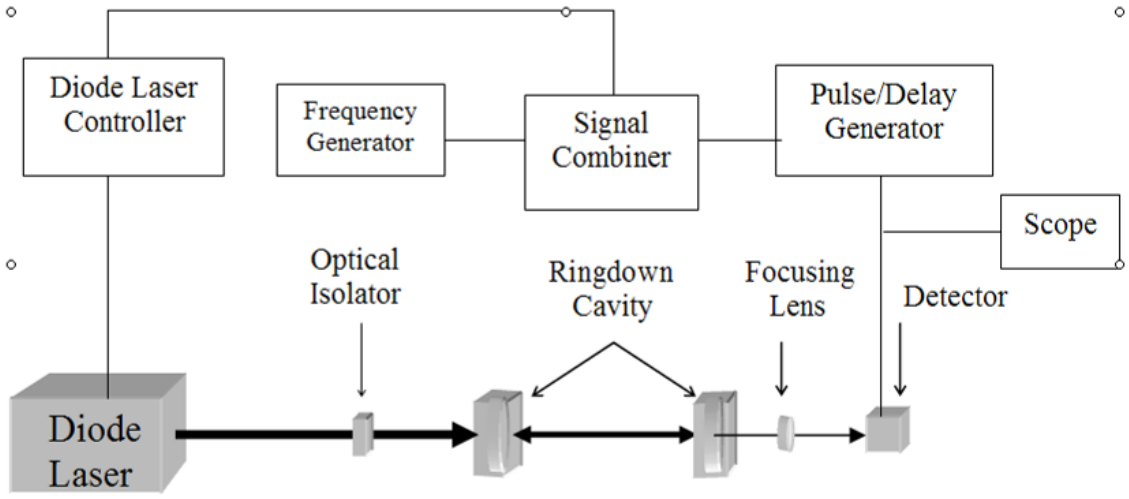

Figure 2.8 Experimental configuration employed with the diode lasers in which the intensity and frequency were not independently controlled.

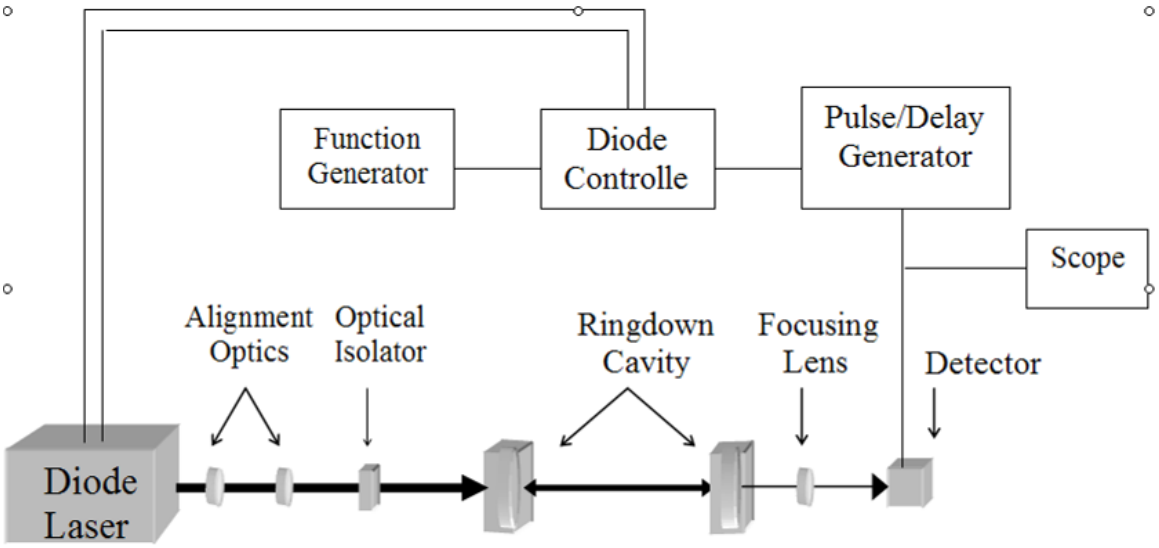

Figure 2.9 Experimental configuration employed with the diode lasers in which the intensity and frequency were independently controlled.

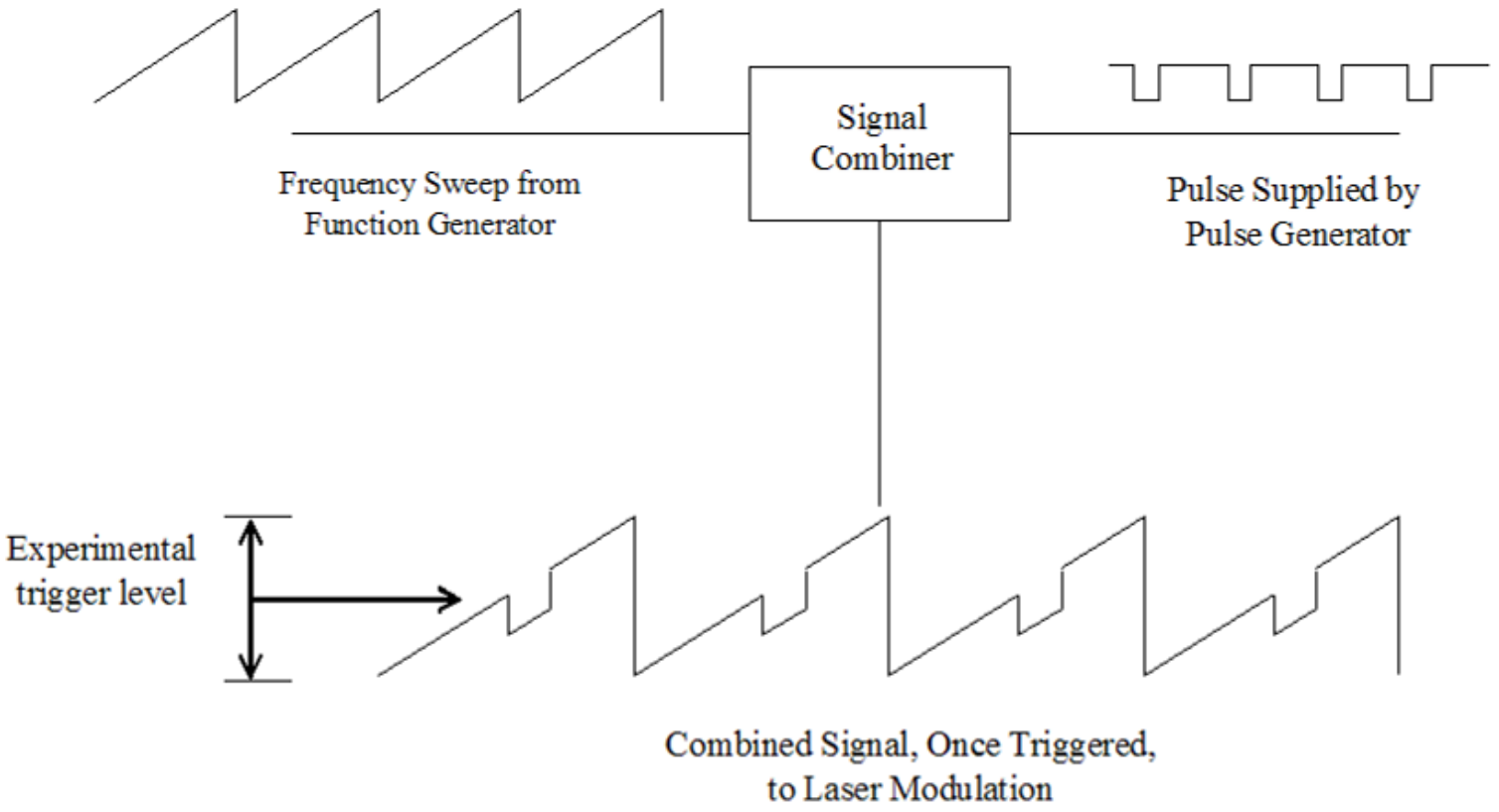

Figure 2.10 CW diode laser 'pulse' when current and frequency are not independently controlled.

The signal combiner couples the input from the function generator with the pulse generator output to rapidly drop the current to the diode, thus changing the wavelength and intensity, when triggered.

2.4.4 Data Acquisition

Proper data handling is a critical parameter in obtaining meaningful and reproducible data. This has been the subject of several current publications.[112, 113] In addition to the ringdown signal, a small digital current (DC) offset voltage, correlated to the gain of the photodiode being employed, was almost always present in the diode laser CW data, which significantly affected the results. Initial efforts for both the pulsed and CW studies incorporated a manual subtraction of the offset, and very linear calibration plots were generated. However, the slopes of the graphs generated to calculate the absorption cross-sections were observed to drift from day to day with the CW studies, sometimes as much as 50 % while generating linear fits (R^2 values) of 0.9999. Once all the other possible sources for this discrepancy, e.g., sample introduction, vacuum chamber robustness, beam steering, beam shape, temperature effects, etc., were ruled out, we determined that a more advanced treatment of the ringdown data was necessary to remove this artificial drift.

As previously mentioned, the ringdown signal is detected by the PMT or PD, and this signal is monitored by a digital oscilloscope interfaced to a computer via a GPIB (IEEE 488) cable. The ringdown waveform is digitized by the scope and interpreted by in-house designed ringdown software loaded on the personal computer (PC). The ringdown software fits the ringdown waveform to a single exponential function to determine the ringdown time. Because of various experimental artifacts, e.g., laser intensity fluctuations, beam steering, electronic noise, etc., shot-to-shot variations in ringdown signals can be easily compensated for by averaging multiple waveforms. With pulsed systems, we generally averaged 50 – 100 ringdown waveforms. With CW

systems, we either obtained data as single waveforms or averaged ten decay waveforms, depending on the experiments. Another benefit of averaging the ringdown signals is the improvement in signal-to-noise (S/N) ratio. For our pulsed-CRDS experiments, the intensity decay was fit to a first-order single exponential decay function: $y = ae^{-\left(\frac{x}{b}\right)}$. With the pulsed system, the drift in the calibration graphs was not readily observed. For most of the CW-CRDS experiments, a more involved approach was needed because of the persistent drift in our calibration plots. We believed that this artifact is primarily an electronic noise that is amplified by the detector and/or the combination of electronics incorporated in the shut off method for these studies. Therefore, after several different trials, we chose to import the raw waveforms into a commercially available software package, SigmaPlot, to fit the ringdown curve to the following: $y = y_0 + ae^{-\left(\frac{x}{b}\right)}$. This yielded highly reproducible and much more accurate results. Employing this approach, the standard deviation of the reproducibility of the measured absorption cross-sections jumped to 0.1 %. The importance of careful consideration to the curve-fitting method utilized in, especially, CW-CRDS studies cannot be overstated.[114]

2.4.5 Sample Devices

The method of sample delivery varied for the different projects. For the VOC studies, very low concentrations of pure vapor phase samples were introduced in the vacuum cavity by implementing the freeze/thaw technique and recording the pressure, which is proportional to the concentration, of the sample introduced into the chamber. A schematic for the sample introduction chamber is depicted in Figure 2.11. For the plasma-CRDS experiments, the standard 1000 μg/mL stock solution of the compound(s) of interest were dissolved in an acidic 'blank' solution (2 % by volume (v/v) nitric acid)

and dilutions of each solution were made to study different concentrations of the sample. The sample solutions were pumped into an ultrasonic nebulizer (CETAC U-5000 AT+), via a Gilson peristaltic pump, to generate an aerosol. This vapor phase sample was then injected into the plasma, after passing through a series of molecular sieves to remove any/most of the residual water vapor, which affected the stability of the plasma and the background signal and, in turn, the S/N ratio. This configuration is portrayed in Figure 2.12. Using this technique, the conversion efficiency was ~ 10 to 15 %. Care must be taken between samples because residual effects were observed, especially with Hg. For the U studies, the sample tubing was flushed with a 20 % v/v acid solution; for Hg solutions, low concentrations of gold solution were used to amalgamate the residual mercury adsorbed to the sample tubing walls.[115, 116, 117] For the studies concerning Hg naturally evaporating from contaminated soils and solutions, the samples were placed in a variety of open air vessels directly under the ringdown path to allow the mercury vapor to enter into the path of the laser light to be detected; no sample pre-concentration or manipulation was necessary. Some of the sampling devices used for these studies are shown in Figure 2.13. The first device is an aluminum 'bomb' which was designed to allow Ar to bubble through solutions placed in beakers inside the chamber. This configuration allowed the sample chamber to be wrapped in heat tape in order to manipulate the temperature in the chamber. The middle component is a 50 cm long stainless steel channel with the ends welded closed and a slit which runs the length of the tube. This configuration allowed mercury solutions to be placed in the channel without leaking and allowed the mercury vapor to enter the ringdown cavity unimpeded. The third pictorial is a set of Petri dishes which were used with the second laser system. The

specifics of each individual experiment will be addressed in the chapters correlating to the particular study.

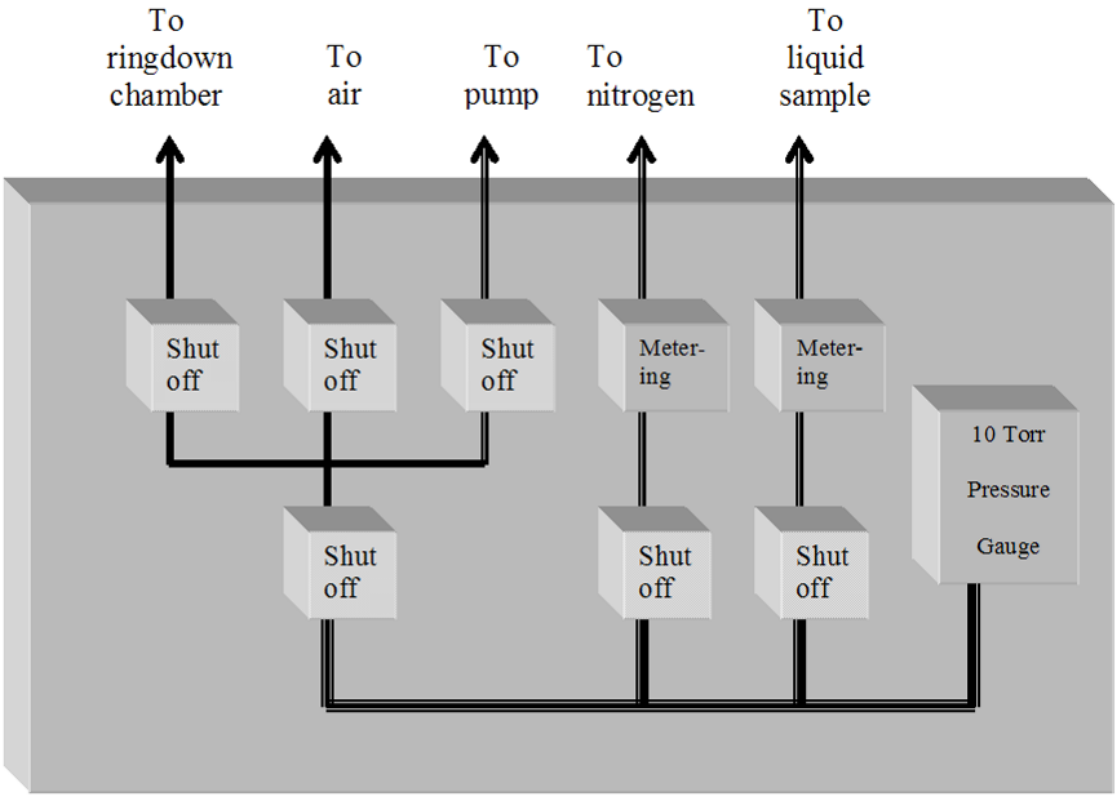

Figure 2.11 Sample introduction for VOC studies.

The liquid samples were placed in a sample tube, connected to the vacuum system. After the headspace was evacuated during a freeze/pump/thaw cycle, the sample was metered into the ringdown cavity.

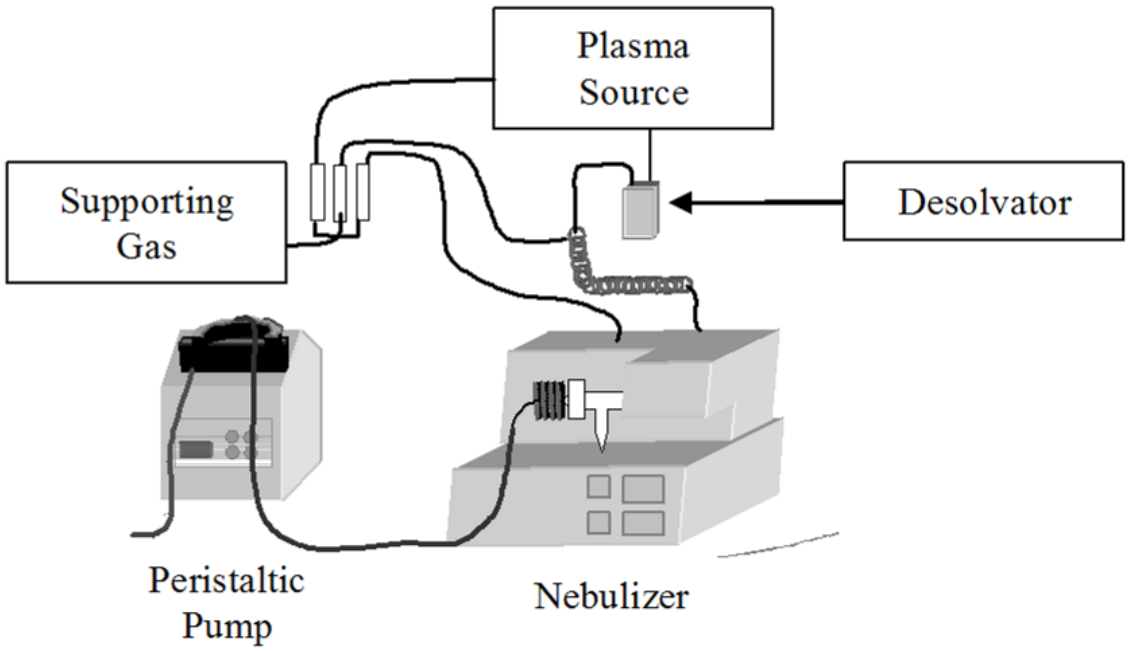

Figure 2.12 Sample introduction for atomization sources.

The liquid samples were pumped via a persistaltic pump to an ultrasonic nebulizer. The vapor sample was then carried to the atomization source through one or more molecular sieves.

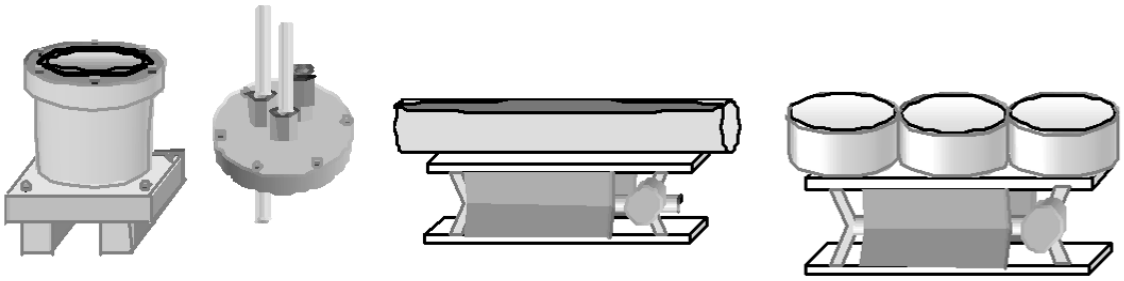

Figure 2.13 Sample cells utilized in Hg naturally evaporating from contaminated soils and solutions.

CHAPTER III

CAVITY RINGDOWN MEASUREMENTS OF ELEMENTAL MERCURY AND ITS ISOTOPES AT 254 NM USING A COMPACT ATMOSPHERIC MICROWAVE PLASMA AS THE ATOMIZATION SOURCE

3.1 Introduction

In the research presented in this chapter, the high sensitivity of the plasma-CRDS technique utilized to measure elemental mercury and its stable isotopes at the 254 nm transition is described. In order to reduce operating costs and move towards a more compact instrument design, the experimental configuration was modified to accommodate a microwave-induced plasma (MIP), as opposed to the inductively coupled plasma (ICP) used in previous studies in this laboratory.[118] Experimental considerations, such as background spectral interference, optimum plasma operating conditions for Hg detection, and beam position relative to the plasma, were thoroughly explored in order to obtain maximum sensitivity with the given experimental parameters.

3.2 Experimental Setup

The MIP-CRDS system, depicted in Figure 3.1, was comprised of four overall sections: the optical system, plasma source, sample introduction system, and data acquisition. Each of these components will be described in detail; however, the plasma source was initially tested and utilized in this laboratory for other studies, so the more detailed description of the MIP utilized in this research will be presented in the chapter referring to the U-plasma-CRDS studies, Chapter VI and references therein.

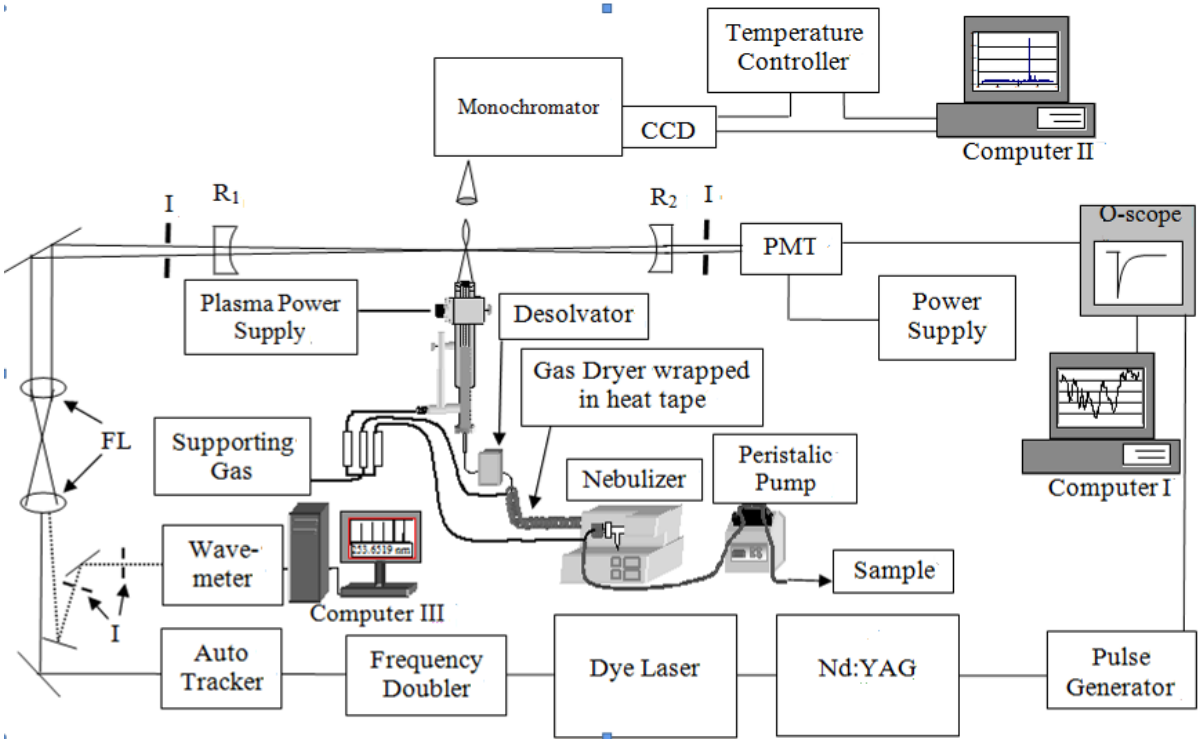

Figure 3.1 Experimental configuration employed with the candle-shaped MIP-CRDS system.

The output of a Nd:YAG-pumped dye laser is frequency doubled to generate the appropriate UV wavelengths; the resulting beam is telescoped with a pair of lenses (FL) into the ringdown cavity, which is comprised of two high reflectivity mirrors (R_1 and R_2), and is then detected by the PMT. A reflection off the telescope was injected into the wavemeter to monitor the wavelength (Computer III). Irises (I) were positioned to reduce feedback and assist in optical alignments. Computer I is used to control the dye laser stepping parameters and to record the changes in ringdown time. Computer II is used to monitor the presence of mercury in the plasma.

3.2.1 Optical Configuration

The 254 nm UV output utilized in this research was generated by frequency doubling (INRAD AutoTracker III) the output of a Radiant NarrowScan dye laser, which was pumped by a 20 Hz repetition rate Continuum 8020 Nd:YAG laser operating at 355 nm. Coumarin 507 (Exciton, Inc.) was chosen as the laser dye, and the output power was ~ 1 μJ. The minimum scanning step of the dye laser in the UV is 0.0003 nm, and the laser linewidth in the UV is ~ 0.08 cm^{-1}, as extrapolated from the < 0.05 cm^{-1} linewidth at 590 nm. A small portion of the UV radiation was then directed into a UV pulsed wavelength meter (Burleigh/ EXFO WA-5500) to allow the wavelength to be continuously monitored during the experiments. The remaining portion of the UV radiation was imaged with a telescope into the ringdown cavity (RDC), which was formed by a pair of 6 m radius, high reflectivity mirrors (Los Gatos Research, Inc.) spaced 78 cm apart. The reflectivity at 254 nm was quoted to be > 99.75 %, but the actual mirror reflectivity was measured to be 99.67 % due to degradation of the coating after extensive use and potentially repeat exposure to high temperatures and radiation generated by the MIP and previous work utilizing an ICP. The optical signal passed through a 10 nm bandpass interference filter (CVI Laser), which was mounted onto the front of a photomultiplier tube (PMT- Hamamatsu R928), to reject emissions from the plasma prior to detection by the PMT. The plasma performance was monitored by recording the emission spectra of mercury as well as the plasma background spectra with a triple-grating monochromator (Princeton Instruments/ ActonSpectraPro-500) coupled with a temperature-controlled charge-coupled device (CCD) array (Princeton Instruments

TEA/CCD-1024). The mercury MIP-CRDS studies utilized the 2400 grooves/mm grating which provided 0.03 nm resolution in its first order.

3.2.2 Plasma Source and Operating Conditions

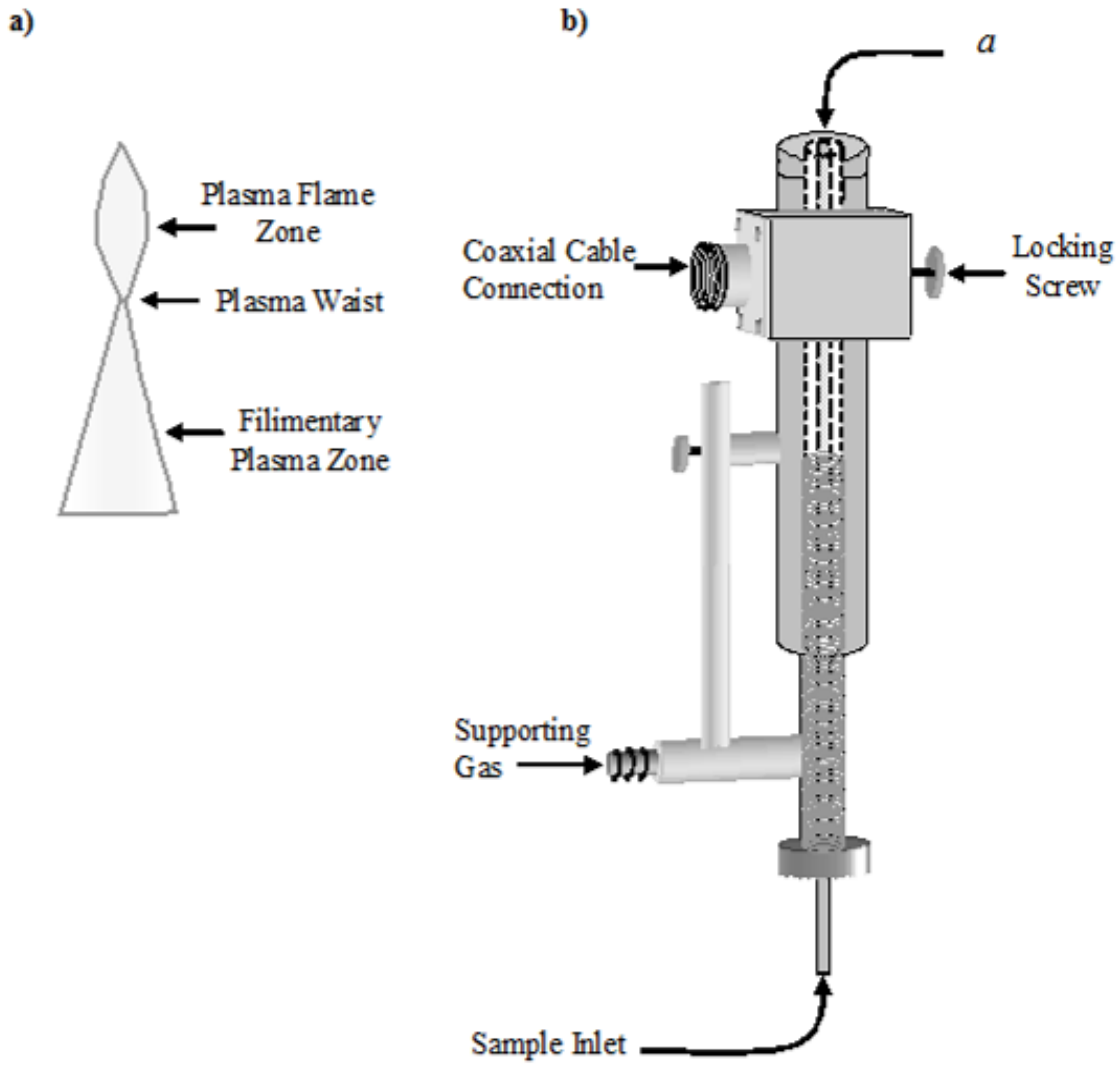

Figure 3.2 a) Plasma shape and b) candle-shaped MIP torch configuration.

A candle-like shape was obtained with the MIP used in these studies. The waist, flame zone, and stability were significantly dependent on the experimental parameters of the operational plasma, such as plasma power, flow rates, and coupling of the coaxial cable and antennae to the interior of the plasma chamber.

In order to effectively implement MIP-CRDS, there were several plasma parameters that had to be optimized for Hg detection. The plasma utilized in this research as the atomization source generated a candle-like shape, sketched in Figure 3.2a. The height, stability, and overall shape of the plasma were significantly affected by the power setting, the supporting gas and the sample gas flow rates, and the presence or absence of a sample and/or moisture. The MIP torch, shown in Figure 3.2b, was connected to a 2450 MHz microwave power supply (Meteix, Inc.) and was ignited by use of a model BD-10A, 120 Volt high frequency generator (ElectroTechnic Products, Inc.). The plasma was positioned in the approximate center of the ringdown cavity and, to prevent human exposure to the vaporized elements and the emitted microwaves, was housed in a metal container with side ports to allow the laser to traverse the ringdown path while interacting with the plasma and accommodate the power supply connection, a cutout in the bottom of the metal housing to allow the plasma gas flow and sample injection lines to be introduced to the plasma, and a cutout in the top, centered over the plasma, where an evacuation vent line was connected.

The entire metal chamber was positioned on a homemade x-y mount to allow the vertical, y, and lateral, x, positions to be adjusted with a spatial accuracy of ± 0.5 mm. Because of the inhomogeneous distribution of electrons in the plasma, the ability to reproducibly position the plasma, relative to the laser beam, was crucial. The laser was typically positioned to pass directly over the center of the sample injection orifice of the plasma, which is the smallest and center-most metal tube of the concentric tubes hosting the gas flows, labeled as '*a*' in Figure 3.2b. For this experiment, the height of the laser beam in the plasma is defined as the distance between the center of the laser beam and the surface of the plasma torch. This distance was measured by removing the first

ringdown mirror and manipulating the height of the plasma torch until the beam was focused directly on the top surface of the torch. In order to accurately center the beam over the plasma and generate reproducible heights relative to the torch surface, a wedge-shaped insert was made and was marked from 0 to 25 mm, with 0 correlating to the rim of the torch. This wedge was inserted into the sample injection tube of the plasma torch (*a*), and the plasma could be readily and reproducibly positioned relative to the laser for the vertical and horizontal scans; additionally, this approach allowed the laser to be reproducibly positioned relative to the plasma for fresh alignment of the optical system, which were generally performed with each dye change. From an experimental point-of-view, the "0" height was practically realized by setting the y = 0 as the position in which the ringdown signal was approximately 40 % of the fully triggered signal, and an advanced system of rulers, external to the plasma housing, was used to determine the experimental change in height of the plasma relative to the optics table; this allowed consecutive experiments to be conducted without necessitating a new cavity alignment for every incremental change of height or lateral repositioning. At the end of several series of height adjustments, the first ringdown mirror was removed and the height was checked on the wedged insert to ascertain reproducible heights were being recorded.

3.2.3 Standards and Reagents

Mercury sample solutions were prepared by diluting a standard 1000 μg/mL Hg solution (Absolute Standards, Inc.) with a 2 % v/v nitric acid solution. The sample solutions were pumped via a Gilson peristaltic pump at 0.75 mL/min to an ultrasonic nebulizer (CETAC U-5000AT^{+}) to generate an aerosol. The heating temperature of the nebulizer chamber was 140 °C, and the cooling temperature of the ultrasonic nebulizer

chamber was -5 °C. The aerosol generated by the nebulizer was carried by argon gas (ultra-high purity argon, 99.999 %, Airgas, Inc.) through a hydrophilic, semi-permeable membrane and into a molecular sieve to remove moisture vapor present with the sample before being injected into the plasma torch. Typical gas phase conversion efficiencies for this system were ~ 10 %. The portion of the sample solution which did not produce an aerosol was collected in residual waste containers. To prevent extraneous Hg signals, the waste containers were closed at all times during data acquisition and a tube was inserted through the cap and sealed off around the edges. This allowed the continuous collection of waste without exposing the surrounding environment to Hg vapor, which also interfered with the true mercury measurements, especially when calibration curves and detection limits were trying to be determined.

In order to ensure proper removal of the plasma exhaust, a ventilation system was erected directly over the plasma's shielding container. The sample containers, peristaltic pump, and nebulizer were housed in a Plexiglass cabinet, which was also continually vented by the aforementioned ventilation system. The mercury samples were found to strongly interact with the tubing, a combination of tygon and nalgene, used to transport the aerosol sample from the nebulizer to the drying chamber and finally to the plasma torch. To circumvent the 'memory effect' exhibited by the system, a 100 ppb gold solution, diluted from a standard 1000 ppm gold stock solution (Absolute Standards, Inc.), was prepared to adequately remove the residual Hg in the sample tubing after each experiment. In order to ensure that residual mercury was not present prior to each new ringdown measurement, the plasma emission was monitored with the spectrometer. When the gold solution had effectively bound the mercury, the signal dropped to typical baseline values. One point to note is that after each gold flush, the system was flushed

with deionized (DI) water and the 2 % nitric acid solution to remove residual gold, which affected the subsequent mercury measurements, especially for low mercury concentration samples. A certified environmental professional regularly disposed of the solid waste and residual Hg solutions.

3.2.4 Data Acquisition

The ringdown signal from the PMT was monitored by an oscilloscope (Tektronix, TDS 410 A) that was interfaced to a computer via a GPIB interface for data processing. The PMT generally operated around 400 V for a fresh dye solution and around 500 V towards the end of the dye lifetime. In-house software was used to determine the ringdown time constant. Each data point, i.e., a single ringdown time, was generated by averaging 50 - 100 ringdown events. Because of the interference of mercury from the overhead lights, all the data were accumulated with the lights off to limit extraneous mercury signals.

3.3 Results and Discussions

3.3.1 Broad Spectral Scan around 254 nm under Ambient Conditions

In order to investigate potential spectral interference from atmospheric constituents, a high-resolution broadband scan under ambient conditions without the plasma operating was performed. The spectrum generated, shown in Figure 3.3, is the compilation of three individual scans, spanning the accessible wavelength regions of the laser dye under the given dye concentrations. In these scans, the laser stepped ~ 0.001 nm per 20 trigger events. There were two major contributing factors to which we had to contend in these long wavelength scans. 1) The increased noise, evident in the higher wavelength (lower wavenumber) region, is a by-product of the laser dye limitation for the

given concentration. This portion of the scan was performed on the outer limits of the wavelength accessible region of the dye without changing the concentration. While modifying the dye concentration is a relatively straight-forward procedure and was briefly explored, doing so necessitated new scan parameters and calibrations, which were not heavily undertaken since the long wavelength scan was not the intended focus of this project. 2) The second competing factor is that the portion of the scan obtained in the lower wavelength (higher wavenumber) region of the figure is near the operational limit of the quoted reflectivity range of the ringdown mirrors. Therefore, the lower wavelength region in the spectra obtained and portrayed in Figure 3.3 has been baseline offset for clarity. In the effective upper wavelength range of the laser dye concentration probed, the laser wavelength was in more favorable overlap with the mirrors' higher reflectivities, thereby negating the need to apply any baseline modification for the scans obtained in the higher wavelength region.

A 'raw' compilation spectrum is shown in Figure 3.4 to delineate the distinct change in ringdown time over the course of these scans. As can be seen in the figure, a 0.14 % change in the effective mirror reflectivity results in a significant change in the experimental ringdown time. This spectrum[36] has been assigned to the Herzberg I bands (7,0) and (8,0) of the O_2 $A^3\Sigma_u^+ - X^3\Sigma_g^-$ system. These scans were repeated several times and the reproducibility of the spectral features and the spectral intensity distribution were noteworthy. The reproducibility of the system can be readily observed in Figure 3.3 by examining the N″ = 19 line, where two scans, depicted in different line weights, were intentionally overlapped. All of the spectral lines have been assigned, and under the atmospheric laboratory conditions, no spectral absorptions attributed to other atmospheric molecules were observed. According to the MIT wavelength tables,[119] the Hg transition

of interest, 6 $^3P_1 \rightarrow 6\ ^1S_0$ is located at 253.6519 nm. The peak of the 254 nm Hg transition is located between two rotational Q branches with rotational quantum numbers N″ = 19 and 21. As indicated in Figure 3.3b, under ambient conditions, there are no spectral interferences at the mercury transition from atmospheric constituents.

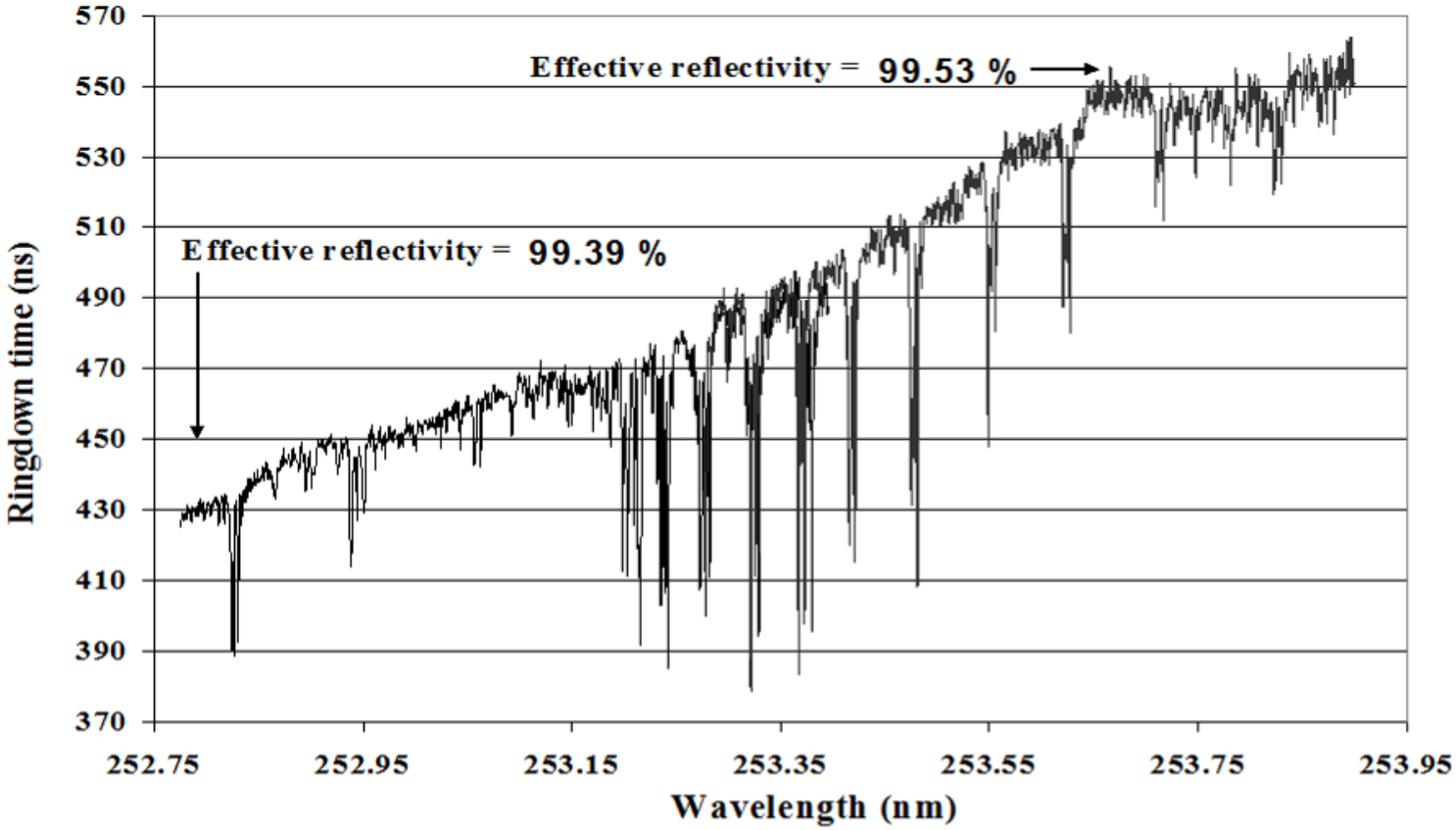

Figure 3.3 Long wavelength scan around the 253.6519 nm mercury transition line – raw spectrum, no plasma.

Towards the lower wavelength region of this scan, the operational limits of the ringdown mirrors were tested. This artifact is evident in the rapid decrease in ringdown time while the baseline stability is approximately constant. Towards the upper wavelength region of this scan, the operational limits of the dye concentration were reached. This is displayed in the significant increase in baseline noise while the ringdown time is approximately constant.

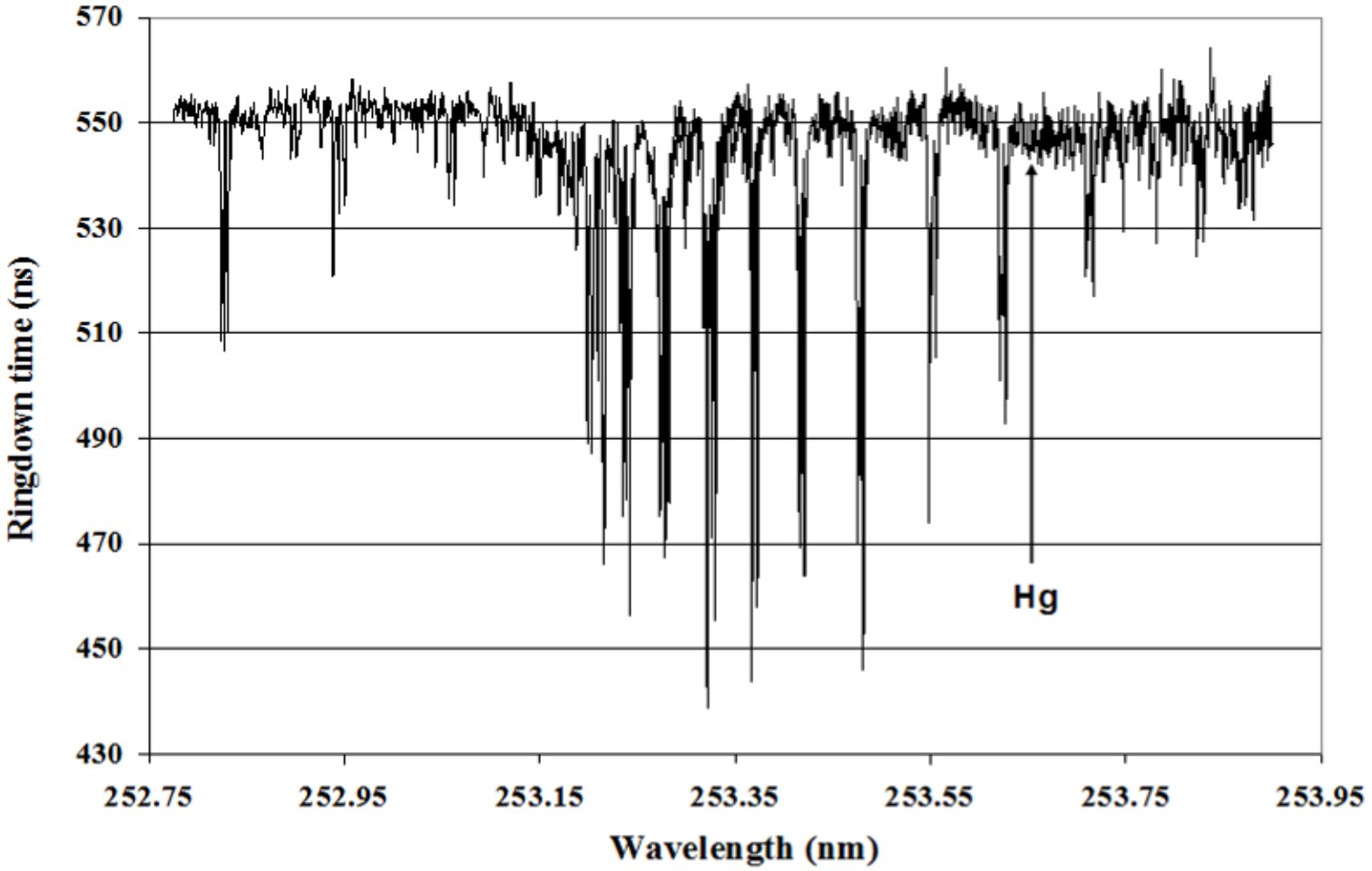

Figure 3.4 Long wavelength scan around the 253.6519 nm mercury transition line – baseline corrected.

Due to the finite reflectivity of the ringdown mirrors and the operational limits of the dye concentration used, the baseline of the long wavelength scan was offset for visual clarity.

3.3.2 Background Spectral Scan around 254 nm with Plasma Operating

Once the question of interfering atmospheric molecules had been eliminated, the next factor addressed was obtaining background spectral scans while operating the plasma. Utilizing the candle-shaped MIP, an interesting background interference pattern was observed. High-resolution spectra obtained in the 253.56 – 253.74 nm spectral range are illustrated in Figure 3.5. As can be seen in Figure 3.5a, there is no discernable spectral interference around the Hg transition line when the plasma is not operating; however, the spectrum obtained with the plasma ON, with no blank solution or sample present, tells a different story. Figure 3.5b depicts a high-resolution scan obtained when the plasma was operating with only the argon supporting gas introduced into the plasma. The left-hand portion of the two spectra have been attributed to the Q branch of the O_2 $A^3\Sigma_u^+ - X^3\Sigma_g^-$ (7,0) band around N″ = 19; the specific assignments are denoted in the upper spectra. Subsequent scans were then obtained with the plasma 'on' and with a blank solution (2 % v/v nitric acid) injected in the plasma to observe any change in the background, relative to the scans recorded with only the plasma operating. A typical high-resolution scan with the plasma operating with the blank solution being injected is portrayed in Figure 3.5c. Clearly, there is no discernable difference between the spectra in Figures 3.5b and c, and the four prominent peaks, in addition to the already assigned O_2 peaks, were present and reproducible

.

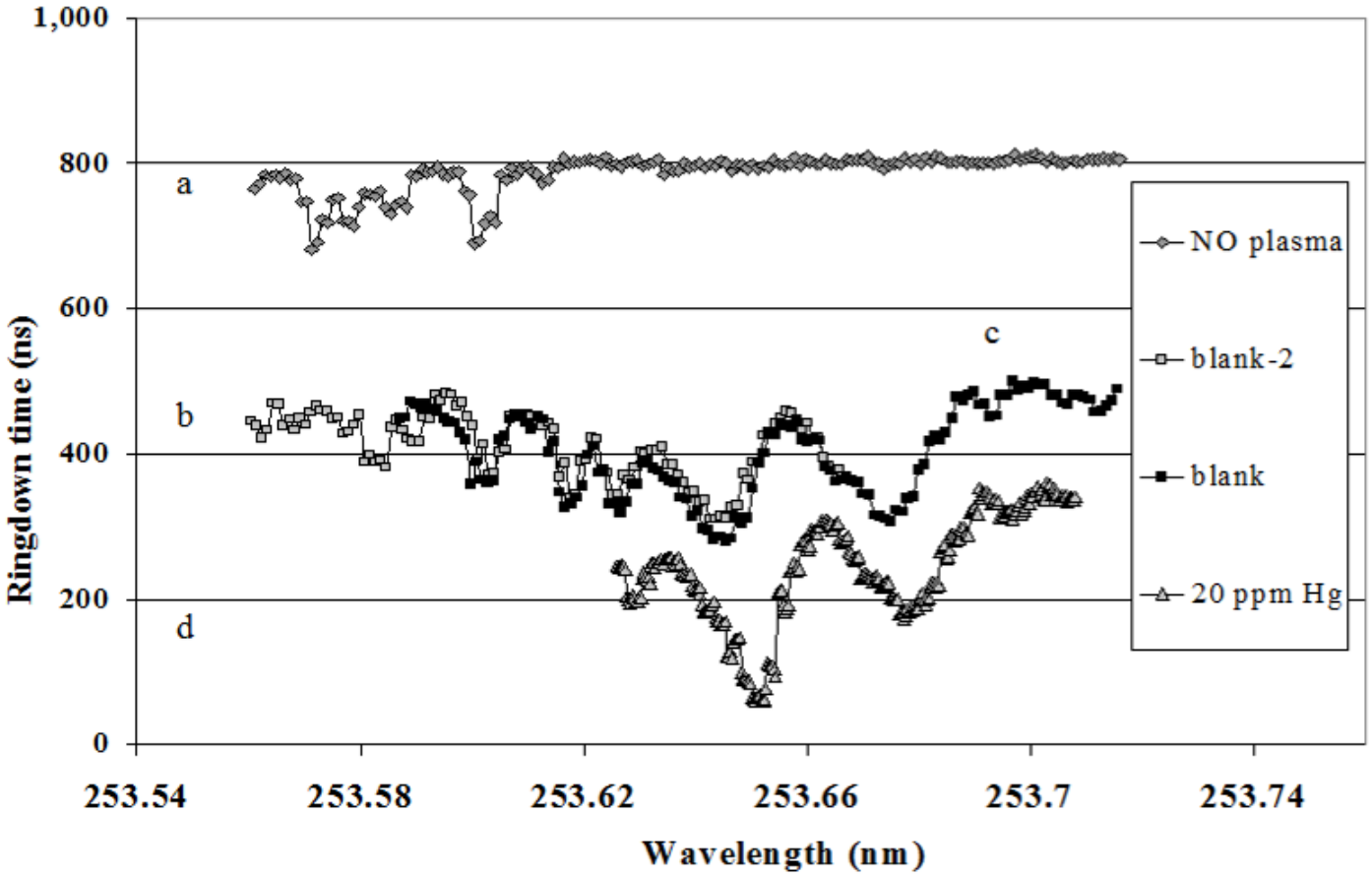

Figure 3.5 Effect of candle-shaped plasma on baseline stability and Hg detection.

A) Background scan in the absence of the plasma. B) and c) depict the 'new' peaks generated by the plasma and their reproducibility. D) 20 ppm Hg solution injected into the plasma; this scan is manually offset for visual clarity. Hg detection at low concentrations is impeded by the presence of the OH generated peak.

As denoted in Figure 3.4, the third 'new' spectral feature, going from lower to higher wavelengths, is in the general vicinity of the mercury transition line. Under the given experimental parameters, flow rates, plasma power, height measurement in the plasma, laser step size, etc., this particular peak is very reproducible. The linewidth of this transition has been assigned to the rovibrational transitions $R_{21}(21)$ and $P_{11}(15)$ of the OH $A^2\Sigma^+ - X^2\Pi_{\frac{3}{2}}$ (0,0) band using simulations obtained with LIFBASE, version 2.0. These two transition lines have been broadened due to the influence of the plasma, such that the overlapped resulting peak is approximately 0.015 nm at full width at half maximum (FWHM) and centered at 253.65 nm. This generates interference with the Hg measurement, as the Hg transition is located at 253.6519 nm. Under plasma conditions, the Hg transition is also broadened and the Hg line appears as a shoulder on the higher wavelength side of the aforementioned overlapped rovibrational transition. The background corrected, broadened Hg transition measured ~ 0.006 nm at FWHM. Typical atomic linewidths obtained in studies utilizing a plasma are generally on the order of 0.0025 nm; when isotopic structure is present and detectable, atomic transition linewidths in a plasma are ~ 0.003 – 0.005 nm. Therefore, the much larger FWHM obtained in the background scan allowed us to conclude that the peak at 253.65 was not due to an atomic transition. Similar analysis of the fourth 'new' peak, which is larger than the Hg interference peak, was conducted. At 0.018 nm FWHM, this peak also appears to be too large to be caused by an atomic transition, so simulations were performed on radicals which are oftentimes present in plasmas, such as OH, CH, and CN. Examining numerous combinations of radicals, atoms, residual elements, etc. did not indicate a probable source for this peak. The first two 'new' peaks generated by the presence of the plasma were also explored. As these peaks are much narrower in

linewidth, ~ 0.005 – 0.006 nm FWHM, atomic transitions were more heavily examined. Common elements to be expected in this particular plasma, such as Ar and Cu, were tested, but to no avail. The MIT wavelength tables[119] in conjunction with the NIST atomic line database[120] were consulted to determine the possibility that the new peaks, especially peaks 1 and 2, were due to residual contamination from previous studies utilizing this plasma, namely, U, Pb, Al, Ba, Br, C, Cd, Cl, Cr, Fe, Mn, Ni, P, Sb, Se, Si, and Tl; however, no correlation was found with any of the aforementioned elements. To rule out oxygen as the source, scans were taken with oxygen mixed with argon, but no plasma-induced radicals or oxygen atoms seemed to alter the intensity or distribution of these peaks. While the various elements were injected into the plasma, the change in ringdown time as well as the presence/absence of spectral peaks in the emission spectra were monitored. As no discernable difference was detected in either for any of the most likely suspect candidates and no acceptable simulation was generated, the first two and the fourth 'new' peaks remain unassigned to date.

3.3.3 Measurement of Mercury at 254 nm

As described in the previous section, an OH absorption, generated by the MIP, is present at approximately the same spectral position as the 254 nm Hg transition. Preliminary scans depicting the systematic determination of the presence of the Hg peak, with the plasma off (background), plasma on with blank solution (plasma background), and plasma on with a 20 ppm Hg sample solution, are shown in Figures 3.4a - d. The scans depicted in Figures 3.5b and c show the reproducibility of the system under the influence of the plasma. Scans a – c are not manually offset. However, in order to provide visual clarity, scan d is shifted off the background peaks. The influence of the

OH peak on the accurate measurement of Hg is clearly evident in the figure. The Hg transition appears as a shoulder on the OH peak, and initial concerns focused on the ability to detect Hg as well as if the interference would produce any inconsistencies when determining Hg concentrations and transition profile. Fortunately, the relative intensity and linewidth of the OH peak are extremely reproducible under a given set of experimental parameters; therefore, the actual profile of the Hg transition can be obtained by subtracting the background absorption of the OH peak (plasma background) from the spectra obtained with Hg present. When the Hg concentration is high, the background interference does not affect the Hg measurement. However, when the sample concentrations are relatively low, approaching the detection limit of the system, lower signal-to-noise ratios are generated, which affected the accuracy of the Hg measurement. The effect of concentration on the detection limit as well as the Hg profile obtained after background subtraction will be described in greater detail shortly.

The importance of baseline stability to detection sensitivity cannot be overstated, especially with competing factors, such as the OH absorption, being present. The inherent baseline stability of the MIP-CRDS technique, as can be inferred from the traces in Figure 3.6, where 10 individual ringdown events in the upper trace and 100 individual ringdown events in the lower trace were averaged to generate each ringdown time constant at a single wavelength, and from Figure 3.4, where a wavelength scan was performed, allows highly sensitive Hg detection. Typical baseline stabilities for this experimental system with 100 averages are 0.3 % without the plasma operating. As can be seen in Figure 3.6, long exposure of the ringdown mirrors to the plasma as well as degradation of the laser dye due to extensive use has a significant impact on the ringdown time. An important point to note is that although these artifacts did effectively reduce the

ringdown time, they did not generate excessive noise in the stability scans. However, when the laser dye was approaching the very end of its lifetime, noticeable instabilities were generated by the AutoTracker frequency doubler as higher gain settings were applied and more 'overcorrecting' was encountered.

Operating a plasma in the ringdown path can cause additional background noise due to optical scattering, changes in the refractive index, and inhomogeneities in the plasma distribution. Therefore, prior to Hg measurements, a comprehensive systematic optimization was undertaken to achieve the lowest baseline noise within the experimental limits of the system. The experimental parameters most rigorously examined to improve the baseline stability while the plasma was operating included the effect of plasma power, gas flow rates, and laser beam position (vertical and lateral) in the plasma. Interestingly, for different elements, each of these parameters had to be re-evaluated on an individual basis, even though the same MIP-CRDS system and instruments were utilized. The baseline noise, which directly influences the minimum concentration of an analyte that can be detected with analytical certainty, is defined as σ/τ,[12, 78] where σ is the standard deviation of the ringdown time and τ is the ringdown time under specific experimental parameters.

In order to obtain the lowest baseline noise, one tries to simultaneously increase τ and decrease σ. Consider, for example, the spectra in Figure 3.5: The average ringdown time over the wavelength region encompassing the mercury transition without the plasma operating was 795 ns and the standard deviation was 4.85 ns; this scan yields a 0.6 % baseline stability. The average ringdown time with the plasma on, under the same experimental conditions at 253.6519 nm, was 254 ns with a 4.16 ns standard deviation, resulting in 1.64 % baseline stability. Clearly, such stabilities are not conducive to

obtaining respectable detection limits. Therefore, operational parameters of the plasma and the laser-stepping configuration had to be more closely examined. Upon optimizing the experimental configuration for mercury detection, typical baseline stabilities obtained with the plasma on were improved to 0.44 %, as shown in Figure 3.7, with the plasma operating at 150 W with each data point generated from the average of 100 individual ringdown events.

In order to illustrate the fine-tuning of a single parameter, consider, for example, the effect that the height of the laser beam in the plasma has on Hg detection. Figure 3.8 provides a plot of the change in observed ringdown time as a function of the laser beam height in the plasma with the plasma operating at 125 W. Under the experimental conditions utilized in the depicted data, the ringdown time decreased as the height of the laser in the plasma increased. The highest ringdown time with the best baseline stabilities will generally yield the best detection limits, but this approach does not always yield the highest detection sensitivity experimentally, as is often the case in plasma-CRDS. This difference arises from the inhomogeneous distribution of atoms in the plasma. This phenomenon is more clearly depicted in Figure 3.9, where the change in absorbance as a function of the laser beam height in the plasma is depicted. As is evident from the figure, the signal intensity under the given experimental conditions can be improved by a factor of six simply by optimizing the height. Clearly, the location in the plasma plays an important role in the sensitivity of the system. For this particular plasma, the best stabilities were obtained by positioning the laser directly over the center of the plasma for the lateral dependence.

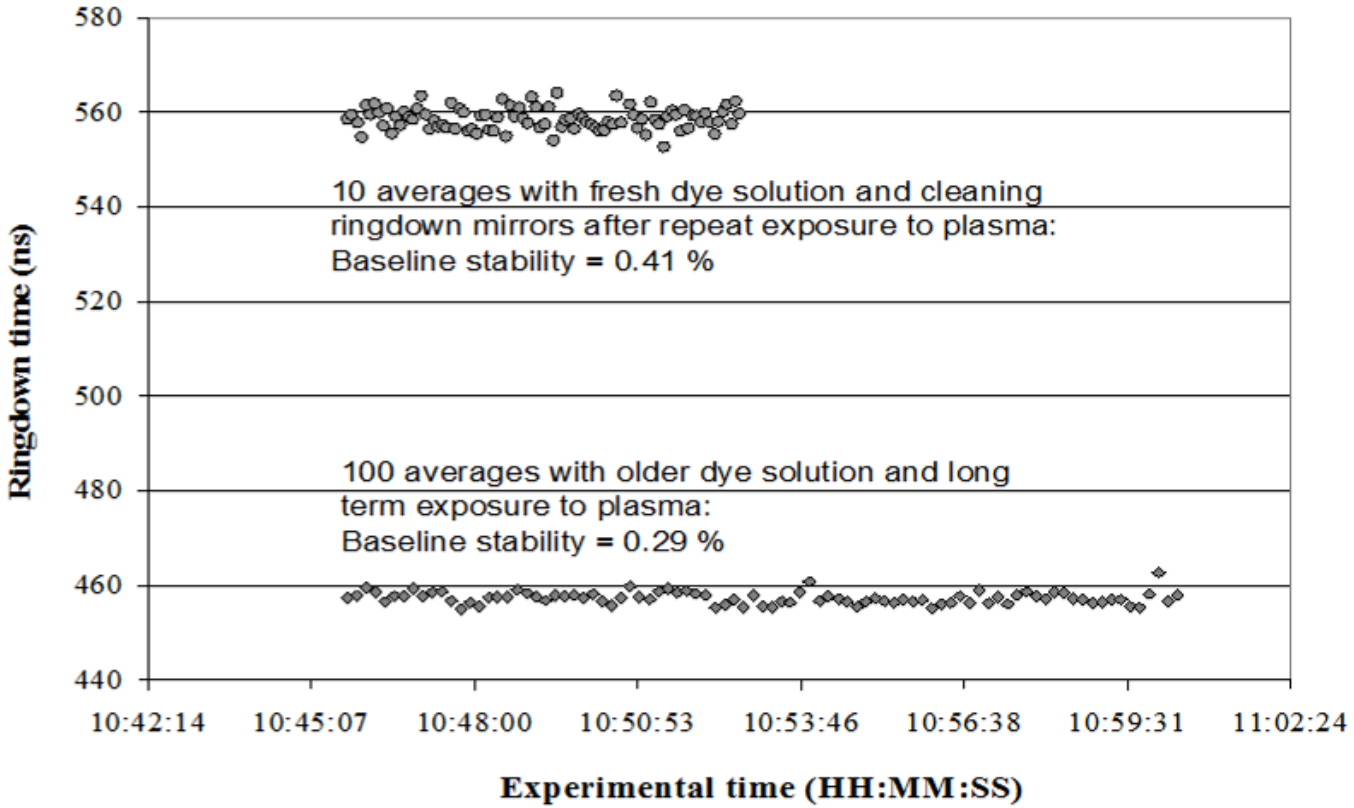

Figure 3.6 Baseline stability without the plasma operating.

Noteworthy baseline stabilities are imperative to exceptional ringdown detection limits. One critical parameter when implementing CRDS with dye lasers is the effect of the dye lifetime on CRDS measurements. While the stability can be affected as the dye ages, the most obvious change is the rapid decrease in ringdown time with 'older' dye solutions, which often results from poorer output mode quality from the dye laser.

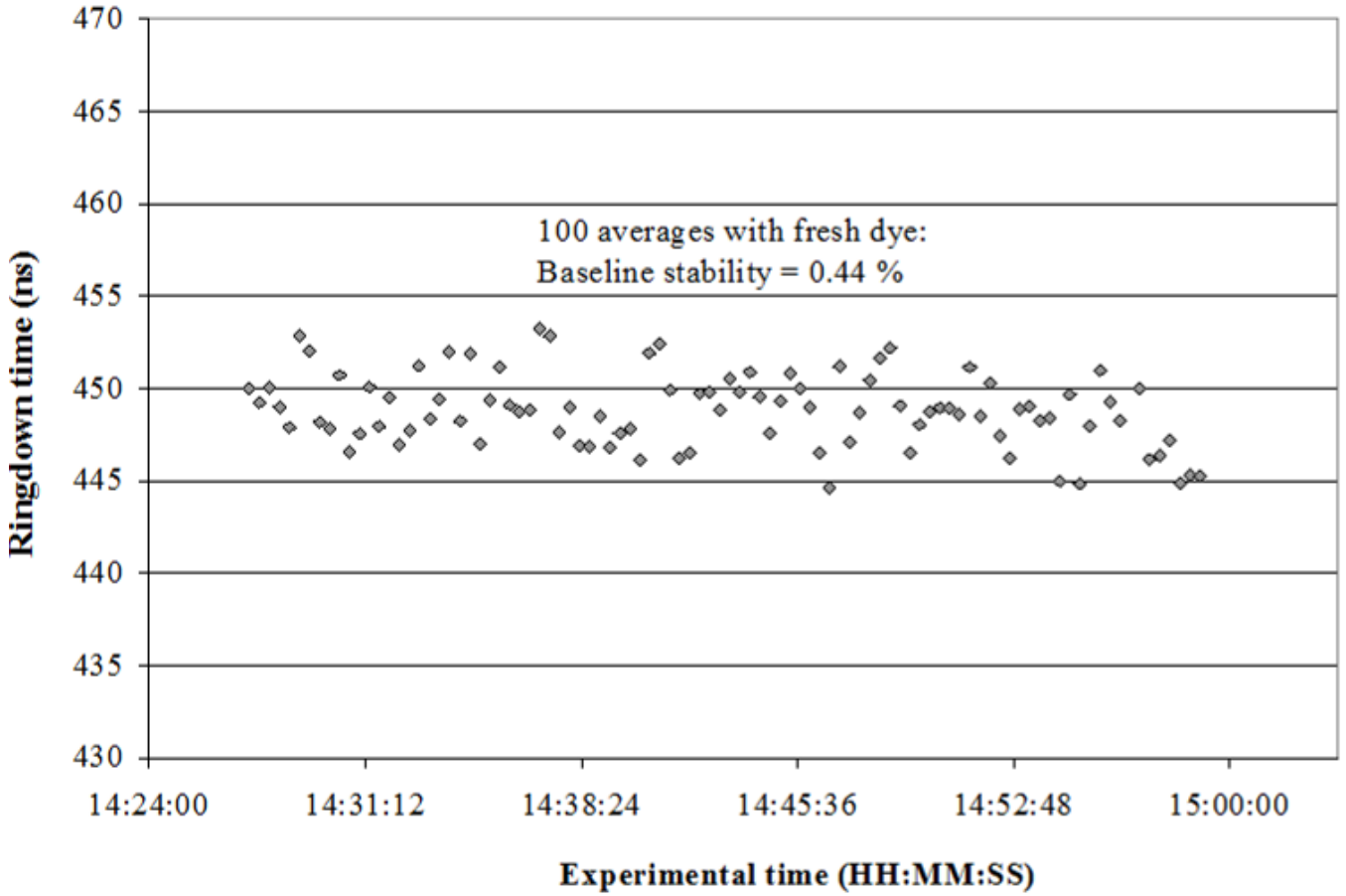

Figure 3.7 Baseline stability observed with candle-shaped MIP-CRDS with the plasma operating.

Baseline stabilities are affected by the presence of the plasma. This scan was obtained after a fresh dye solution was introduced and the ringdown mirrors were cleaned and re-aligned. The plasma was operating at 150 W with a supporting gas flow rate of 0.5 L/min and a sample rate of 0.3 L/min.

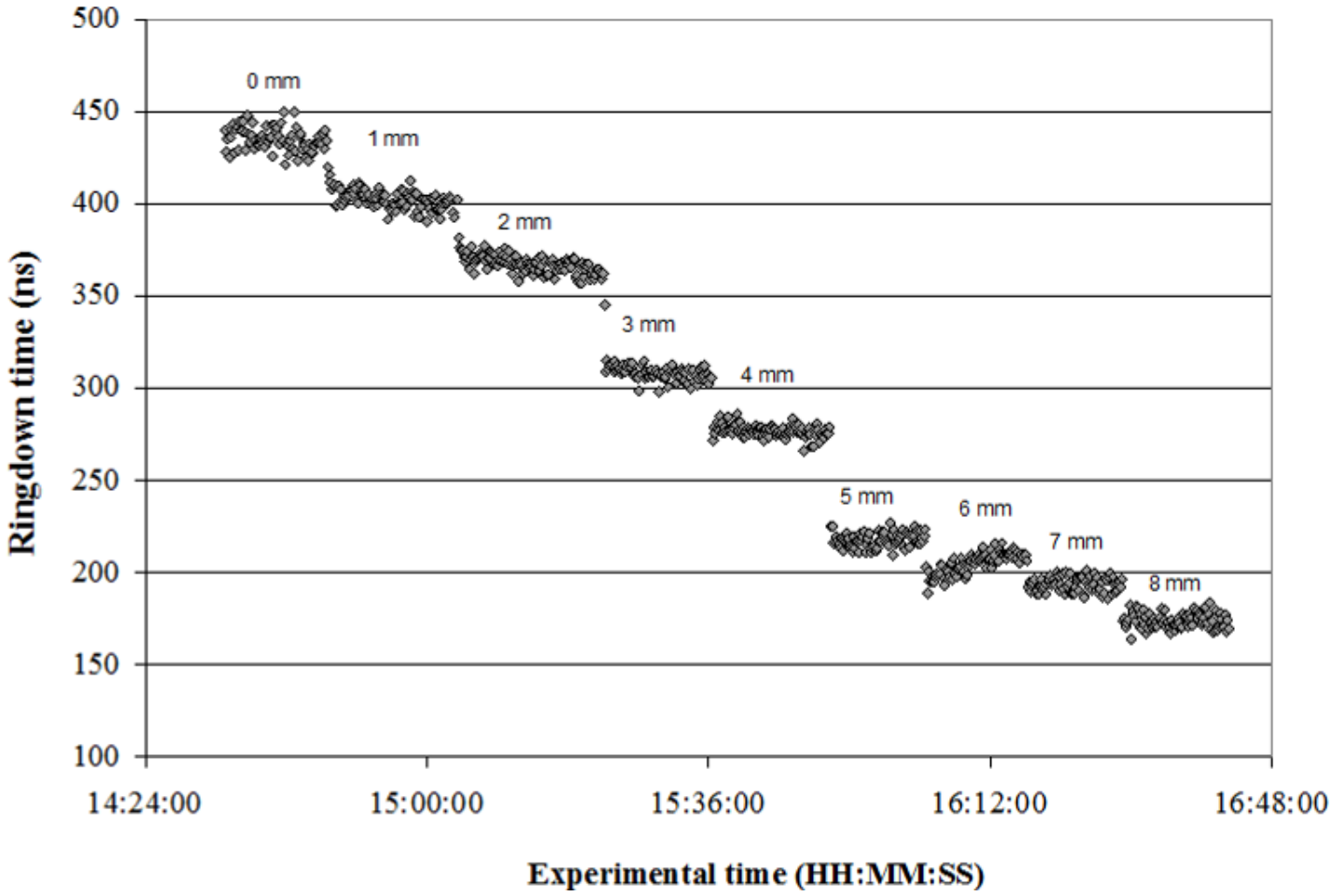

Figure 3.8 Change in ringdown time as a function of the height of the laser in the plasma.

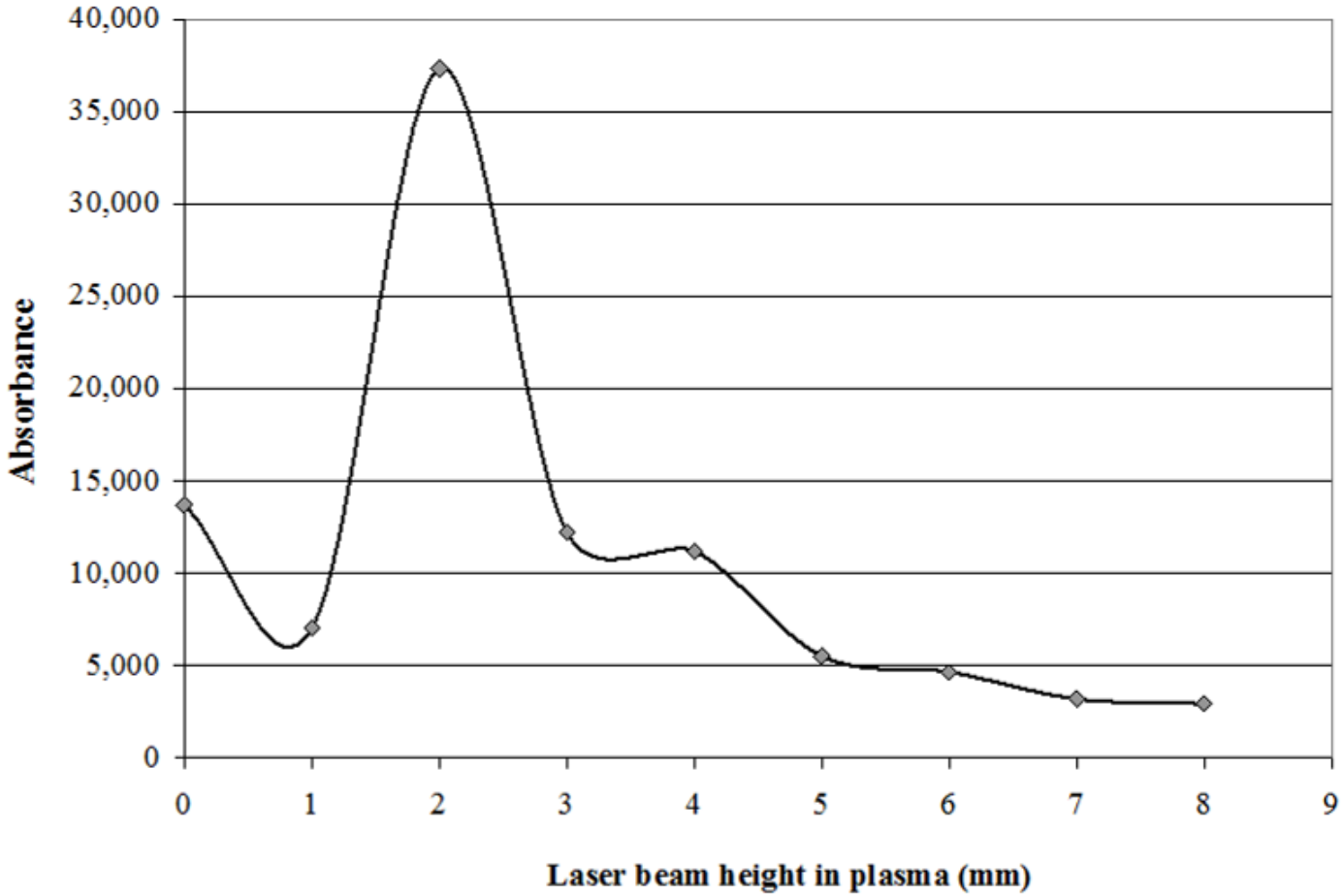

Figure 3.9 Change in absorbance as a function of the height of the laser in the plasma.

By optimizing the laser beam height in the plasma for a given element, the detection limit for that species can be enhanced by a factor of 6.

Similar analyses were conducted to explore improvement in signal strength and stability by examining the effect of plasma power and flow rates, which were generally modified incrementally and in series because changes in either the power or the gas flow rates affected the overall shape and color distribution of the plasma. Upon observing a particular shape/sound/color pattern, which consistently produced much more stable baselines, efforts were made to systematically step the plasma and gas flow rates to achieve this combination by eye, which would almost always yield the lowest baseline noise. Typical operational parameters utilized in the majority of this research are listed in Table 3.1. As compared to Hg-ICP-CRDS studies conducted in this laboratory, this particular approach (MIP-CRDS) required relatively low plasma powers (100 W vs 800 W) and low gas flow rates (0.5/0.35/0.5 mL/min vs 15/.25/1.25 mL/min) and took up a much smaller geometric footprint (~ $1/10^{th}$ the size of the ICP, even when the protective shield and microwave generator are compared to the generator and water cooling system for the ICP). Additionally, the MIP and its protective enclosure weighed ~ 7 lbs, whereas the ICP and its protective enclosure weighed ~ 55 lbs.

Table 3.1 MIP Operational Parameters

Plasma		
Plasma power	80 - 100	W
Plasma supporting gas flow rate	0.35 - 0.5	L/min
Plasma central gas flow rate	0.5 - 1.0	L/min
Sampling System		
Sample up-take rate	0.75 - 1.0	mL/min
Heating temperature of nebulizer	120	°C
Cooling temperature of nebulizer	-5	°C
Temperature applied to membrane tubing	80	°C
Ar flow rate in the drier	0.5	L/min

Initially, since the mercury absorption peak appears as a shoulder on the OH peak, efforts to calibrate the system and determine the experimental detection limits were presumed to be somewhat hampered by the presence of the OH peak. As the reproducibility of the shape and intensity of the OH peak was being explored, instrumental considerations as well as the sample introduction system were simultaneously being investigated. When the electronic and mechanical portions of the experiment were thoroughly explored, attention focused on two probable suspects which were affecting the reproducibility. The first factor addressed was the degree of certainty in the wavelength reproducibility. The dye laser was set to step at 0.0003 nm per step; however, 0.0003 ± 0.0001 nm in the deep UV was the average step value. Additionally, the mechanical control of the dye stepper generated a hysteresis effect in that the wavelength would sometimes slightly over or under shoot the initial wavelength, which resulted in significant measurement error for the low Hg concentration data. After ascertaining that the dye laser did not always change wavelength in reproducible step sizes and factoring in the extensive usage of the mechanical components, a pulsed UV wavemeter (Burleigh/EXFO, WA-5500) was incorporated into the system. Depending on the particular alignment of the system, i.e., either before or after the internal helium/neon (He/Ne) of the wavemeter expired and the system was shipped back to have the laser replaced and the unit calibrated, the back reflection off either the first ringdown mirror or off one of the telescoping lenses was directed into the wavemeter. This allowed the laser wavelength to be continuously monitored with ± 0.0001 nm confidence, as extrapolated from the specification and test sheets for the Burleigh wavemeter. Therefore, measurement errors due to any drift of the laser wavelength, which would be readily enhanced when subtracting the OH absorption peak, were minimized. It was found that a

0.002 nm wavelength drift could introduce up to a 20 % error, a phenomenon especially evident with low concentration samples. As a side note, towards the end of this research, a spring-like component in the stepper motor of the dye laser broke and had to be replaced. The entire stepper motor assembly was sent back to Germany to be repaired, polished, and re-calibrated. With the new internal components, the step size reproducibility was greatly improved. The second electronic/mechanical system addressed was the efficiency of the auto tracker. A noticeable amount of baseline instability was generated during wavelength scans due to the inconsistent stepping of the AutoTracker and during single wavelength data acquisition in which the AutoTracker seemed to 'stick' and then over-correct itself. This artifact became significantly obtrusive as the dye reached, and sometimes exceeded, its lifetime. Figure 3.10 depicts typical fluctuations in a single wavelength ringdown baseline stability scan that were generated with the AutoTracker enabled and the plasma operating at 150 W. By disabling the AutoTracker and manually tuning the Beta Barium Borate (β-BaB2O4 or BBO) crystal during data acquisition, baseline stabilities over the course of single wavelength scans, as shown in the figure, improved significantly. Manually tuning the BBO during scans over a specified wavelength region generated much smoother and reproducible spectral features.

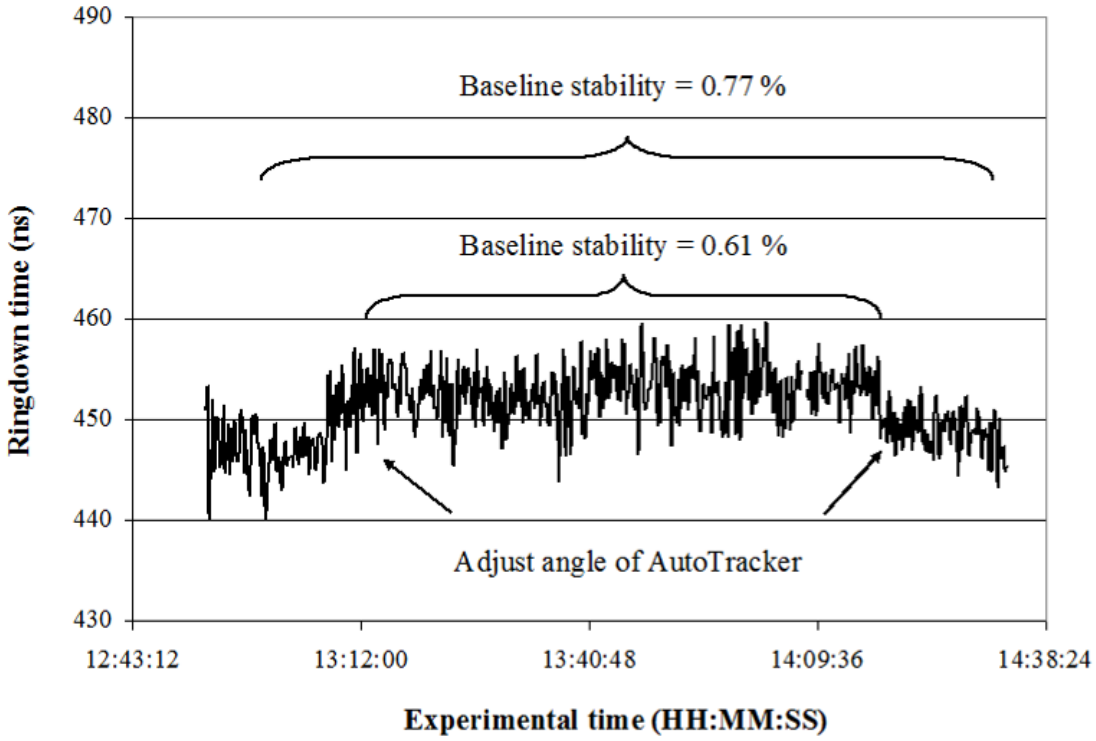

Figure 3.10 Importance of accurate positioning of the AutoTracker output.

Generally, a calibration curve generated under specific experimental parameters at a single wavelength is used to determine the experimental detection limit of the ringdown system. Experimental results indicated increased signal fluctuation in the ringdown baseline with the presence of Hg samples in the plasma; however, the noise fluctuation was not consistently proportional to the sample concentration and seemed to decrease with increasing sample concentration. The presence of Hg in the plasma emission was confirmed by monitoring the plasma emission with a triple grating 0.5 m monochromator (Acton/Spectra-Pro). As was observed with lower concentration Hg samples and the resulting negative effect on ringdown stability, the peak intensity observed by the monochromator was not proportional to the concentration of the mercury present in the plasma. Concentrations higher than the 3-σ limit, as determined by the additional noise with low concentration Hg samples present in the plasma, were used in the calibration.

The effect of Hg concentration vs peak height was as predicted for higher concentrations of Hg; however, after introducing high concentrations of Hg into the system, a residual Hg signal was evident, even after the system was flushed following each Hg scan. In order to insure that the Hg adsorbed to the sample tubing would not contaminate subsequent samples, a 100 ppb gold solution (Absolute Standards, Inc., 1000 μg/L) was implemented to amalgamate the residual Hg, thereby efficiently removing Hg from the sample tubing and molecular sieves. One important point to note is that high concentrations of gold solution used to purge the system caused low Hg sample concentrations to be either completely obscured or underestimated. Measurement uncertainties as large as 20 % were observed in the lower concentration solution samples, e.g. 0.5 - 5 ppm. Due to this artifact, we were not able to determine an accurate calibration curve for data collected with sample concentrations below 0.5 ppm; however, using the higher concentration samples, a linear response and, in turn, a calibration plot, depicted in Figure 3.8, was obtained. Additionally, a second potential source of residual mercury could be found in the desolvator chamber. In order to minimize the amount of residual mercury in the desolvator chamber, the Dry-Rite crystals were periodically removed and dried overnight in a 100 °C oven. Scans performed with a blank solution flowing through new tubing into the freshly dried desiccant yielded no increased instability at the mercury peak when scanning the laser wavelength nor did they reveal spurious mercury peaks with the spectrometer. Several tests were conducted to by-pass the desolvator chamber to eliminate this artifact; however, the presence of the moisture in the plasma introduced significant levels of instability in the ringdown spectra at single wavelengths with the given configuration.

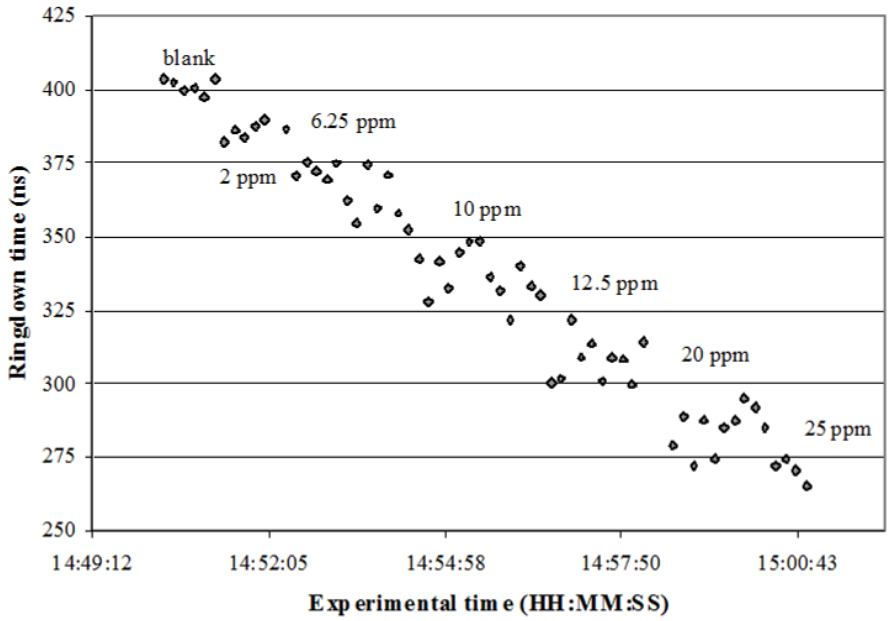

Figure 3.11 Change in ringdown time as a function of concentration.

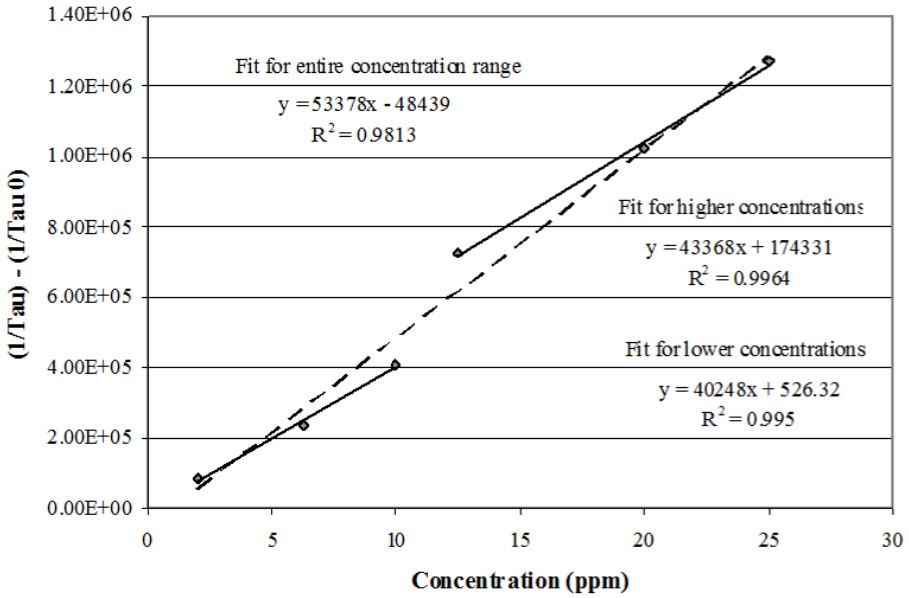

Figure 3.12 Calibration plot for Hg-MIP-CRDS at 253.6519 nm.

While the overall linearity is acceptable, the fits obtained for the individual portions (higher and lower concentrations) were consistently more linear than the combined data for the entire concentration range. This artifact could be due to a drift in the laser wavelength as well as interference in the lower concentration range due to the OH background at this wavelength.

Based on the experimental results obtained with the 20 ppm sample solution, an estimated experimental detection limit was obtained. As can be seen in Figure 3.4, the difference in the experimental ringdown times between the blank scan and the scan obtained with the Hg sample present is 175 ± 3 ns. As previously mentioned, the standard deviation and baseline noise when the plasma was on with no sample present were 4.85 ns and 0.6 %, respectively. Using the 3-σ criteria for analytical confidence, the minimum ringdown time difference which can be observed with 95 % confidence is 14.55 ns. Under the given experimental conditions, this is equivalent to a vapor phase detection limit of 421 pptv of Hg. This is, of course, based on the assumption that the change in ringdown time as a function of concentration is linear in the entire range 0 to 250 ppm.

3.3.4 Isotopic Structures of Mercury

There are seven stable mercury isotopes, and five spectral peaks attributed to these isotopes are typically observed within the 254 nm transition envelope.[41] These isotopic transitions are partially overlapped under atmospheric conditions, and Doppler broadening makes them even less well resolved in higher temperature environments,[121] such as a plasma. Table 3.2 shows the seven naturally-occurring isotopes of Hg and their isotopic abundance.[122] As previously mentioned, the two odd isotopes have nuclear spin, and all of the isotopes have slight spectral shifts. Additionally, the hyperfine interaction results in a split and shift of the odd isotopomers, which have both been experimentally measured by Schweitzer.[123] Figure 3.13 shows a schematic plot of the isotopic shifts and hyperfine splittings for the seven stable isotopes of mercury. Figure 3.14 depicts a typical high-resolution mercury spectrum generated with this MIP-CRDS system. This

spectral profile is in good agreement with the well-documented mercury literature. The contour of the transition, as well as the relative abundance ratios, is very reproducible.

As indicated in the figure, there are six features of the mercury transition that are noteworthy and highly reproducible. Five of the peaks have been assigned to specific isotopes or combinations of them. Table 3.3 shows the wavelength, experimental abundance ratio, and the isotopic designation assigned to each line position. The feature indicated with an * in the figure has not been assigned to a particular isotope or combination of them, but this 'shoulder' is present in each spectra obtained with the MIP-CRDS system after baseline subtraction. A second feature, marked with an #, was an artificial artifact generated by the laser. The threading of the stepping motor rod of the dye laser was extremely worn down from extensive use in this particular wavelength region, the region accessed to examine the Hg peak. As such, a 'jump' was routinely observed in many of the background scans; and this jump was not always of the same intensity on each pass across the threading with the wavelength scans. Therefore, the peak (#) was observed more often than not in the scans conducted prior to the replacement of the dye stepper motor and threaded rod. A "fresh" plasma background spectrum was obtained for each scan to ensure more accurate results during the background subtraction corresponding to each sample. The relative abundance ratios, which were determined by taking the 'height' (intensity) of each background-subtracted peak relative to the total of the peak intensities, are in good agreement with the theoretical values, also listed in the table.

Table 3.2 Isotopic abundance of mercury

Isotope	% Natural Abundance	Atomic Mass
196	0.15	195.965807
198	9.97	197.9668
199 (a)	11.23	198.9683
199 (b)	5.61	198.9683
200	23.13	199.9683
201 (a)	6.61	200.9703
201 (b)	4.41	200.9703
201 (c)	2.2	200.9703
202	29.86	201.9706
204	6.85	203.9735

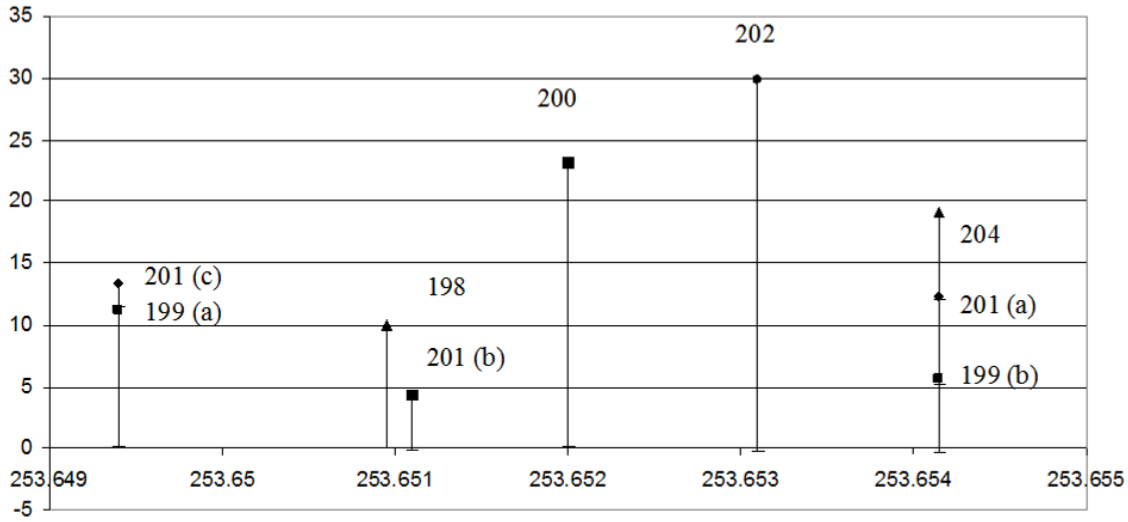

Figure 3.13 Schematic plot of the isotopic shifts and hyperfine splitting for the seven stable isotopes of Hg.

Table 3.3 Isotopic ratios of Hg at 254 nm with the candle-shaped MIP

Line Position	Wavelength (nm)	Exp. Ratio (%)	Theo. Ratio (%)	Isotope Assignments
1	253.647	12.9	13.4	201(c) + 199(a)
2	253.65	15.1	14.4	201 (b) +198
3	253.652	23.7	23.1	200
4	253.653	26.9	29.8	202
5	253.654	21.4	19.1	204 + 201(a) + 199(b)
*	253.656			Undetermined

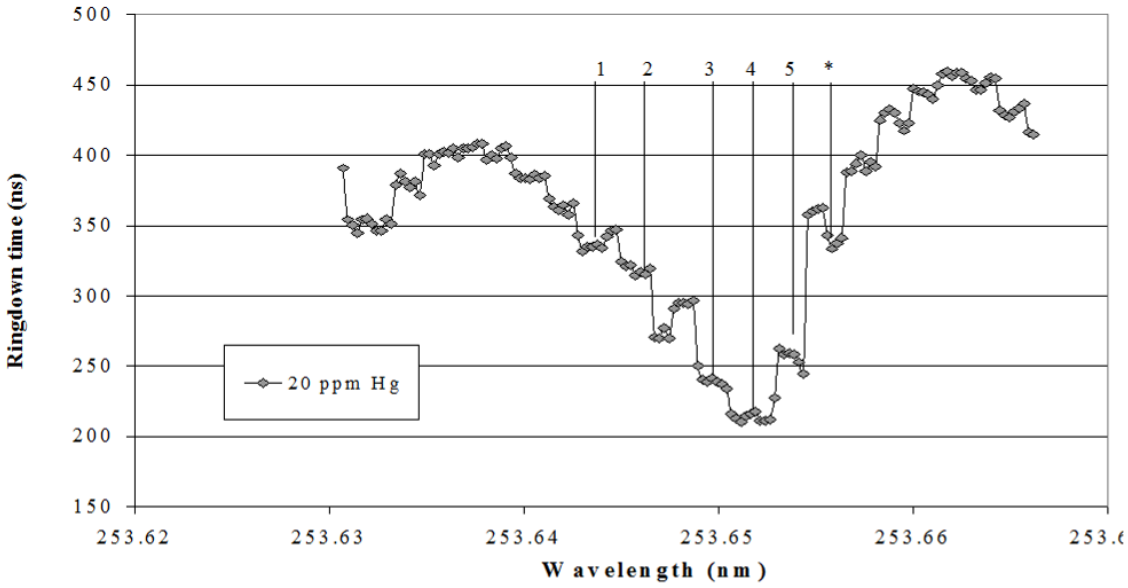

Figure 3.14 Isotopic structure of Hg at 253.6519 nm with candle-shaped MIP.

A 20 ppm Hg solution was injected into the plasma, operating at 100 W. As indicated in the text, the peak (#) observed between 3 and 3 is an artificial artifact generated by the laser stepping mechanism, which was not completely eliminated with the background subtraction.

CHAPTER IV

DESIGN AND FABRICATION OF PLASMA CONFIGURATIONS FOR TESTING CAVITY RINGDOWN MEASUREMENTS OF MERCURY

4.1 Introduction

In an effort to improve the experimental mercury detection limits using plasma-cavity ringdown spectroscopy (P-CRDS) and move towards a more compact, portable system, the research emphasis turned towards modifying the existing MIP-CRDS system[36] to incorporate an alternate atomization source.[124, 125] As previously observed with the candle-shaped MIP, atmospheric spectral interferences, namely an intense OH peak generated by the plasma at 253.650 nm, and scattering losses resulted in large uncertainties at low Hg concentrations. Therefore, a system which could effectively eliminate or significantly reduce the OH background could readily enhance the experimental detection limits. Toward this aim, the tube-shaped plasma was implemented as the atomization source to demonstrate the technical feasibility of measuring mercury while reducing the OH interference peak with this design, and various configurations of the plasma discharge tube were tested. The overall system performance was characterized by detecting and measuring a range of mercury vapor concentrations for multiple discharge tube configurations. The results of employing this series of discharge tube configurations yielded improved sensitivities and significantly reduced spectral interference. The new configurations of the plasma discharge/ absorption tubes allow the plasma to sufficiently operate at low powers and reduced gas

flow rates. The isotopic structures of the 253.6519 nm mercury transition are also clearly resolved.

4.2 Experimental Setup

4.2.1 Optical Configuration

The experimental setup used in the research presented in this chapter is essentially the same as the instrumental configuration presented in Chapter III, except the choice of plasma source. The experimental system, depicted in Figure 4.1, consists of five major components: the combination of laser components used to generate the desired wavelengths, plasma source, ringdown cavity, sampling device, and detection electronics. The electronic transition of mercury from the $6s^2$ ground state to the $6s^16p^1$ first excited state occurs at 253.6519 nm. In order to generate this UV wavelength, the same laser system and optical configuration utilized in the research presented in Chapter III was employed. Coumarin 500 was selected for the dye for these studies, too, however, the mixing ratio of the dye, the amount of dye (g) to the amount of solution (L), was adjusted to provide stronger signal output at the desired wavelength region. The adjusted mixing ratio was 4.32 g of dye to 1L of ACS grade spectranalyzed methanol, instead of the quoted 4.00 g/L ratio previously used. With the new ratio, several μJ of output power were generated at 253.65 nm. The output laser beam was mode-matched to the ringdown cavity by inserting a spatial filter system, composed of two focusing lenses and a 400 μm pinhole. The ringdown cavity consisted of two high reflectivity mirrors (99.72 %) from Los Gatos Research, Inc., mounted in a pair of high precision Gimble mounts and spaced approximately 27.5" (69.85 cm) apart. The laser beam was initially aligned to pass through the absorption arm of the discharge tubes, which will be discussed in detail in the

Results and Discussion section. The same detector and detection electronics were incorporated in this research. Each ringdown time constant measurement is the average of 100 ringdown events.

4.2.2 Microwave Plasma Source

This research incorporated a copper surfatron microwave cavity plasma source. This particular MIP, which was based on the design presented by Moison, et al. in 1975, was modified to lock the distance between the discharge tube and the microwave antenna, which couples the microwave energy into the quartz discharge tubes, once the position has been manually optimized. With this configuration, the plasma exhibits an annular shape and can be readily manipulated into alternate configurations. The outer diameter (O.D.) of each discharge and absorption tube examined in this study was ~ 6 mm. The inner diameter (I.D.) as well as the geometric configuration of each plasma tube varied, and the dimensions and configurations will be described in more detail shortly. Each discharge tube was concentrically centered in the cylindrical surfatron cavity, regardless of the individual tube's geometry, and the distance between the tip of the discharge tube and the outer edge of the copper casing was adjusted for maximum plasma and baseline stability for each individual tube. One example of the positioning of a discharge tube in the microwave cavity is shown in Figure 4.2a. The plasma is connected to a 2450 MHz microwave power supply (Meteix, Inc.) via a 1 m coaxial cable. Operational powers with this MIP were on the order of 50 – 120 W, depending on the flow rates and tubing configuration. Typical operational parameters implemented in this study are listed in Table 4.1. One interesting point to note is that the orientation of the coaxial cable at the MIP connection and the spatial alignment of the cable between the plasma and power

supply were critical for stable plasma generation. This became especially crucial for studies examining ringdown measurements in different parts of the plasma. The plasma was mounted on a home-made 2-D adjustable stage. CRDS measurements were made by passing the optical beam perpendicular to the discharge tube or through the absorption portion of the plasma discharge tube, if present, to obtain maximum overlap of the beam with the plasma to yield longer sample pathlengths and, in turn, maximize absorption. The aerosol samples were carried from the nebulizer and introduced into the discharge tube while the plasma was operating.

Table 4.1 Operational parameters

Major Section	Component	Value
Laser	Repetition rate	20 Hz
	Pump wavelength	355 nm
	Dye	Coumarin 500
	Dye mixing ratio	4.32
	Step rate	0.0003 nm +/- 0.0001 nm (high resolution scans)
		0.001 - 0.002 nm (lower resolution scans)
	Autotracker	Manually tuned
Plasma Source	Microwave forward power	50 - 120 W median: 85 W
	Microwave reflected power	1 - 20 W
	Gas flow rates	0.35 - 1.0 L/min
Ringdown Cavity	Mirror spacing	27.5" = 69.85 cm
	Mirror reflectivity	99.72 % @ 253.65 nm
	Transmission range	± 10 nm
Sampling Device	Sample uptake rate	0.85 mL/min
	Carrier gas flow rate	0.5 L/min
	Heating temperature of nebulizer	140 °C
	Cooling temperature of nebulizer	- 5 °C
	Heating temperature of tubing connecting nebulizer to desolvator	80 °C
Detection Electronics	Detector voltage	500 - 900 W
	Avg ringdown events/ recorded waveforms	50 - 100

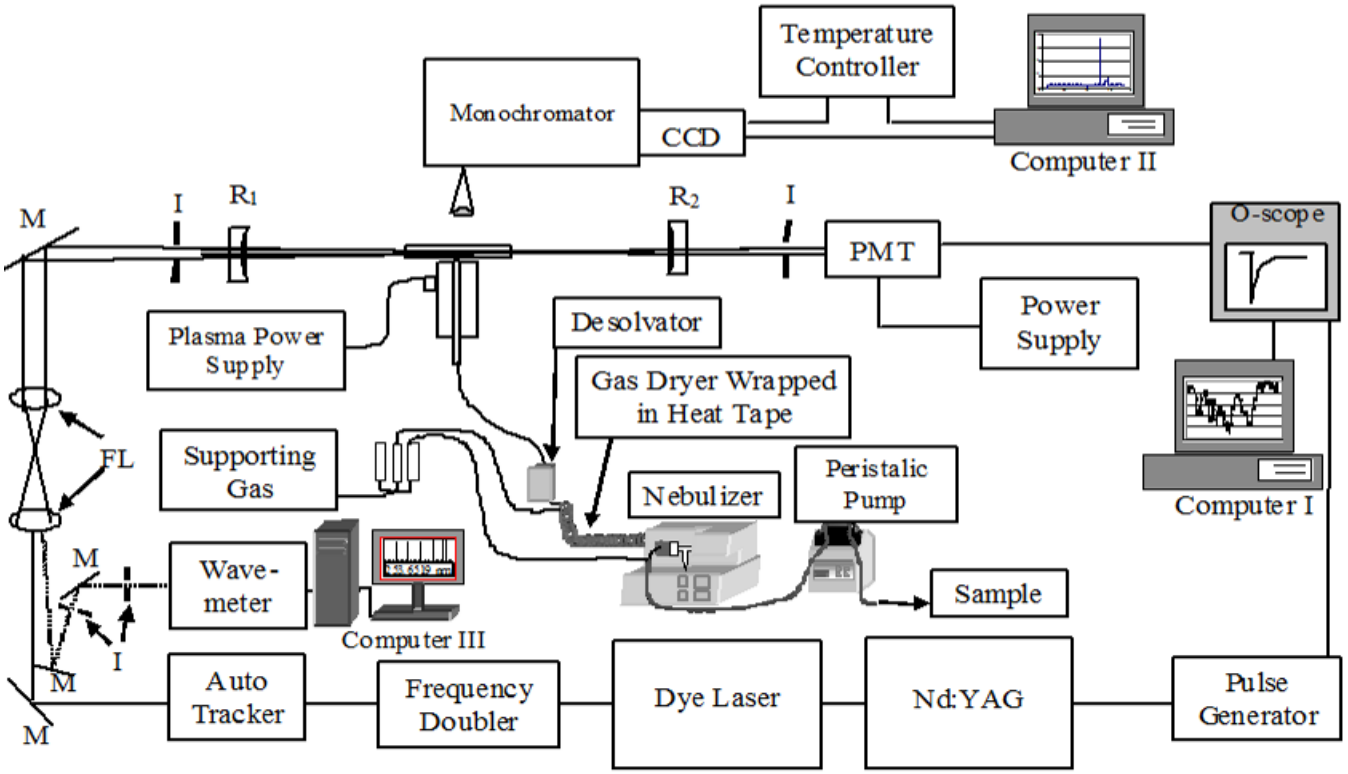

Figure 4.1 Experimental configuration employed with tube-shaped MIP-CRDS system

The output of an Nd:YAG-pumped dye laser is frequency doubled to generate the appropriate UV wavelengths; the resulting beam is telescoped with a pair of lenses (FL) into the ringdown cavity, which is comprised of two high reflectivity mirrors (R_1 and R_2), and is then detected by the PMT. A reflection off the telescope was injected into the wavemeter to monitor the wavelength (Computer III). Irises (I) were positioned to reduce feedback and assist in optical alignments. Computer I is used to control the dye laser stepping parameters and to record the changes in ringdown time. Computer II is used to monitor the presence of mercury in the plasma.

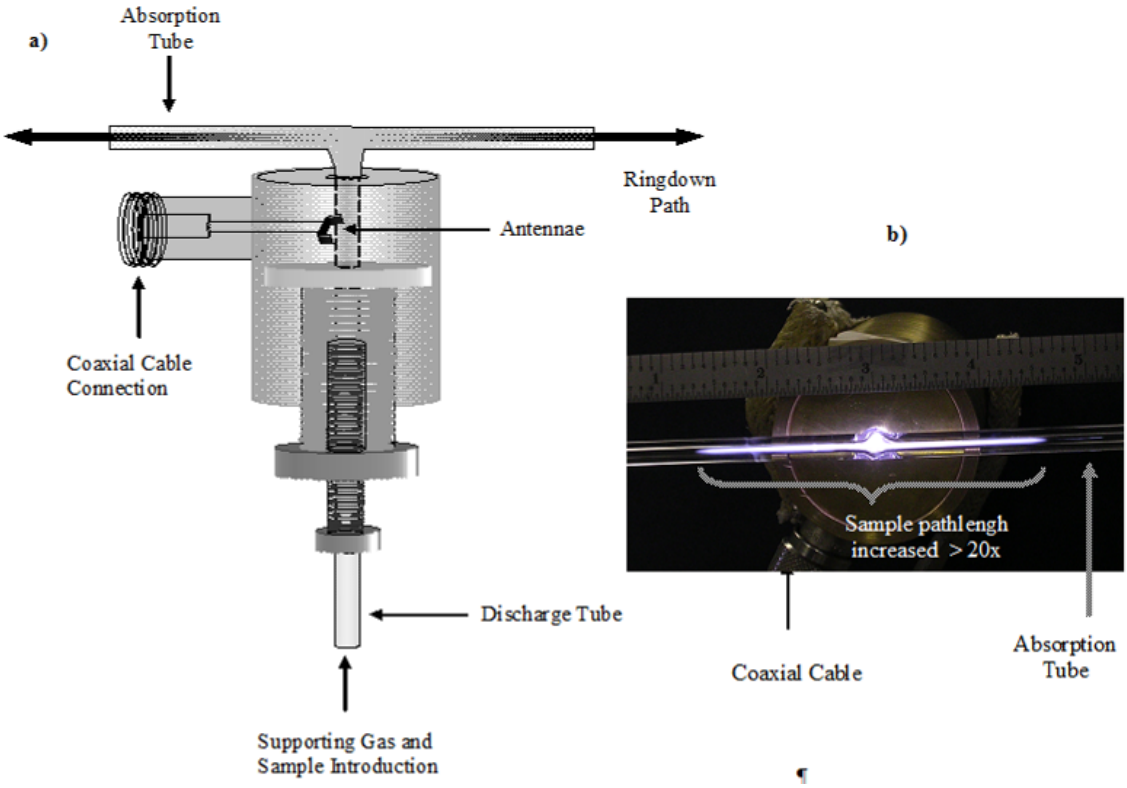

Figure 4.2 T-shaped microwave induced plasma torch.

a) Sketch of microwave cavity implementing T-shaped quartz tube to enhance sample pathlength. b) Plasma operating at 120 W/ 11W with a 0.7 L/min gas flow rate. Sample pathlength is effectively 20 times longer than the pathlength obtained with the straight tube.

4.2.3 Sample Introduction

The sample introduction system utilized in this research is essentially the same system as reported in Chapter III. The Gilson Minipulse 3 peristaltic pump delivered solution samples to a CETAC U-5000 AT+ ultrasonic nebulizer. The sample uptake rate of the peristaltic pump was 0.75 mL/min. When the liquid sample impinged upon the ultrasonic transducer, an aerosol sample was generated. The aerosol generation efficiency with this experimental set up is ~ 10 %. The heating temperature inside the nebulizer and the cooling chiller temperature at the aerosol outlet are approximately 140 °C and -5 °C, respectively. In order to remove the water vapor from the aerosol sample

prior to injection into the microwave-induced plasma, a desolvator and a molecular sieve (Perma Pure, LLC.), were introduced into the sample line and the sample tubing from the nebulizer to the desolvator was wrapped in thermotape and heated to ~ 80 °C with a commercial rheostat to help reduce the water vapor from condensing in the tubes. Reducing the solvent load in the plasma resulted in significantly more stable plasmas, which, in turn, enhanced the overall system performance. The plasma supporting and sample carrying gas flow rates were controlled with Cole-Parmer low flow meters, and a high flow meter, also Cole-Parmer, was employed to control the Ar flow responsible for purging the water from the desolvating membrane.

4.2.4 Chemicals

Sample solutions were prepared by successive dilutions of a standard 1000 μg/mL mercury solution (Absolute Standards, Inc.). The aerosol samples were carried from the nebulizer to the plasma via the desolvator by ultrahigh purity (UHP) argon (99.999 %). In addition to functioning as the carrier gas, the UHP argon (Airgas, Inc.) was also utilized as the plasma supporting gas. Typical flow rates employed during this research for the plasma gas flow were 0.35 – 1.0 L/min and 0.5 L/min for the carrier gas; these values were optimized for each individual discharge tube prior to mercury measurements. The laser dye was prepared from Coumarin 500 (Exciton, Inc.) and ACS grade spectranalyzed methanol.

4.3 Results and Discussion

4.3.1 Plasma Source Design

The surfatron plasma design was explored in this research effort because several advantageous qualities can be readily introduced to the existing experimental setup. For

example, the cylindrical plasma shape, extending most of the length of the discharge tube, facilitates sample introduction, provides a relatively long sample residence time in the discharge, and promotes efficient atomization of the sample. In order to initiate the plasma, the plasma flow rates and power are initially turned on, and, using a high frequency generator (BD-10A, 120 Volt, Electro Technic Products, Inc.), the plasma is ignited. The plasma is generated in the discharge tube and then expands into the adjoining, perpendicular absorption tube, if one is present and if the flow rates and plasma powers are conducive to the particular plasma shape. Once running, the flow rates and forward and reflected powers are adjusted to optimize the plasma stability. The plasma is sustained in the discharge tube, which runs through the center of the copper surfatron microwave cavity. An example of the plasma operating in a T-shaped configuration is shown in Figure 4.2b. With this particular design, the discharge tube is seated inside the copper surfatron microwave cavity and the absorption tube is connected perpendicular to the discharge tube to form the "T" shape. The plasma illustrated in Figure 4.2b is operating at 120 W with a 0.7 L/min supporting gas flow rate. While the sample pathlength has been clearly enhanced, excessive turbulence inside the "arms" of the T-shaped tube and at the intersection of the absorption and discharge portions, which can negatively influence the experimental measurements, had to be taken into consideration and will be discussed shortly. Utilizing a surfatron design, various discharge tube configurations can readily be explored. Regardless of the discharge tube configuration utilized, the laser beam is aligned such that the ringdown measurements are made perpendicular to the discharge tube in the surfatron cavity, as indicated in Figure 4.2a.

In order to generate longer sample pathlengths, one could use higher reflectivity ringdown mirrors to induce additional passes through the plasma and/or lengthen the plasma itself to increase the overlap of the laser with the plasma, i.e., increase the sample pathlength. For these proof-of-concept studies, we chose to use the ringdown mirrors (Los Gatos Research, Inc.) utilized in the previous Hg-MIP-CRDS research in our lab; therefore, attention was directed to lengthening the plasma in order to increase the interaction of the laser with the additional plasma length. Increasing the overlap of the beam with the plasma proved to be relatively straightforward; however, complications due to the increased turbidity and plasma interaction with the beam did arise and will be addressed shortly. Utilizing this type of microwave-induced plasma allowed us to readily alter the configuration of the plasma discharge tubes. We have designed and implemented several discharge tube configurations to determine the feasibility, stability, and/or detection sensitivity of each type. Because quartz has a relatively high thermal tolerance and can be modified into the desired shapes, the discharge tubes used in this research are all quartz; and six dominant configurations were explored in this work. These configurations were either directly incorporated or modified during the testing procedure to reduce instability in the plasma and/or ringdown signal. The discharge tubes were carefully named to reflect their specific attributes, for example, the 'straight' tube, 'off-centered hole T-shaped' tube, the 'long slit in short arm T-shaped' tube, the 'long path/large diameter T-shaped' tube, the 'long path/large diameter T-shaped tube with 2 ports', and the 'diagonally cut' tube. These discharge tubes are depicted in Figure 4.3 and their physical dimensions are listed in Table 4.2. The straight tube (Figure 4.3a) was used initially to test the feasibility of detecting mercury with the tube-shaped MIP in place of the candle-shaped MIP utilized in the research presented in Chapter III. Using

the straight tube, the plasma was set to extend beyond the opening of the discharge tube, forming a thin tail plume, as is evident in Figure 4.4. The laser was aligned to pass through this tail and the distance from the discharge tube as well as the height in the plasma were modified to achieve the best baseline stability and signal sensitivity. While mercury detection was obtained with this 6 mm O.D./ 2 mm I.D. straight tube, the absorption pathlength was only up to 2 mm in some places, less depending on the position of the laser in the plasma as well as the plasma orientation. Therefore, the detection limits with the straight tube were not as impressive as we would have liked. However, once the feasibility of using the tube-shaped microwave plasma for mercury detection was established, research efforts turned to alternative configurations which would effectively increase the pathlength. Two discharge tube designs proved to be more suitable to our experimental needs, the 'off-centered hole T-shaped' tube and the 'diagonally cut' tube; both of these discharge tube configurations were modifications of 'stock' quartz tubes, and the evolution of each, as portrayed in Figures 4.6 and 4.9, respectively, into the configuration best suited for the marriage of CRDS with the compact MIP for mercury detection will be briefly addressed.

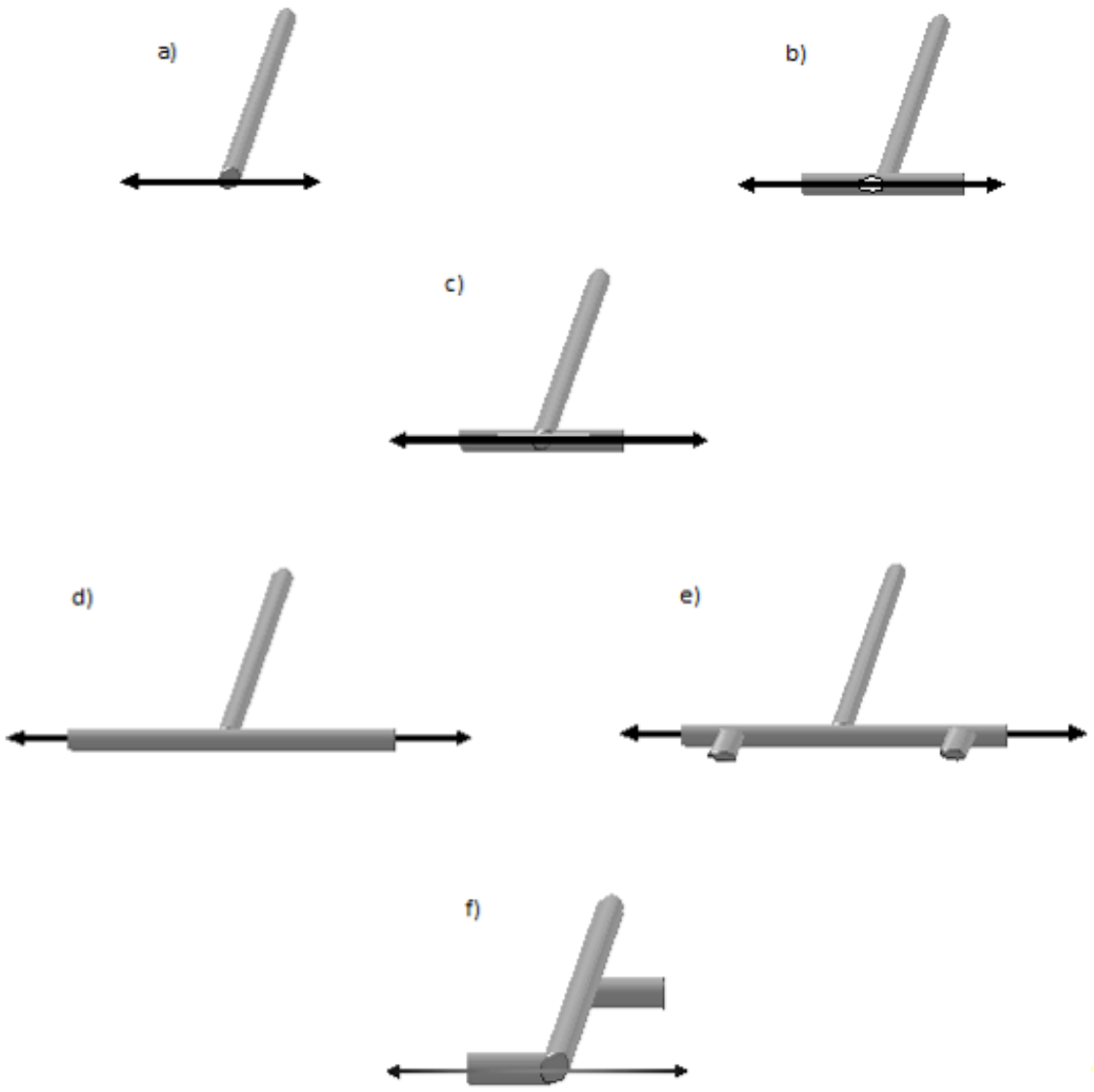

Figure 4.3 Plasma discharge tubes explored in this research.

The final configuration of the a) straight tube, b) off-centered hole T-shaped tube, c) long slit in short arm T-shaped tube, d) long path/large diameter T-shaped tube, e) long path with 2 ports/large diameter T-shaped tube, and f) the diagonally cut tube are depicted.

Table 4.2 Discharge Tube Dimensions

Tube Configuration	Discharge Tube			Absorption Tube			Special Features
	Length (mm)	I.D. (mm)	O.D. (mm)	Length (mm)	I.D. (mm)	O.D. (mm)	Final configurations
Straight tube	170	2	6				Proof of concept
Off-centered hole T-shaped tube	200	2	6	33	3	6	1 mm diameter hole, sligthly off center from discharge tube
Long slit in short arm T-shaped tube	183	2	6	36	2	6	Gas flow generates excess ringdown noise
Long path/large diameter T-shaped tube	184	4	6	195	4	6	Too noisy with gas flow
Long path/large diameter T-shaped tube with 2 ports	184	4	6	195	4	6	(2) 4 mm diameter holes towards ends of T; too noisy with gas flow
Diagonally cut tube	198	4	6.5	25	4	6	Plasma does not enter arm
							107 mm side arm which plasma may or may not enter, depending on power and gas flow rates

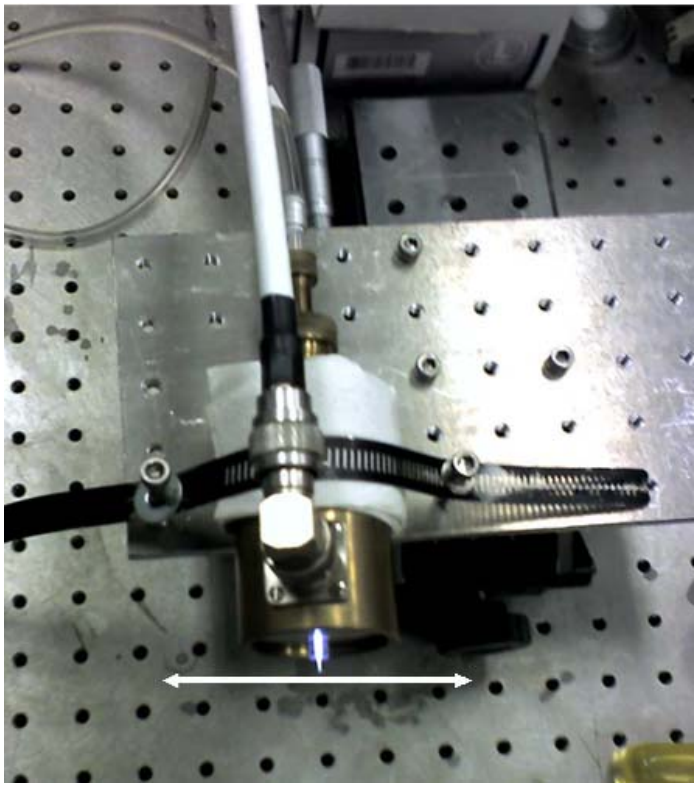

Figure 4.4 Plasma operating with straight tube.

The MIP was operating at 100 W/14 W and 0.80 L/min flow rate.

4.3.2 Plasma Discharge and Absorption Tubes

As previously mentioned, the O.D. of all the discharge tubes is ~ 6 mm, except the diagonally cut tube which was 6.5 mm, to accommodate the I.D. of the microwave cavity. The I.D.'s of the discharge tubes varied from 2 mm to 4 mm, and the effect of the I.D. of the discharge tube on the plasma stability was briefly explored. The optimum discharge diameter for the combined technique was a compromise of two dominant yet competing factors: 1) smaller inner diameters generated much more stable plasmas, but interfered with ringdown measurements and 2) larger diameters were more conducive to rapid ringdown alignment but did not sustain the best plasmas. The 2 mm I.D. was chosen as the minimum acceptable I.D. which still allowed the laser to be aligned through the center of the absorption. One thin-walled discharge tube explored (I.D. > 5 mm), not pictured in Figure 4.3, did not generate a plasma stable enough to pursue ringdown studies within that tube and was, therefore, discarded from further study. With the exception of the 5 mm I.D. tube, the effects of changes in I.D. could be compensated for by adjusting the plasma power and flow rates. Many of the original T-shaped tubes were disregarded due to imperfections in their manufacturing, which included asymmetry in the discharge/absorption tube junction and bending of the absorption tube at the junction such that the laser could not cleanly pass through the entire length of the tube.

While baseline stabilities obtained with the discharge tube labeled as 'straight tube' were sufficient for ringdown measurements, difficulties arose when incorporating the absorption tube in the system to increase the plasma length. The addition of an object perpendicular to the flow of the plasma generated a lot of turbulence at the intersection of the two tubes. The increased gas turbulence and corresponding plasma turbulence were sufficient enough to effectively saturate or almost completely obstruct the observed

ringdown signal in some instances. Therefore, even though relatively stable ringdown baselines were obtained with the laser passing through some of the absorption tubes, the addition of the carrier gas often generated excess noise in the ringdown signal, as can be seen in Figure 4.5, for example, in which the 'long path/large diameter T-shaped tube', illustrated as f) in Figure 4.3, was used. In this figure, the addition of the carrier gas into the tubes caused ~ 50 % change in the ringdown time and the baseline stability drastically fluctuated from 0.75 % with no gas in the discharge tube to 4.6 % when a flow of 0.5 L/min Ar was introduced into the tubes. When this plasma was first ignited, instability, both audibly and visually, was observed and the ringdown decay curve was almost non-existent on the oscilloscope, whereas a distinct, smooth curve was present prior to ignition. Clearly, the effects of the presence of the plasma in terms of ringdown signal strength, plasma stability, and baseline stability had to be thoroughly evaluated for each tube prior to mercury measurements. Towards this aim, a rigorous series of systematic changes were examined to enhance the ringdown baseline stability and the overall system performance by incorporating alternate plasma discharge tube configurations.

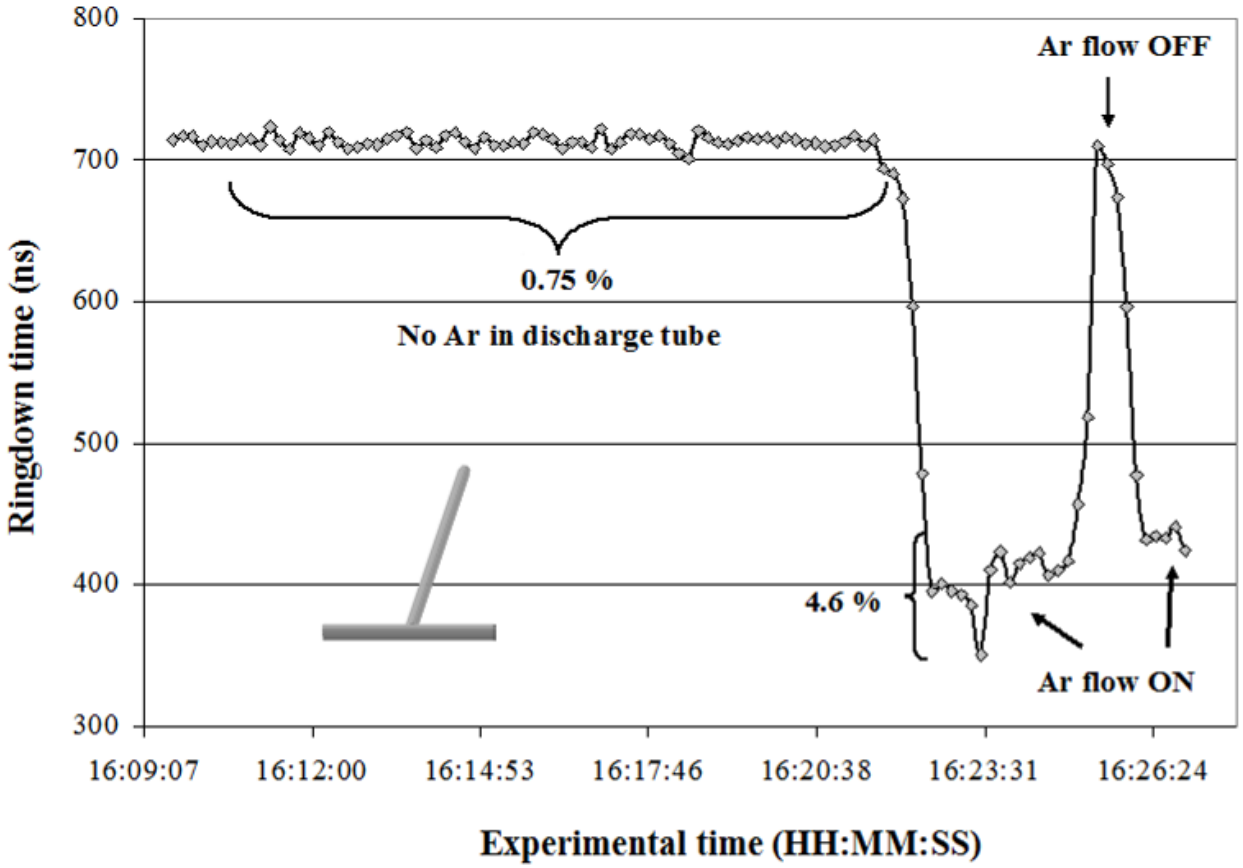

Figure 4.5 Baseline stabilities obtained with the long path/large diameter T-shaped plasma discharge tube.

Reasonable ringdown stabilities were obtained with the laser passing through the center of the absorption tube when no argon was present; however, introduction of the carrier gas resulted in highly unstable baselines. Therefore, this tube configuration was not explored further for this study.

The first configuration we examined in detail after the feasibility of the tube-shaped plasma source employing the straight discharge tube was confirmed implemented a small diameter T shape, as shown in Figure 4.6a. In the original design, the absorption portion of the tube configuration measured 200 mm long with an inner diameter of 3 mm and the discharge portion was 200 mm long with a 2 mm inner diameter. When the gas flow was turned on, the measured ringdown signal was severely restricted. When the plasma was ignited, the ringdown scans were instantly cut off due to a combination of turbulence and excessive optical losses. Upon careful alignment of the ringdown system and optimization of the position of the laser through the absorption tube in conjunction with the plasma power and flow rates, the ringdown signal could be maintained but the excessive instability of the ringdown baseline was counterproductive to improved detection capabilities. At this preliminary stage, the feasibility of significantly enhancing the plasma pathlength for increased sample-laser interaction was proven; for the aforementioned sample tube, the sample pathlength increased from 1.5 mm with the straight tube to 32 mm, approximately 20-fold longer pathlength for a potentially proportional enhancement in detection sensitivity once the instability is reduced. Figure 4.2b shows this configuration when operating at 120 W.

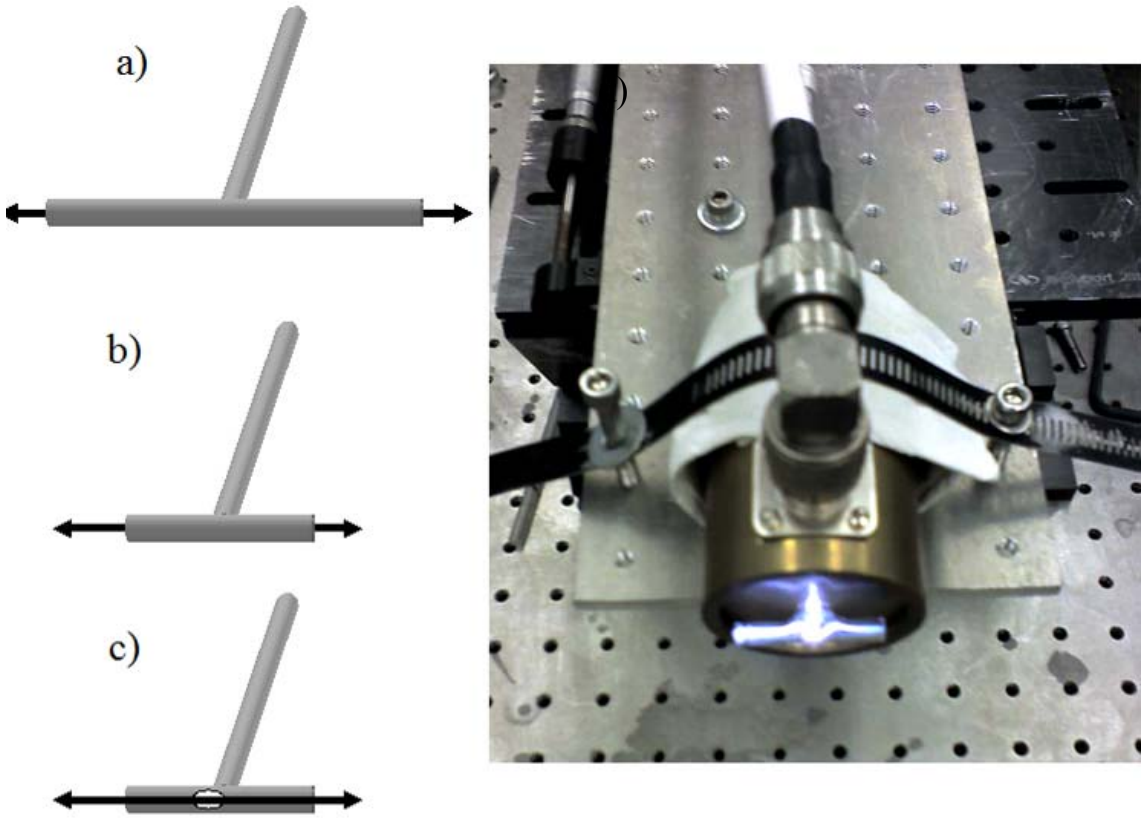

Figure 4.6 Generation of off-centered hole T-shaped plasma discharge tube.

The original tube would not sustain adequate ringdown in the absorption tube with the plasma operating. The arms were shortened (b), but the turbulence was still too excessive. A hole was inserted (c) to reduce the turbulence in the junction of the tubes. An example photo of the plasma operating at 80 W with 0.5/0.35/0.5 ml/min is given in d).

To determine if the length of the absorption tube with the plasma operating could affect the stability of the ringdown signal, the arms of the "T" were reduced, such that the absorption tube measured 33 mm (Figure 4.6b). While the shorter tube facilitated quicker and easier ringdown alignment, a diminished signal was observed upon ignition of the plasma. In order to reduce the turbulence in the absorption tube, a hole was introduced into the absorption tube, perpendicular to the gas/plasma flow. Because the edge of a diamond-tipped grinding wheel was used to insert a small diameter hole (~ 1 mm) at roughly the center of the junction of the two tubes by eye while free-handing the cutting, the hole ended up slightly off-center, and, thus, the discharge tube became known as the 'off-centered hole T-shaped' plasma, which is depicted in Figure 4.6c. Typical baseline stabilities obtained with this configuration with the gas flow on and the plasma operating are shown in Figure 4.7, where the plasma was operating at 85 W with a 1.0 L/min Ar flow rate and 50 individual ringdown events were averaged to generate each data point. An extensive series of experiments were conducted with this modification and the operational parameters with this discharge tube were rigorously anaylzed. The ignition of the plasma routinely generated the large spike observed in Figure 4.7. Interestingly, the optimum laser alignment which generated the best Hg detection sensitivity and most stable ringdown baselines with this tube configuration proved to be on the outside of the absorption tube with the plasma extending through the absorption tube wall by approximately 2 mm, as shown in Figure 4.6d.

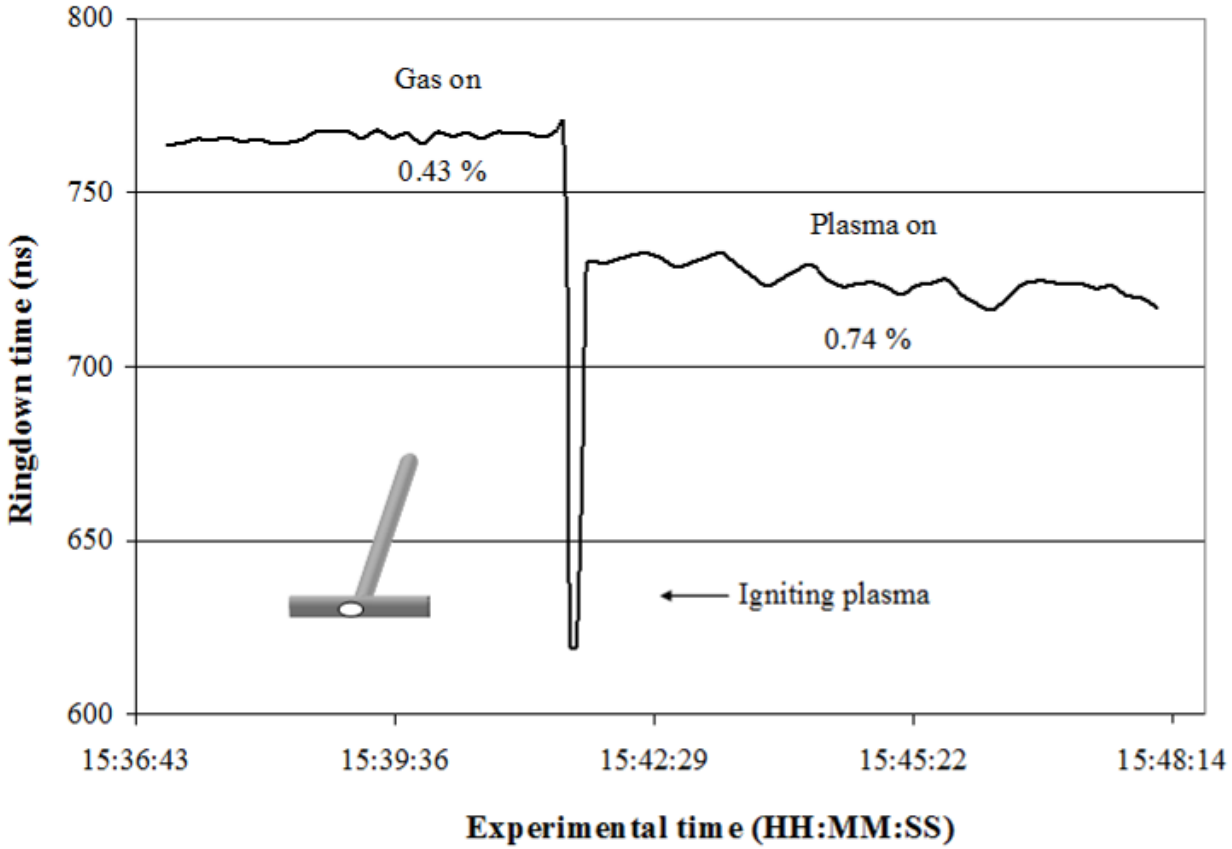

Figure 4.7 Baseline stabilities obtained with the off-centered hole T-shaped plasma discharge tube.

Each data point is the average of 50 individual ringdown waveforms. Baseline stabilities with the gas on and with the plasma operating are sufficient for MIP-CRDS studies.

In order to try to increase the absorption pathlength and simultaneously decrease the turbulence, this arrangement was further modified by implementing a long slit down the entire length of the short arms on a second small diameter T-shaped tube, as depicted in Figure 4.3c, labeled as "long slit in short arm" tube. Unfortunately, we did not have a second T shaped tube of the same inner diameter in the absorption portion of the configuration which was manufactured straight enough for the laser to pass through the entire tube; the available tube configuration with the closest matching configuration consisted of a T with a 2 mm I.D. in both the absorption and discharge portions. Figure 4.8 clearly displays the difference in baseline stabilities with the plasma on and off as well as at different flow rates while the plasma was off. The noise generated by the presence of the plasma in this configuration is prohibitive for sensitive mercury measurements. It remains unclear if this excessive plasma noise is exclusively a function of the presence of the slit cut into the tube or the geometry of the cut itself or if the difference in the internal diameter could have significantly contributed to the additional instability, especially with the introduction of the slit. Therefore, we cannot conclusively state that this discharge tube, with the opening extended as a small 'trench' down the length of the absorption tube, also free-handed on the grinding wheel, would not have been as efficient if it would have had a similar I.D. Stability scans obtained with the gas flowing through the tube prior to the addition of the slit were slightly noisier than the stabilities observed with the off-centered hole T-shaped tube prior to the introduction of the hole. Research efforts to reduce the turbulence generated employing a different approach were also examined.

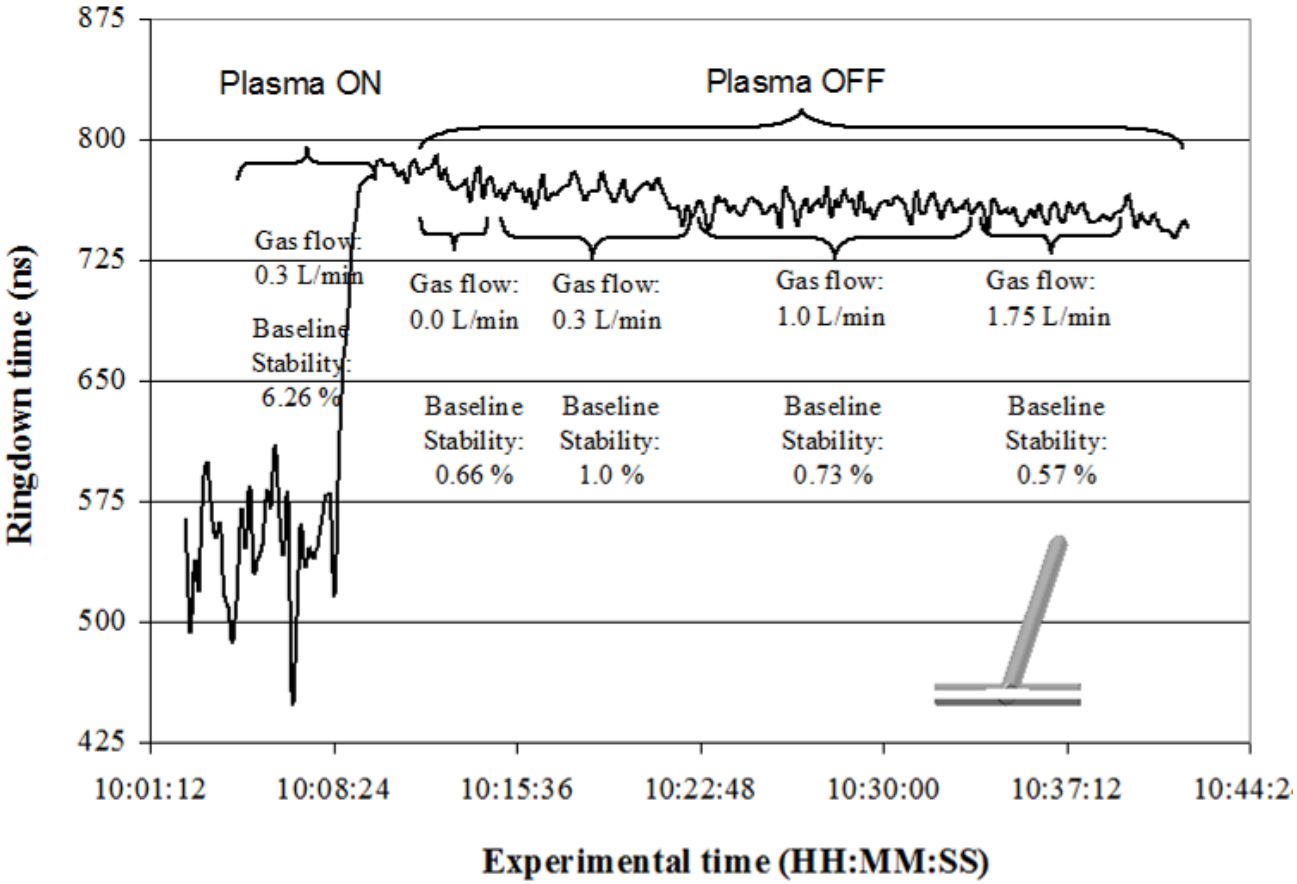

Figure 4.8 Baseline stabilities obtained with the long slit in short arm T-shaped plasma discharge tube.

Each data point is the average of 100 individual ringdown events. Baseline stabilities with the plasma operating are insufficient for MIP-CRDS studies. Baseline stabilities are defined as $\frac{\sigma_\tau}{\tau}$.

In this study, an intact discharge tube, depicted in Figure 4.9a, which featured a "side arm" was implemented. This introduced a little more stability to the ringdown baseline scans due to the reduced gas flow into the absorption arm, but the resulting baseline stabilities were not sufficient for high sensitivity ringdown measurements. This configuration allowed the plasma to branch into the side arm and extend up towards the "T". By adjusting the power and flow rates, the plasma could be further extended into the "T", where it branched again, and, depending on the plasma settings, appeared either pink, blue, violet, or almost white. Increasing the flows to levels sufficiently high to force the plasma into the absorption portion of the T generated excess instability in the ringdown spectra. In an effort to alleviate part of this influence, the "arms" of the T were shortened by scoring the quartz and then applying pressure to snap the tube along the scored line. This resulted in slightly better baseline stabilities with the gas flow on, but there was still no discernable ringdown decay curve with the plasma on, regardless of the flow rates or power settings. The addition of the sample through the side arm of the discharge tube and optimizing the power and flow rates to accommodate this configuration were attempted; however, the baseline stabilities decreased, so this approach was discontinued and focus returned to the original configuration.

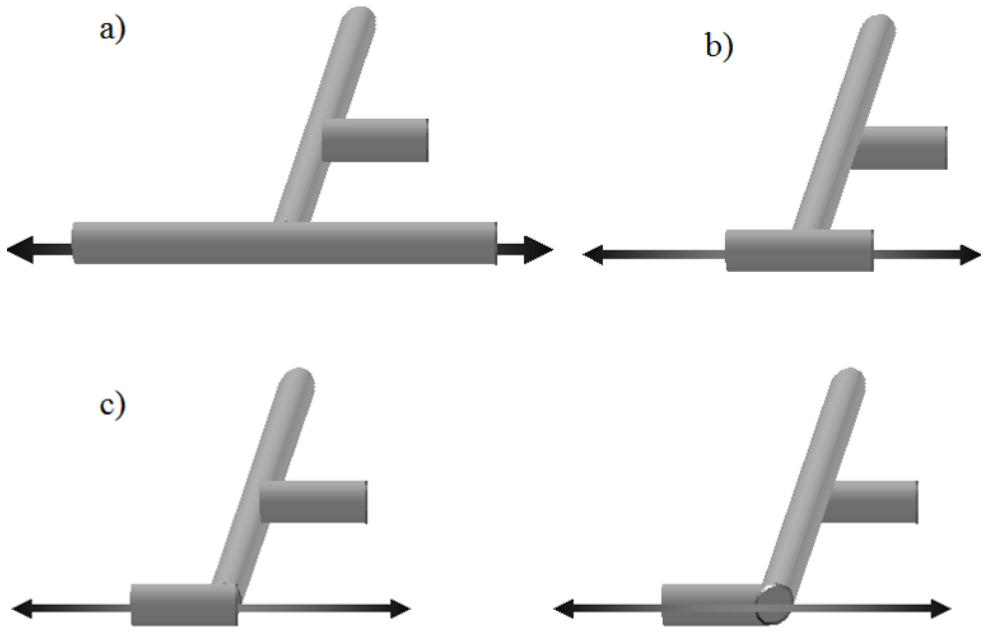

Figure 4.9 Generation of the diagonally cut plasma discharge tube.

The original tube would not sustain adequate ringdown in the absorption tube with the plasma operating. The arms were shortened (b), but the turbulence was still too excessive. One arm was completely removed to reduce turbulence while still keeping some of the sample in the absorption portion of the discharge tube (c). The entire portion of the absorption tube blocking the plasma was removed d).

The next modification was to completely remove one arm of the T. Upon igniting the plasma with this configuration, the ringdown signal became insufficiently stable for ringdown measurements. Therefore, the alteration was extended one step farther and the portion of the discharge tube directly in the path of the plasma was 'opened' while the second arm of the T was kept intact. The diamond-tipped grinder was employed again to angle the quartz, resulting in the "diagonally cut" tube. The evolution of the diagonally cut tube is pictorially displayed in Figure 4.9. Using the "diagonally cut" discharge tube, the laser could be aligned to pass through either the center of the absorption tube or parallel to the outside of the absorption tube. Both alignments are relatively clear of generated turbulence effects.

The final plasma discharge tube configuration examined in this work, shown in Figure 4.3e, consisted of a large diameter/long path T-shape which featured a 4 mm opening approximately 10 mm from either end of the absorption portion of the T. Extremely stable baselines were obtained with the laser passing through the absorption tube with no gas flow present and also when the laser passed on the outside of the absorption tube, within 1 – 5 mm of the ports' openings with the gas flowing. The large diameter of the discharge tube was not as conducive for a stable plasma, which drastically affected the ringdown baseline stabilities obtained with the laser aligned through the absorption tube. With the laser aligned to pass outside the tube, Hg could be detected, but the increased plasma instability resulted in a corresponding decrease in sensitivity so this configuration was abandoned for the remainder of this study.

4.3.3 CRDS Measurements on Mercury and Instrument Performance

With each of the aforementioned discharge tube configurations, efforts were made to optimize the baseline stability and, when feasible, mercury CRDS measurements were made. Baseline stabilities were measured with an undisturbed discharge tube, with the gas flow on, and then with the plasma on. Figure 4.7 depicts a typical baseline scan obtained with the "off-centered" T-shaped plasma with the gas on and then igniting the plasma. The left portion of the figure was obtained with the argon flowing at approximately 1.0 L/min, and the laser was aligned parallel to the outside of the absorption tube, such that the gas flow through the "off-centered" aperture entered into the ringdown path. When the plasma was ignited, a sharp drop in the recorded ringdown was routinely observed. This fluctuation could be attributed to increased turbulence during the plasma generation, a rapid temperature change, an instrumental/electronic

artifact, and/or a change in the ion concentration entering the ringdown path during the initial excitation. On average, this spike was only observed long enough to generate one data point in a scan averaging 50 ringdown events and then rapidly stabilized at a 'plasma on' baseline. Depending on the discharge tube being studied, the difference between the 'no gas' and 'gas flow on' studies could be drastic or almost non-existent. In general, when the difference between the baseline stabilities obtained with and without gas flow is small, more stable scans with the plasma on were obtained. When the difference was substantial, ringdown signals with the plasma on were not usually obtainable.

When a suitable discharge tube configuration was identified and optimized, the next step was to obtain a background scan. One key element which limited the overall sensitivity of the candle-shaped MIP-CRDS for mercury detection was the presence of an OH band that was generated in the plasma. By collecting low-resolution scans in the wavelength area of interest with the plasma operating with the various discharge tube configurations, the presence of a competing background signal could be quickly determined. If the baselines were stable enough to proceed, a sequence of high-resolution scans were recorded: first, a scan was obtained with no plasma; then a scan was collected with only the plasma running; the next scan consisted of the plasma with a blank solution introduced into the ringdown cavity; and the final scan for each discharge tube examined was to observe the presence of mercury. If the mercury signal was readily detected, the next step was to introduce various concentrations of mercury into the plasma in order to try to determine the detection limits for each discharge tube. One example of the series of background scans with the "off-centered" tube is shown in Figure 4.10, where the individual scans have been manually offset for clarification. The

Q branch of the O_2 $A^3\Sigma_u^+ - X^3\Sigma_g^-$ (7,0) band around N″ = 19 was used to visually ensure the proper wavelength region prior to each scan.

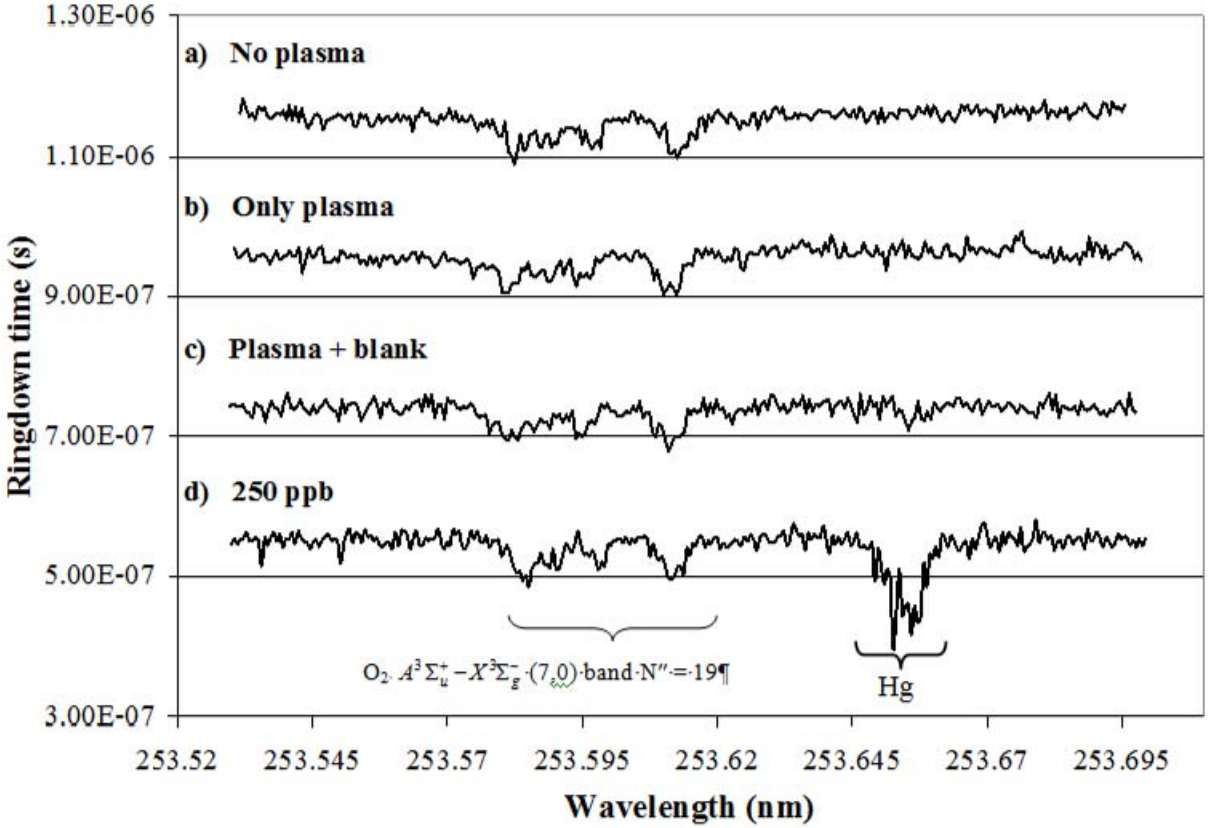

Figure 4.10 High-resolution wavelength scans around the mercury transition with the off-centered hole T-shaped plasma discharge tube.

Scans were conducted with a) ambient conditions, b) with the plasma operating at 85W, c) with a 2% nitric acid solution injected into the ringdown cavity, and d) with a 250 ppb Hg solution present in the plasma sampling system.

Figure 4.10 depicts a series of high resolution scans, starting with an open ringdown cavity (a), only the plasma on (b), the 2 % HNO_3 blank introduced into the plasma (c), and a 250 ppb Hg solution is the experimental sample in the bottom scan (d). Clearly, a 250 ppb aqueous sample introduced into the nebulizer with a 10 % conversion efficiency is readily observed with this plasma operating at only 85 W in the forward direction and 19 W in the reverse direction and the flow rate only 0.85 L/min. The scanning step rate of the laser was 0.0003 nm; and each data point is an average of 100 ringdown events. One important point to note is that residual mercury was detected when a blank solution was introduced into the plasma, as seen in scan c of Figure 4.10. This artifact, which affected the detection limit determination, was overcome by thoroughly flushing the sample introduction system with a 100 ppb Au solution prior to each mercury measurement. Another interesting point to note is that the plasma-generated OH peak, which hindered low concentration measurements of mercury with the candle-shaped MIP, is not present with this tube- shaped MIP.

Upon completing the background scans to determine the presence of interfering peaks or residual mercury, successive scans were then performed with various concentrations of Hg introduced into the ringdown cavity, some of which are depicted in Figure 4.11 for the off-centered hole T-shaped discharge tube, where the baselines have been manually offset for visual clarity. Utilizing this discharge tube, saturation of the signal was observed for concentrations higher than 250 ppb when the laser wavelength was tuned to the peak of the absorption profile; therefore, the 500 ppb data, as depicted in the figure, was not used in the subsequent calculations generated at the peak wavelength.

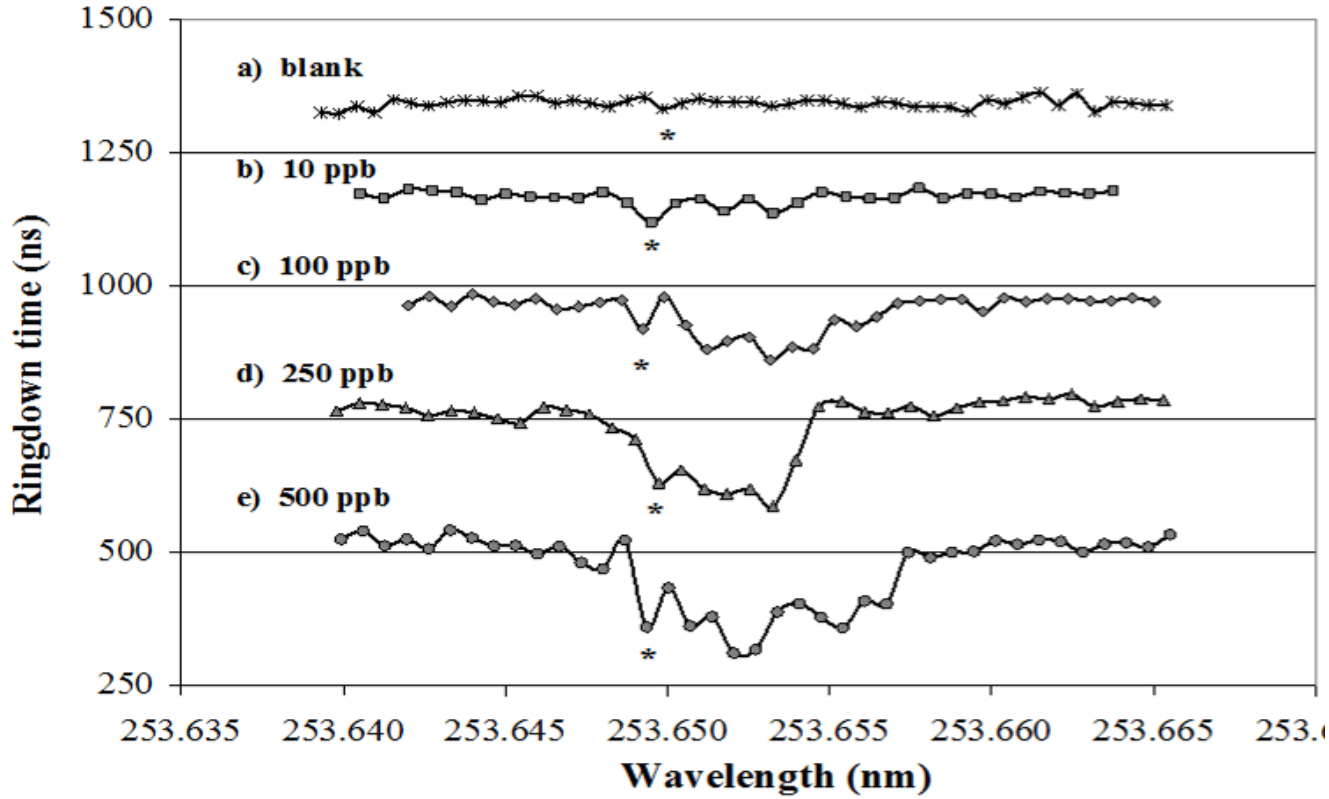

Figure 4.11 Wavelength scans conducted around 253.65 nm with the off-centered hole T-shaped plasma discharge tube.

The plasma was operating at 85W/18W and 0.85 L/min with a) 2 % nitric acid solution, b) 10 ppb Hg solution, c) 100 ppb Hg solution, d) 250 ppb Hg solution, and e) 500 ppb Hg solution injected into the ringdown cavity. Scans were obtained with a 0.0003 nm/step resolution with 100 averages per ringdown event. The spike in the Hg signal is due to a stepping artifact of the laser, as it is present in each of these scans but not in subsequent scans with the same plasma tube configuration, powers, and flow rates.

Utilizing the same off-centered hole T-shaped plasma discharge tube, a calibration plot, in which the absorption was plotted as a function of concentration, was generated. In accordance with Beer's Law, the correlation between the absorption of the laser light and the concentration of the absorbing species produced a very linear fit, as illustrated in Figure 4.12a. As previously mentioned, the data from the 500 ppb samples are not included in this graph due to the saturation of the signal observed at this concentration; however, when the remaining, lower concentrations are plotted, the resulting fit yields $R^2 = 0.9989$ ($R^2 = 0.9995$ if single point measurements are made in lieu of average values). In order to ascertain the reproducibility of the system, the same procedure was performed on a different day and the results are displayed in Figure 4.12b. The plasma powers and flow rates for a) were 80W/11W and 0.75 L/min and for b) were 85W/18W and 0.85 L/min. In both concentration series, each ringdown event is the average of 100 individual ringdown waveforms. The linearity of both plots is sufficient and the reproducibility of the slopes of the graphs is within the uncertainty of the minor laser wavelength drift that was experienced prior to the catastrophic failure of the stepping motor of the dye laser as well as the slight differences in powers and flow rates. With this configuration, the experimental detection limit is determined to be 0.3 ppb and 0.4 ppb for a) and b) in Figure 4.12, respectively, for these concentration series. In the preliminary studies utilizing this discharge tube, the same experimental procedure was performed at 253.6511 nm, slightly off the peak wavelength due to a minor drift in the output wavelength during the alignment and sample preparation. As shown in Figure 4.12c, notable linearity was obtained and higher concentrations were readily apparent. When the laser was not tuned directly on the peak of the Hg absorption feature, very low concentrations were undetectable with this discharge tube configuration, i.e., the 1 ppb

solution samples could not be distinguished, but the 500 ppb solution samples were clearly evident. In the original study, the 3-σ detection limit was calculated to be 5 ppb. By tuning onto the peak of the Hg transition line, the detection limit improved to 0.3 ppb.

Interest then turned to the potential to improve the mercury detection limit with the other discharge tube configurations. The next tube examined in detail was the 'diagonally cut' plasma discharge tube. A series of scans were obtained with a) the plasma operating at 80W/13W with a 1.0 L/min flow rate and a 2 % nitric acid solution introduced into the ringdown cavity, b) 420 ppb Hg solution injected into the plasma, and c) a 500 ppb Hg solution inserted into the plasma, as depicted in Figure 4.13. In this series, the background scans as well as the 500 ppb scan were obtained at a lower resolution, ~ 0.002 nm/step, to quickly determine the ability to detect mercury with the diagonally cut discharge tube. The 420 ppb scan was obtained at 0.0007 nm/step in order to discern spectral features of the mercury transition when the signal was not saturated. As can be seen in the figure, the mercury absorption profile displays a distinct structure in the high resolution scan whereas the lower resolution scan generates a broader, smoothed profile which will be addressed shortly.

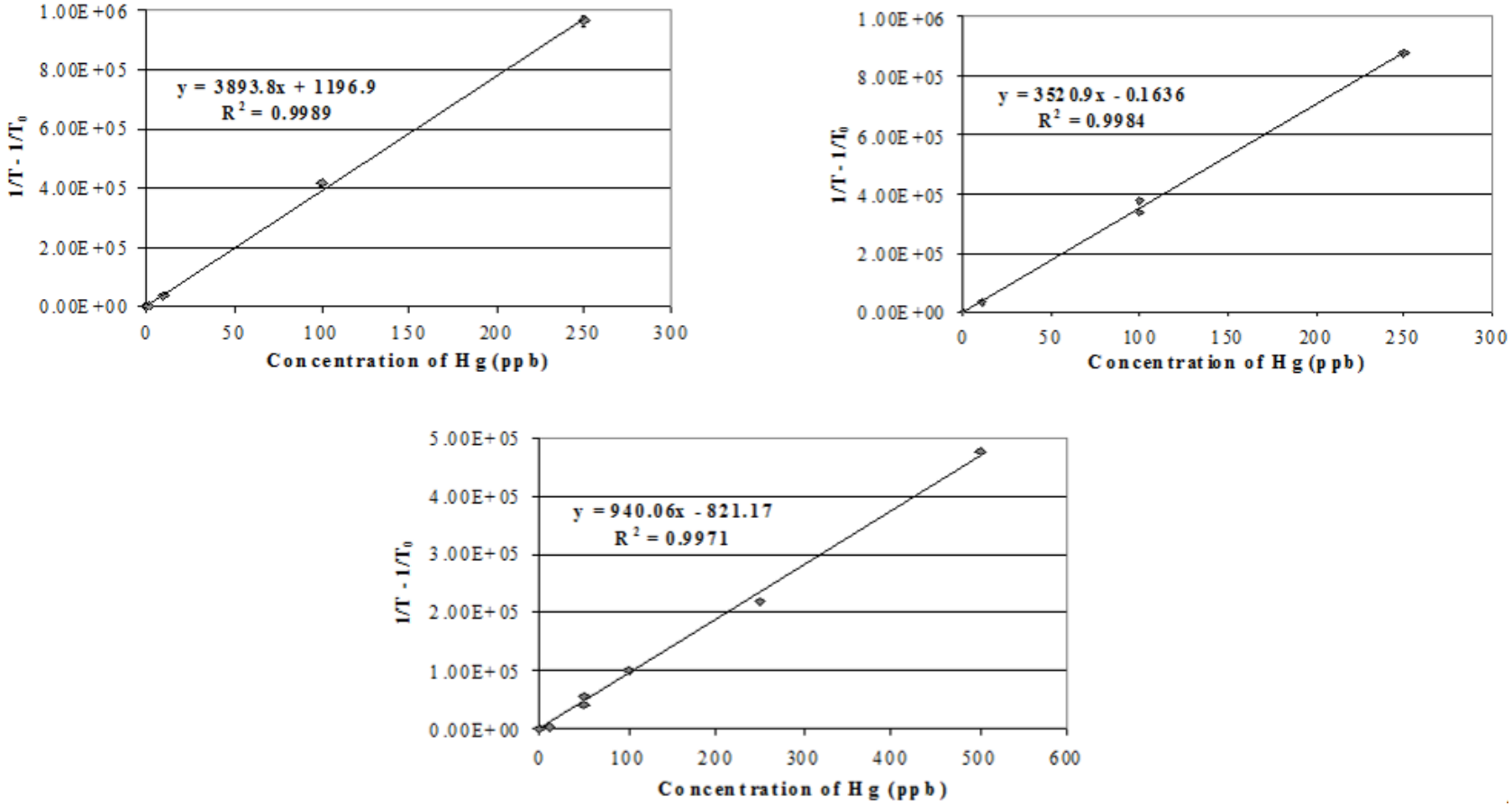

Figure 4.12 Absorbance vs mercury concentration obtained with the off-centered hole T-shaped plasma discharge tube.

a) 1 – 250 ppb mercury sample solutions introduced into the ringdown cavity with the laser tuned to the peak of the absorption feature. b) Reproducibility of the system. c) Linearity obtained with laser on the shoulder of the mercury spectrum.

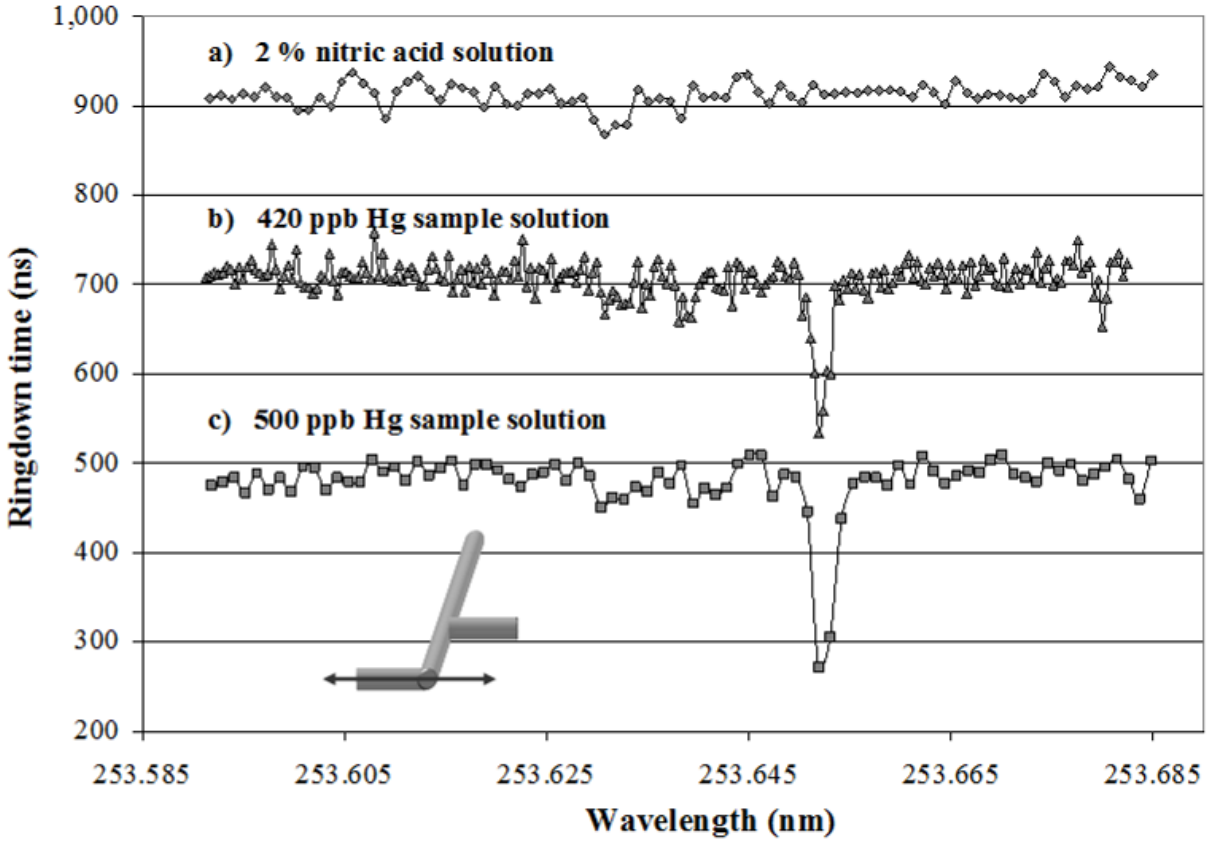

Figure 4.13 Wavelength scans conducted around 253.65 nm with the diagonally cut plasma discharge tube.

The plasma was operating at 80W/13W and 1.0 L/min with a) 2 % v/v nitric acid solution, b) 420 ppb Hg solution, and c) 500 ppb Hg solution injected into the ringdown cavity. Scans a) and c) were obtained with a 0.002 nm/step resolution and scan b) utilized a 0.0007 nm/step resolution to discern spectral information about the mercury transition.

The laser was tuned to the peak of the Hg absorption spectrum and various concentrations of mercury solutions (10 – 500 ppb) were then introduced into the plasma. The corresponding changes in ringdown time as a function of concentration are shown in Figure 4.14. With the diagonally cut discharge tube, the system was also saturated at 500 ppb when the output laser was tuned to 253.6519 nm. This artifact is evident in the figure by examining the disproportional change in ringdown time for the 500 ppb sample data as compared to the lower concentration data. When the data in Figure 4.14 are plotted in terms of absorbance vs concentration, the linear response of the system is clear. The plot, given in Figure 4.15, results in $R^2 = 0.9969$, as long as the 500 ppb data is disregarded. If the 500 ppb data is included, as portrayed in the insert in Figure 4.15, the absorbance vs concentration correlation changes drastically, which is indicative of saturation of the optical signal. Utilizing the experimental parameters and the corresponding results, the 3σ detection limit for this particular discharge tube was determined to be 0.4 ppb.

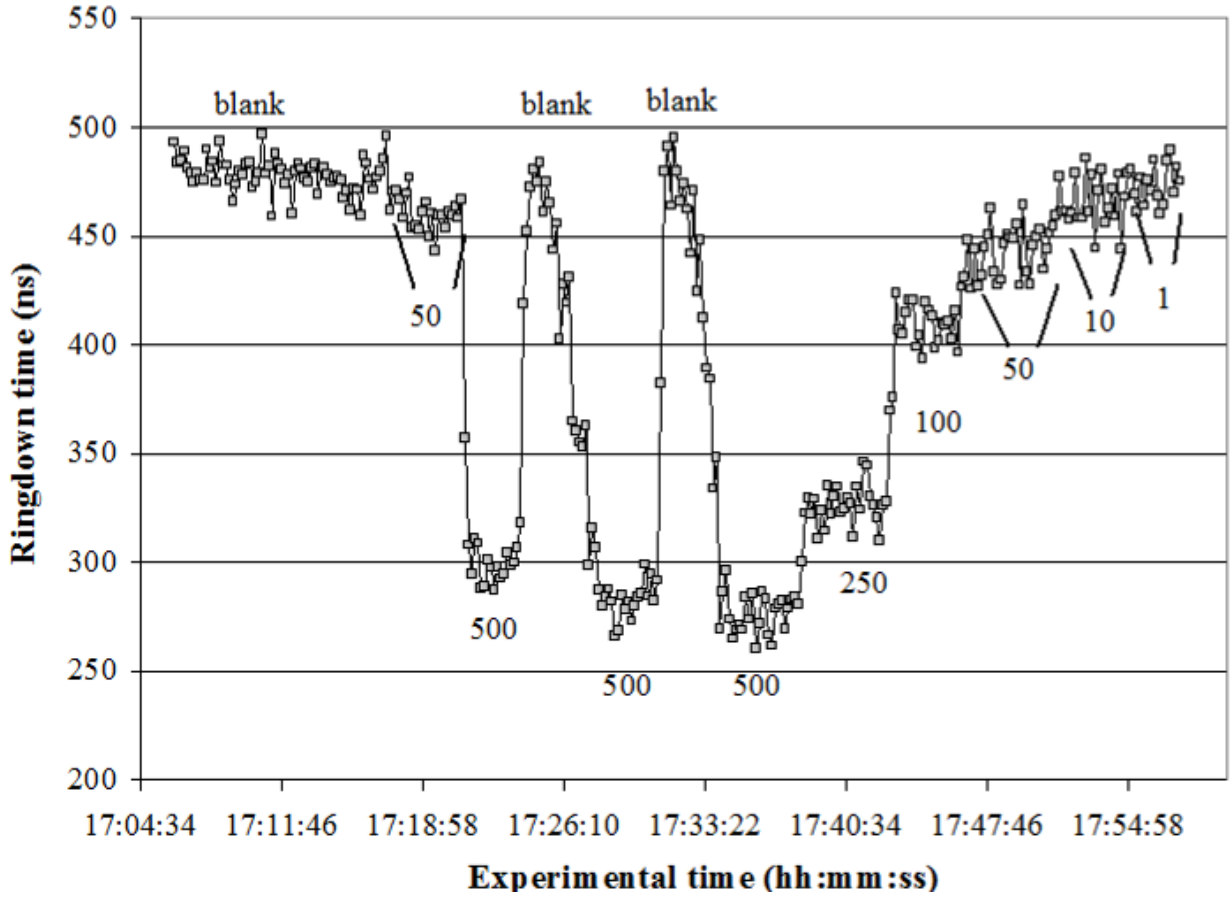

Figure 4.14 Ringdown time vs mercury concentration obtained with the diagonally cut plasma discharge tube.

Mercury concentrations ranging from 1 – 500 ppb were introduced into the ringdown cavity and the corresponding change in ringdown time is observed. The wavelength drift of the laser, prior to rebuilding the stepper motor of the dye laser, is evident in the inconsistency in the repeated 500 ppb data.

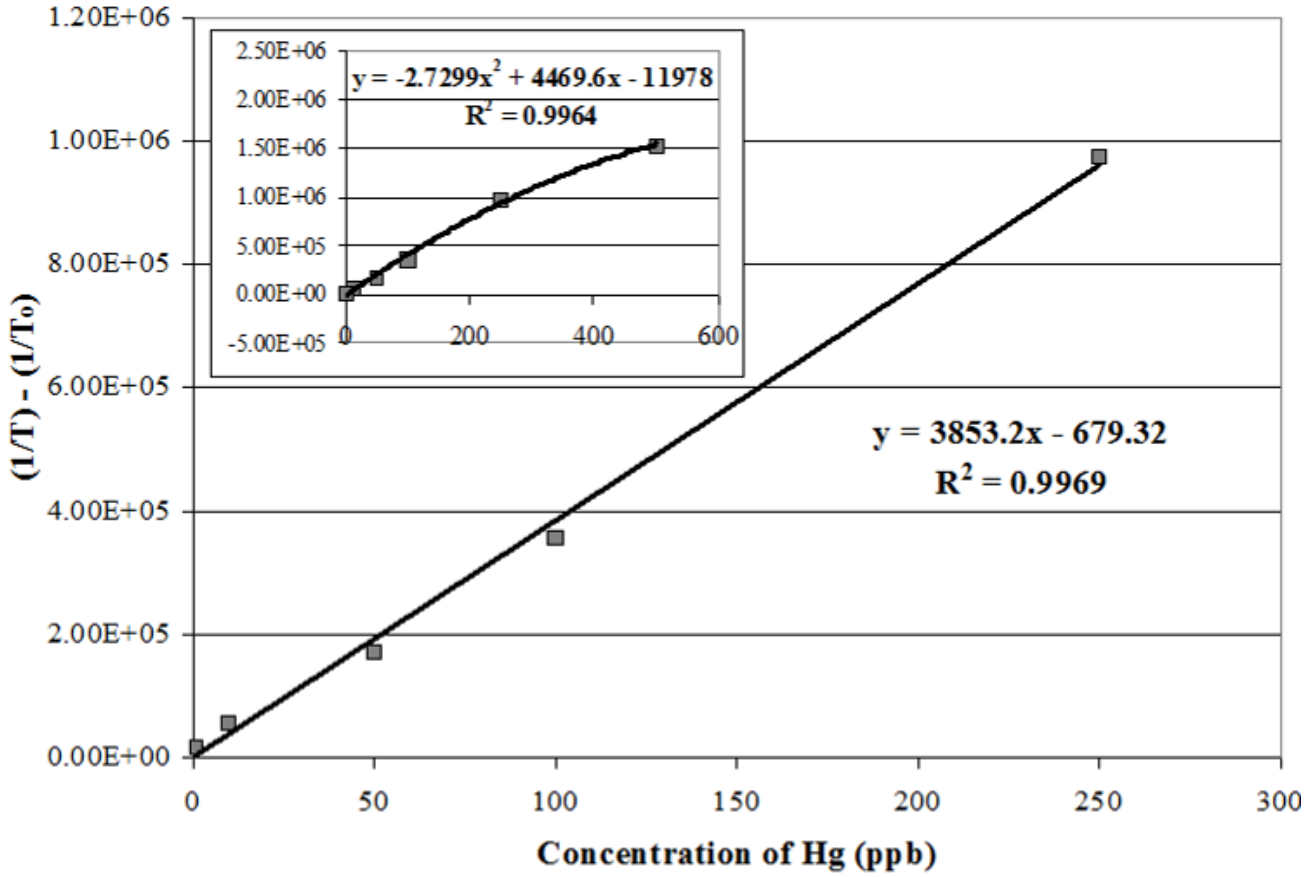

Figure 4.15 Absorbance vs mercury concentration obtained with the diagonally cut plasma discharge tube.

Acceptable linearity was obtained with the diagonally cut discharge tube with the plasma operating at 85 W. The insert depicts the non-linear behavior experienced when the mercury concentrations began to saturate the ringdown signal.

As is evident from the preceding figures, the baseline stabilities obtained and the background interference observed with the tube-shaped plasmas are much more conducive to elemental mercury detection than the 'standard' candle-shaped MIP-CRDS technique. The strong OH interference observed with the candle-shaped plasma was either not observed or greatly reduced with the various tube-shaped plasmas. This could be attributed to the lower powers utilized, a function of the quartz tubing used, or the confining nature of the tubing, thus reducing the amount of plasma discharge interaction with the ambient air. The OH interference had a negative impact on obtaining improved detection sensitivities and limited the accuracy of mercury measurements with the candle-shaped MIP-CRDS studies. Predictably, even if none of the other experimental parameters improved, as compared to the candle-shaped MIP measurements, the elimination/reduction of the background OH signal should improve the overall detection sensitivity and accuracy of this technique. The experimental detection limit for the candle-shaped MIP-CRDS system for mercury was 9 ppb for the input solution sample concentration, which is equivalent to 421 ppt in the vapor phase after the conversion due to the sample introduction efficiency and atomization of the plasma source. Utilizing the "off centered hole" and "diagonally cut" tube-shaped plasmas, the experimental solution detection limits were determined to be 0.3 ppb and 0.4 ppb, respectively, which are equivalent to 8 ppt and 10 ppt in the vapor phase. Utilizing the tube-shaped MIP, in lieu of the candle-shaped MIP, resulted in a drastically reduced background spectral interference, which was generated by the plasma, and more than an order of magnitude improvement in overall sensitivity.

4.3.4 Isotopic Structures of the Hg 254 nm Envelope

In addition to gaining an order of magnitude in detection capabilities for elemental mercury with the tube-shaped plasma-CRDS approach, another important advantage of the CRDS technique is the high spectral resolution. Mercury atomization requires little additional energy, and elemental mercury will naturally evaporate at standard temperature and pressure; therefore, utilizing a low-power, low-temperature atomization source, which resulted in higher ground state population and smaller Doppler-broadening effects, as compared to an ICP or the candle-shaped MIP, is more favorable for structural and isotopic measurements of mercury. The mercury transition line explored in this research is a combination of overlapping, pressure-broadened lines of the seven naturally occurring, stable mercury isotopes. The seven isotopes include five even ones due to isotopic shifts and two odd ones due to nuclear spin, and they, along with their corresponding abundances, are listed in Table 4.3. The isotopic shifts and hyperfine splitting of the isotopomers is given in Table 3.2 and Figure 3.9. A background-subtracted, high-resolution scan of the mercury transition using the off-centered hole T-shaped plasma discharge tube is shown in Figures 4.16, and the isotopes are indicated in the figures. The scanning step rate of the laser was 0.0003 nm/step. Comparison of the isotopic peaks in each scan with the theoretical data is given in Table 4.3. In a couple of instances, the individual peaks in the absorption profile are comprised of two or more isotopes, and in some cases, the isotopic peak is portrayed as two peaks in the spectral scan. This is believed to be an artifact of the instrumental limitations, especially for the reproducibility and accuracy of the dye stepper motor. As was observed in Figure 3.9, the artificial, laser-induced peak (#) and the undetermined,

reproducible peak on the shoulder of the Hg transition (*) were also observed with this system.

Table 4.3 Isotopic ratios of Hg at 254 nm with the off-centered hole T-shaped plasma discharge tube

Line Position	Wavelength (nm)	Exp. Ratio (%)	Theo. Ratio (%)	Isotope Assignments
1	253.647	12.8	13.4	201(c) + 199(a)
2	253.65	13.4	14.4	201(b) + 198
3	253.652	22.2	23.1	200
4	253.653	27.4	29.8	202
5	253.654	24.1	19.1	204 + 201(a) + 199(b)
*	253.656			Undetermined

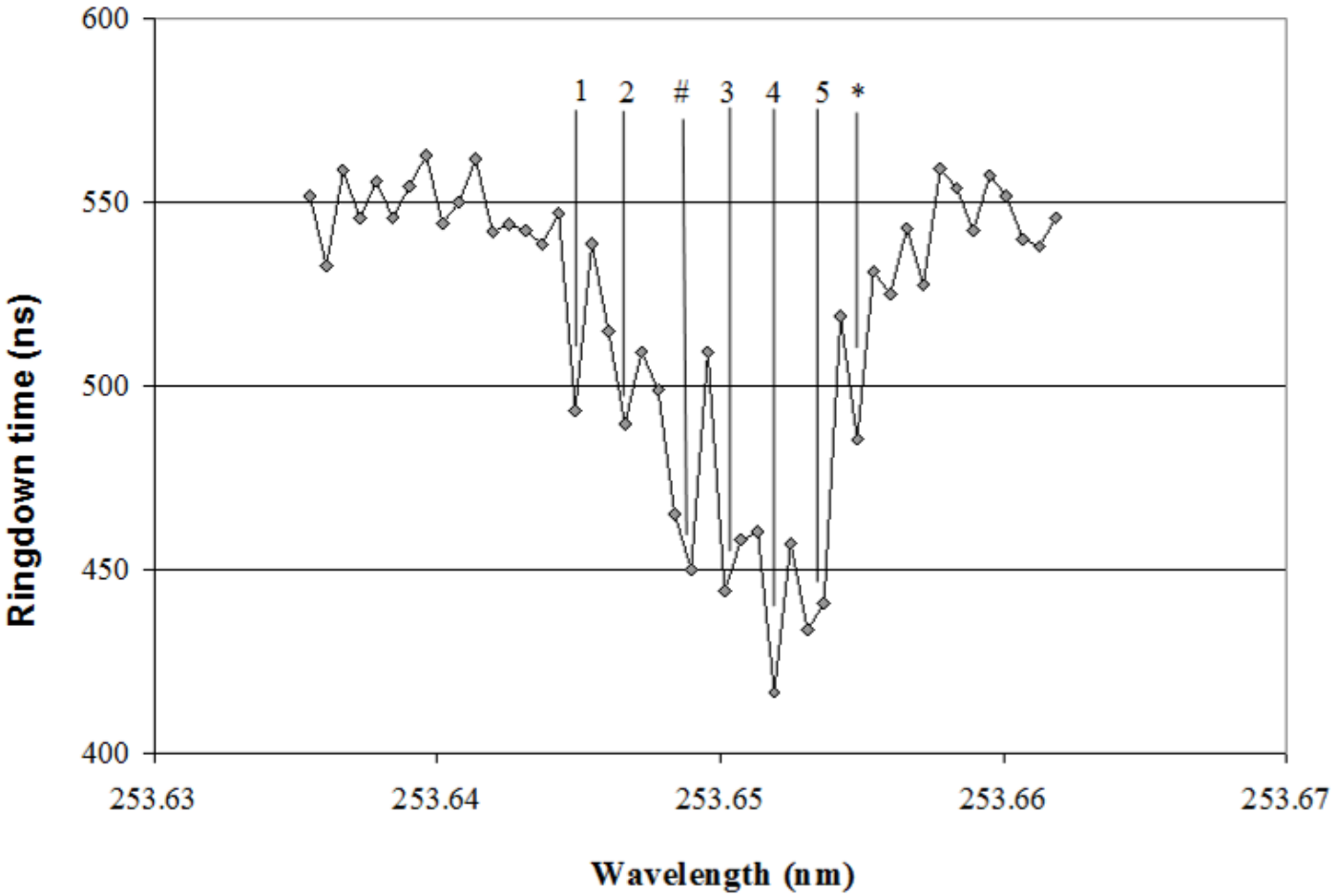

Figure 4.16 Isotopic structure of Hg at 253.6519 nm with off-centered T-shaped plasma discharge tube.

A 250 ppb Hg solution was injected into the plasma, operating at 120 W. The peak labeled # is an artificial artifact of the laser stepping mechanism, and the peak labeled * is undetermined but reproducible.

CHAPTER V

REAL-TIME MONITORING OF ELEMENTAL MERCURY NATURALLY EVAPORATING FROM CONTAMINATED SOILS AND SOLUTIONS USING CAVITY RINGDOWN SPECTROSCOPY

5.1 Introduction

In addition to measurements of Hg using the plasma-CRDS technique, as described in Chapters III and IV, this research also explored the feasibility of directly detecting elemental mercury naturally evaporating from contaminated soils and solutions under atmospheric conditions using CRDS. The inherent sensitivity of CRDS towards the direct detection of both naturally-occuring[40] (7 ppt) and artifically-enhanced[38] (14 ppt) background atmospheric mercury has previously been reported. The first was due to naturally-occurring background Hg; the latter was traced to an unsealed waste receptacle with a broken thermometer, and the signal went away upon removal of the container. However, employing this ultra-sensitive absorption spectroscopic technique, which readily yields absolute absorption measurements, as a means of detecting and monitoring Hg from soil and solution samples intentionally spiked with varying concentrations with no chemical manipulation of the sample after the addition of Hg had not previously been reported. The literature available at the time which incorporated CRDS for Hg detection[37, 39, 41, 122, 126] involved some type of chemical manipulation when examining various concentrations of Hg. Several Hg compounds were preliminarily tested, and two laser sources were employed throughout the course of this research. The results of this

study have proven the feasibility of measuring elemental mercury vaporized directly from mercury-spiked soils and solutions of different concentrations without any sample preparation, such as heating, preconcentration, or any type of chemical manipulation, while employing the cavity ringdown spectroscopic technique.

5.2 Experimental Setup

The experimental system employed in this study consists of three major divisions: the optical systems, sample preparation and measurement cells, and data acquisition, which are briefly described below.

5.2.1 Optical Systems

Two laser systems were utilized in this research. The first system was also employed in the previous Hg studies presented in Chapters III and IV. The same optics and detector were used without further modification. The ringdown cavity was 56 cm long, and the mirrors' average reflectivity was calculated to be ~ 99.67% due to extensive use in these studies. The second laser system employed to generate 253.652 nm laser light was a Nd:YAG-pumped (SpectraPhysics, Pro-290-10) MOPO-HF with the frequency doubler option (FDO). The output linewidth of the high finesse (HF) optical parametric oscillator (OPO) is < 0.075 cm^{-1} and the FDO generated the appropriate UV wavelengths. The same wavemeter used with the first system was applied to this set up to monitor the output wavelength. For this system, the same ringdown mirrors and detector were also incorporated.

5.2.2 Samples

Various concentrations of mercury solutions were prepared by diluting a standard mercury solution (1000 μg mL^{-1}, Absolute Standards, Inc.) with a 2 % nitric acid

solution. The sample solutions were housed in a Plexiglass cabinet, which was continuously evacuated to prevent accidental contamination of the measured samples. Contaminated soil samples were acquired in two ways. The first series of soil samples were obtained within proximity to the Oak Ridge National Laboratory site and then doped with ~ 800 ppm mercury at I.C.E.T. (Institute for Clean Energy Technology) for a heavy metal plant sequestration study ~ 2 years prior to this research. The samples had physically been used in the plant study for more than 12 months and then were stored in an outdoor shed where they were exposed to seasonal temperature variations, humidity, and direct sunlight for approximately another 12 months before this analysis began. These soil samples were doped with mercuric salts, including $HgCl_2$, HgS, and $Hg(NO_3)_2$. The second series of contaminated soil samples were generated by doping "real world" soil samples obtained in close proximity to the laboratory with various concentrations of mercury-spiked solutions. The dry soil samples were gently sifted to remove rocks, roots, and plants, and then ground into a fine powder with a mortar and pestle prior to the addition of the mercury solutions. In order to ensure the containment of the mercury vapor, the spiked soil samples were also housed in the vented Plexiglass cabinet and the experimental area was continuously evacuated by a separate ventilation system.

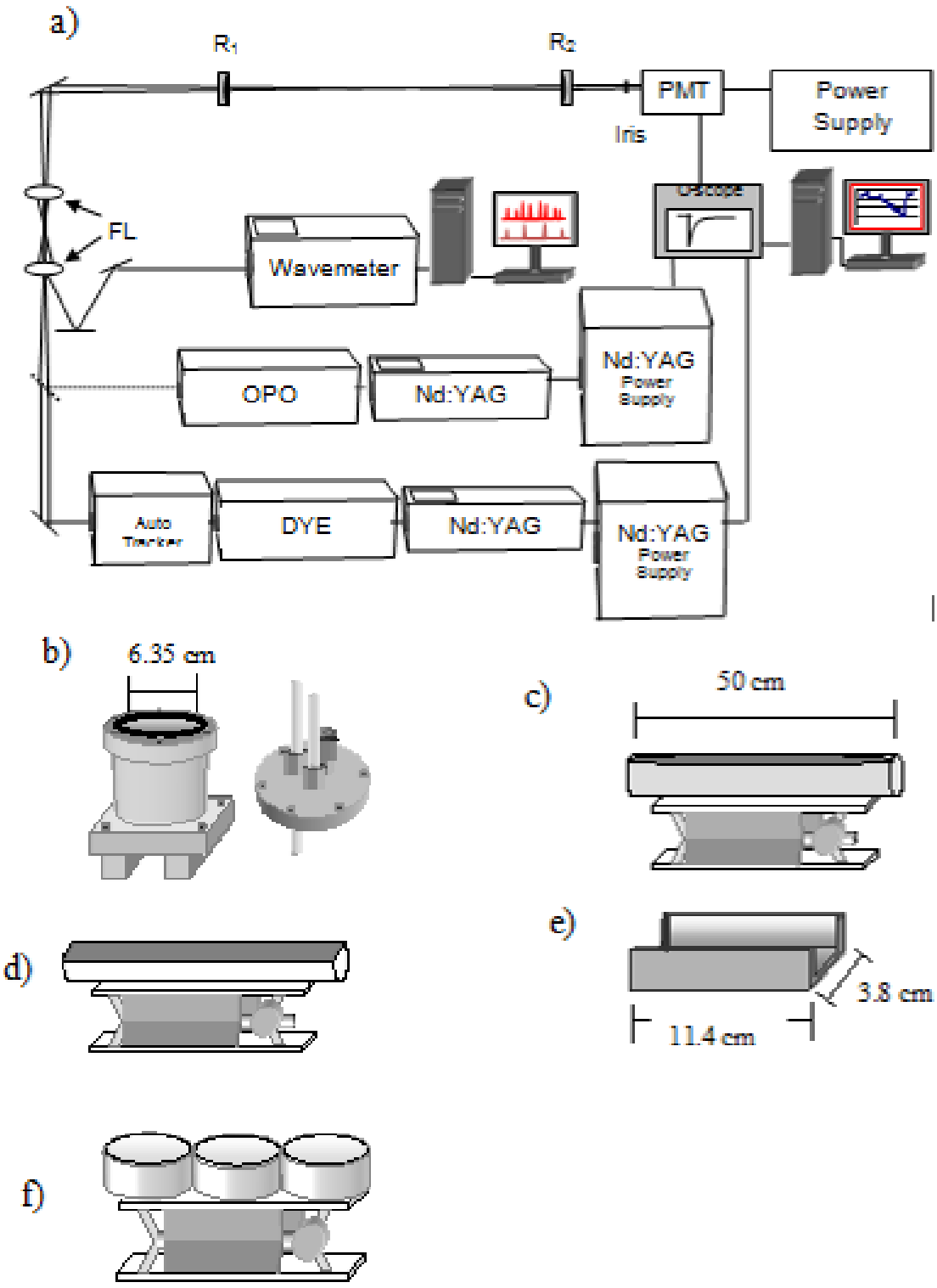

Figure 5.1 Experimental setup and sample cells.

The experimental set up incorporating both the laser systems is shown in a). b) through f) are the sample cells predominantly utilized in this research.

5.2.3 Sample Cells

The sample containers utilized in this research underwent several modifications as were deemed necessary as the study progressed. Several of the explored configurations are depicted in Figure 5.1, along with the experimental set-up incorporating both laser systems. This is only for pictorial purposes, as the laser systems were not employed simultaneously. For solution samples, a 1" diameter, hollow stainless steel tube with a 0.25 " length-wise slit, depicted in Figure 5.1c, was initially employed. Endcaps were welded onto both ends of this 50 cm tube to prevent any leakage of the sample. The sample tube was mounted on a laboratory jack to allow adjustment of the height of the sample, relative to the path of the beam in the ringdown cavity. Due to the construction of the ends of the sample tube, the laser passed ~ 8 mm above the solution samples. Subsequent iterations incorporated plastic tubing with endcaps and Petri dishes. With the plastic tubing, openings were cut in the endcaps to allow the laser to pass through the tube ~ 5 mm above the solutions. The laser was aligned ~ 1 mm above the Petri dish(es), which placed the beam ~ 5 mm above the samples. For the initial soil sample studies, 0.5 " PVC pipes were cut ~ 44.5 cm long and then, lengthwise, cut in half, as shown in Figure 5.1d. The PVC sample holders were also mounted on the jack and the height was adjusted so as to allow the laser beam to pass through the top portion of the PVC channel, approximately 2.5 mm above the samples. Additional sample cells were constructed from foil (Figure 5.1e), Nalgene bottles (not shown), Pyrex beakers (not shown), and Petri dishes (Figure 5.1f). In order to ensure the observed Hg signals were not due to used sample cells, after it was determined that large memory effects were present with some of the sample containers, fresh cells were used with each new concentration series examined.

5.3 Results and Discussion

Mercury has an intense absorption at 253.6519 nm, and a broad, initial ambient background scan in this wavelength region indicated the presence of the well-documented, weak transitions of the Q branch of the O_2 $A^3\Sigma_u^+ - X^3\Sigma_g^-$ (7,0) band around N″ = 19.[36] However, as opposed to elemental mercury detected with the microwave plasma, where significant background interference was observed at 253.65 nm, the baseline measurements at this particular wavelength were unimpeded, and no additional spectral absorptions due to atmospheric interference were found, as can be seen in Figure 5.2, where background spectral scans observed with both the Nd:YAG-pumped dye laser and the MOPO-HF-FDO systems are shown. Typical baseline stabilities observed with the dye laser system were 0.3 – 0.5 % and with the MOPO were 0.5 – 1.0 %. Figure 5.3 illustrates the baseline stabilities obtained with each laser system.

5.3.1 Elemental Mercury Vapor from Spiked Solutions

In order to examine proof of concept, mercury vapor evaporating from mercury-spiked solution samples was directly probed. In the initial studies, the mercury vapor above a 50 mL beaker containing a 20 mL aliquot from the standard 1000 ppm mercury solution was probed. The sample beaker was placed in a specially constructed aluminum container, "the bomb," with an inner diameter of 6.35 cm, depicted in Figure 5.1c. The bomb was designed to allow argon to bubble through the Hg solution and provide a means to easily heat contained solutions. An example spectrum obtained with 0.5 L/min Ar bubbling through a 20 ppm Hg solution placed in the bomb with no external heat applied to the chamber is shown in Figure 5.4. However, it was quickly realized that reasonable detections could be obtained without bubbling or heating the solutions. This ability became more clearly evident when the bomb was left open one day during a

routine stability scan. The laser wavelength drifted across part of the Hg profile and the conclusion reached upon analysis of the results, portrayed in Figure 5.5, lead the research in a new and simpler detection direction. The open sample container, with no Ar flow or heating apparatus, was placed directly under the path of the laser beam in the ringdown cavity, and the laser wavelength was scanned across the mercury absorption peak. Absorption profiles obtained in this fashion were susceptible to changes in the airflow in the room, which were most likely due to the location of the adjustable vent for the exhaust system, the status of the plasma exhaust line, and the performance of the building's air conditioning system, which potentially affected the concentration being detected. By pulling air and the mercury vapor into the vent, field conditions, such as wind and light scattering due to particulates, were preliminarily simulated, and Hg was consistently detected. For these feasibility studies, the system was not rigorously optimized to obtain the best detection limits. However, utilizing this configuration, the detection limits obtained were in the ppt level, several orders of magnitude below the maximum exposure limit set by the EPA.

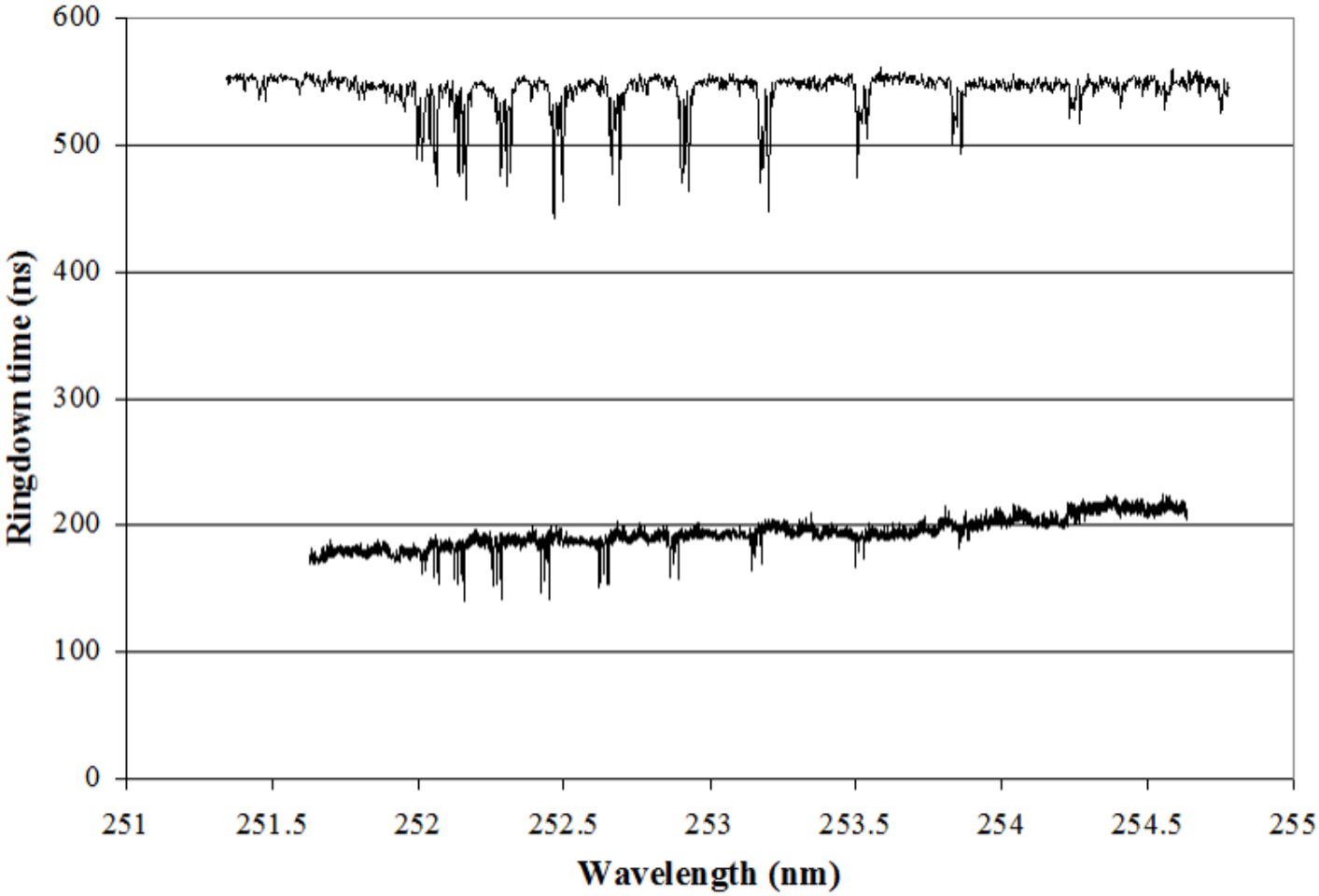

Figure 5.2 Background scans with both laser systems.

The upper trace was obtained with the Nd:YAG-pumped dye laser system, and the lower trace was obtained with the MOPO-HF system.

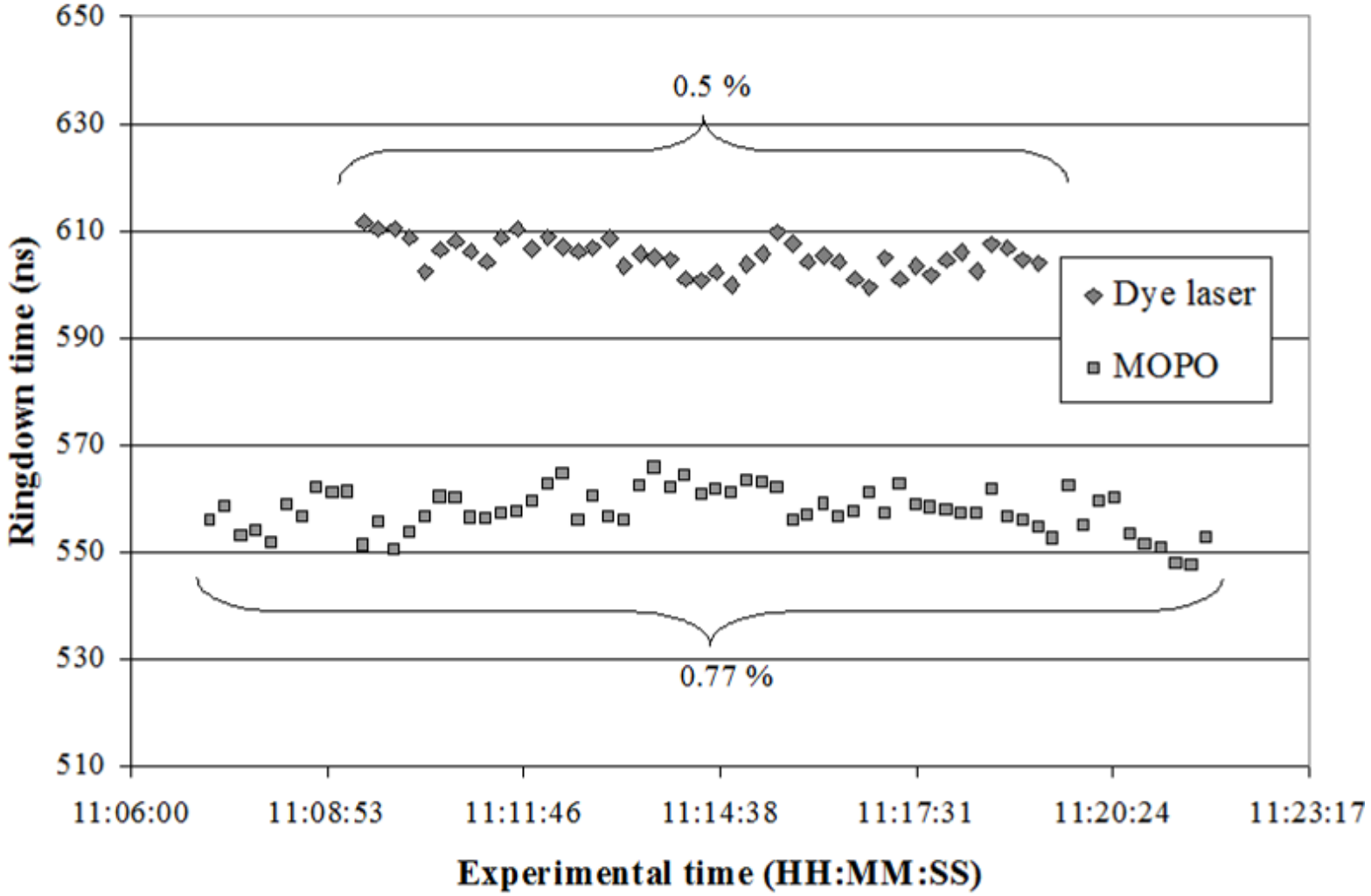

Figure 5.3 Typical baseline stabilities observed for 100 averages per ringdown event with the laser systems employed in this research.

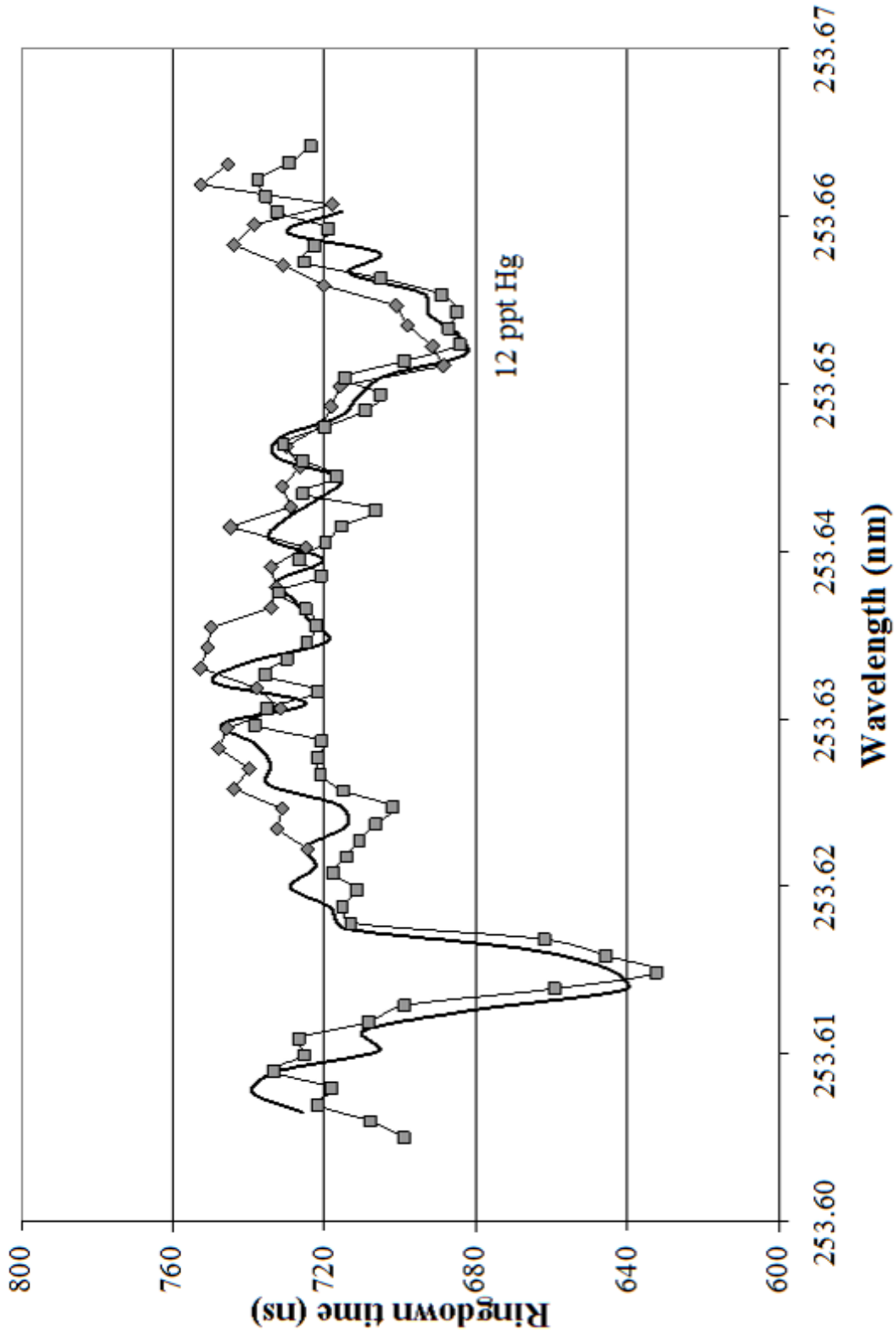

Figure 5.4 Hg signal observed with argon bubbling through 20 ppm solution.

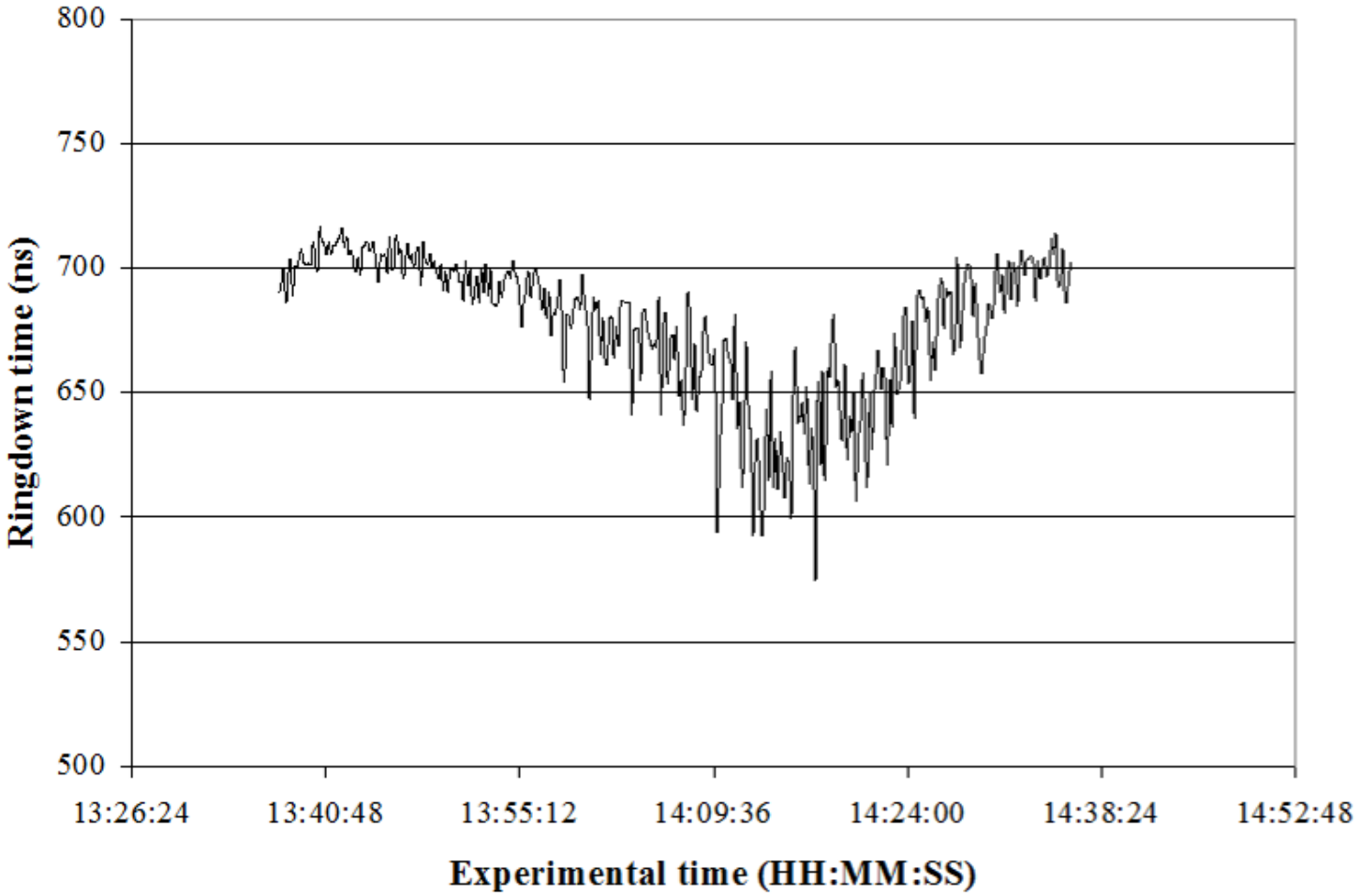

Figure 5.5 Wavelength drift of laser generated Hg absorption “scan”.

During a routing warm-up and baseline stability scan, the wavelength of the laser drifted such that the entire Hg profile was covered. A 5 ppm Hg soil sample was positioned in ‘the bomb,’ which was open to the atmosphere.

Upon the confirmation of mercury signal using the standard mercury solution, high-resolution spectral scans were performed on the vapor escaping from multiple solution samples at various concentrations. Figure 5.6 illustrates a typical scan observed with 1000 ppm Hg in the 50 cm long metal tube with the lengthwise slit across the top. Each data point is the result of averaging 100 individual ringdown events and the laser step rate was coordinated such that one data point/wavelength step was acquired. For the high resolution scans, the spectra were relatively reproducible, as can be seen in Figure 5.7. These spectra were obtained with the Nd:YAG-pumped dye laser system. Subsequently, various concentrations of Hg solution were also examined. For example, as shown in Figure 5.8, mercury vapor is readily observed from a 50 mL aliquot of 100 ppm Hg solution sample in the ringdown cavity. An example spectrum of a 1 ppm Hg solution sample present in the sample cell below the ringdown cavity is depicted in Figure 5.9. Using this configuration, the detectable gas phase mercury concentrations from the 1000, 100, and 1 ppm sample solutions were determined to be ~ 0.1 ppb, 0.5 ppb, and 0.2 ppb, respectively. A calibrated plot for Hg at 253.6519 nm was generated in order to determine the detection limit for this approach. As seen in Figure 5.10, a change in the concentration of Hg solution, which was generated by removing half of the sample in the cell and replacing the extracted quantity with an equivalent amount of 2 % v/v nitric acid solution, resulted in a corresponding change in ringdown time. The insert of the figure denotes the calibration curve obtained for this series. The noise-equivalent detection limit for mercury in this scan was calculated to be ~ 0.5 pptv. The noise-equivalent detection limit, α_{min}, is estimated using the following:[127]

$$\alpha_{\min} = \frac{d}{l_s c} \frac{\Delta\tau_{\min}}{\tau_0^{\,2}} , \qquad \text{Eq 5.1}$$

where d is the cavity length, l_s is the sample pathlength, c is the speed of light, $\Delta\tau_{min}$ is the smallest measureable difference between τ and τ_0 based on 3-σ, and τ_0 is the ringdown time with no absorbing species present in the cavity.

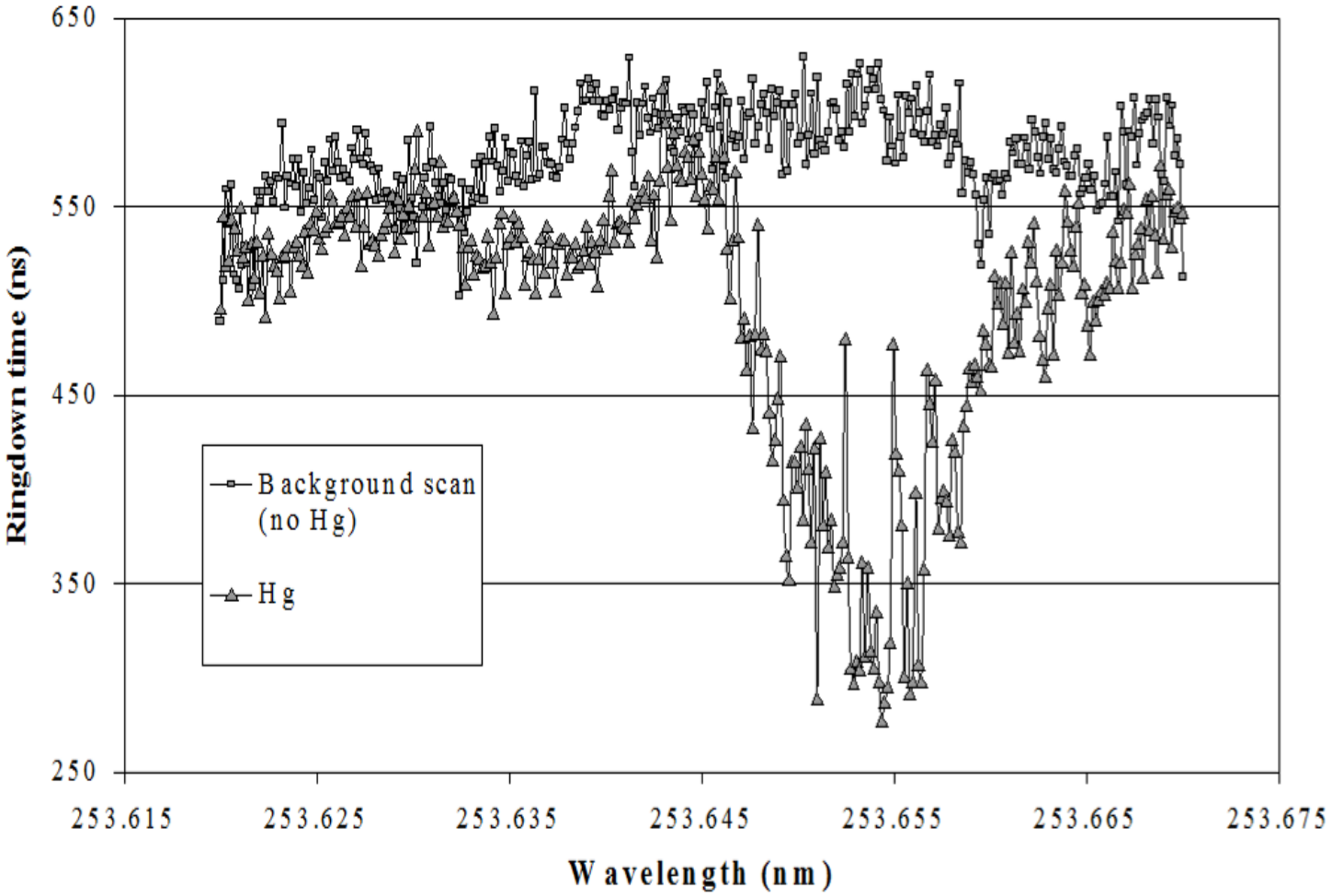

Figure 5.6 High-resolution CRDS spectra for 1000 ppm Hg solution and the observed background.

This scan was obtained with the dye laser system. The scan rate was 0.0008 nm/step. Each data point is the average of 100 ringdown events.

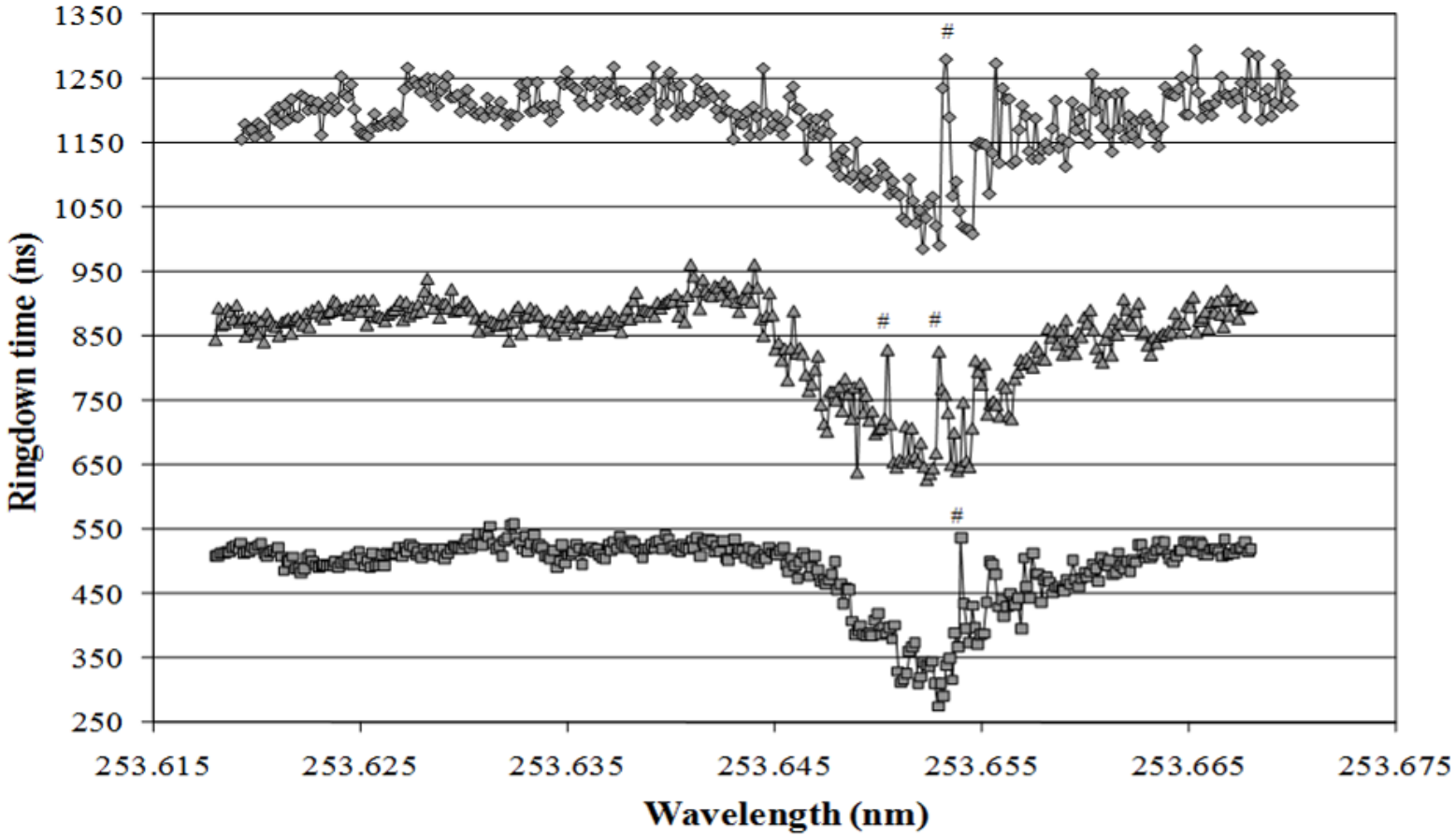

Figure 5.7 Reproducibility of Hg peak with dye laser-CRDS system.

The same 1000 ppm solution was used in all three scans which were acquired on different days, different laser alignments. The scan rate was 0.0008 nm/step. Each data point is the average of 100 ringdown events. The peaks marked # were artificial artifacts generated by the stepping mechanism of the dye laser.

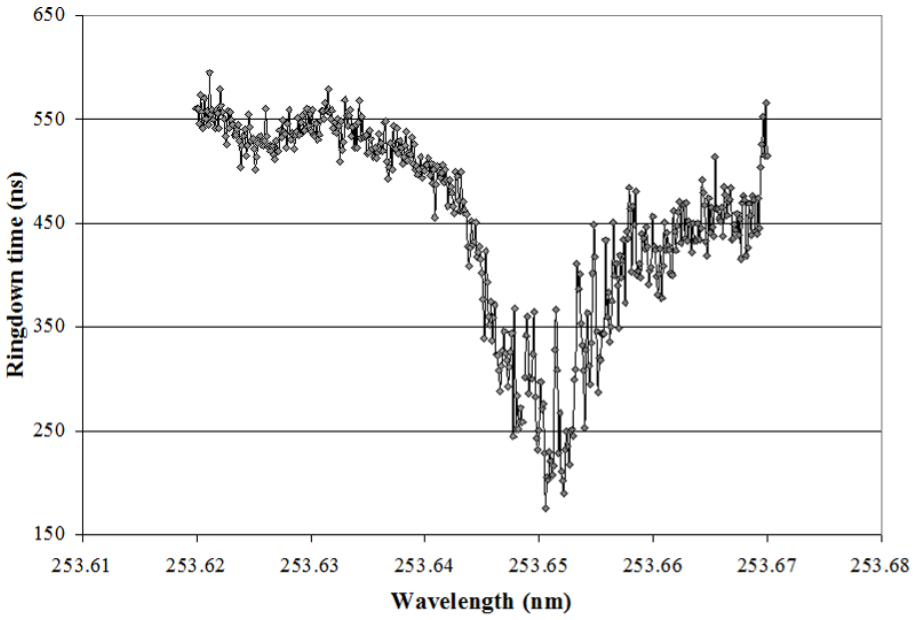

Figure 5.8 CRDS spectrum generated from Hg vapor naturally evaporating from a 100 ppm Hg solution placed under the ringdown cavity.

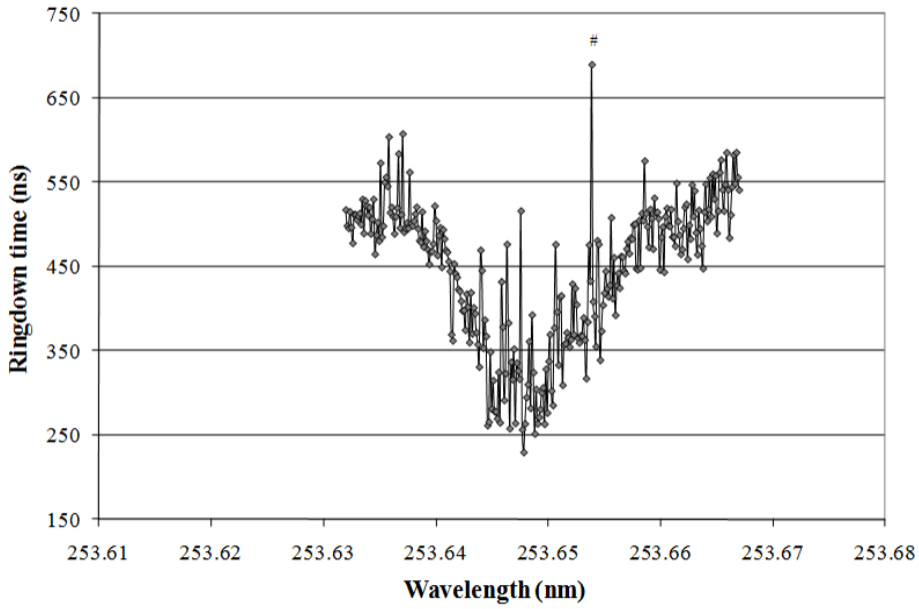

Figure 5.9 CRDS spectrum generated from Hg vapor naturally evaporating from a 1 ppm Hg solution placed under the ringdown cavity.

The peak marked # is an artificial artifact of the stepping mechanism of the dye laser system.

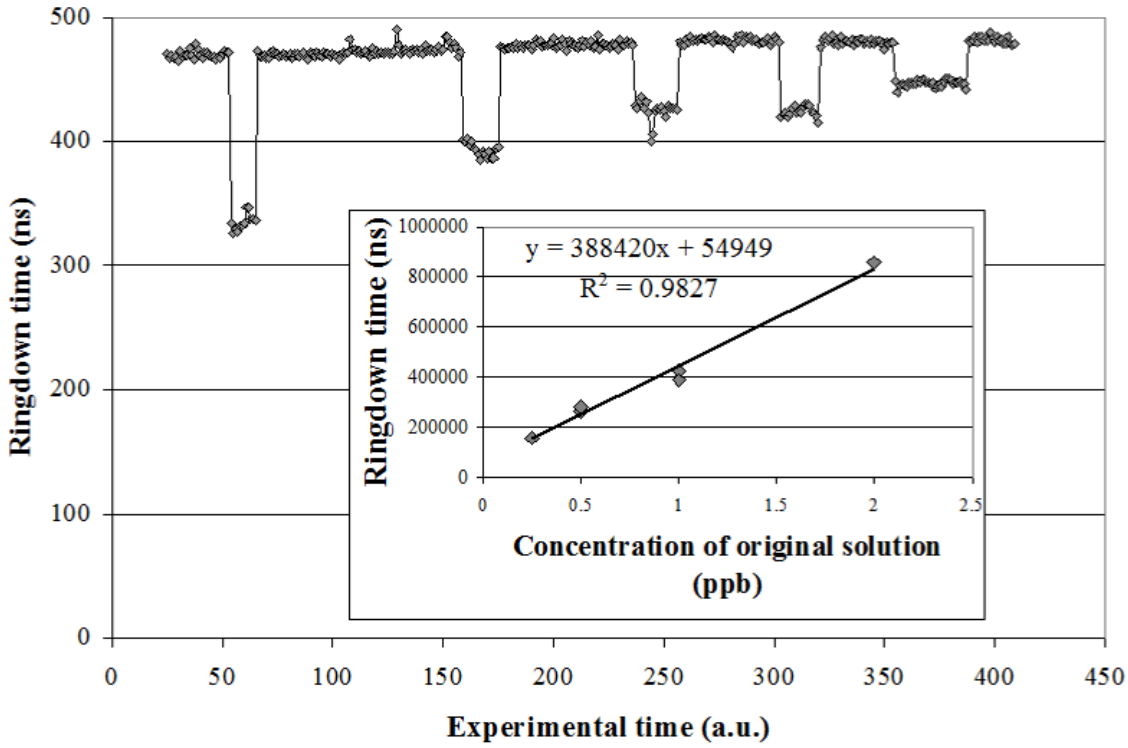

Figure 5.10 Calibration plot for the 253.65 nm Hg line.

Various concentrations of Hg solution were placed under the ringdown cavity and the corresponding change in ringdown time is depicted. These values were then used to determine the detection limit for the system.

During the course of this research, an MOPO laser system was also used. The reproducibility and ability to detect Hg naturally evaporating from 100 ppm solutions with the MOPO are shown in Figure 5.11. In these scans, 100 averaged ringdown waveforms were used to calculate each ringdown time. A minor wavelength correction was necessary in order to account for hysteresis in the four micrometers utilized in the stepping of the laser wavelength; hence, the wavelength scan was expanded beyond just the mercury transition in order to include the Q branch (N″ = 19) of the O_2 A←X (7,0) band. When first determining the reproducibility and detectability of Hg with this system, a series of wavelength scans were conducted with this laser system to explore the

ability to detect Hg from various concentration samples. Figure 5.12 illustrates the ability to detect Hg vapor from a 5 ppm Hg solution. For this figure, 3 Petri dishes were placed on a lab jack, directly under the laser beam path, and the ringdown cavity was either covered with Al foil or open to the atmosphere, as indicated in the figure. Covering the cavity resulted in better detection, as one would expect for vapor studies. Somewhat unexpectedly, however, it was observed that the detected Hg concentrations for the 5 and 100 ppm samples did not differ significantly. This approach was extended even farther to 1 ppm. In this series, various combinations, incorporating either one or three Petri dishes with or without foil covering the ringdown cavity were tested. Some of these scans are depicted in Figure 5.13. While the presence of more or less sample cells and the cavity being covered or not is evident in the detected vapor concentration per sample concentration examined, as given in Table 5.1, the overall detected Hg vapor for samples ranging from 1 ppb to 100 ppm were not appreciably different. Scans obtained with 500 ppb Hg are shown in Figure 5.14. In order to eliminate the potential that contamination was generating these values, background spectra were obtained prior to and following each series and new sample cells were constructed for each concentration.

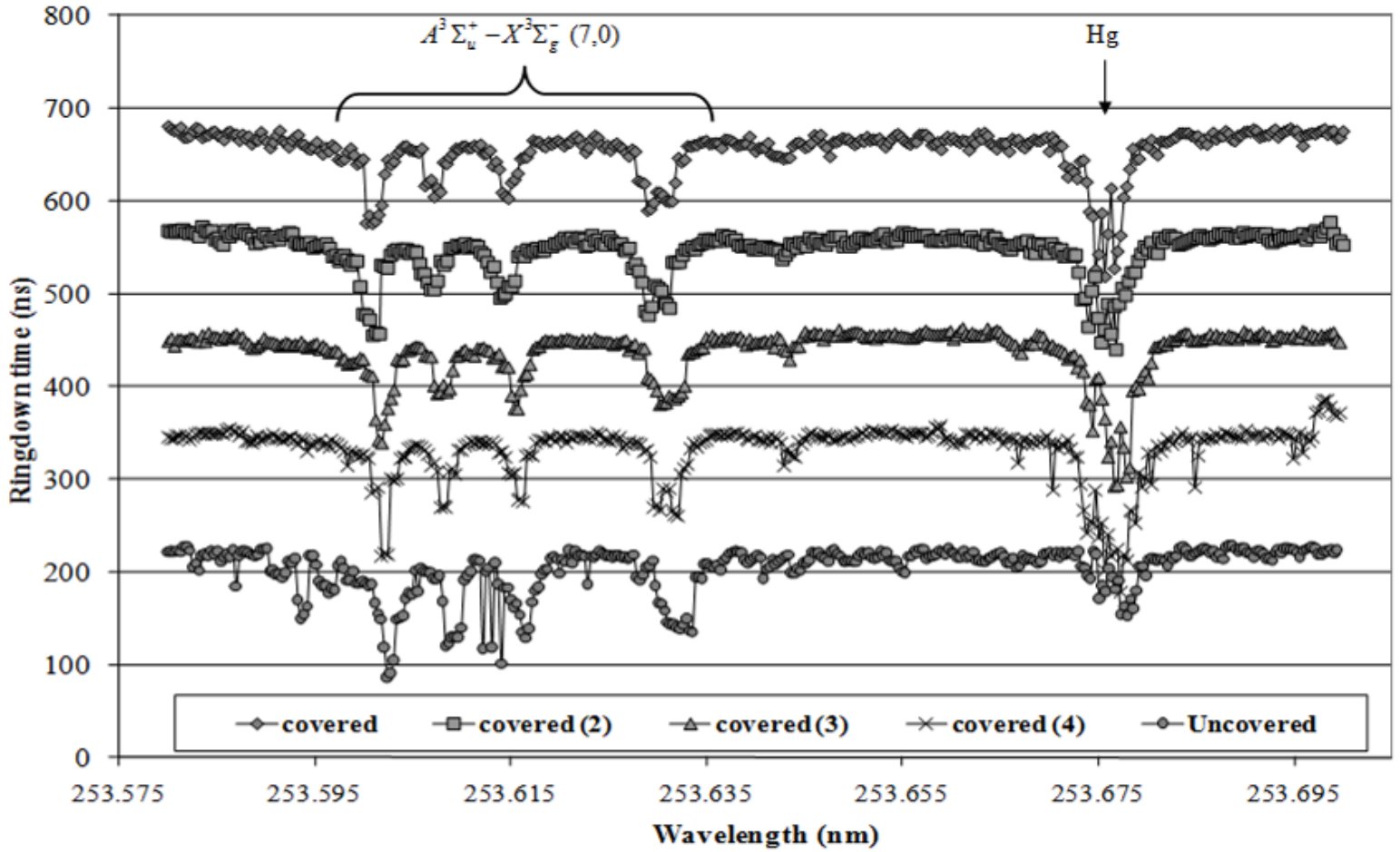

Figure 5.11 Reproducibility of Hg peak with CRDS utilizing the MOPO laser system using 100 ppm solutions.

The 100 ppm solution samples were placed directly under the ringdown cavity. Each data point is the average of 100 individual waveforms.

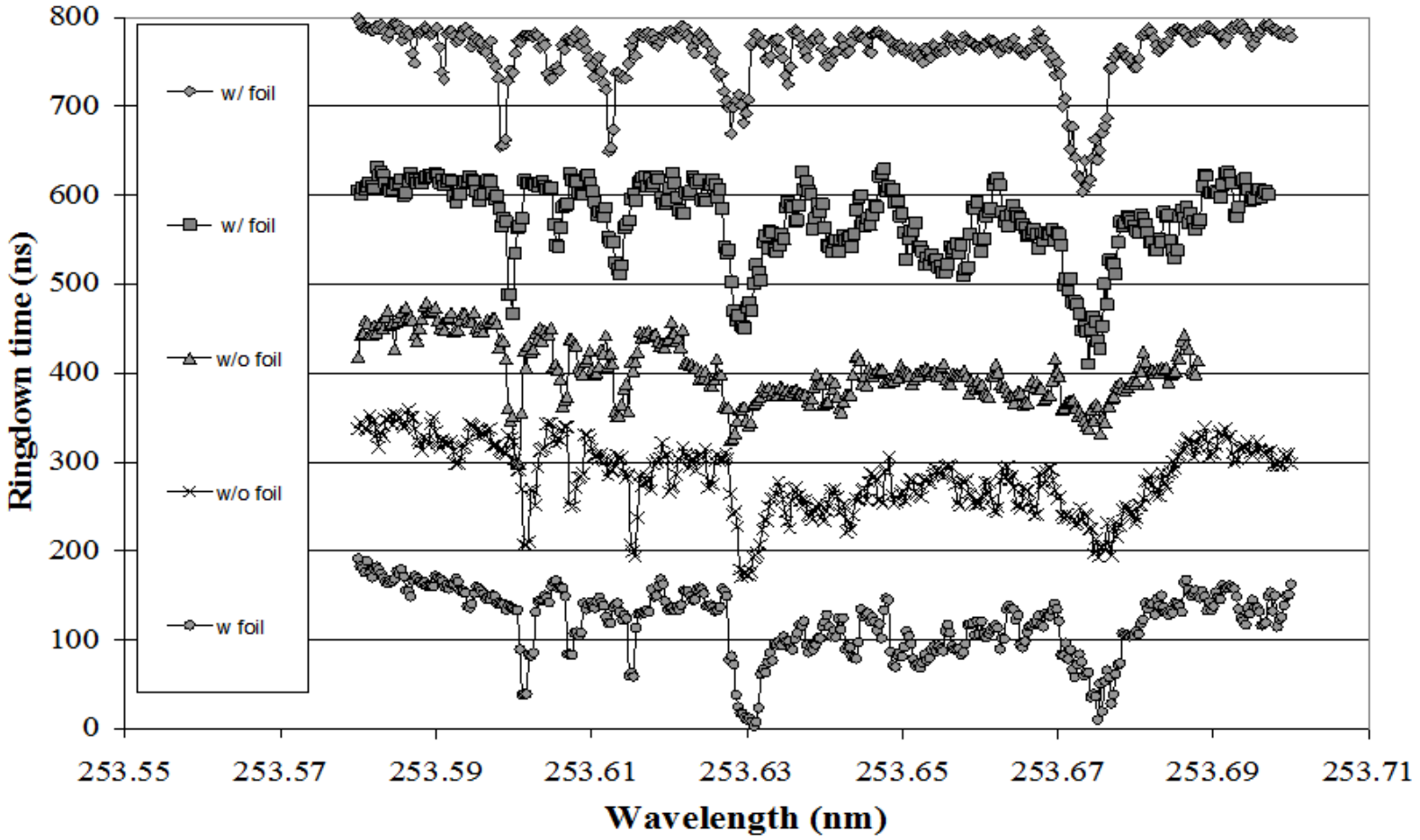

Figure 5.12 Reproducibility of Hg peak with CRDS utilizing the MOPO laser system using 5 ppm solutions.

The 5 ppm solution samples were placed directly under the ringdown cavity. As indicated, the ringdown cavity in some of the scans was open to the atmosphere, and the cavity was covered in others. Each data point is the average of 100 individual waveforms.

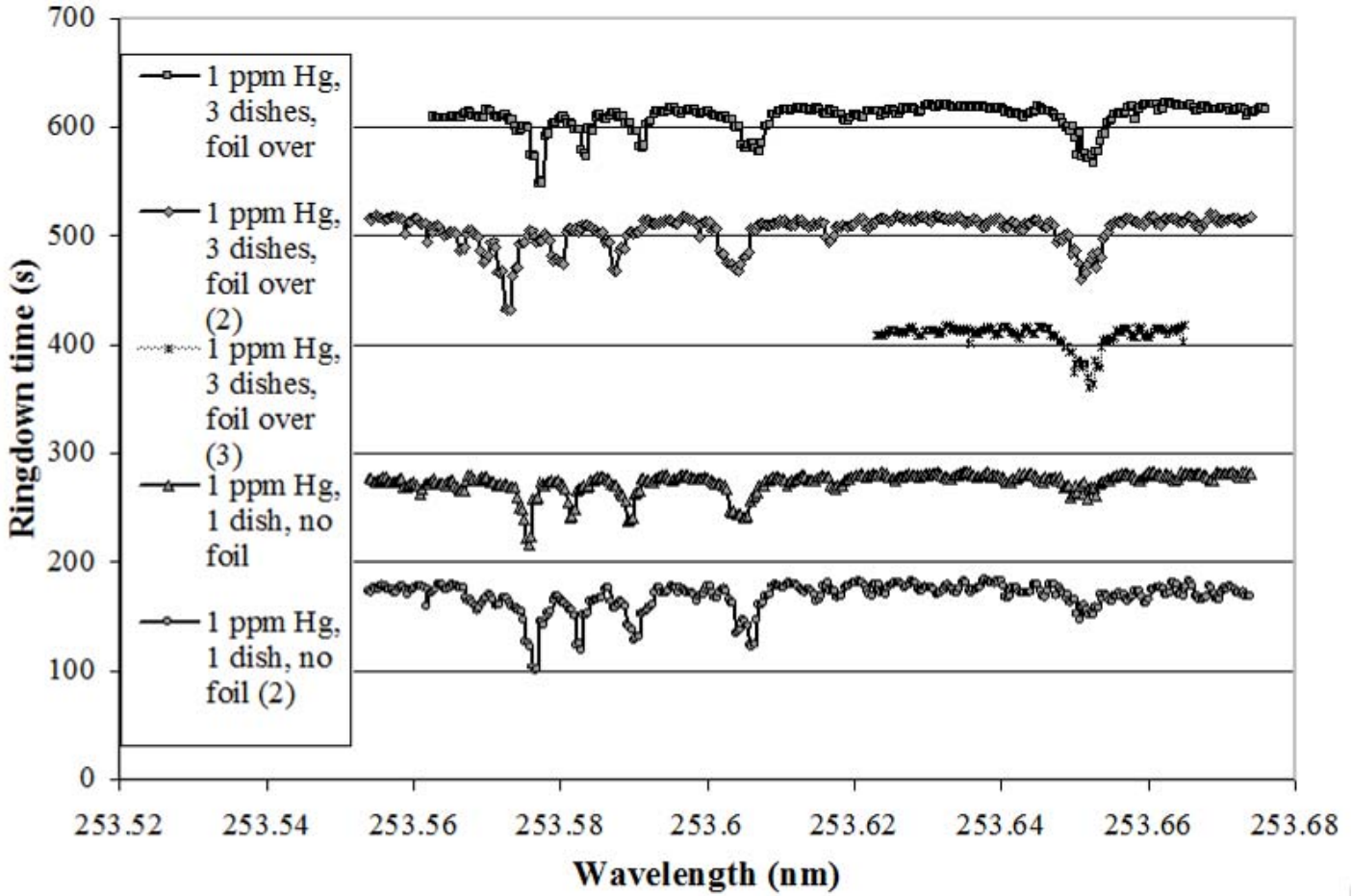

Figure 5.13 Reproducibility of Hg peak with CRDS utilizing the MOPO laser system using 1 ppm solutions.

The 1 ppm solution samples were placed directly under the ringdown cavity. Each data point is the average of 100 individual waveforms. Intensity changes are proportional to number of dishes under the cavity per concentration and very reproducible.

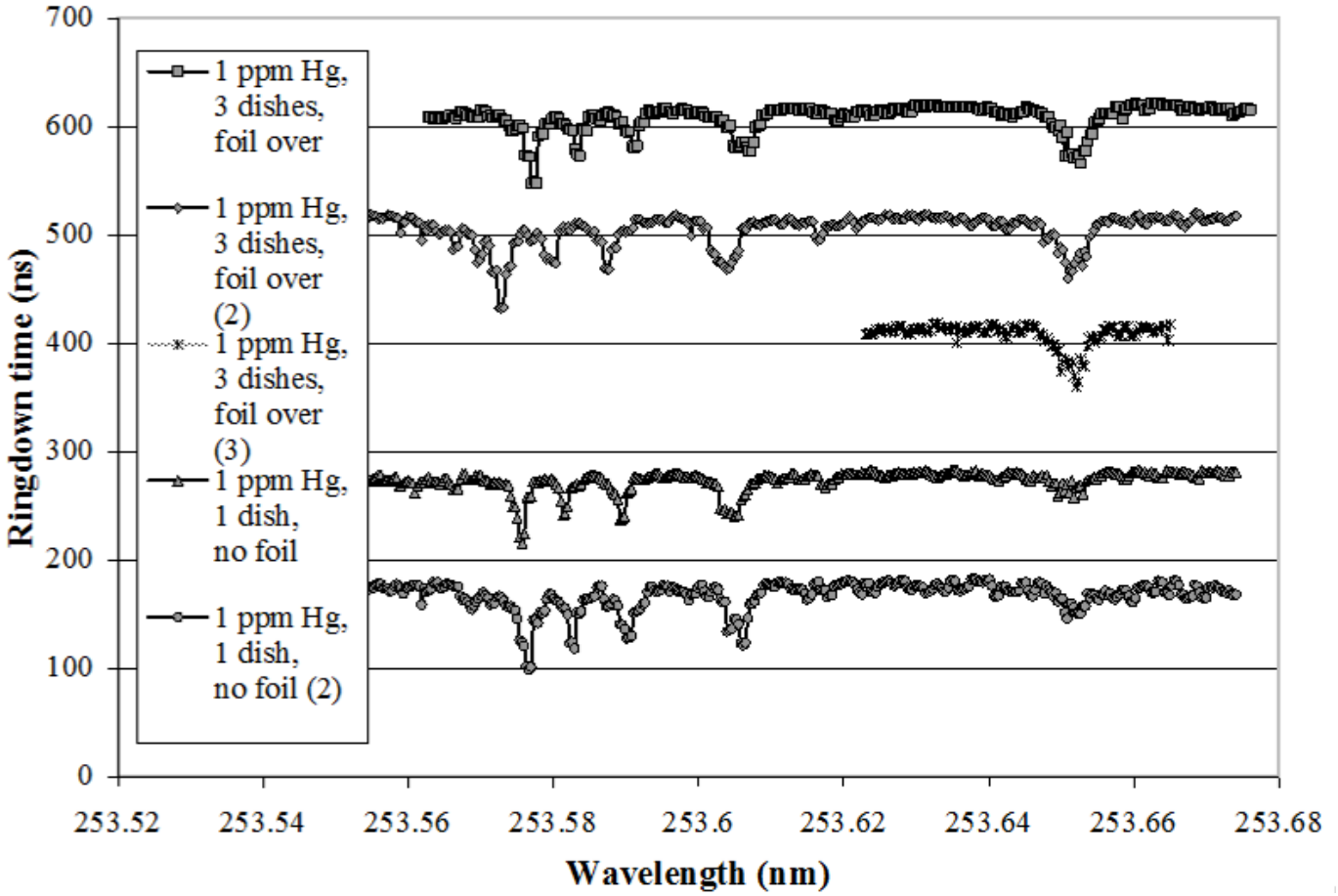

Figure 5.14 Reproducibility of Hg peak with CRDS utilizing the MOPO laser system using 500 ppb solutions.

The 500 ppb solution samples were placed directly under the ringdown cavity. Each data point is the average of 100 individual waveforms. Intensity changes are proportional to number of dishes under the cavity per concentration and very reproducible.

Table 5.1 Detection limits of Hg obtained with CRDS utilizing the MOPO laser system

Sample Conc (ppm)	1 Dish	3 Dishes	Foil	No Foil	Conc (pptv)	Peak
0.001		X	X		29	
0.01		X	X		10	21
		X	X		25	36
0.025	X			X	16	
0.05	X			X	33	*Noisy*
0.1		X	X		13	
		X	X		11	
		X		X	4	
0.5		X	X		11	
		X	X		11	
		X		X	6	
		X		X	3	
1	X			X	9	
	X		X		13	
		X	X		30	
		X	X		33	
		X	X		33	
		X		X	26	
	X			X	12	16
	X			X	9	
	X			X	13	
5		X	X		56	
		X	X		70	
		X		X	31	
		X		X	34	
		X	X		45	
100		X	X		38	
		X	X		30	
		X	X		45	
		X	X		40	
		X		X	14	

Mercury is extremely volatile for a main group element, giving a monatomic vapor with an appreciable vapor pressure of 1.3 x 10^{-3} mm at 293.15 K[128] and also

reported as 0.002 mm Hg at room temperature.[129] The National Institute of Standards and Technology states that the ideal gas density of mercury vapor in a sealed chamber at 298.15 K is 21.14581 ng/mL and 14.09436 ng/mL at 293.15 K. Evasion of elemental mercury from soils, vegetation, and surface waters is a highly temperature-driven reaction.[130] When solving for the Dumarey equation,[131, 132] $\gamma_{Hg} = \delta \frac{D}{T} 10^{-\left(A+\left[\frac{B}{T}\right]\right)}$, which calculates the mass concentration of saturated elemental mercury vapor in air for the calibration of mercury vapor measurement equipment, the calculated mass concentration of saturated mercury in a sealed container under ideal conditions, with no deviations of the theoretical saturated vapor mass concentration of mercury in the container (δ = 1), is equivalent to 19.84 ng/mL. In this equation, γ_{Hg} = the mass concentration of saturated mercury in the calibration vessel, T is the temperature inside the calibration vessel (298.15 K in the previous calculation), and A, B, and D are constants equal to -8.134459741, 3240.871534 K, and 3217522.61 K ng/mL, respectively. The Dumarey equation is valid for temperatures ranging between 288 to 298 K. For comparison to the aforementioned NIST values, this equation predicts that mass concentration of mercury at 293.15 K to be 13.17 ng/mL. The accuracy of the Dumary equation has been validated by analyzing various certified reference materials in different matrices and comparing the results via a thermal desorption and CVAAS techniques.[133, 134, 135] Clearly, the saturated mercury vapor pressure in a closed container under ideal conditions is several orders of magnitude higher than was observed in the open sample cells in these experiments.

Interestingly, the Dumary equation and the corresponding plot of mass concentration of saturated mercury in the sealed sample cell as a function of temperature between 288 and 298 K, Figure 2 in Ref. 11, imply that the equation is independent of the

total mass being measured, i.e., the same mass concentrations of saturated mercury in the sample cell were obtained, regardless of the input concentration. Therefore, using this argument in conjunction with the fact that open and quasi-open sample cells were utilized in this research, one could readily begin to understand the experimental results given in Table 5.1. According to this data, the amount of mercury released from the initial samples was approximately the same, regardless of the introduction of 100 ppm or 1 ppb mercury solutions into the sample dishes, in accordance to the behavior anticipated from the Dumary equation.

Due to time constraints on usage of the laser system, the effect of closed cell measurements, temperature, and air flow were not investigated. Due to the configuration of the laboratory in which the OPO laser system was located, there were to separate ventilation systems in addition to the intake/output of the building's air conditioning system in the room which might have drastically reduced the concentration of mercury vapor in the headspace above the sample cells. The opening of a laboratory fume hood was located only 70 cm from the center of the ringdown cavity. The flow of the system was strong enough to create a 'wind tunnel' effect in the room between the hood and the main corridor's hallway. The second ventilation system consisted of four drop-down exhaust lines, one of which was centered over the ringdown cavity, two of which were ~ 6 ft away, and one of which was closed. The performance of these systems could easily alter the air flow directly above the ringdown path, thereby reducing the concentration of mercury in the ringdown path.

5.3.2 Elemental Mercury Vapor from Contaminated Soils

According to Cotton *et al.*,[128] "mercury is readily lost from dilute aqueous solutions and even from solutions of mercuric salts owing to reduction of these by traces of reducing materials and by disproportionation of Hg_2^{2+}." In agreement with this statement, Hg° was observed directly vaporized from solutions prepared with $HgCl_2$ solutions. Once the feasibility of directly detecting elemental mercury vapor from solutions had been established, the next step was to directly probe mercury vapor evaporating out of contaminated soil samples. Contaminated soil samples near the Oak Ridge National Laboratory site were explored initially.[136] These soil samples were spiked with various concentrations of Hg ~ 2 years before they were acquired for this research and then used in a heavy metal plant sequestration study prior to these ringdown measurements. The mercury compounds were introduced as a powder and mixed into the soils. Figure 5.15 indicates the feasibility of detecting Hg naturally evaporating from contaminated soil samples using the dye laser system. The soil sample was poured from a storage bottle into one of the halved PVC tubes and placed under the laser beam path in the ringdown cavity with no additional manipulation to the sample. This scan was taken at lower resolution in order to first discern the presence of the Hg peak and also the influence of distance from the ringdown path as well as the amount of sample present. As indicated in the figure, placing the sample closer to the ringdown path resulted in higher concentrations of Hg vapor being detected. Additionally, increasing the length of the sample holder to allow more overlap of the vapor escaping from the sample directly under the laser and the ringdown path resulted in higher concentrations being observed.

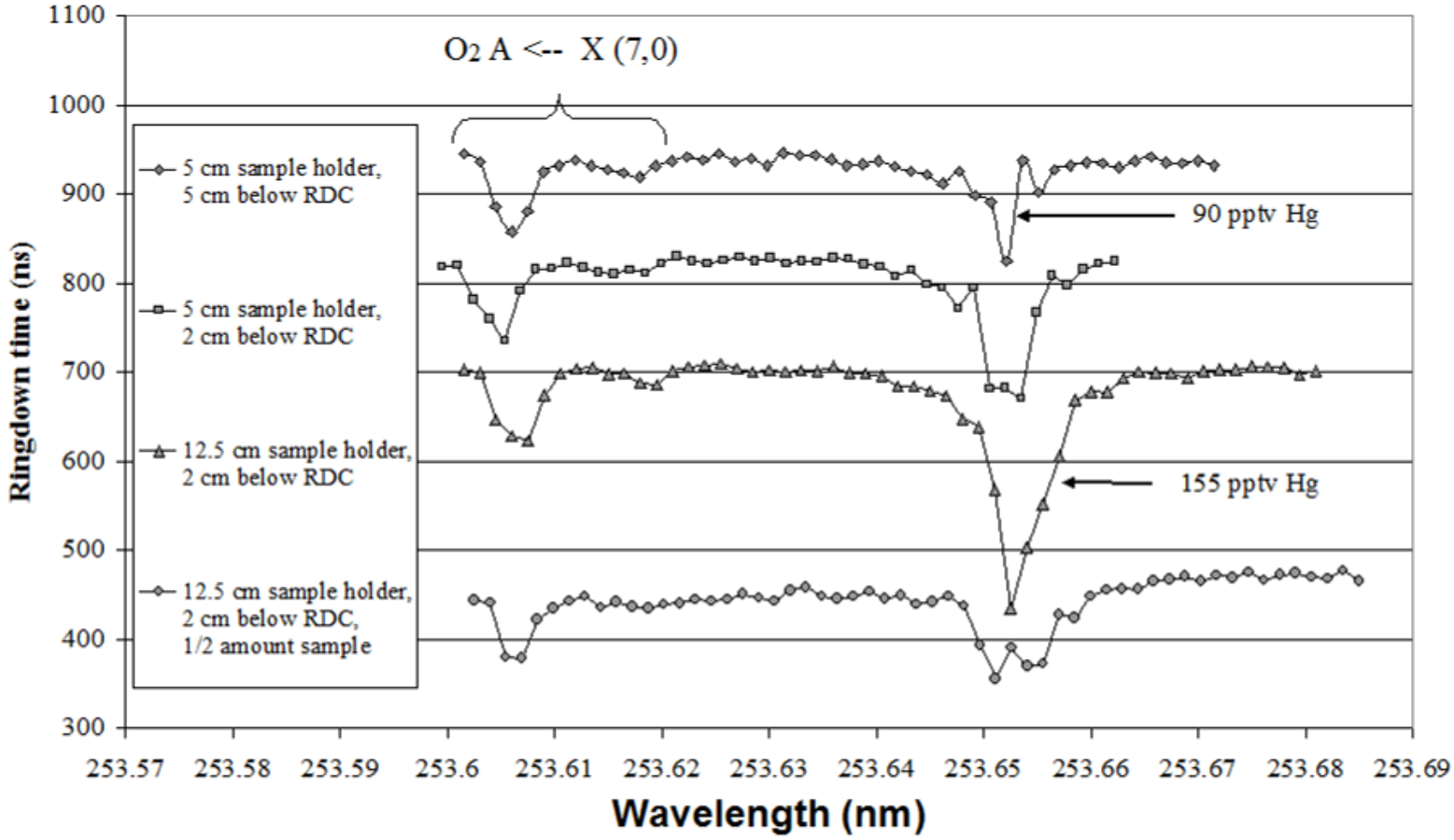

Figure 5.15 Soil samples from the vicinity of Oak Ridge, TN.

Position and quantity of the soil sample directly affected the detectable Hg from the contaminated samples. The same amount of sample placed closer to the ringdown path resulted in higher quantities detected. Less sample at the same position resulted in lower quantities detected. Baseline is manually offset for visual clarity.

Once the ability to detect Hg with this approach was confirmed, the effect of contamination by various types of mercury compounds was quickly examined. Research to examine the volatility of Hg in soils spiked with various crystalline Hg compounds is not a new idea;[137, 138] however, attempting this without heating or digesting the samples was a novel approach. In addition to $HgCl_2$, elemental mercury evaporating from soils collected near the Oak Ridge area, which were doped with HgS and $Hg(NO_3)_2$, was also investigated. According to the available literature, HgS is generally considered to be a stable Hg-compound in soils, clays, and sediments due to its limited solubility.[137] HgS is also the predominant mercury-containing form in the Oak Ridge area, and, therefore, information is needed to examine the ability to remediate the area. As seen in Figure 5.18 after introducing 5 mL of 10 ppm Hg solution to the HgS soil samples, HgS # 1, which was doped with 1000 mg/kg HgS powder, had a lower detectable level than HgS # 2, which was spiked with 2000 mg/kg HgS powder. According to the data presented by Obrist *et al.*,[139] terrestrial carbon and nitrogen play a large role in the uptake, deposition, sequestration, and emission of atmospheric mercury and the accumulation of organics in soils affects the resilience of Hg in the ecosystem. Additionally, it has been reported that increased Cl^- concentration leads to an increase in the chemical availability of Hg in HgS-contaminated soils. While this artifact may contribute to the data obtained, a larger analysis is necessary to better understand the phenomenon observed and draw more meaningful conclusions.

Experimental results did not reveal elemental mercury directly evaporating from the HgS or $Hg(NO_3)_2$ soil samples, indicating that the mercury was more tightly bound to the sulphur and nitrate groups than mercury bound to chloride, in agreement with the literature. In order to compare the results of the Oak Ridge samples to soils not from that

region, soil samples within proximity to ICET were also obtained and subsequently spiked with various, but lower, concentrations of mercury. While initial background readings recorded 0 ppm Hg evaporating from the samples, Hg was readily detected upon spiking the soils, as seen in Figure 5.16, where 10 mL of 100 ppm Hg solution were applied to the surface layer of the soil. A representative spectrum is shown in the figure.

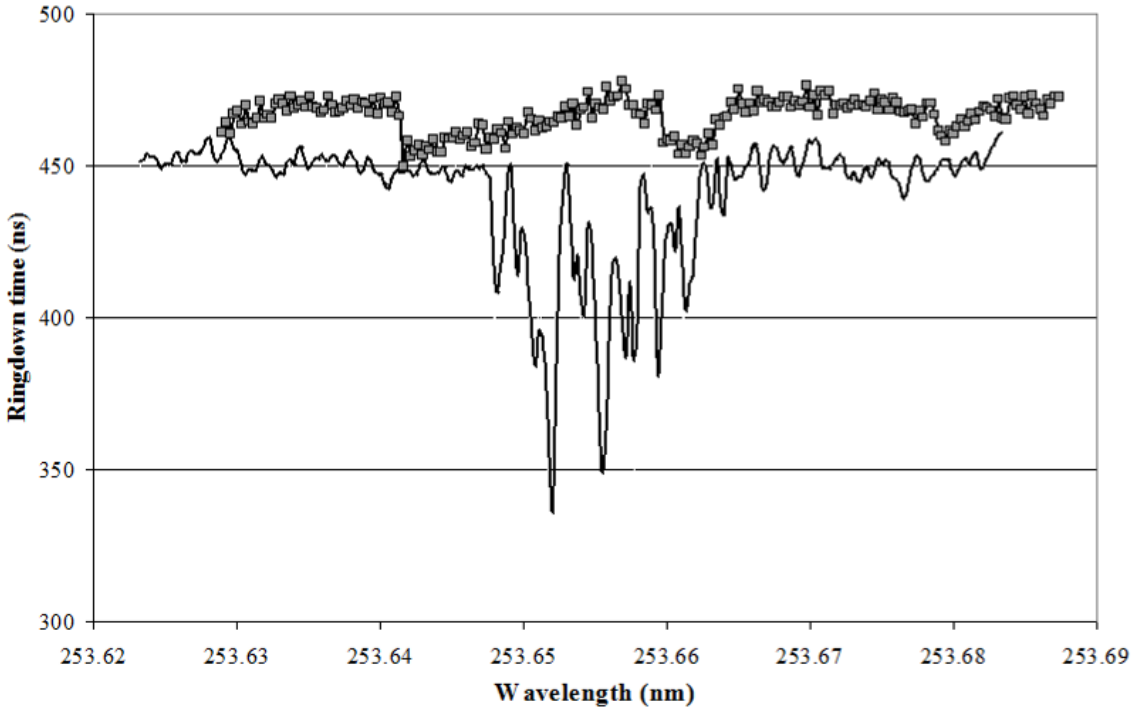

Figure 5.16 Preliminary CRDS spectra of Hg-spiked soil from Starkville, MS.

10 mL of 100 ppm Hg were added to a soil sample which was placed in a PVC channel, directly under the ringdown path. "Fresh spiking" generates noisier signals.

5.3.3 CRDS Monitoring Mercury Vapor Temporal Behavior

Elemental mercury emissions are known to be dependent on temperature,[140, 141, 142] sunlight,[143, 144] air Hg concentrations,[145] air chemistry,[146] and soil Hg concentration.[147] Additionally, Hg is readily released from dry soils upon the addition of water, especially when the quantity of water added is well below saturating the soil.[148, 149, 150] Three

mechanisms have been attributed to Hg release from dry soil following a precipitation event: "1) physical displacement of elemental Hg (Hg^0) enriched soil as by water filling the soil pores, 2) replacement of Hg^0 adsorbed to the soil by H_2O molecules, and 3) desorption of Hg(II) bound to the soil and subsequent reduction to Hg^0."[140] In order to examine the temporal behavior of mercury in the soil samples, sequential measurements were conducted on the $HgCl_2$-spiked soils from the Oak Ridge area as well as soil from near the lab: 1) upon spiking the soils samples, 2) thirty minutes after spiking the sample, 3) the next day after minor agitation, and 4) adding water to the soil, thereby simulating the effects of rain on mercury-contaminated soils. The results of this study are presented in Figure 5.17. Regardless of the type of soil examined, the addition of measured aliquots of standard mercury solutions to the various soils which had previously been spiked with different types of mercury contamination yielded observable mercury vapor. 10 mL of 10 ppm Hg were added to samples # 1, # 3, and the local soil sample. 4 mL of 20 ppm were added to sample # 2. The samples were placed in a laboratory fume hood after the measurement and not disturbed prior to the next measurement. After approximately thirty minutes, the samples were recorded again, and although less significant, an appreciable amount of mercury was still easily detected for each sample species, as indicated in the figure. The samples were then placed in a hood overnight. They underwent two measurements the following day; the first measurement was taken after being shaken slightly, and the second measurement was after the addition of deionized (DI) water, 5 mL of DI water to approximately 25 g of soil. Upon the addition of water, mercury vapor was readily detected from the soil samples. Detection limits obtained after the addition of water varied from 30 to 65% of the initial amount of mercury measured. The observed detection limits are listed in Table 5.2.

Table 5.2 Soil Samples

	Oak Ridge, TN		
		$HgCl_2$	
	# 1 (pptv)	# 2 (pptv)	# 3 (pptv)
Original spiking	100 mg/kg	250 mg/kg	1000 mg/kg
Initial	2	1	3
Hg-spiked	84	70	106
	(10 mL 10 ppm)	(4 mL 20 ppm)	(10 mL 10 ppm)
30 min	61	33	38
next day - agitate	17	8.3	6.1
next day - water	55	25	31

	HgS		Hg(NO3)2
	# 1 (pptv)	# 2 (pptv)	(pptv)
Original spiking	1000 mg/kg	2000 mg/kg	100 mg/kg
Initial	0	0	0
Hg-spiked	90	99	102
	(5 mL 10 ppm)	(5 mL 10 ppm)	(7.5 mL 10 ppm)
30 min	48	28	30

	Starkville, MS
Initial	0 (pptv)
Hg-spiked	61
	(10 mL 10 ppm)
30 min	29
next day - agitate	4.3
next day - water	27

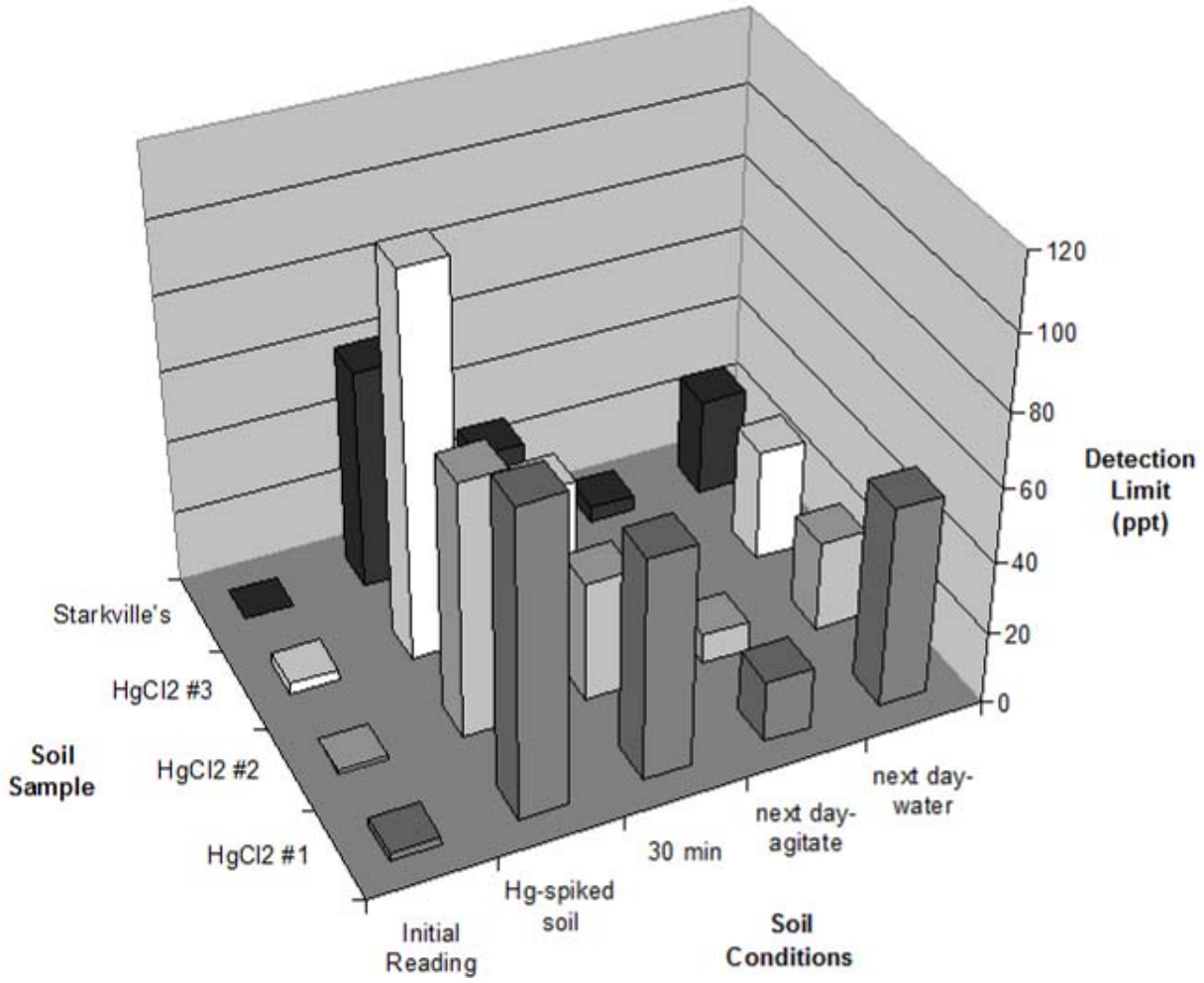

Figure 5.17 Temporal behavior of $HgCl_2$'s and local soil in the presence of $HgCl_2$.

10 mL of 10 ppm Hg solution were added to #1, #3, and Starkville's, and 4 mL of 20 ppm were added to #2.

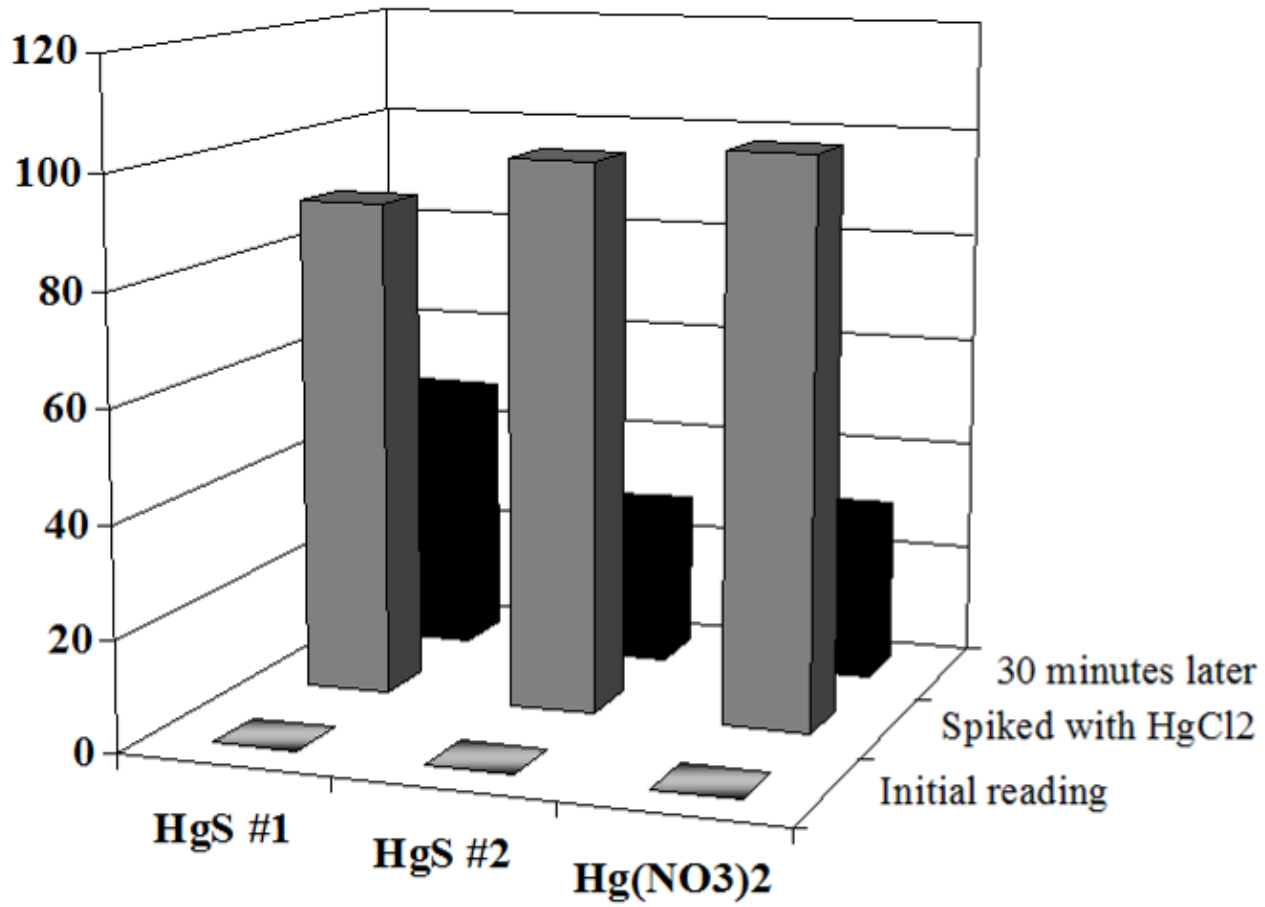

Figure 5.18 Temporal behavior of HgS and $Hg(NO_3)_2$ in the presence of $HgCl_2$.

The initial reading was taken after pouring the sample into individual PVC channels. To sample #1, 5 mL of 10 ppm Hg solution were added; to sample #2, 5 mL of 10 ppm; and 7.5 mL of 10 ppm were added to the mercury nitrate soil. A subsequent reading was taken 30 minutes after the initial spiking.

This analysis was then extended to the HgS- and $Hg(NO_3)_2$-spiked soils to see if the same behavior was observed. 5 mL of 10 ppm Hg solution were added to samples # 1 and # 2, and 7.5 mL of 10 ppm were added to the $Hg(NO_3)_2$ soil sample. Figure 5.18 depicts the initial, spiked, and 30 minute later readings. The preliminary results were encouraging, but an obstacle was encountered that prevented the completion of the overnight portion of the figure (leak was detected in Nd:YAG, which was due to degradation of O-rings holding flashlamps in place. This allowed water to pool in the laser head, and the rod was sent back for polishing). Nevertheless, the general trend between the initial addition of mercury solution and the measurement thirty minutes later is clearly evident. One important facet of this study is the ability to detect elemental Hg naturally-evaporating from contaminated soils and solutions. While this approach is not applicable for determination of total Hg or Hg-speciation, it is a valid approach for the determination of the presence of Hg0. Based on this analysis, the residual effects of mercury contamination in soils and the resulting interaction with aqueous media warrant further exploration.

CHAPTER VI

URANIUM EMISSION SPECTRA WITH A LOW-POWER MICROWAVE PLASMA SOURCE

6.1 Introduction

The research presented herein explored the potential of effectively generating uranium atoms and ions with a low power MIP. At the time of this research, the available literature was limited to analyses using high-power plasma sources. Uranium emission spectra generated with a low-power, low-temperature microwave plasma source, utilizing low gas flow rates, are obtained and analyzed. Experimental parameters, such as the effect of plasma power, gas flow rates, and temperature, were explored. The uranium peaks, obtained with a 200 W candle-shaped MIP around 285 nm as well as in the 320 to 430 nm wavelength range, are examined, labeled, and compared with results for high-power plasma sources. The effect of concentration was also studied. Using select U lines, calibration curves were generated and detection limits of uranium are estimated to be ~ 0.4 ppm, with the linear dynamic range spanning 2.5 orders of magnitude. In addition to uranium, the feasibility of atomizing multiple species with this compact, low-power plasma source was also examined, and the emission spectra collected for some of the elements tested will be included.

6.2 Experimental Setup

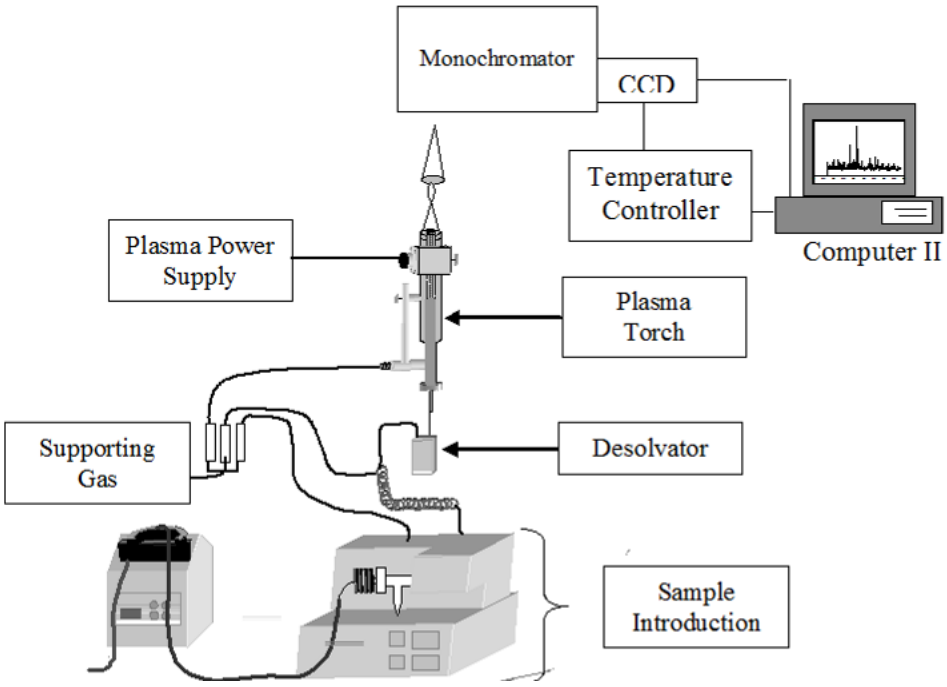

Figure 6.1 Experimental Configuration utilized with candle-shaped U-MIP studies.

The liquid samples were pumped via a persistaltic pump to an ultrasonic nebulizer. The vapor sample was then carried to the plasma torch through a series of molecular sieves. The emission spectra were recorded on the monochromator and displayed on a PC.

The experimental configuration, shown in Figure 6.1, consists of the atomization source, the sampling system, a triple grating monochromator with a CCD detector, and the corresponding electronic controls. The microwave plasma employed in this research is referred to as a candle-shaped plasma because of the distinctive operational shape observed.[118] Whereas the ICP used in previous work in this laboratory assumed a 'domed' shape,[63] this MIP clearly resembles a burning candle with a triangular portion stemming from the top of the plasma torch into a thin cross-section which opened up into a flame-like shape, as shown in the figure. This plasma was also used in the research presented in Chapter III and is described in more detail there. In this work, typical

operational plasma powers were 200 W in the forward direction and negligibly small in the reverse direction. As shown in Table 6.1, the plasma gas flow rates and the sample up-take rate were generally around 0.5 L/min. The operational parameters were optimized for uranium detection by systematically adjusting the various flow rates and the plasma power as well as the position of the plasma torch, relative to the monochromator, by implementing an X-Y home-made adjustable base.[151] One important experimental feature which was crucial to obtaining a stable plasma was the position and orientation of the 1 m coaxial cable; if this cable was not taunt and stationary, the reflected power increased dramatically and less stable plasmas were observed. One possible explanation for this behavior is that because the coaxial cable used was semi-rigid, any angle experienced by the cable could place strain on the coupling antennae, which could lead to inefficient coupling of the energy to the plasma cavity and could generate a standing wave along the coaxial cable.

A commercially available peristaltic pump (Gilson, Inc., MINIPULS 3) pumped the sample solutions into a U-5000 AT^{+} ultrasonic nebulizer (CETAC Technologies, Inc.). When the solution contacted the ultrasonic transducer, a fine aerosol was generated. The operational parameters of the nebulizer are also listed in Table 6.1. The uranium sample solutions were prepared by dilutions of the standard 1000 μg/mL uranium solution (Absolute Standards, Inc.) with a 2 % v/v nitric acid solution. The sample up-take rate was 0.75 mL/min and a molecular sieve was inserted in the delivery line in order to minimize the solvent loading and thereby improve the system performance. This particular MIP[36] was susceptible to extreme fluctuations when the input sample was too 'wet', so an additional line was plumbed to incorporate a PermaPure desolvator membranous tubing to extract additional water vapor which was

carried away from the plasma by argon at 0.5 L/min. All argon used in this work was 99.999 % pure.

Table 6.1 Operational parameters of MIP for U studies

Plasma		
Forward power	200	W
Reflected power	0 - 6	W
Supporting gas flow rate	0.35 - 0.5	L/min
Central gas flow rate	0.5 - 1.0	L/min

Sampling system		
Sample up-take rate	0.75	mL/min
Nebulizer heating temp	140	°C
Nebulizer cooling temp	-5	°C
Heat wrap on desolvator	80	°C
Ar flow rate in desolvator	0.5	L/min

Spectrometer		
Grating	2400	Grooves/nm
Slit width at entrance	10	µm
Resolution	0.1	nm
Accumulations	0.01 - 0.1	s
	1 - 20	spectra

The uranium spectra were obtained on an ARC SpectraPro500 triple grating monochromator (Acton Research Corporation/ Princeton Instruments, Inc). A Spectrum One CCD-200 detector (Princeton Instruments, Inc.) was mounted on the 0.5 m monochromator and was used to record the emission spectra. In this research, the 2400 grooves/mm grating was selected to yield the highest resolution in the UV for this instrument, ~ 0.1 nm. Most of the spectra obtained consisted of 10 – 20 accumulations and the CCD was set for 0.01 – 0.1 s/scan. The entrance slit of the monochromator was adjustable from 10 – 120 µm, and the narrowest setting was employed for this research to

reduce spurious light. Because some of the wavelength regions were subject to strong background emissions, for example, the OH emission spectra at 308 and 315 nm and mercury at 254 nm, a background measurement was taken in each wavelength range prior to each uranium measurement. The background spectra were generated by recording the spectra obtained with the same plasma operational conditions with a 2 % HNO_3 solution used in lieu of the U solution. As previously mentioned, the U samples were made by diluting the standard 1000 ppm solution with the 2 % nitric acid solution; therefore, the background spectra were more accurate when they incorporated the acid solution as the blank, as opposed to just the plasma operating at the same conditions or the plasma with just water as the blank. Once the background was obtained, the sample spectra, sometimes at various uranium concentrations, were then recorded. The background was subtracted from the corresponding sample spectra to yield the final emission spectra. A 1 m focusing lens was inserted between the plasma flume and the monochromator. The monochromator and CCD were connected to a PC which contained the Princeton Instruments/Acton software that was used to control the scan parameters and display as well as to record the results.

6.3 Results and Discussion

6.3.1 Determining Plasma Temperature

In order to efficiently generate uranium atoms, the temperature of the plasma is a crucial experimental element. Uranium has a low ionization potential (597.6 kJ/mol),[64] and, therefore, a low-power, low-temperature ionization source is necessary for the successful generation of U atoms. When high-power atomization sources are used, uranium ions are readily generated, thus, hampering atom formation. In this research, the

temperature of the plasma was estimated by examining OH emission spectra around 308 nm, the OH $A^2\Sigma^+ - X^2\Pi_{\frac{3}{2}}$ (0,0) band, generated by the plasma. In order to determine the presence of temperature gradients in the MIP, as experienced with the ICP,[63] the OH emission spectra were obtained at different locations along the vertical axis. An example of an OH emission spectrum obtained near the converging point with the MIP operating at 180 W is depicted in Figure 6.2a. The majority of the uranium emission spectra were obtained at the converging point, also referred to as the waist in the literature, where higher energies are concentrated. Using LIFBASE software,[152] the OH emission spectrum in Figure 6.2a was simulated by implementing a Voigt lineshape with a 50 % Lorentzian component and a 0.5 % noise allowance in addition to a 0.15 nm spectral resolution, and this simulated spectrum is shown in Figure 6.2b. While typical instrumental baseline stabilities were on the order of approximately 0.2 %, a conservative 0.5 % was used in the simulations. The simulated spectrum was calculated at thermal equilibrium, with the rotational and vibrational temperatures both equal to 2800 K. The experimental and the simulated spectra are in good agreement. The uncertainty in the estimated plasma temperature is less than ± 10 %, which is due to the deviation of the plasma uniformity from thermal dynamic equilibrium and the plasma background obtained in addition to the experimental OH spectra.

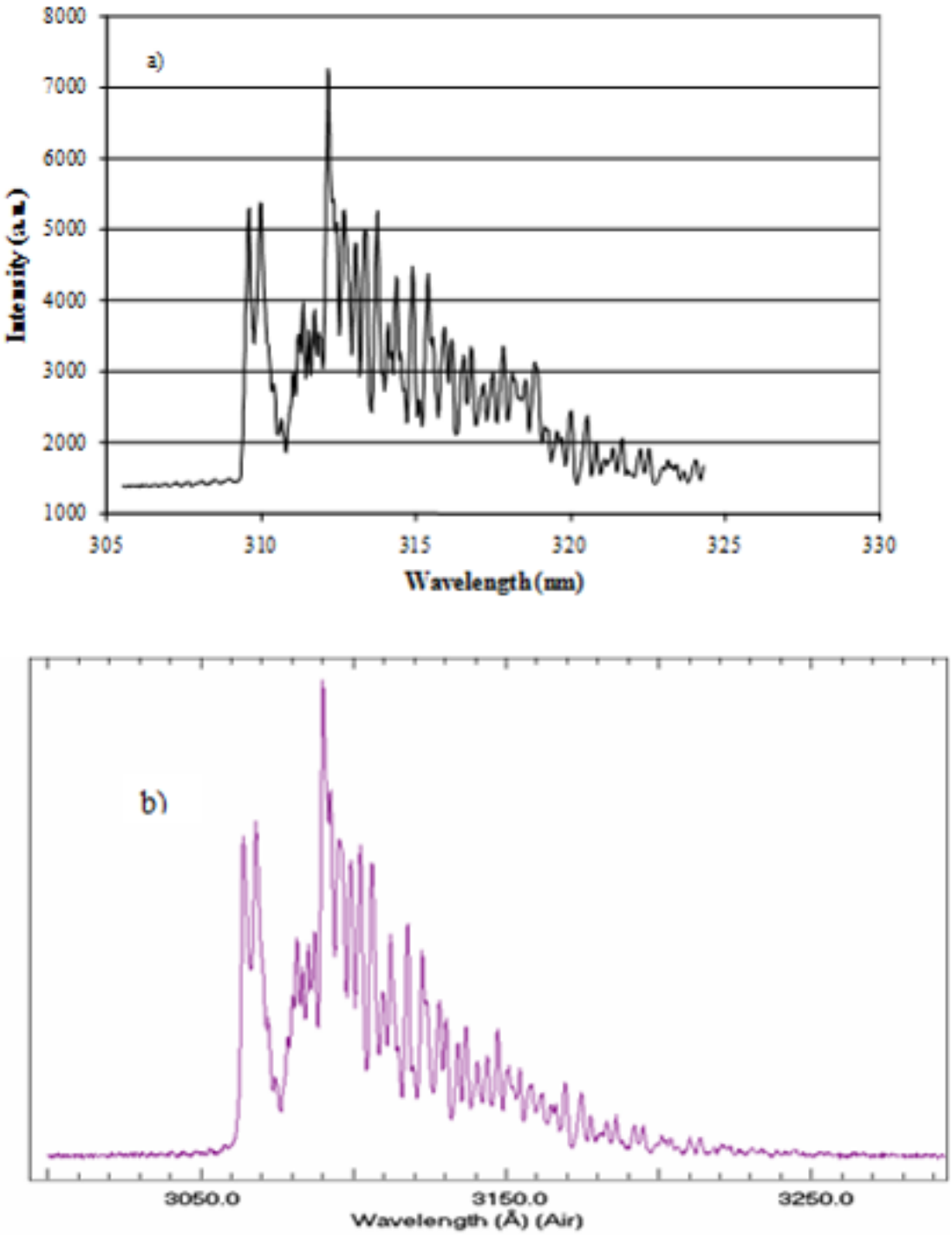

Figure 6.2 OH emission spectra obtained (a) experimentally and (b) simulated with LIFBASE 2.0 at the converging point of plasma.

Spectral parameters include 0.5% noise, 0.15 nm instrument resolution, Voigt lineshape with a 50 % Lorentzian component, and thermal equilibrium at 2800 K.

As previously mentioned, the temperature gradient along the vertical axis of the plasma was also examined. OH emission spectra were obtained from the top-most, flame region of the plasma down to the base of the triangular portion generated near the plasma torch orifice, shown in Figure 6.3. Simulated spectra were generated to match the OH spectra at these plasma positions, and the simulations indicate that there was less than a 25 % variation in temperature in the MIP from the top to the bottom, or approximately ± 700 K. Although ± 700 K might seem substantial, the available literature of atomic uranium lines were generated with an ICP with temperatures ranging from 5600 K to 6700 K for > 1000 W ICP and 5500 to 10,500 K for flow- and wall-stabilized arc sources, respectively; thus, 2800 ± 700 K is still well below the previously published values for uranium atom/ion generation to be considered a low-temperature atomization source. Experiments involving the 5500 K flow-stabilized arc allowed a few of the strongest atomic spectral lines to be observed, and all of the reported temperatures from the aforementioned sources readily produced numerous UII lines. Therefore, successful generation of uranium atoms with this low-power, low-temperature microwave power source seemed feasible.

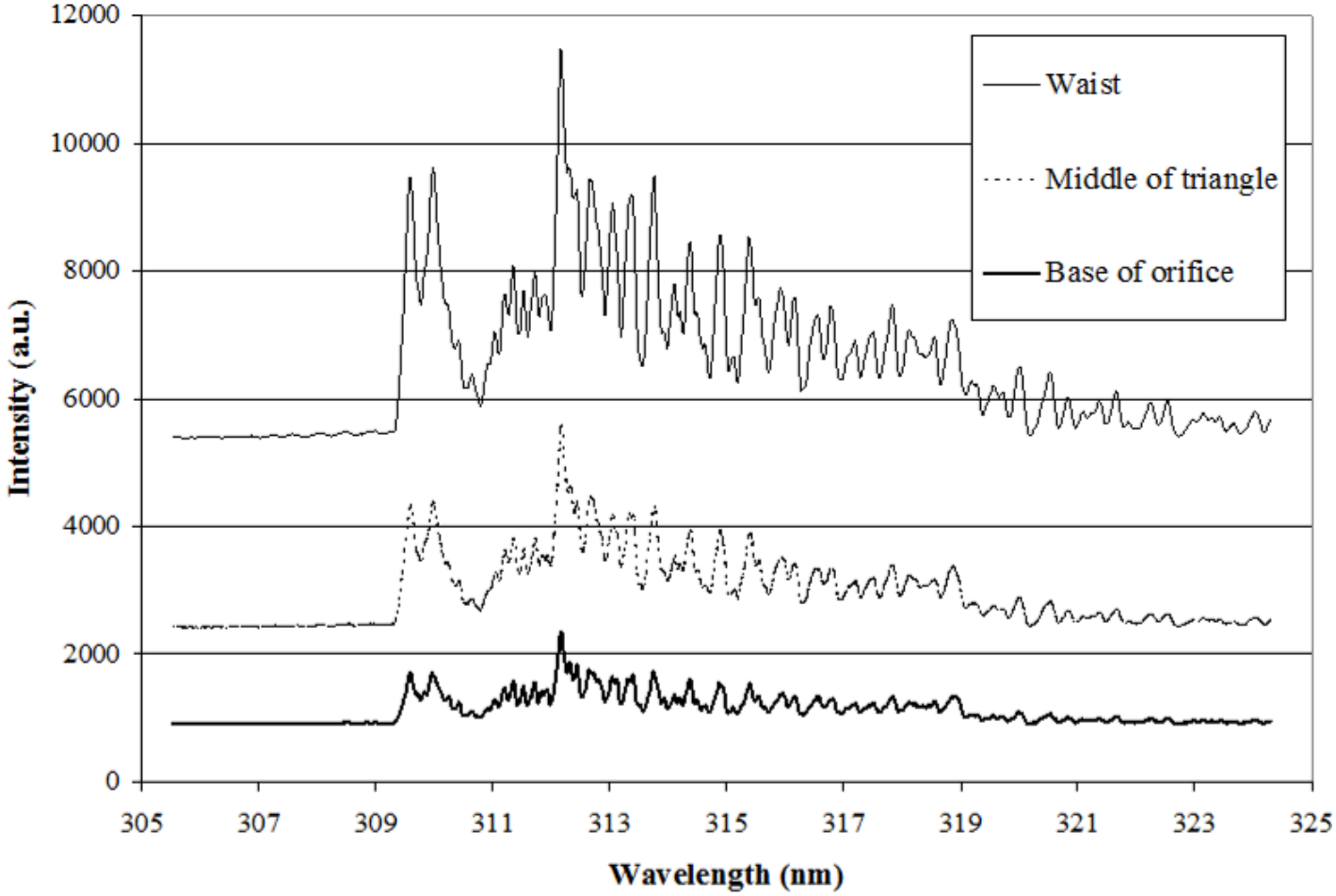

Figure 6.3 OH emission spectra three heights in the plasma.

The three heights include the base of the orifice, in the center of the triangular portion, and at the converging point.

6.3.2 Uranium Atomization/Ionization

The ultimate goal of this research is to determine the experimental conditions which readily, reproducibly, and efficiently allow the atomization of uranium so that this atomization source could be easily implemented as the atomization source for the highly selective and sensitive detection of uranium using plasma-CRDS. With this in mind, the wavelength regions examined were chosen to concurrently enhance the likelihood of success by a joint technique. For example, uranium is very rich in spectral lines in the UV region and high reflectivity mirrors for CRDS studies of U in this region were already acquired for previous research conducted in this lab; therefore, the uranium emission spectra were recorded around 286 nm and over the 325 - 440 nm wavelength range. Uranium also exhibits a clear peak around 680 nm, so this region was also briefly explored. As previously mentioned, a large background OH signal is generated by the plasma in the 300 – 325 nm region; therefore, this region was not included in the U detection spectra compilation.

In order to encompass the majority of this wavelength region with reasonable resolution, a series of spectra were obtained in ~ 20 nm increments. The spectra were partially overlapped to monitor the presence of baseline shifts due to background interference as well as to monitor the reproducibility of the uranium peaks and stability of the overall system. The background subtracted spectra are depicted in Figures 6.4 -6.8. The operational parameters of the plasma and the spectrometer for these figures are given in Table 6.1. The sample concentration for the majority of the scans in this series was 200 ppm. Almost the entire wavelength region is marked with uranium peaks. The peaks at 367.007, 385.464, 385.957, 393.098, 393.202, 409.013, and 424.167 nm are

noticeably distinctive; and the overall correlation between peak positions and intensity with the available literature is in good agreement. Initially, the peaks were evaluated by comparing the wavelengths and the intensities to those listed in the NIST website[120] as well as in *Inductively Coupled Plasma-Atomic Emission Spectroscopy: An Atlas of Spectral Information*.[153] While the peaks listed in those references were readily correlated to peaks observed in the MIP emission spectra obtained in this research, there were several uranium spectral peaks, particularly towards the higher wavelengths explored, that were extremely reproducible but not addressed in those references. Upon further examination of the U emission spectral peaks obtained in this research with the MIT wavelength tables,[119] excellent agreement was obtained for all of the peaks generated with the MIP.

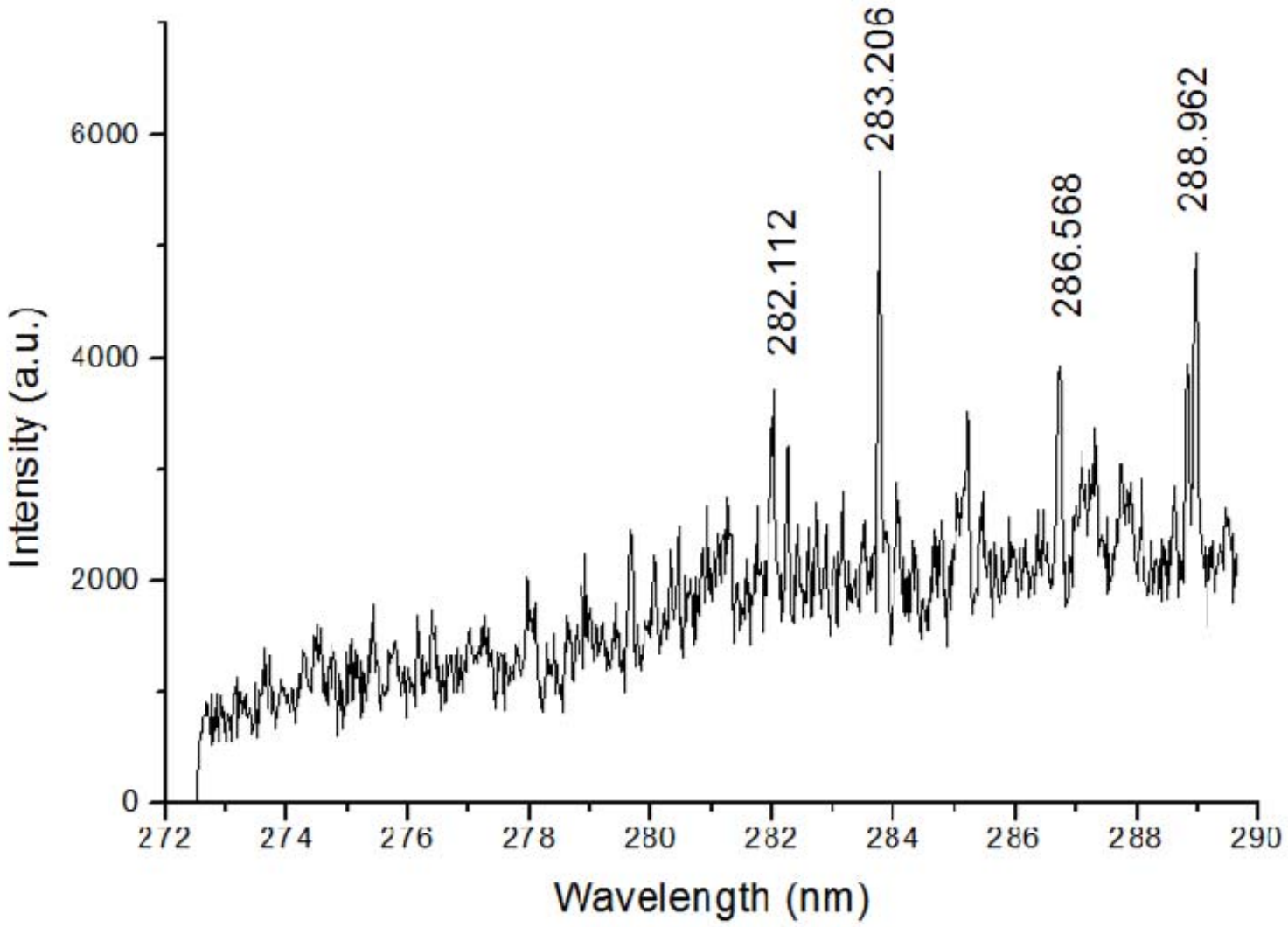

Figure 6.4 Uranium emission spectra around 280 nm.

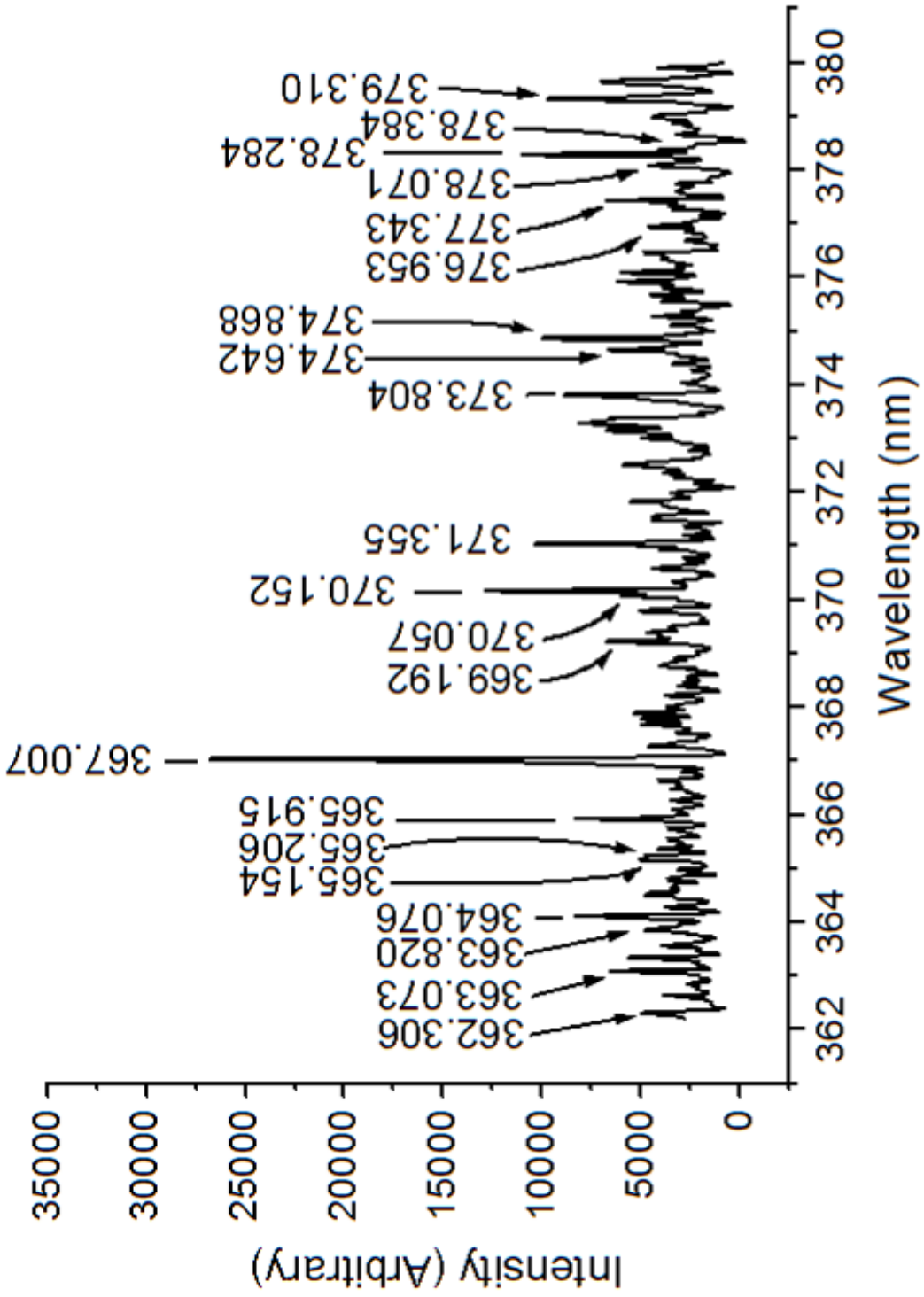

Figure 6.5 Uranium emission spectra around 370 nm.

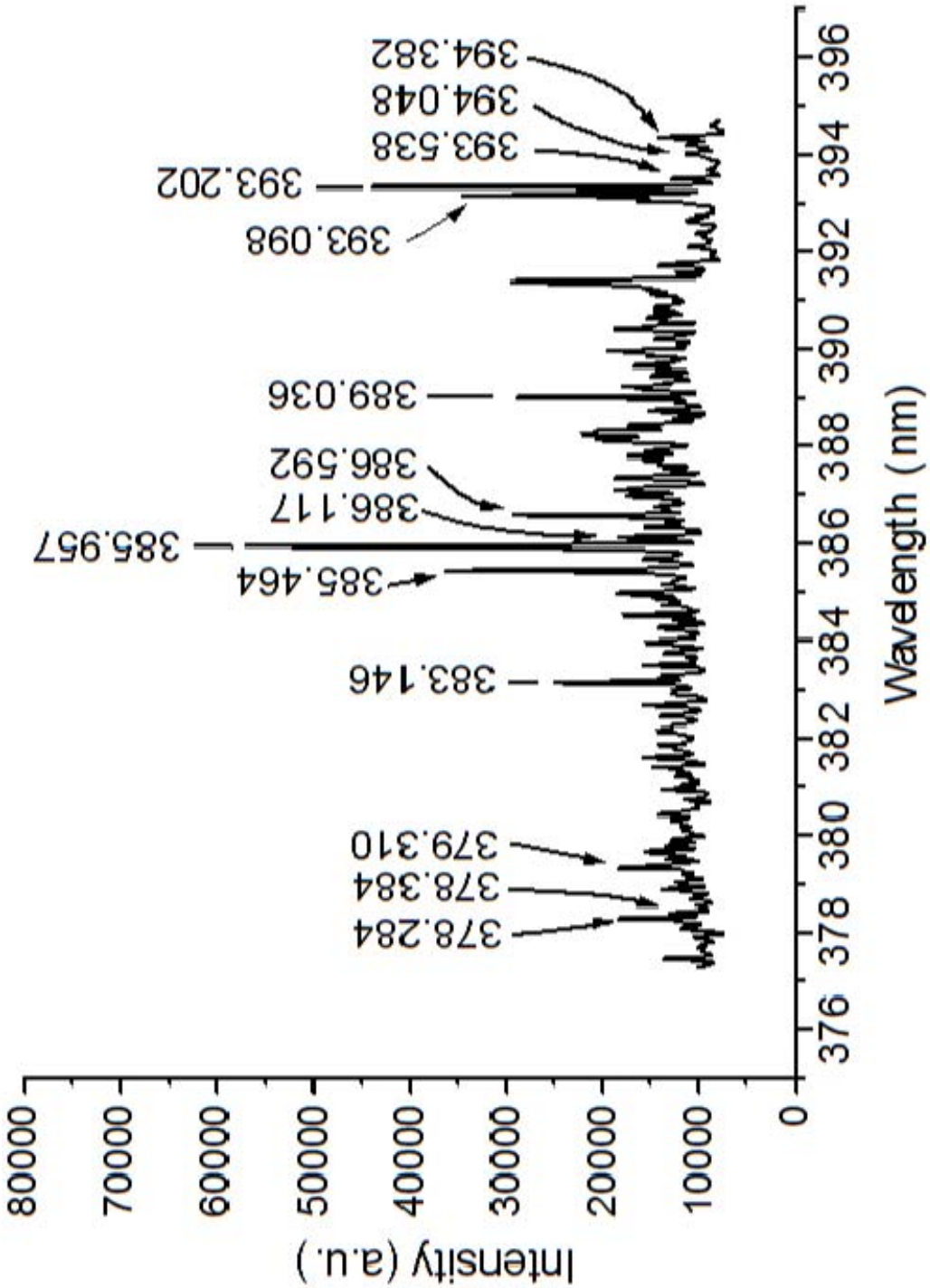

Figure 6.6 Uranium emission spectra around 385 nm.

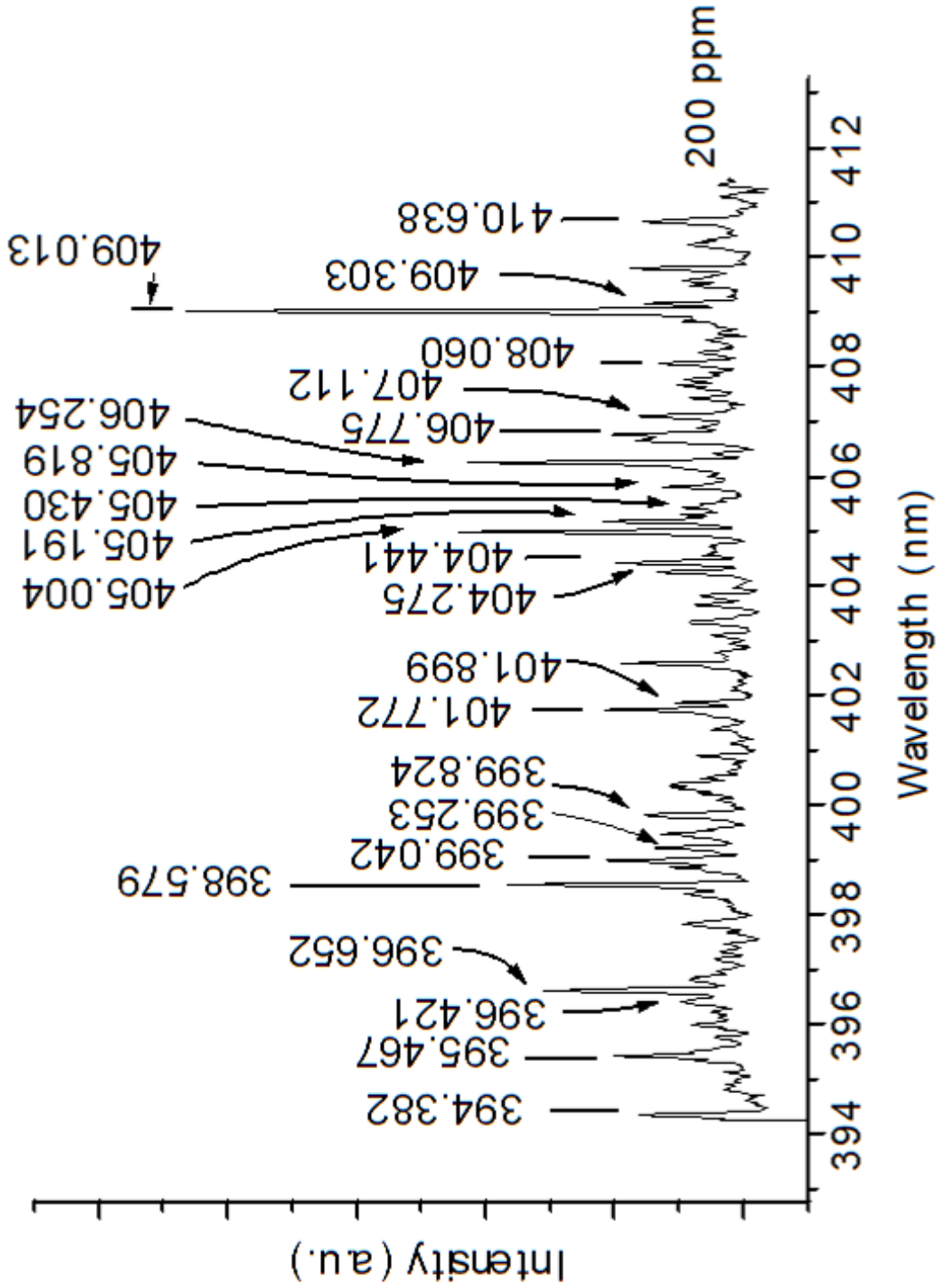

Figure 6.7 Uranium emission spectra around 400 nm.

Figure 6.8 Uranium emission spectra around 420 nm.

Over the wavelengths examined, approximately 80 uranium lines were observed. These lines, given in Table 6.2, include both U (I) and U (II). The relative intensities of these lines as well as their corresponding literature values are also included in the table. These values have been normalized to the intensity of the most intense peak, 385.957 nm. Due to limited literature discussing the relative intensities of the uranium lines generated with low-power sources, the potential for discrepancies between higher temperature atomization sources and this system does exist, which may account for some of the differences in relative intensities. One important point to note is that no additional noise correction or instrumental attributes were accounted for in these spectra, only a subtraction of the background spectra obtained with the 2 % nitric acid blank. While this artifact may be minor, any deviation in these parameters may give rise to deviations from the reported intensity values. This aspect was not fully explored as the intention of this research was to ascertain uranium atomization with this low-power, low-temperature plasma source.

Several spectra were taken on different days in order to ascertain the reproducibility and stability of the plasma system as well as uranium atomization. Figures 6.9 and 6.10 portray spectra taken on different days for two sets of wavelength regions. A) and b) of these figures clearly display the reproducibility of the uranium peaks and their intensities for spectra acquired on consecutive days. The first wavelength region covered ~ 399 to 415 nm, and the second covered 408 – 425 nm. The spectra also exhibit reproducibility between the portion of the scans in which the wavelengths overlap. The spectra illustrated in Figures 6.9 c and 6.10 c display the consistency observed for scans obtained weeks later for the same spectral regions.

Table 6.2 Uranium peaks observed in emission spectra

	Literature values corresponding to observed wavelengths		Relative intensities	
U	Wavelength (nm)	Wavenumber (cm^-1)	NIST (%)	Experimental (%)
II	322.950	30965	14.9	10.3
II	323.216	30939	13.9	6.7
II	324.422	30824	9.0	15.2
II	326.579	30620	6.9	5.5
II	327.012	30580	9.0	15.0
II	328.821	30412	9.0	7.8
II	329.133	30383	14.9	25.0
II	330.589	30249	22.4	26.5
II	333.779	29960	8.0	14.9
II	334.166	29925	9.0	12.7
I	335.784	29781	8.0	7.9
II	362.306	27601	8.0	8.8
II	363.073	27543	9.4	11.0
I	363.820	27486	17.1	6.8
II	364.076	27467	6.3	14.9
I	365.154	27386	13.5	7.0
I	365.206	27382	10.0	6.4
I	365.915	27329	19.6	13.9
II	367.007	27247	57.1	55.6
II	369.192	27086	11.0	11.5
II	370.057	27023	11.0	10.0
II	370.152	27016	22.4	25.0
I	371.355	26928	7.1	19.6
II	373.804	26752	12.2	17.2
II	374.642	26692	13.9	10.2
II	374.868	26676	19.4	18.1
II	376.953	26529	6.7	8.0
I	377.343	26501	11.0	13.2
II	378.071	26450	7.8	10.0
II	378.284	26435	38.8	20.9
II	378.384	26428	8.8	8.2
II	379.310	26364	11.6	18.5
II	383.146	26100	40.8	31.9
II	384.860	25983	10.0	16.1
II	385.464	25943	49.0	55.3
II	385.957	25910	100.0	100.0
II	386.117	25899	10.0	17.9
II	386.592	25867	38.8	38.5
II	389.036	25706	44.9	40.8
II	393.098	25439	8.8	54.8
II	393.202	25432	40.8	75.2
II	393.538	25411	10.0	9.9
II	394.048	25378	6.7	6.3
I	394.382	25356	24.5	13.2

Table 6.2 (continued)

	Literature values corresponding to observed wavelengths		Relative intensities	
U	Wavelength (nm)	Wavenumber (cm^-1)	NIST (%)	Experimental (%)
II	395.467	25287	7.3	19.4
I	396.421	25226	7.1	29.6
II	401.899	24882	6.1	10.1
	404.275	24736	*	19.6
	404.441	24725	*	4.3
II	405.004	24691	32.7	41.9
II	405.191	24680	11.0	20.1
II	405.430	24665	6.1	6.4
II	405.819	24642	8.8	11.1
II	406.254	24615	18.0	37.9
	406.775	24584	*	14.8
II	407.112	24563	8.4	16.5
II	408.060	24506	6.7	12.5
II	409.013	24449	44.9	78.2
II	409.303	24432	9.4	12.5
II	410.638	24352	7.8	11.6
II	411.610	24295	16.5	32.7
II	412.473	24244	8.4	17.6
II	412.834	24223	8.4	18.4
II	414.122	24147	9.4	22.1
I	415.397	24073	18.0	14.4
I	415.665	24058	7.8	9.6
II	416.368	24017	7.1	12.2
II	417.159	23972	28.6	42.9
II	418.927	23871	6.1	12.2
	419.750	23824	*	10.6
	420.140	23802	*	9.9
I	422.237	23683	7.1	41.5
	423.600	23607	*	10.7
II	424.167	23576	20.4	56.9
II	424.437	23561	10.6	26.4
	425.240	23516	*	8.6
	426.960	23421	*	12.5
	428.203	23353	*	17.4
	428.780	23322	*	11.7

1) The literature values utilized in comparison of the relative intensities were obtained from the NIST database. The ratios compare the intensity of the observed peak to the intensity of the most intense peak, 385.957 nm.

2) This list does NOT include all of the NIST values for this wavelength range. Only values corresponding to observed peaks in the lab are reported here.

3) * indicates peaks not reported by NIST and, therefore, no ratio is reported. These peaks were listed in the MIT wavelength tables.

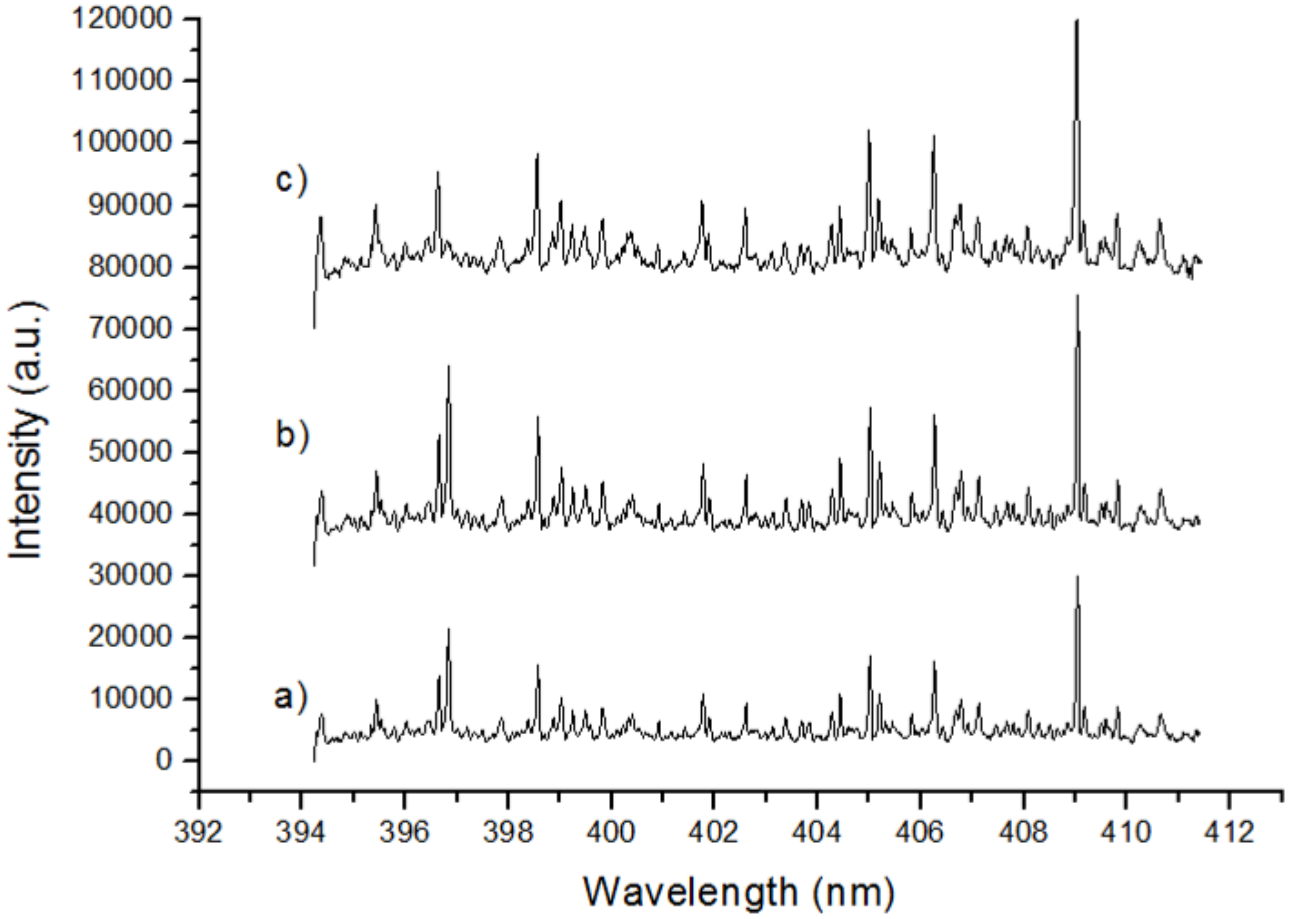

Figure 6.9 Reproducibility of emission spectra around 400 nm.

The scans depicted in a) and b) were taken on consecutive days with a 200 ppm uranium solution present and the plasma operating at 200 W. The trace presented in c) was taken several weeks later under the same operational conditions. The uranium peaks were very reproducible.

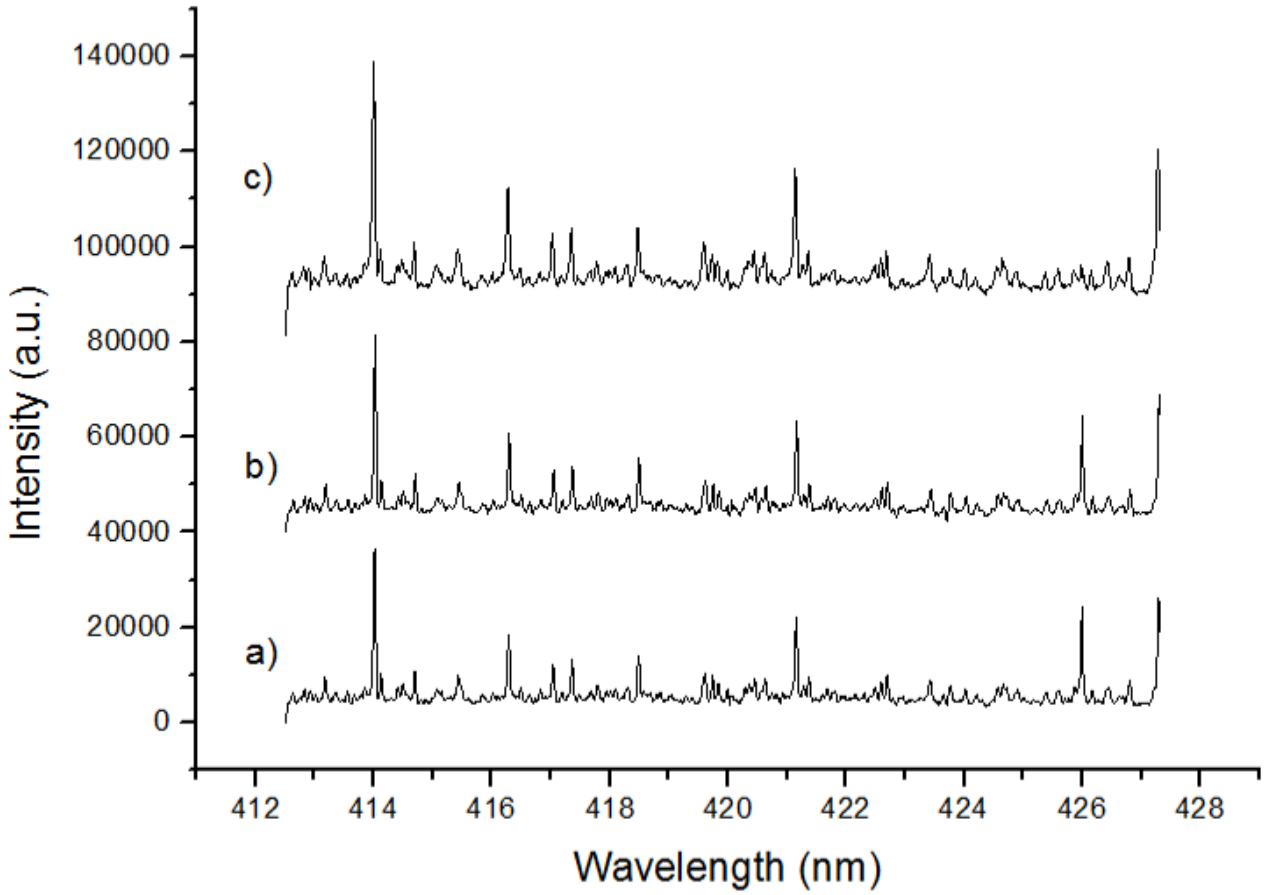

Figure 6.10 Reproducibility of emission spectra around 420 nm.

The scans depicted in a) and b) were taken on consecutive days with a 200 ppm uranium solution present and the plasma operating at 200 W. The trace presented in c) was taken several weeks later under the same operational conditions. The uranium peaks were very reproducible.

6.3.3 Effect of Plasma Power on Uranium Signal

Determination of the optimal plasma power for the given experimental parameters was also investigated in this research. Achieving uranium atomization with relatively low powers was the emphasized goal as this would allow a smaller, portable plasma source to be incorporated in a field deployable instrument. As can be seen in Figures 6.7 and 6.8, the observation of various uranium emission lines is a function of the plasma power. While the transition strengths of the lines included in these figures differ, the effect of incrementally increasing the power does not produce a proportional increase in the observed emission peak at each corresponding step. Even at powers as low as 80 W, U emission was observed for each of these spectral lines. The particular lines examined in these figures were chosen due to their compatibility with the existing cavity ringdown system for uranium detection employed in this lab. For the data presented in Figure 6.11, a 200 ppm U sample solution was used. The change in intensity as a function of power for the 287 and 289 nm spectral lines was barely discernable. While a combined technique, such as MIP-CRDS, might readily display the effect of power on these lines, the attention was directed to the stronger intensity lines. A 50 ppm sample solution was injected into the plasma for the data plotted in Figure 6.12. As evident in Figure 6.12, power is a significant factor for U generation for the 385.464 and 393.202 and, especially, for the 385.957 nm transition lines. Clearly, the development of a portable system for uranium detection will be dependent upon the transition line selected and optimizing the plasma power for that specific line.

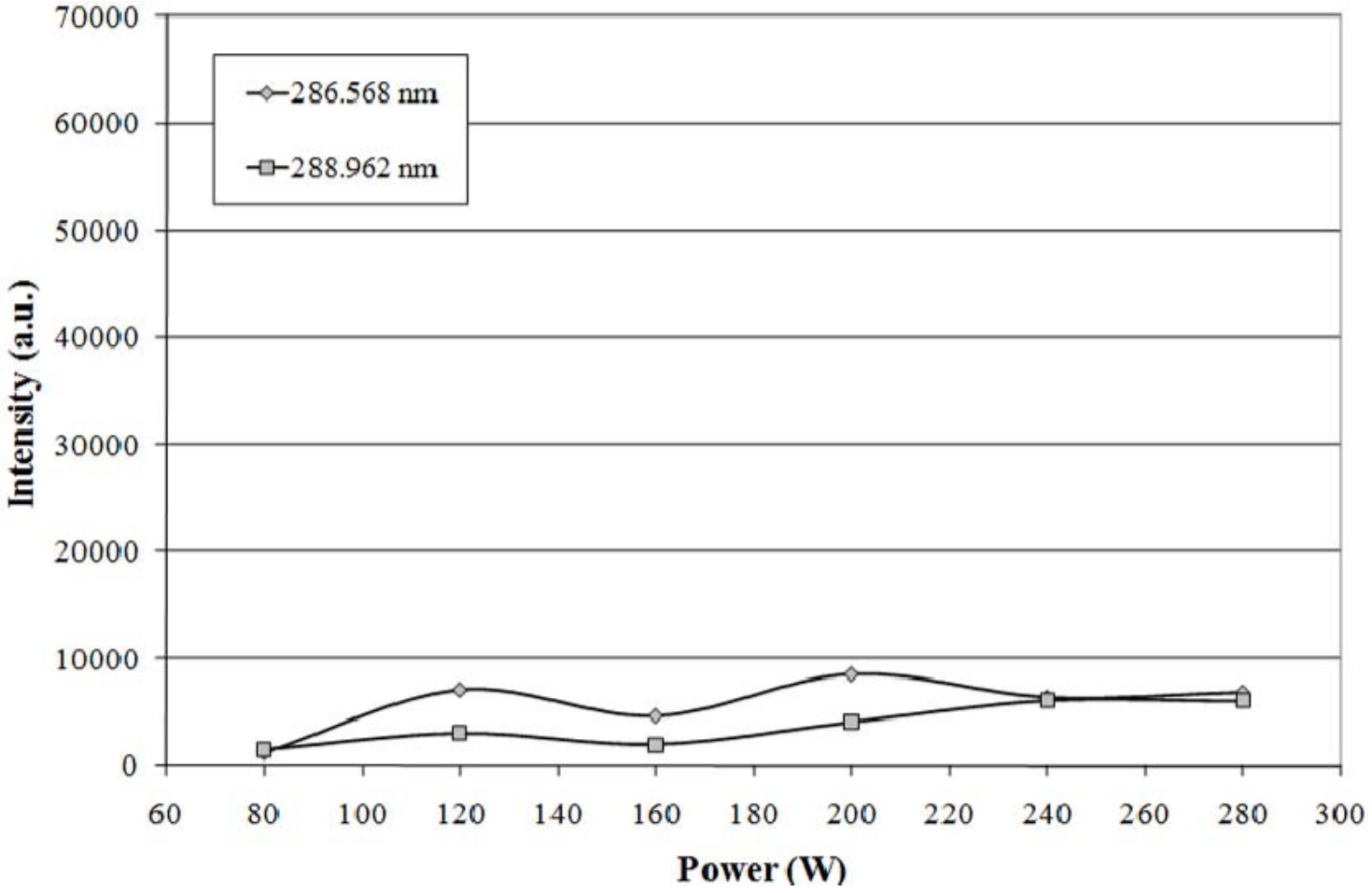

Figure 6.11 Uranium emission intensity of the 286.568 and 288.962 nm lines as a function of power.

A 200 ppm U sample solution was introduced to ultrasonic nebulizer in order to generate an aerosol which was, in turn, injected into the MIP. The background subtracted emission intensities are shown.

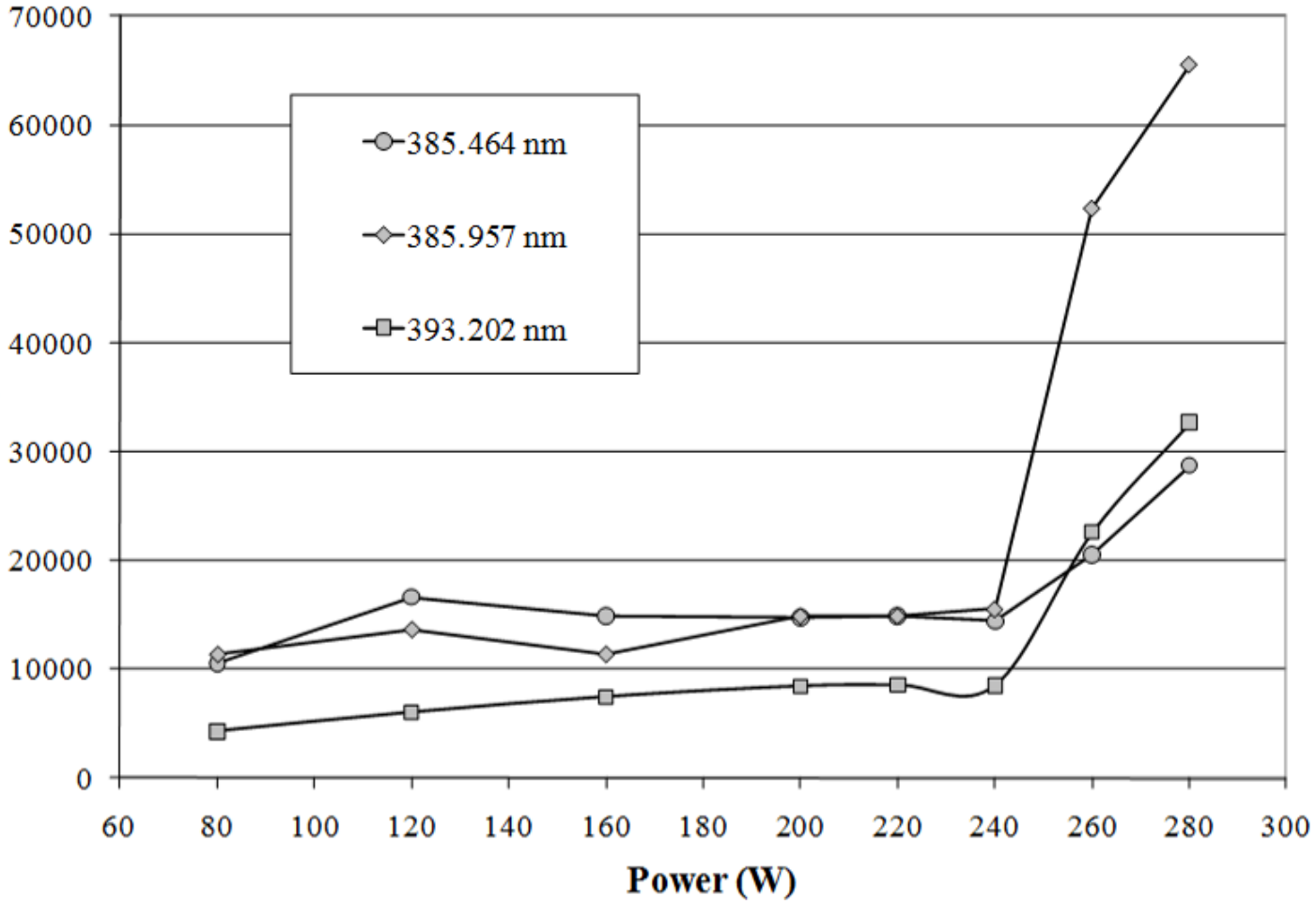

Figure 6.12 Uranium emission intensity of the 385.464, 385.957, and 393.202 nm lines as a function of power.

A 50 ppm U sample solution was introduced to ultrasonic nebulizer in order to generate an aerosol which was, in turn, injected into the MIP. The background subtracted emission intensities are shown.

6.3.4 Effect of Sample Concentration

The change in signal intensity as a function of concentration was also explored in order to determine the detection limits for several of the uranium transition lines. Figures 6.13 - 6.15 depict the instrument response to concentrations ranging from 5 to 200 ppm for wavelengths around 385, 400, and 420 nm. These spectra were acquired with 10 accumulations over a 10 ms integration time. The various concentrations generated reproducible scans and the change in intensity as a function of concentration is evident. The intensity of three relatively strong lines, 385.957, 409.013, and 417.159 nm, were examined at each of the concentrations examined. The background subtracted intensities for each concentration for these lines are given in Figure 6.16. Using a 200 W plasma, good linearity was observed for all three transition lines. Using the 3σ criteria for analytical certainty, the detection limits were determined to be 0.4, 0.5, and 0.8 ppm for the 385.957, 409.013, and 417.159 nm lines, respectively. These detection limits are somewhat higher than can be achieved with newer ICP's; however, marrying this low-power, low-temperature plasma source with the cavity ringdown technique could improve the detection limits by several orders of magnitude, while still utilizing a compact, portable plasma source, and will be the topic of future research.

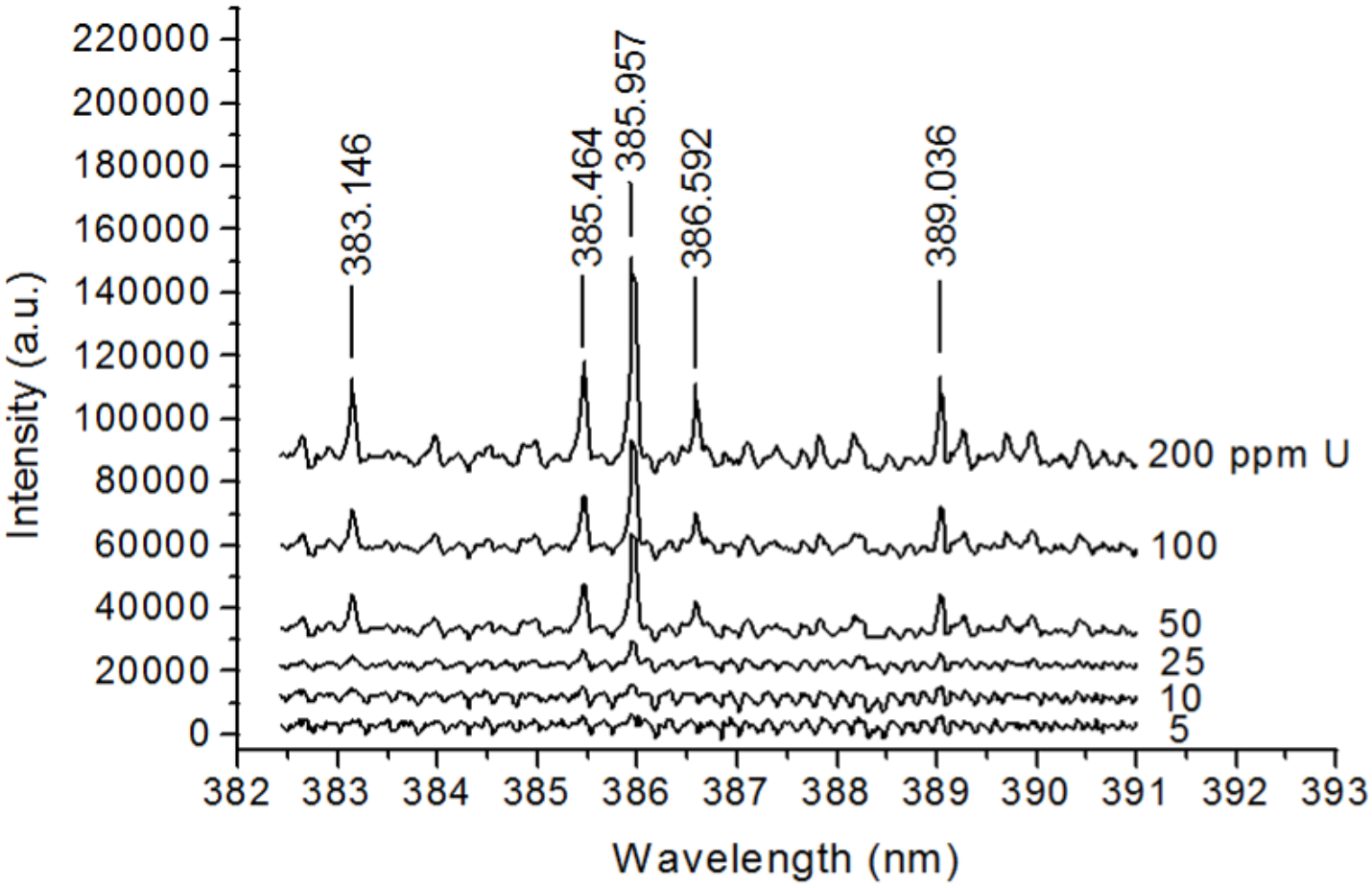

Figure 6.13 Emission spectra observed for various concentrations of uranium around 385 nm.

Solutions ranging from 5 to 200 ppm were introduced in to the plasma, and the observed spectra are shown. The plasma was operating at 200 W/ 6 W, and the flow rates were 1.0/0.5/0.5 L/min.

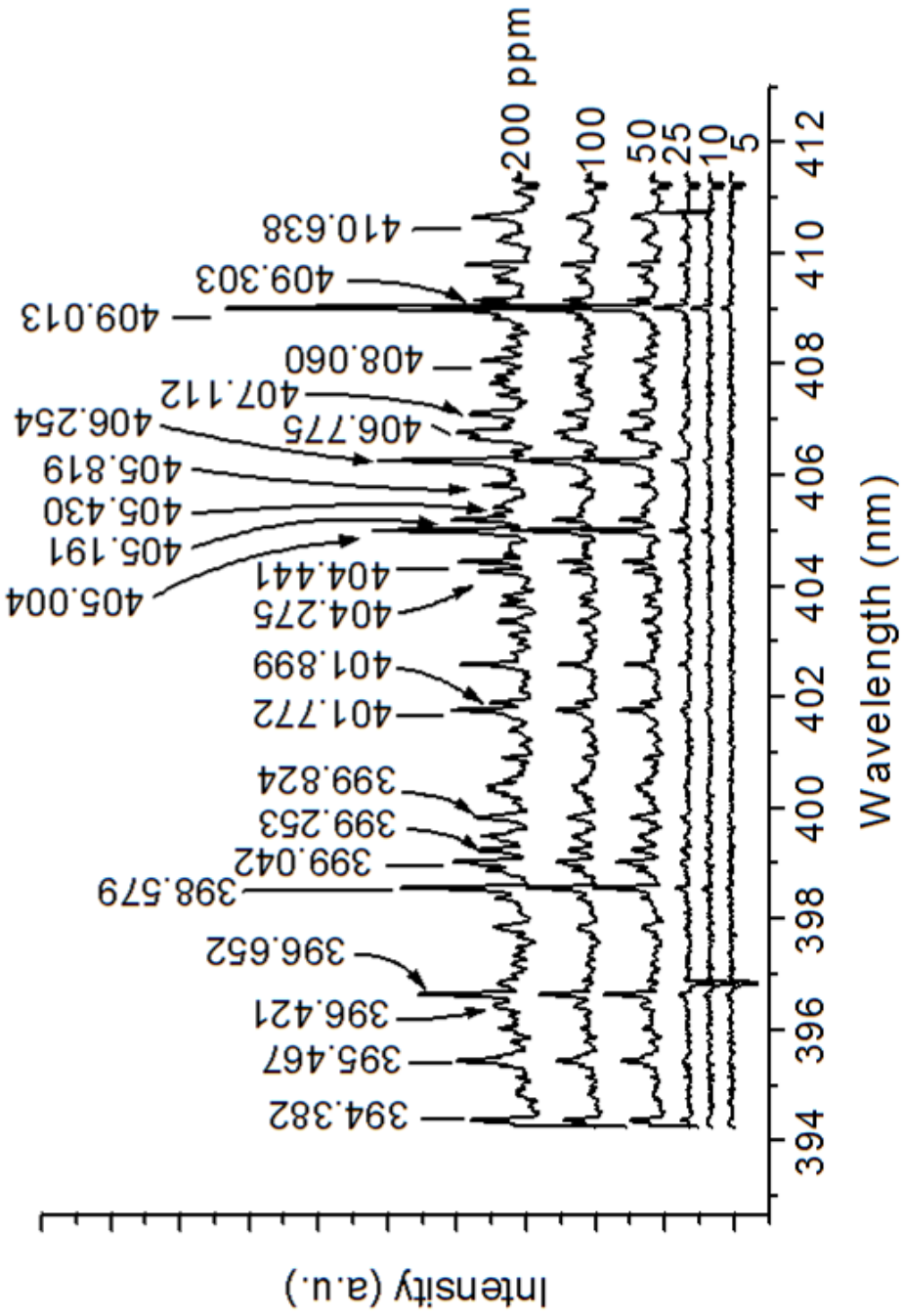

Figure 6.14 Emission spectra observed for various concentrations of uranium around 400 nm. Solutions ranging from 5 to 200 ppm were introduced in to the plasma, and the observed spectra are shown. The plasma was operating at 200 W/ 6 W, and the flow rates were 1.0/0.5/0.5 L/min.

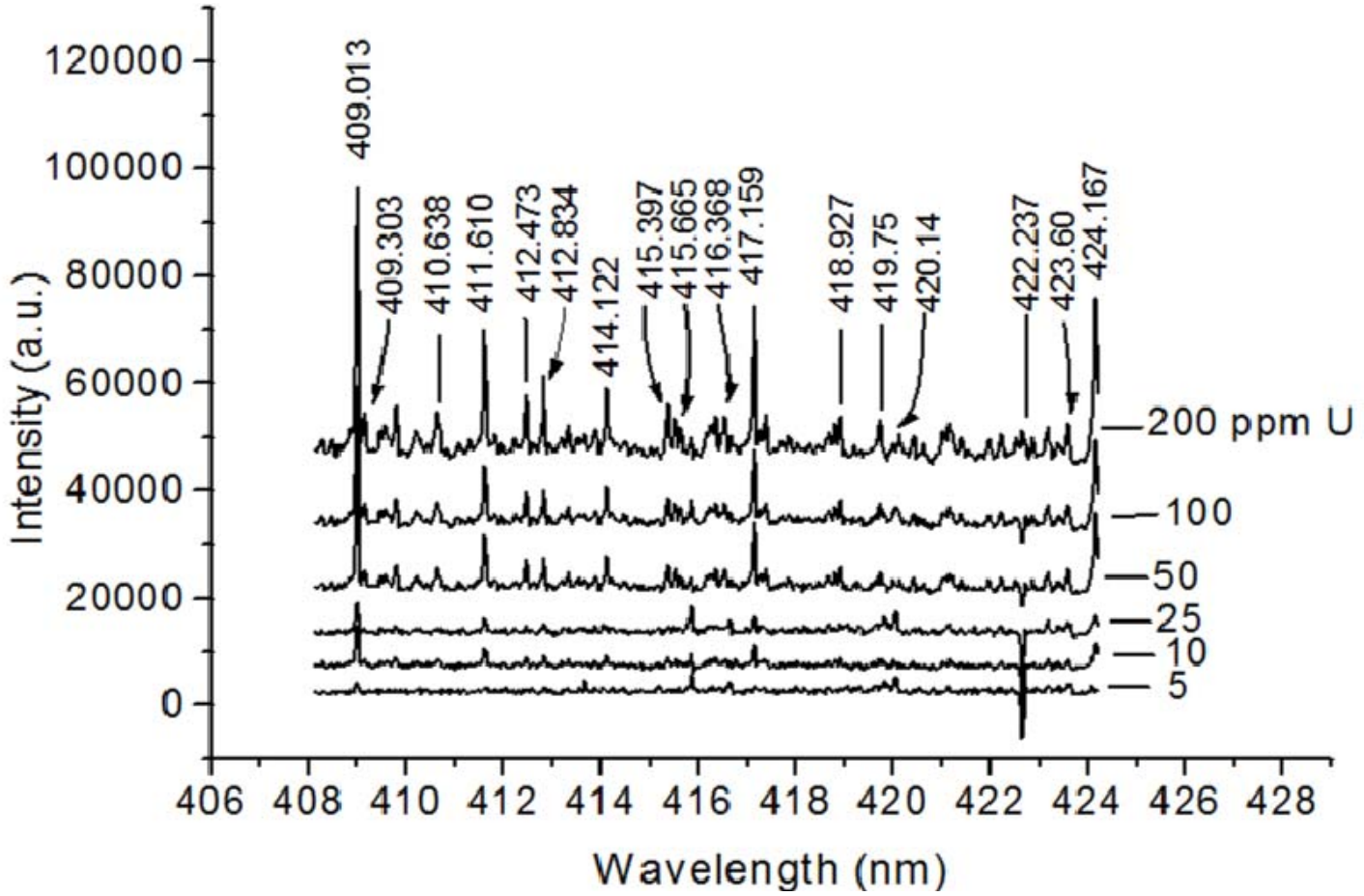

Figure 6.15 Emission spectra observed for various concentrations of uranium around 420 nm.

Solutions ranging from 5 to 200 ppm were introduced in to the plasma, and the observed spectra are shown. The plasma was operating at 200 W/ 6 W, and the flow rates were 1.0/0.5/0.5 L/min.

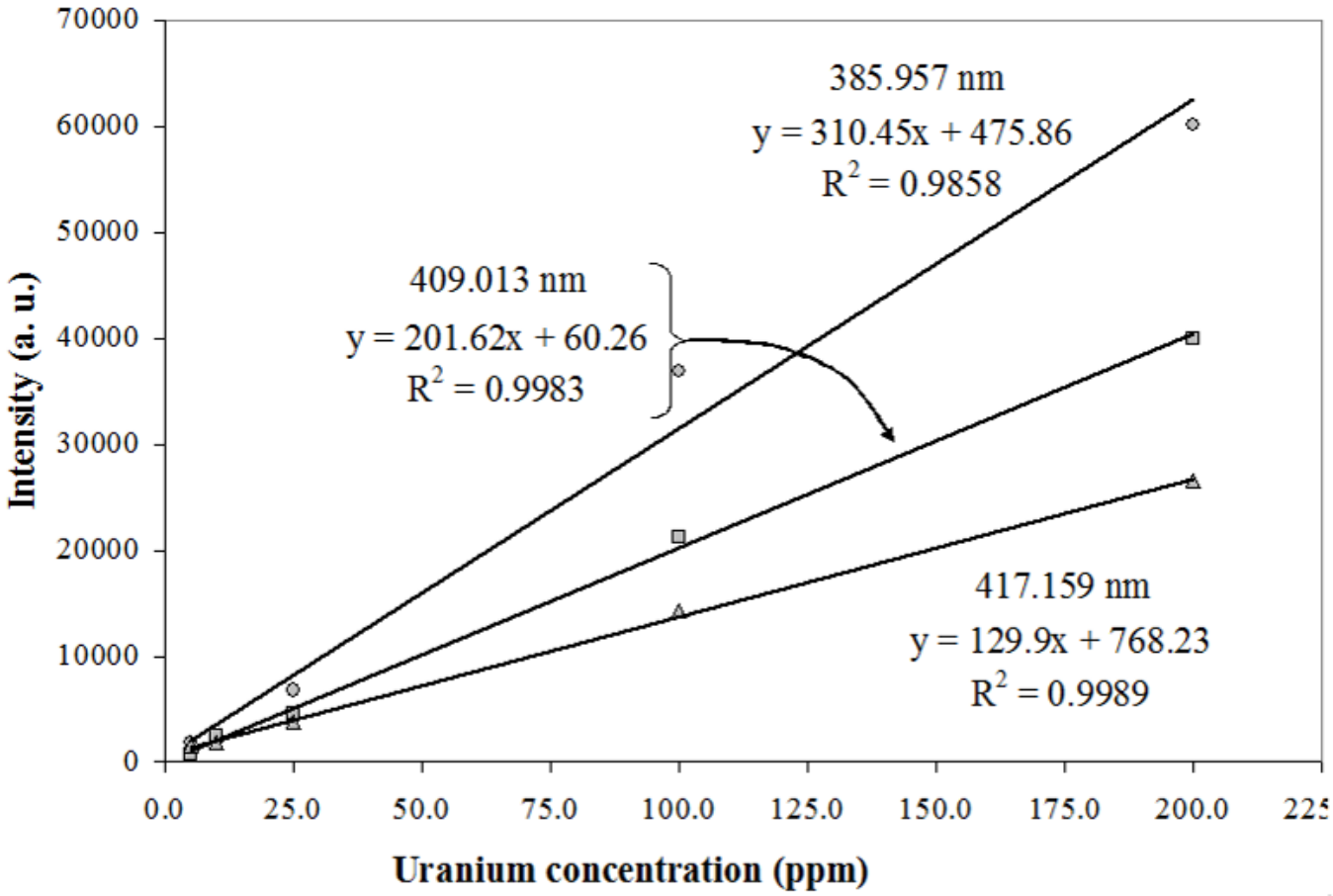

Figure 6.16 Uranium emission intensities of the 385.957, 409.013, and 417.159 nm lines as a function of concentration.

Various concentrations of uranium solutions were sequentially introduced into the ultrasonic nebulizer in order to generate an aerosol which was, in turn, injected into the MIP. The background subtracted emission intensities for each concentration are plotted. The plasma was operating at 200 W/2W, and the flow rates were 10/0.5/0.57 mL/min.

6.3.5 Other Elements Successfully Atomized

In order to develop a field portable instrument using this MIP as the atomization source, the ability to efficiently atomize additional atoms was briefly explored. The primary objective of this research was to ascertain the feasibility of successfully generating uranium atoms; therefore, the detection of additional elements was not fully examined, only confirmed. Some of the elements which were tested and emission spectra obtained include As, Ba, Cd, Cr, Fe, Hg, Mn, Ni, P, Pb, Sb, Se, Si, Sr, and Tl. An example of the spectra obtained for some of these elements is given in Figures 6.17 – 6.20. Clearly, the ability to generate and subsequently detect multiple species with this atomization source will be instrumental in the design of a field portable plasma system.

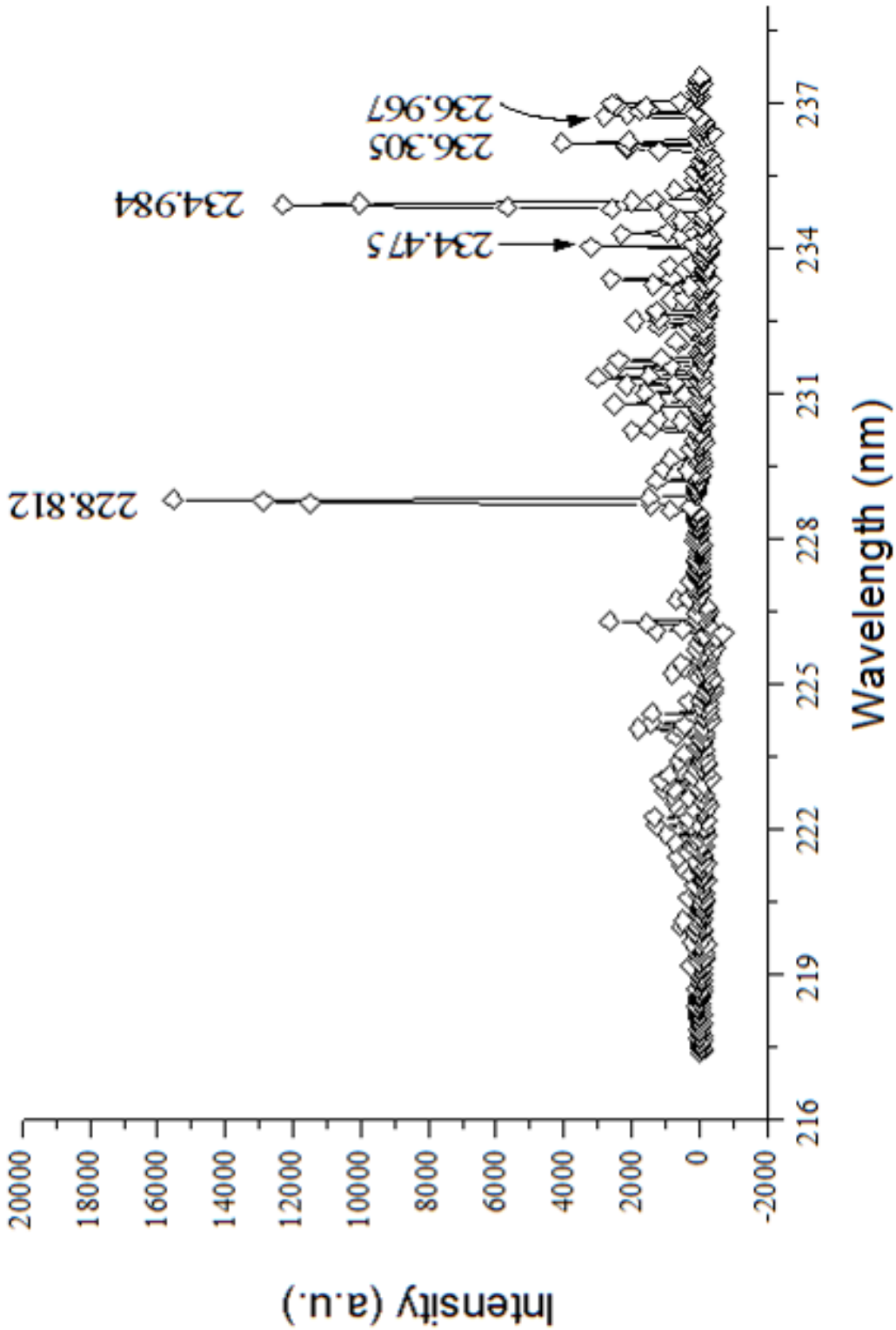

Figure 6.17 Emission spectrum of As obtained with the candle-shaped MIP utilized in the U studies.

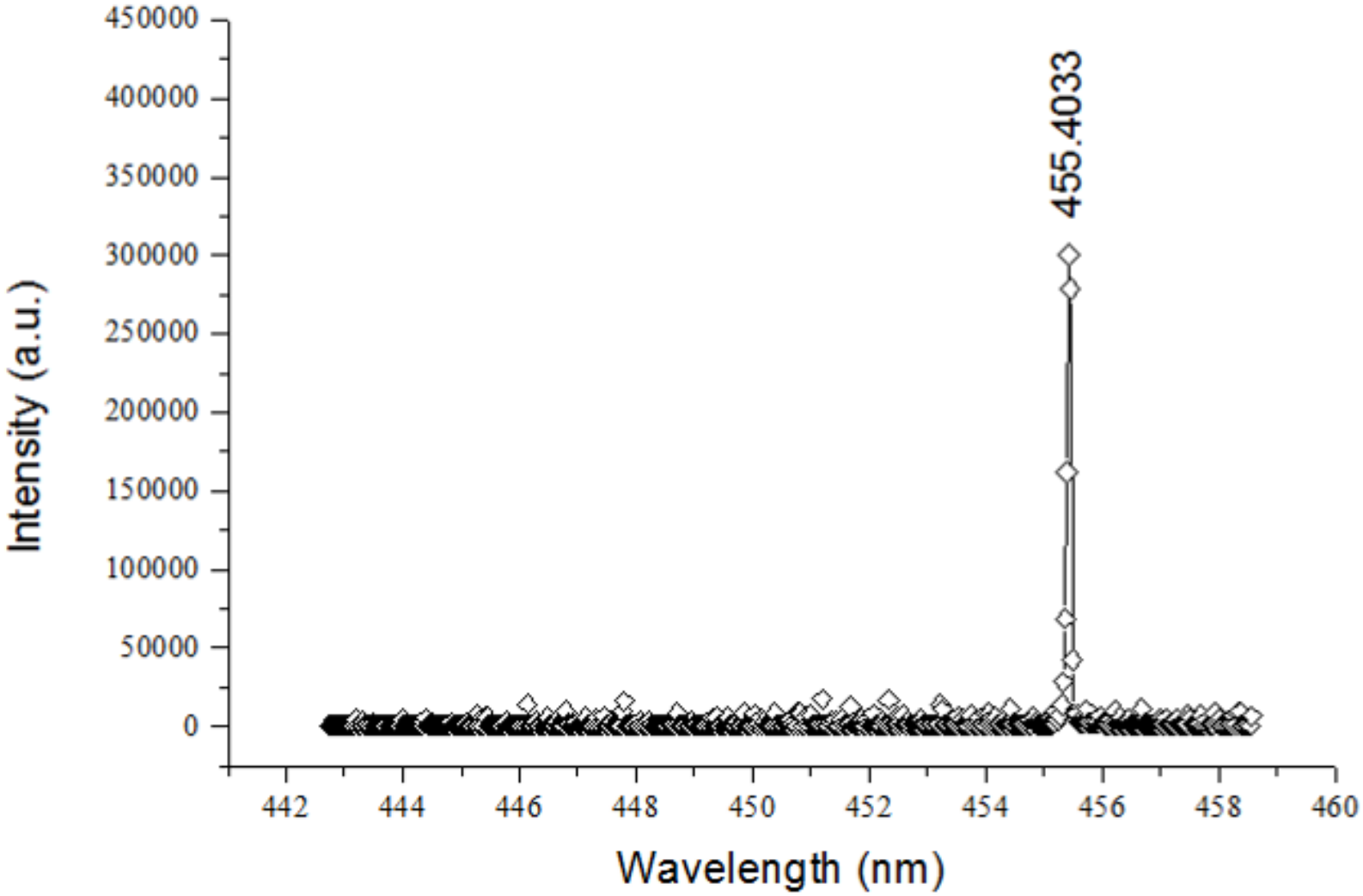

Figure 6.18 Emission spectrum of Ba obtained with the candle-shaped MIP utilized in the U studies.

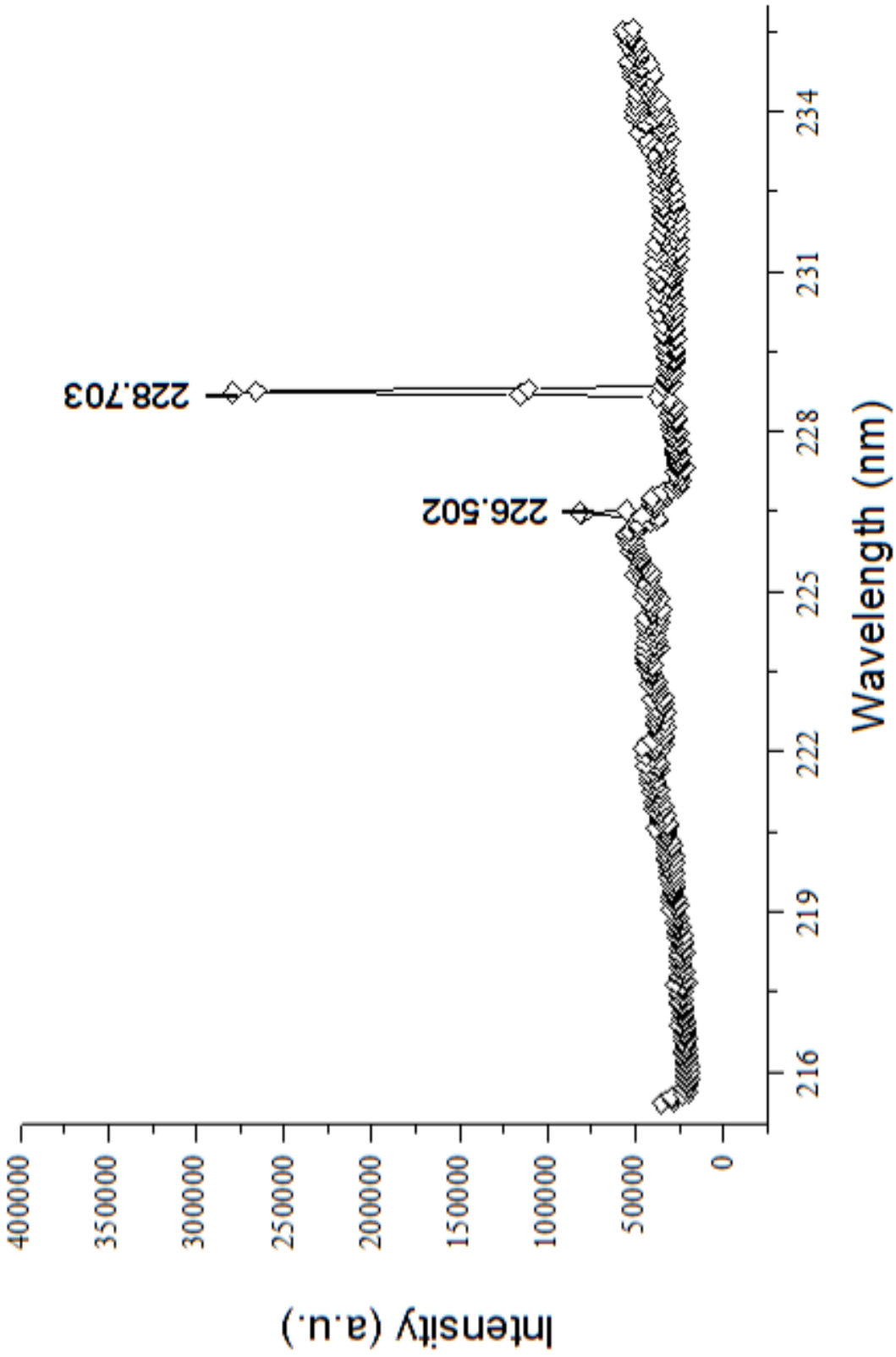

Figure 6.19 Emission spectrum of Cd obtained with the candle-shaped MIP utilized in the U studies.

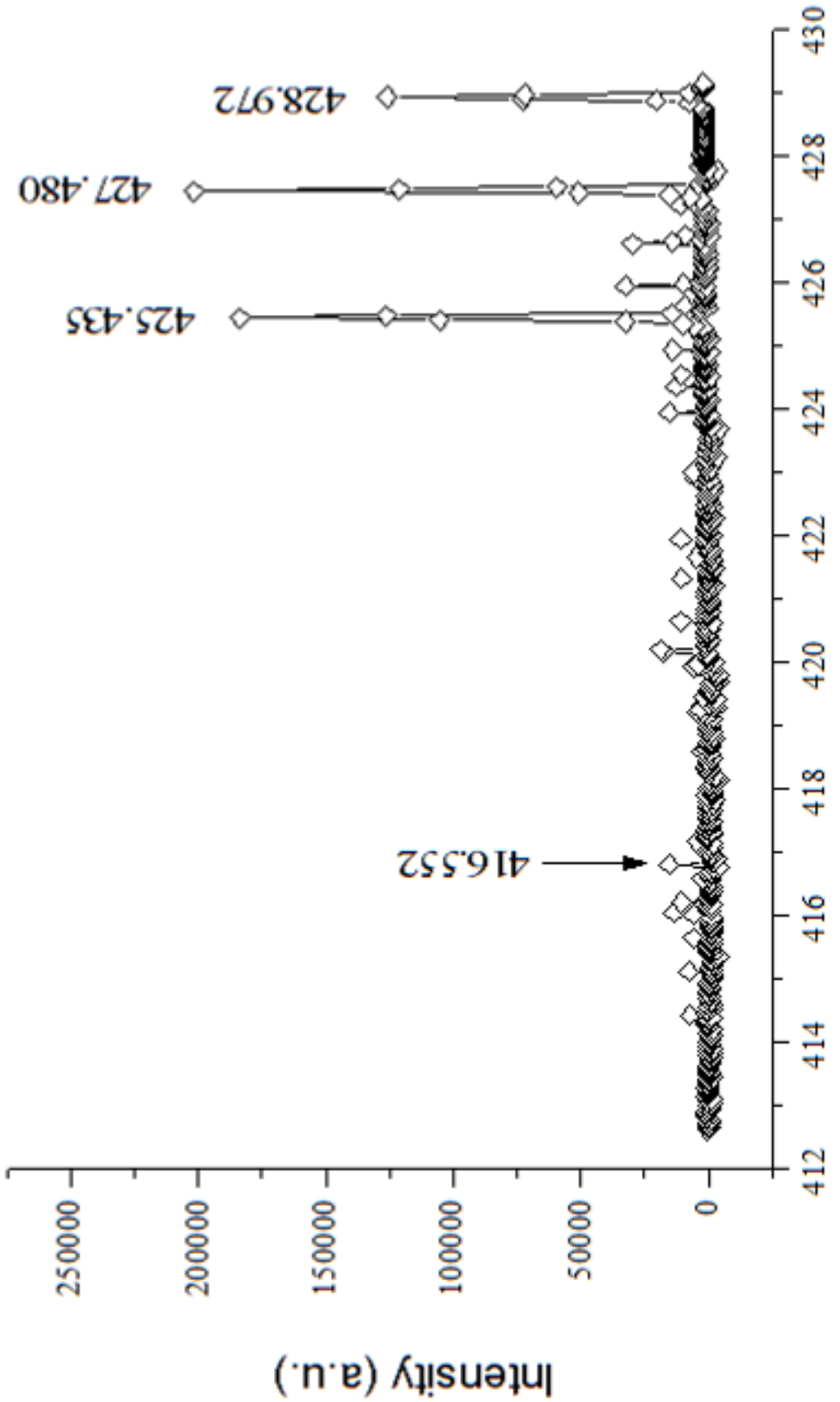

Figure 6.20 Emission spectrum of Cr obtained with the candle-shaped MIP utilized in the U studies.

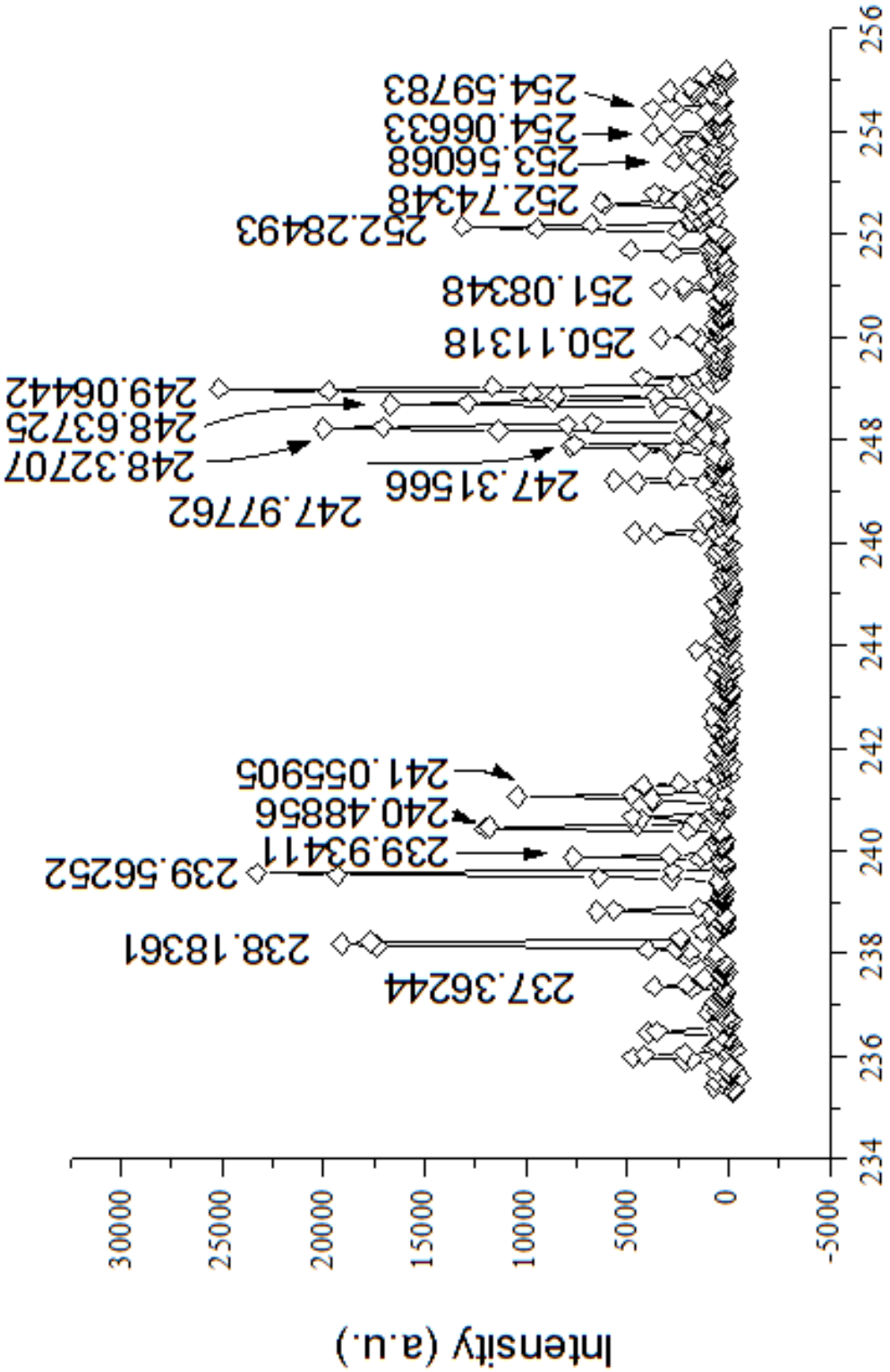

Figure 6.21 Emission spectrum of Fe obtained with the candle-shaped MIP utilized in the U studies.

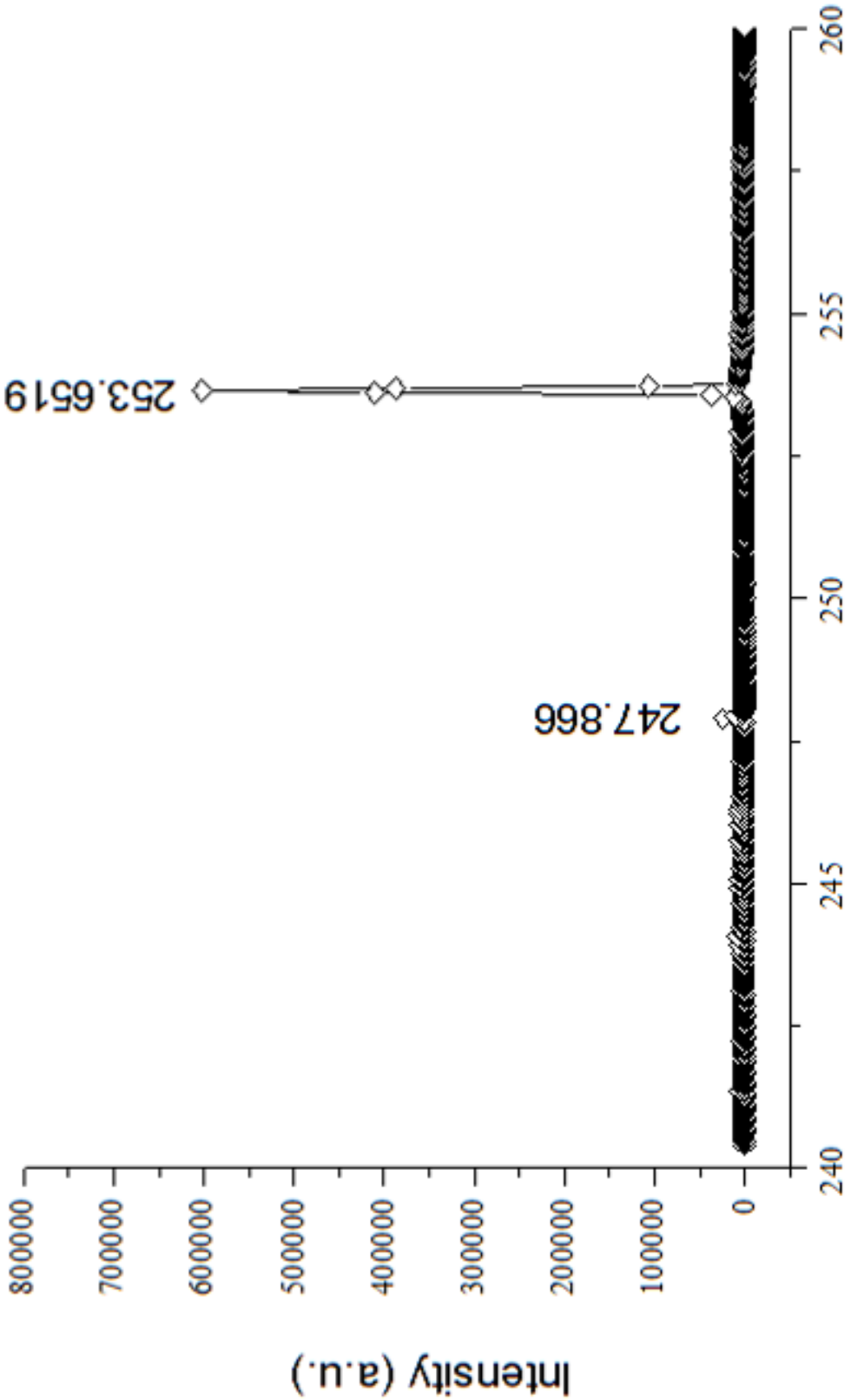

Figure 6.22 Emission spectrum of Hg obtained with the candle-shaped MIP utilized in the U studies.

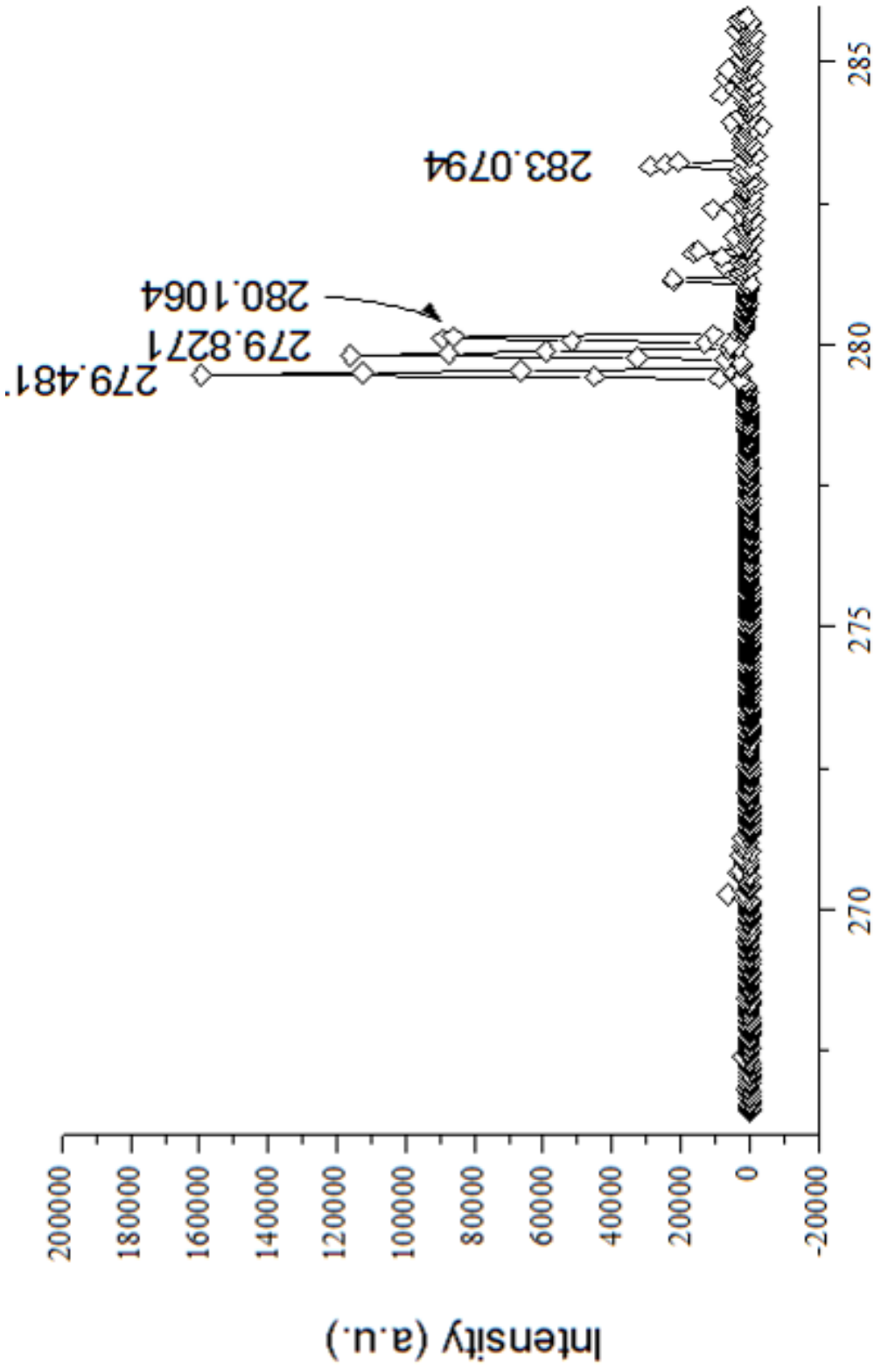

Figure 6.23 Emission spectrum of Mn obtained with the candle-shaped MIP utilized in the U studies.

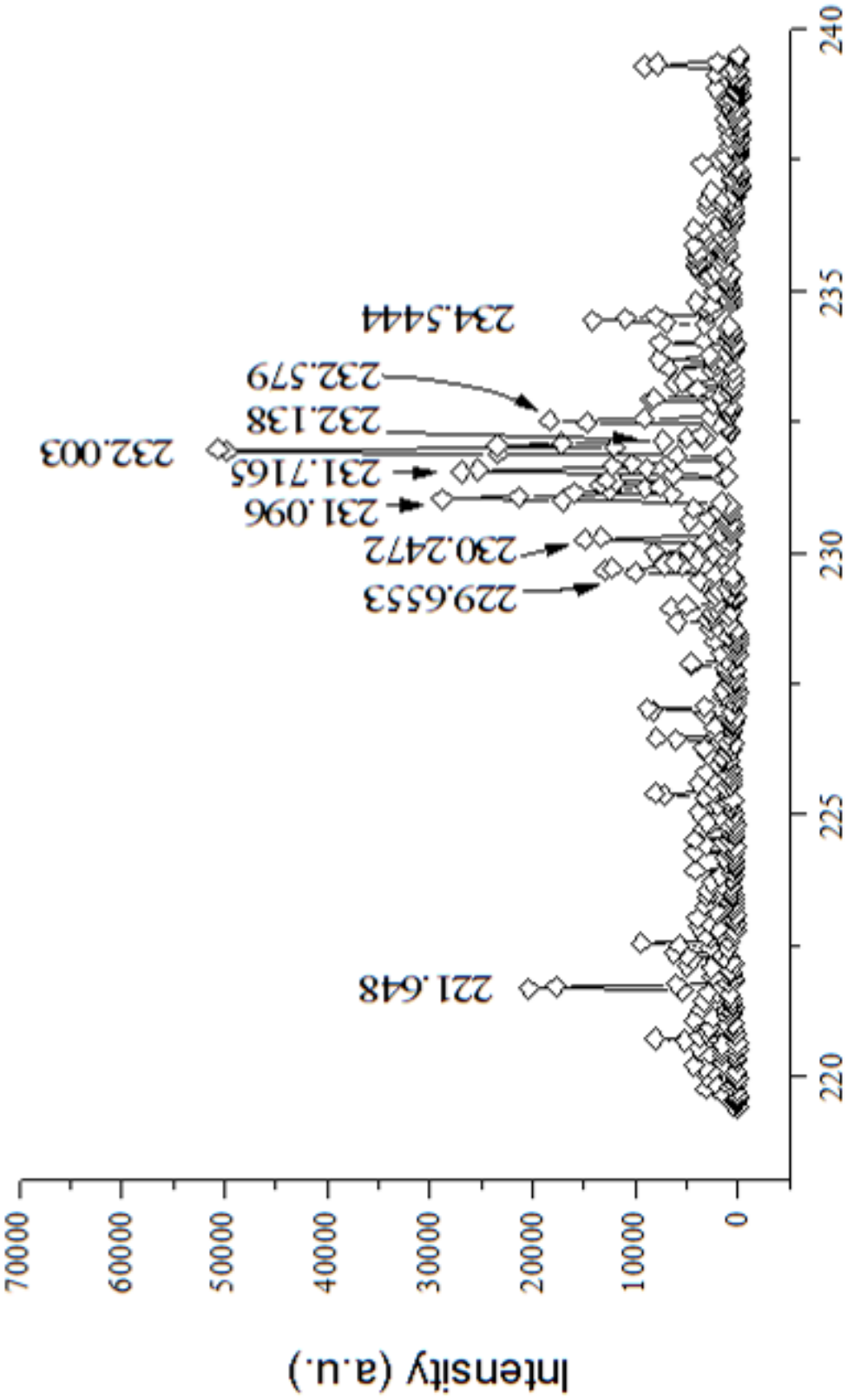

Figure 6.24 Emission spectrum of Ni obtained with the candle-shaped MIP utilized in the U studies.

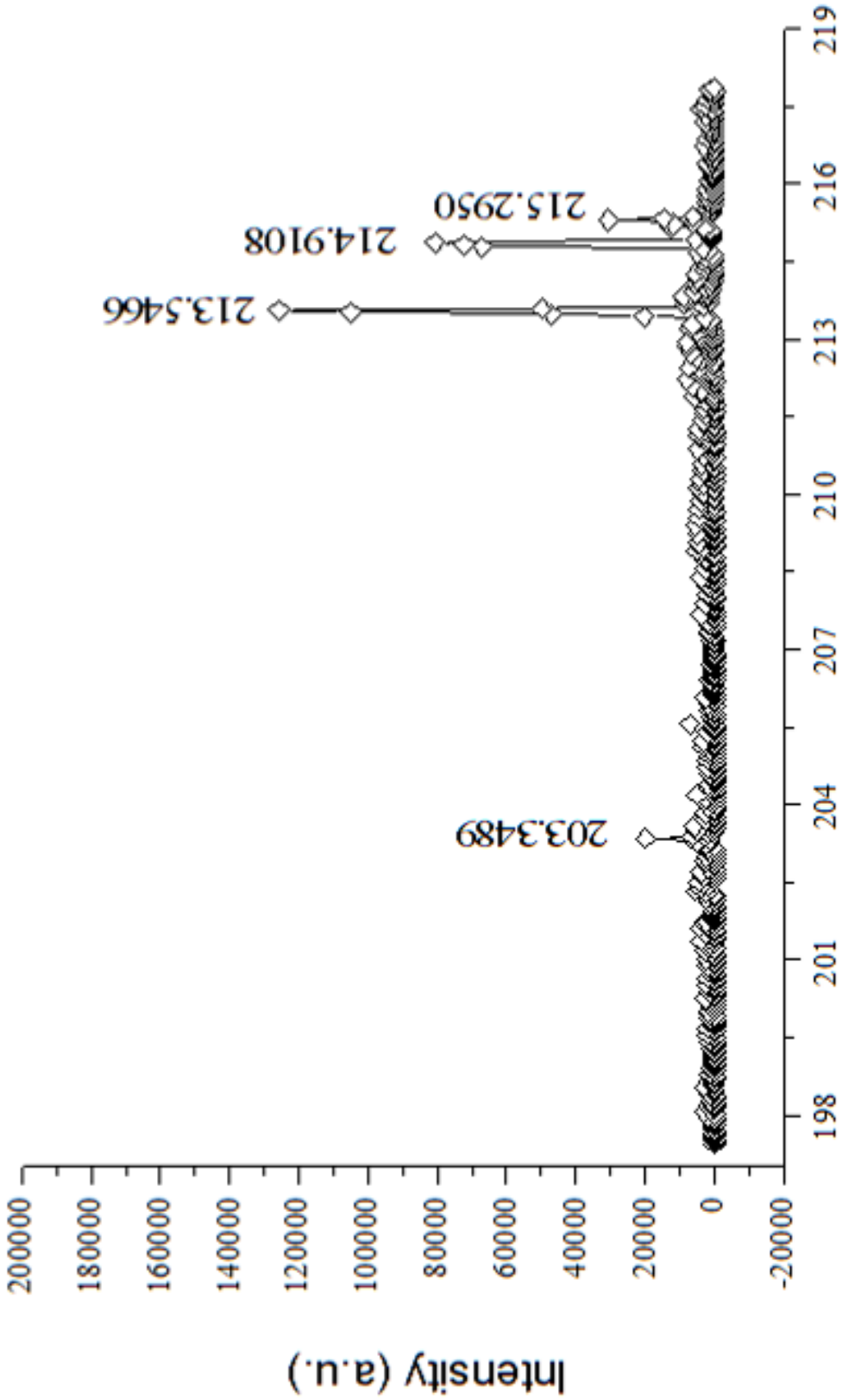

Figure 6.25 Emission spectrum of P obtained with the candle-shaped MIP utilized in the U studies.

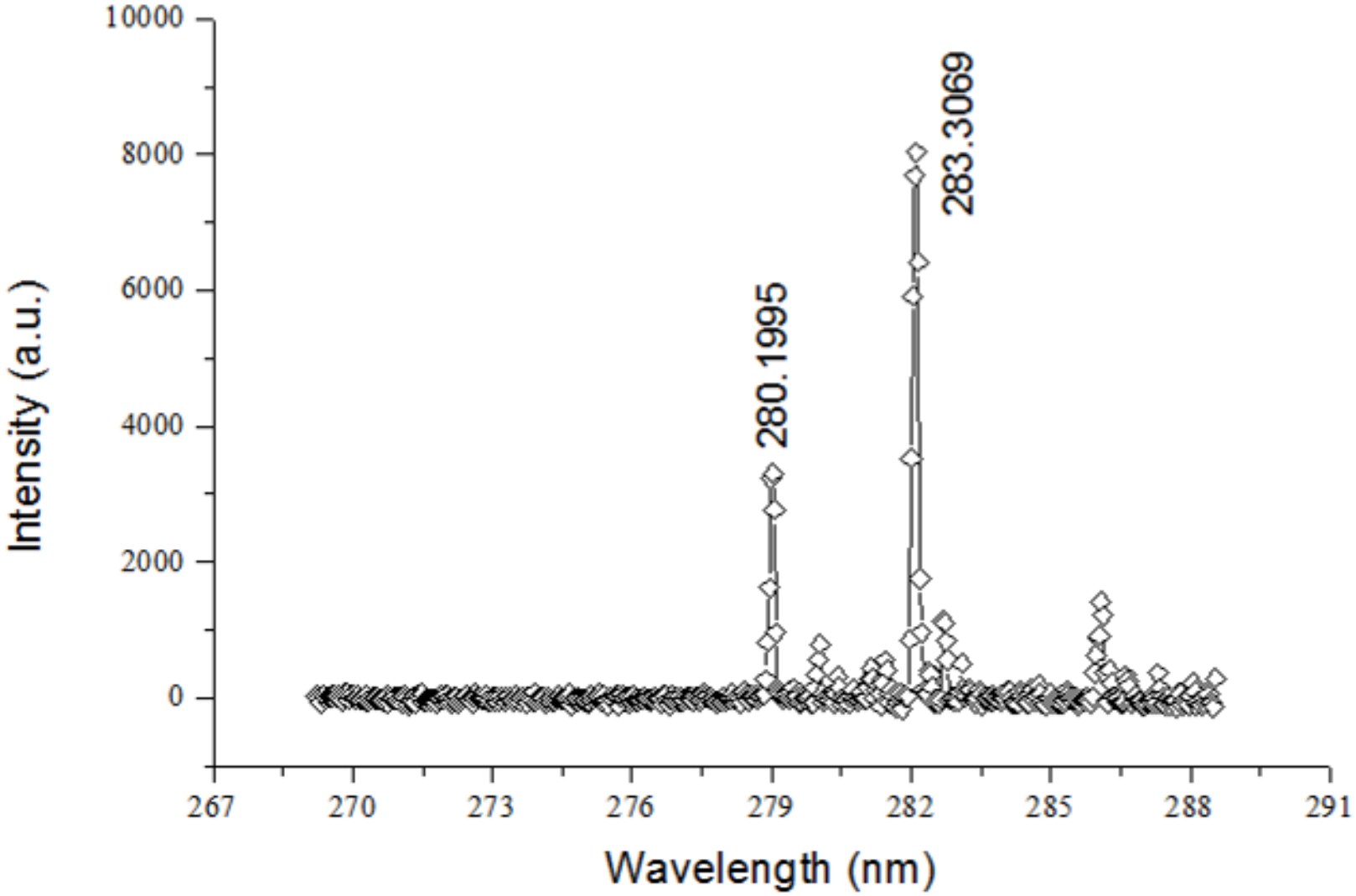

Figure 6.26 Emission spectrum of Pb obtained with the candle-shaped MIP utilized in the U studies.

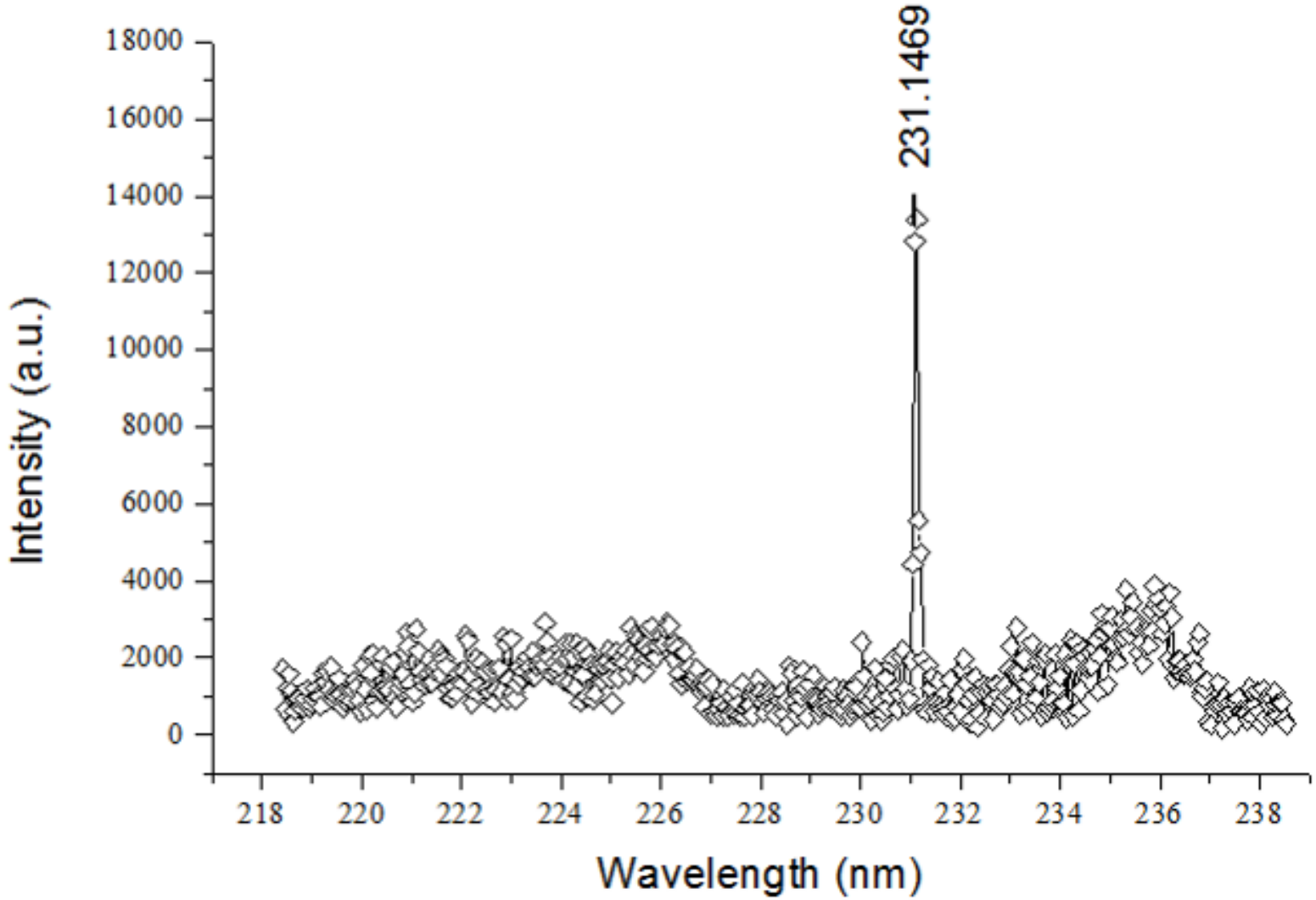

Figure 6.27 Emission spectrum of Sb obtained with the candle-shaped MIP utilized in the U studies.

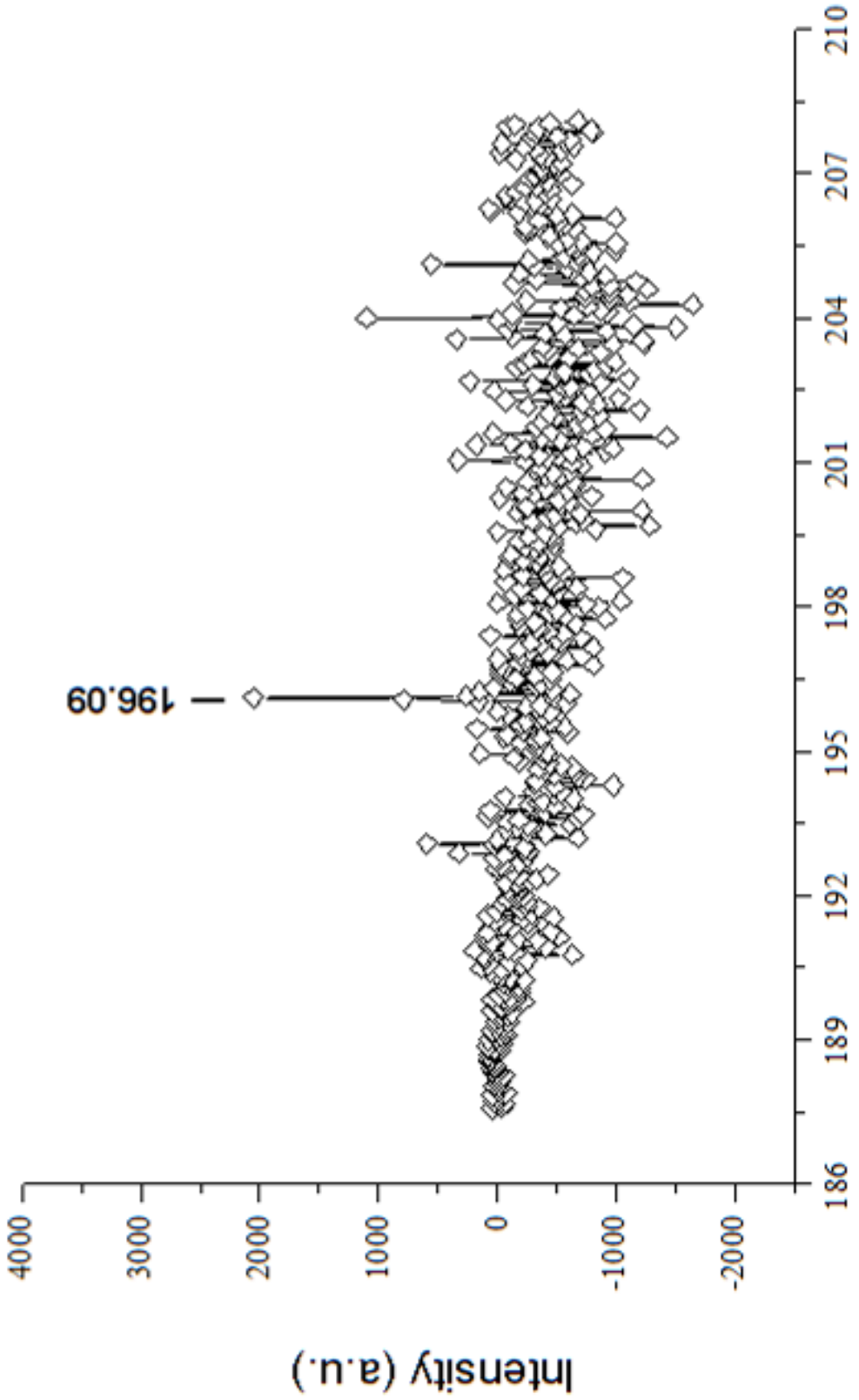

Figure 6.28 Emission spectrum of Se obtained with the candle-shaped MIP utilized in the U studies.

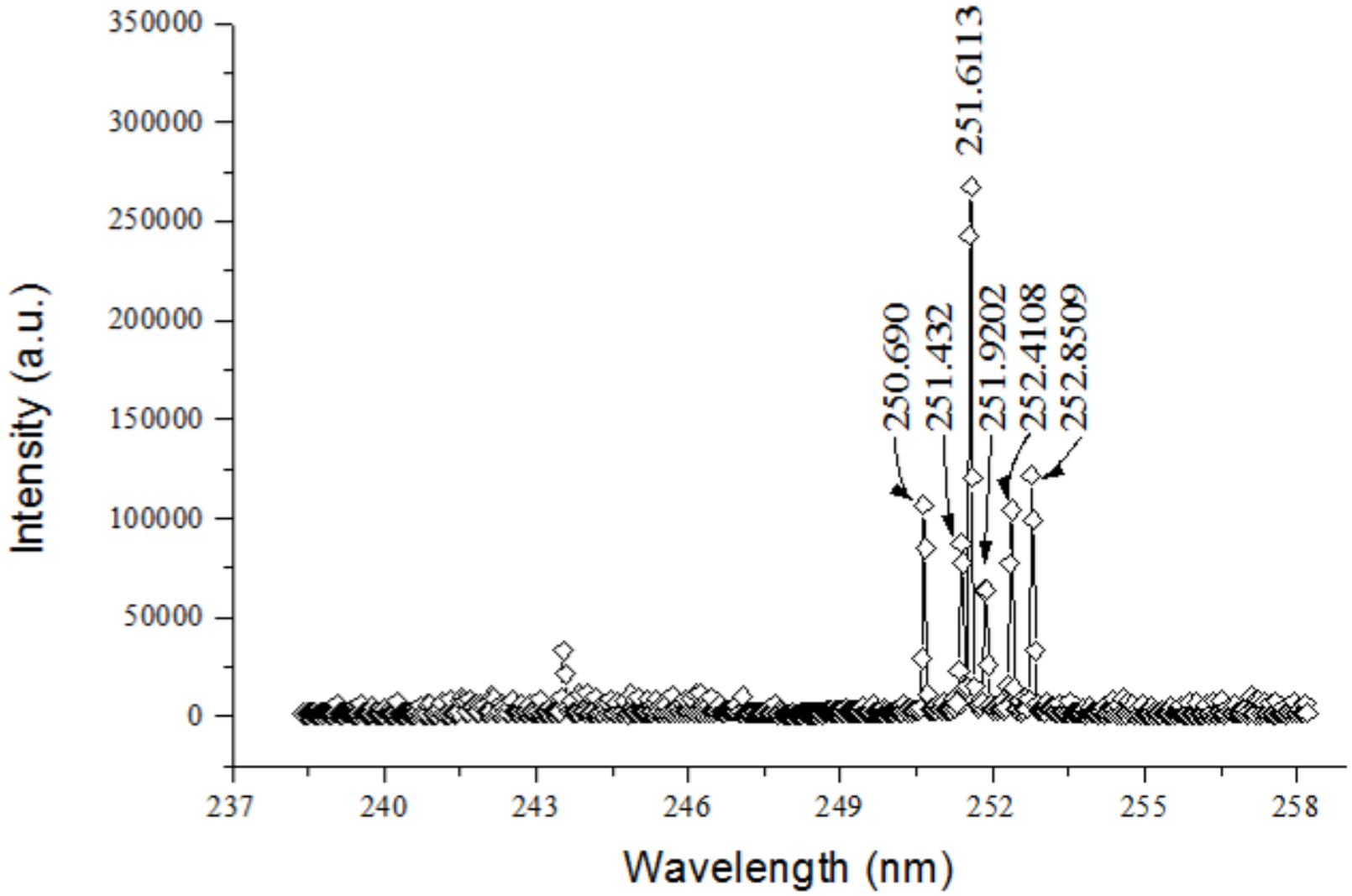

Figure 6.29 Emission spectrum of Si obtained with the candle-shaped MIP utilized in the U studies.

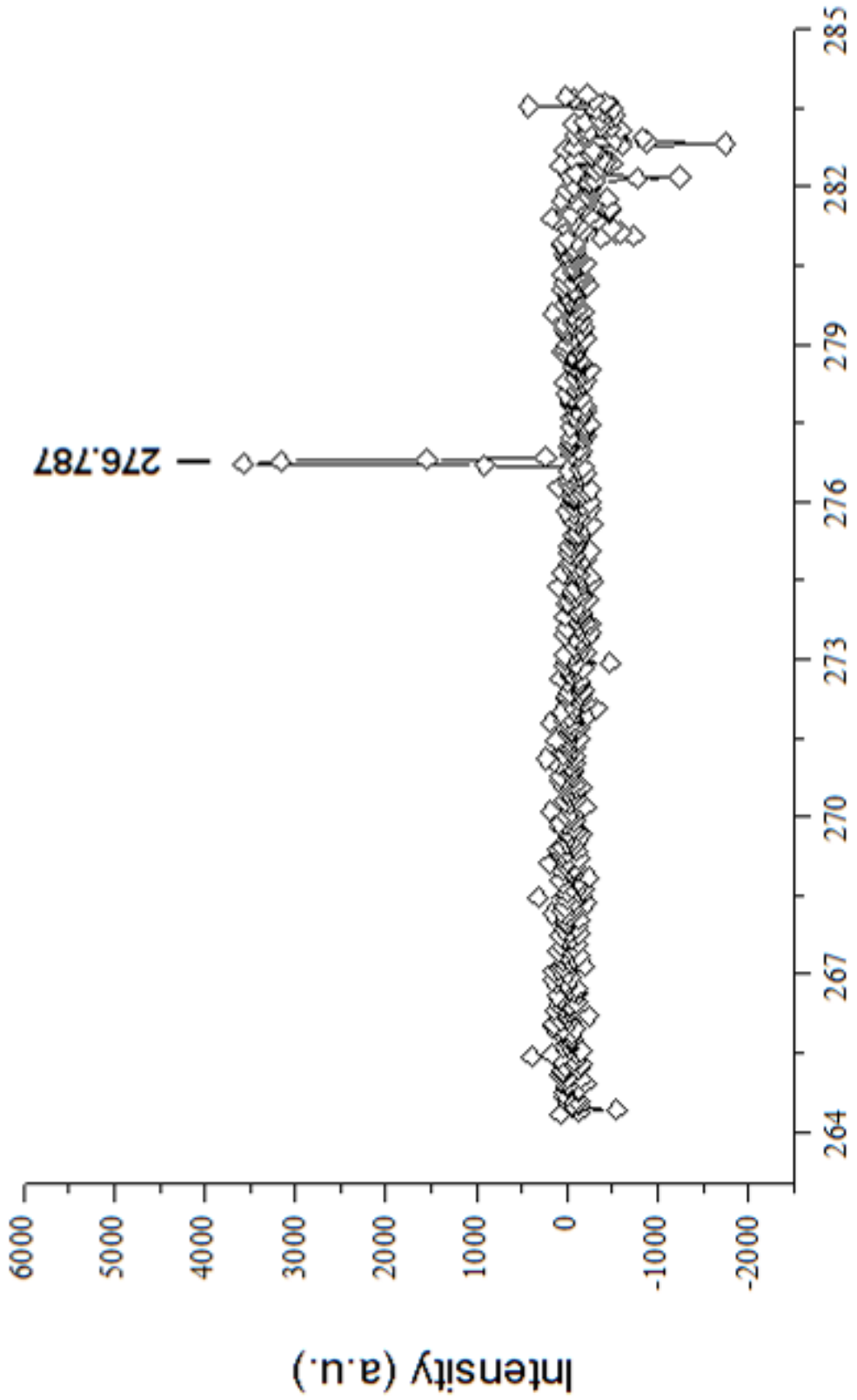

Figure 6.30 Emission spectrum of Tl obtained with the candle-shaped MIP utilized in the U studies.

CHAPTER VII

FEASIBILITY STUDIES FOR URANIUM DETECTION IMPLENTING DIODE LASER INDUCTIVELY COUPLED PLASMA-CAVITY RINGDOWN SPECTROSCOPY (DIODE LASER-ICP-CRDS)

7.1 Introduction

In an effort to move towards a field-deployable plasma-CRDS spectrometer for real time, *in situ* measurements of uranium, sequential investigations have been undertaken in this laboratory. The initial studies[118] examined ICP-CRDS in the UV and employed a 20 Hz Continuum Powerlite 8020 Nd:YAG laser to pump a Radiant NarrowScan dye laser. The output was frequency doubled with an INRAD AutoTracker frequency doubling system to generate the wavelengths of interest. Once the feasibility of detecting uranium with the ringdown technique had been established, the research effort examined the potential of incorporating a low-power, low-flow rate microwave induced plasma (MIP) to efficiently atomize uranium from solutions in lieu of the ICP. The geometric footprint of the MIP is significantly more compact, and the MIP does not require external cooling or additional electronics to operate. Uranium emission spectra and detection limits obtained with the MIP were the subject of Chapter VI. In addition to reducing the size of the atomization source, the next limitation to portability is the very large, expensive laser system which was employed for the ICP-CRDS studies of uranium. In an effort to address this aspect, a continuous wave (CW) diode laser operating at 409 nm was employed to test the feasibility of detecting uranium with diode laser-ICP-CRDS.

An in-depth characterization of the diode laser was conducted. The operational parameters of the ICP and the beam position in the plasma were optimized for U detection. The preliminary uranium measurements obtained with this system will be the subject of this chapter.

7.2 Experimental Setup

A schematic for the experimental setup employed in this research is given in Figure 7.1. The system consisted of five distinct sections: the light source, optical components, detection electronics, sample introduction, and atomization source.

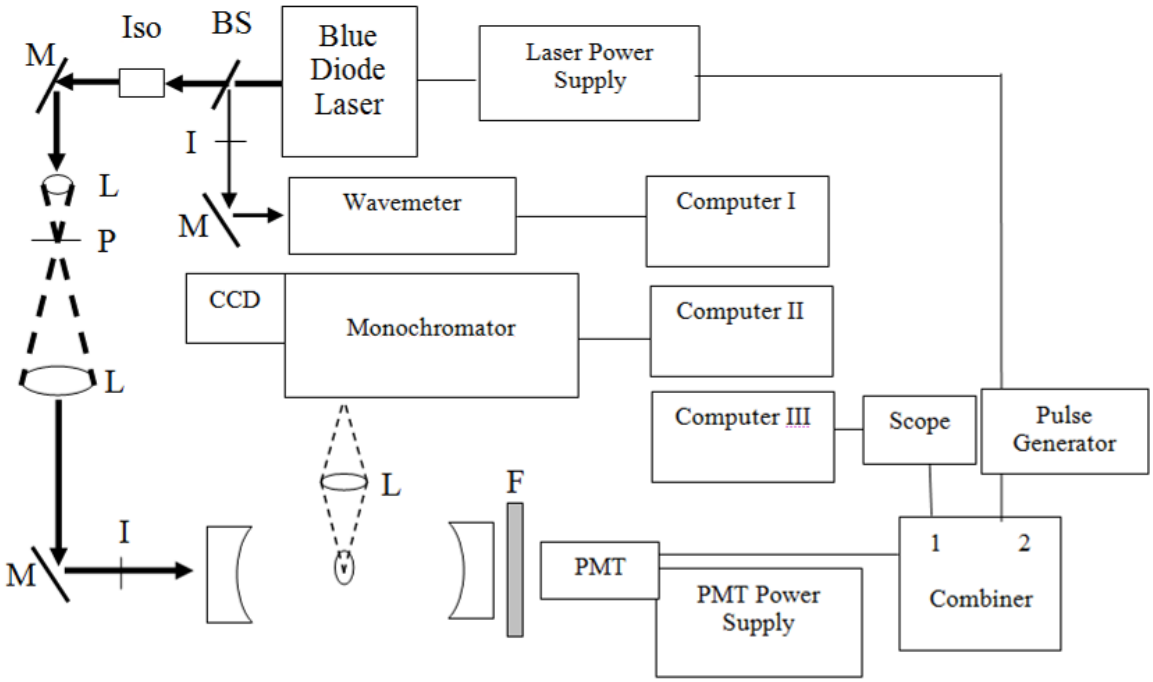

Figure 7.1 Experimental configuration employed with diode laser ICP-CRDS.

M's are mirrors; L's are focusing lenses; BS is a beam splitter; Iso is the double stage optical isolator; I's are irises; P is a pinhole; F is a neutral density filter; PMT is the photomultiplier tube detector; CCD is the charge coupled device detector.

7.2.1 Laser Light Source and Optical Components

Continuous wave laser light was generated by an external cavity UV diode laser (DL 100, Toptica Photonics AG) implementing the DL 100 high frequency (HF) modulator. The mode hop free-tuning range was 21 GHz at 62 mA and 20.0 °C. The output power of this diode was ~ 30 mW at 71 mA in free-running mode and 17.8 mW at 65 mA at the factory preset wavelength (409 nm). The lasing threshold of the diode at 409 nm is 43 mA. In free-running mode, the output wavelength is 407.8 nm at maximum power and the laser threshold is 46 mA. In order to generate specific output wavelengths with minimal-to-no mode hops, the temperature, current, and scan rate of the diode had to be simultaneously optimized. Particular attention focused on preventing mode hops, which, according to the pulsed UV wavemeter (WA-5500, Burleigh/EXFO, Inc.), resulted in large changes in the output wavelength (~ 2 nm). Because of the finite reflectivity of the mirrors over a specific wavelength range, different wavelengths produced different ringdown baselines; furthermore, different modes entering the ringdown cavity resulted in different ringdown times. To ensure single wavelength output during a scan, the wavemeter and ringdown software were heavily utilized.

Diode lasers are extremely sensitive to optical feedback; therefore, to minimize the instability induced in the laser function (e.g., mode hops) because of feedback between the back side of the first ringdown mirror and the diode laser housing, an optical isolator (Optics for Research, Inc.) was positioned between the aforementioned optics. The 35 dB isolator is a narrowband, free space Faraday isolator which effectively eliminates the feedback by rotating the polarization of the beam, upon the second encounter with the isolator, by 90°. The optimized laser output consisted of an intense peak at the wavelength of interest as well as a broad background peak, as shown in

Figure 7.2. The power of the output beam could not be reduced electronically without changing the output wavelength or stability significantly, and the broadened component of the output in conjunction with the peak was intense enough to still be visible by eye after passing through the second ringdown mirror. This artifact distorted the ringdown measurements. The laser light emitted from the diode was directed onto a neutral density (ND) filter, which was positioned at a slight angle to prevent direct feedback to the diode, to reduce the intensity of the output beam prior to entering the ringdown cavity. The first reflection from the ND filter was used to align the wavemeter to continuously monitor the output wavelength. The portion of the beam passing through the ND filter then traversed through the optical isolator and was imaged into the ringdown cavity with a pair of focusing lenses. The ringdown cavity was comprised of two highly reflective mirrors, experimentally determined to be 99.91 % reflective. The 6 m radius of curvature plano-concave mirrors (Los Gatos Research, Inc.) were housed in Gimble mounts and spaced 122 cm apart. The laser light exiting the back-side of the ringdown cavity passed through another ND filter prior to encountering a photomultiplier tube (R928, Hamamatsu Corp.), which hosted a 10 nm bandpass filter (CVI-Melles Griot, LLC.) to reject emissions from the ICP and interference from the overhead fluorescent lights.

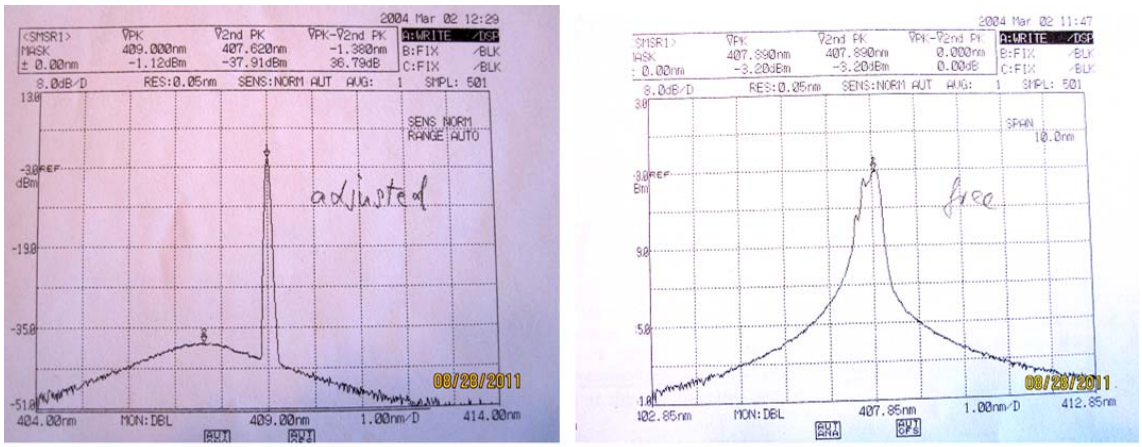

Figure 7.2 Blue diode laser output specifications.

The output wavelength was tunable from 406.810 to 409.490 nm by adjusting the current, temperature, and frequency. When the laser was running in free mode, multiple wavelengths were simultaneously emitted.

7.2.2 Detection Electronics

Multiple configurations for the detection electronics were explored to determine the set-up which resulted in the most stable ringdown signals as a product of mode hop free triggering. The internal HF modulator, which operated at 8 MHz, did not come equipped with a 50 Ω terminator, and the manual specified the insertion of an external terminal resistance. When a 50 Ω terminator was incorporated, the laser stability was unsatisfactory. Therefore, a T with a 50 Ω terminator on it was applied, but the signal did not improve. After many iterations and communications with the manufacturer, the most stable triggering mechanism was observed when the photomultiplier tube (PMT) was connected to a signal combiner (Mini-Circuits ZFRSC-2050) in an inverted orientation. Channel 1 of the combiner was connected to a digital oscilloscope (TDS 410A, Tektronix, Inc.), and channel 2 was connected to the 'Trigger' of a function generator (Stanford Research Systems, Inc.). Once the signal detected by the PMT exceeded the trigger level set on the function generator, a negative pulse was sent to the current control

of the diode laser to rapidly decrease the current below the operational threshold of the diode, thereby, effectively cutting off the laser intensity into the ringdown cavity. Experimental limitations imposed by this approach will be discussed in greater detail shortly.

7.2.3 Atomization Source and Sampling Device

A 1.6 kW, 27.12 MHz atmospheric pressure argon ICP (SEREN IPS I1600-27) was employed as the atomization source. In order to accommodate lower power and lower flow rates than typically explored with ICP's at the time of this study, a modified quartz torch was examined. The plasma was maintained in the upper quadrant of the torch and was cooled by 20 °C deionized water flowing through a 3-turn coil around this portion of the torch. A Neslab chiller was utilized for the cooling system. Typical ICP powers were 200 - 400 W in this study. The ICP was positioned on a homemade mount which allowed ± 0.5 mm adjustments in the lateral and vertical directions in order to optimize the laser/plasma interaction for uranium detection.

Uranium sample solutions were prepared from dilutions of the standard U solution (1000 µg/mL, Absolute Standards, Inc.). A peristaltic pump (Minipuls 3, Gilson, Inc.) was used to introduce the solutions to an ultrasonic nebulizer (U-5000 AT^{+}, CETAC Technologies, Inc.) and the resulting vapor was injected into the ICP. Typical flow rates of UHP Argon (99.999 % pure, Airgas, Inc.) were 15/ (0.1 – 0.25)/ (0.25 – 1.25) mL/min for the supporting, auxiliary, and sample gas flow rates, respectively, and the calculated conversion efficiency was > 10 %.

7.3 Results and Discussion

Measurements of different uranium transition lines and reactions involving uranium release using the CRDS technique have previously been reported.[63, 154] The laser source utilized in those studies was large, expensive, and labor intensive. Therefore, in order to develop a field-portable spectrometer implementing plasma-CRDS, a more compact, relatively inexpensive, and user-friendly light source must be incorporated. Toward this aim, a commercially available diode laser, operating at 409 nm, was studied to test the feasibility of employing a diode laser with plasma-CRDS for uranium detection. At the time this research was conducted, the majority of commercially available diode lasers only operated at visible to IR wavelengths and around a few select wavelengths near 400 nm. Elemental transitions are particularly intense in the UV. This research examined the spectral fingerprint of uranium in the wavelength region where diode lasers were available and found a clear overlap at 409.0135 nm and around 680 nm. A New Focus Vortex diode laser (TLB 6009) operating around 682.88 nm with a 70 GHz mode hop free tuning range was initially tested using Sr as a surrogate for uranium in an MIP. A broad SrOH signal was observed. Because background absorption induced by the MIP were reported in multiple studies, the ICP was implemented in the preliminary blue diode laser-plasma-CRDS studies in order to avoid background interference, which was not observed in the YAG-pumped dye laser studies of uranium with ICP-CRDS at 409 nm.

7.3.1 Diode Laser Parameters and Considerations

While examining feasibility methods to efficiently trigger the electronics to obtain clean ringdown signals for the wavelength of interest, the need for an in-depth characterization of the diode stability and the effect of applying the current modulation

arose. Table 7.1 portrays the relationship between the temperature, current, and output wavelength when no current modulation is applied. These values changed slightly on a day to day basis, depending on the room temperature of the lab. Observing the laser output stability over ~ 2 hours around 409.0139 nm with no current modulation, T = 16.5 °C, and I = 58 mA, the laser only drifted 0.0004 nm from the incident wavelength, as given in Table 7.2.

Once the experimental parameters to generate the appropriate wavelength were determined, the insulated current modulation BNC was connected to the diode laser head. Even with $\Delta I = 0$, the wavelength changed 0.0756 nm. Simply adjusting the current did not produce the wavelength of interest. Adding a current modulation, such that $\Delta I > 0$, resulted in mode-hops, exceeding the current threshold, and different wavelength output being observed on the wavemeter. Therefore, a separate set of values was generated to obtain 409.0135 nm output with the current modulation applied to the diode head. Because the voltage change always produced an increase in the current, special consideration was given to optimizing the temperature-current-scanning frequency combination to allow the ringdown event to be captured with minimal artificial interference from the laser.

Table 7.1 Output wavelength as a function of temperature and current

Temperature (°C)	I (mA)	Wavelength (nm)	
20.0	48	409.0409	
19.9	48	409.0371	
19.8	48	409.0358	
19.7	48	409.0328	
19.6	48	409.0314	
19.5	48	409.0297	
19.4	48	409.0289	
19.3	48	407.3885	*
19.5	48	409.0281	
19.3	48	409.0273	
19.2	48	409.0274	
19.1	48	407.4207	*
19.1	49	409.0263	
19.0	49	409.0258	
18.9	49	407.3857	*
18.9	50	409.0245	
18.8	50	409.0237	
18.6	50		*
18.6	51	409.022	
18.4	51		*
18.4	53	409.023	
18.2	53		*
18.2	54	409.024	
17.9	54	409.017	
17.8	55	409.0193	
17.7	56	409.0188	
16.6	60	409.0154	
16.4	60	409.0134	
16.1	60	409.0094	
16.0	60	409.0063	

* indicates mode-hop of the laser.

Table 7.2 Laser stability over two hours

409.0289			409.0139
407.3885	*		409.0139
409.0281			409.0142
409.0273			409.014
409.0274			409.0139
407.4207	*		409.0139
409.0263			409.0138
409.0258			409.0142
407.3857	*		409.0139
409.0245			409.014
409.0237			409.014
	*		409.014
409.022			409.014
	*		
409.023		Average:	409.0140
	*	St Dev:	1.21E-04
409.024		Stability:	2.97E-05
409.017			

In order to introduce a pulse of light into the ringdown cavity when employing a continuous wave (CW) diode laser, the beam must be physically, optically, or electronically removed from the cavity to allow the 'ringdown' event to occur. While physically chopping the beam does introduce a pulse, the entire beam is not instantaneously blocked as the rising edge of the blade crosses through the beam; this allows a portion of the beam to continue to enter the cavity after the detection electronics have been triggered. Other physical approaches have utilized a piezoelectric transducer (PZT) attached to the back-side of the second ringdown mirror to physically change the length of the ringdown cavity or vibrations induced from an external source, such as a pumping mechanism, to disturb the mirror alignment, thereby disrupting the cavity

buildup. Optical approaches employing acousto-optical modulators (A.O.M.s), in which the beam is rapidly diverted from the ringdown cavity once the trigger threshold is reached, have been demonstrated. However, electronically altering the laser parameters, such as the current or frequency sweep, to rapidly change the laser power or wavelength is a robust, cost-effective approach to generate reproducible laser pulses from a CW diode laser. While physical, optical, and electronic pulse generation have all been explored during the course of diode laser CRDS in this lab, an electronic approach was incorporated in these studies.

When electronically pulsing a CW laser, attention must focus on the specific attributes of the individual diode laser. For instance, the diodes used in the material presented in Chapter VIII and the author's M.S. thesis employed two different triggering configurations. This difference arose because the outputs of the frequency sweep, controlled by the temperature setting, and the current were independent with the external cavity tunable diode laser (ECDL), but their combined output was used to modulate the distributive feedback diode (DFB) laser. While the temperature, frequency sweep, and current of the Toptica blue diode laser employed in this research were independently controlled, the same triggering mechanisms utilized with the near infrared (NIR) ECDL and the 682 nm ECDL could not be used. Unlike the ECDL, the sign of the input signal from the pulse generator did not correspondingly change the direction of the current change, i.e., + 1 V and – 1 V applied to the current modulation always produced a + 10 mA change in the output current. Moreover, the current threshold with an applied modulation at 409 nm was 62 mA. In order to generate stable 409.0135 nm output with a current modulation applied to the diode, the optimum temperature and current settings were determined to be 23.8 °C and 56 mA, respectively, with a minimal scan frequency.

With the aforementioned parameters, applying a 1 V change to the current controller caused the current threshold value to be exceeded. The possibility of implementing the output beam produced with lower currents to align the ringdown cavity and trigger the detection electronics to yield a 10 mA higher current, thereby generating the desired current and, in turn, wavelength was explored. However, the signal stability was less than desirable, and the wavelength reproducibility was not exact.

As previously mentioned, the current, not temperature, is modified to rapidly and reproducibly change the wavelength and/or current in order to effectively 'pulse' the laser. This is mainly due to the large hysteresis of the temperature control electronics, which required ~ 30 minutes to 2 hours to stabilize, depending on the magnitude of the change as well as the room temperature stability. In order to test the long-term stability, an over-night scan was performed. As illustrated in Figure 7.3, the output stability fluctuated with the room temperature changes due to the building's central heat and air conditioning unit turning on/off as has been observed with other laser systems in this facility. Clearly, field portability would be limited unless a temperature-control chamber were constructed to enclose the diode head.

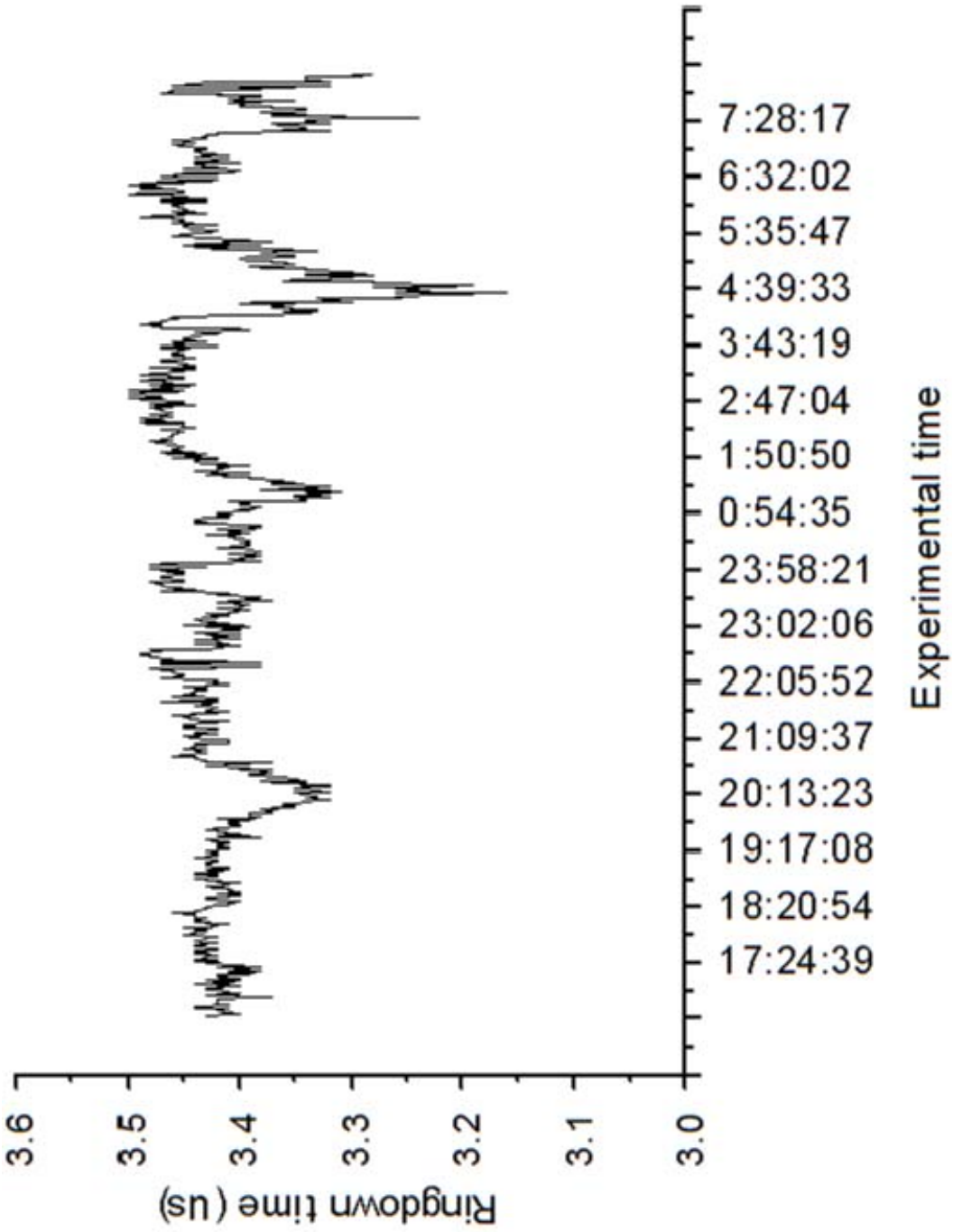

Figure 7.3 Overnight stability scan conducted with 409 nm blue diode laser.

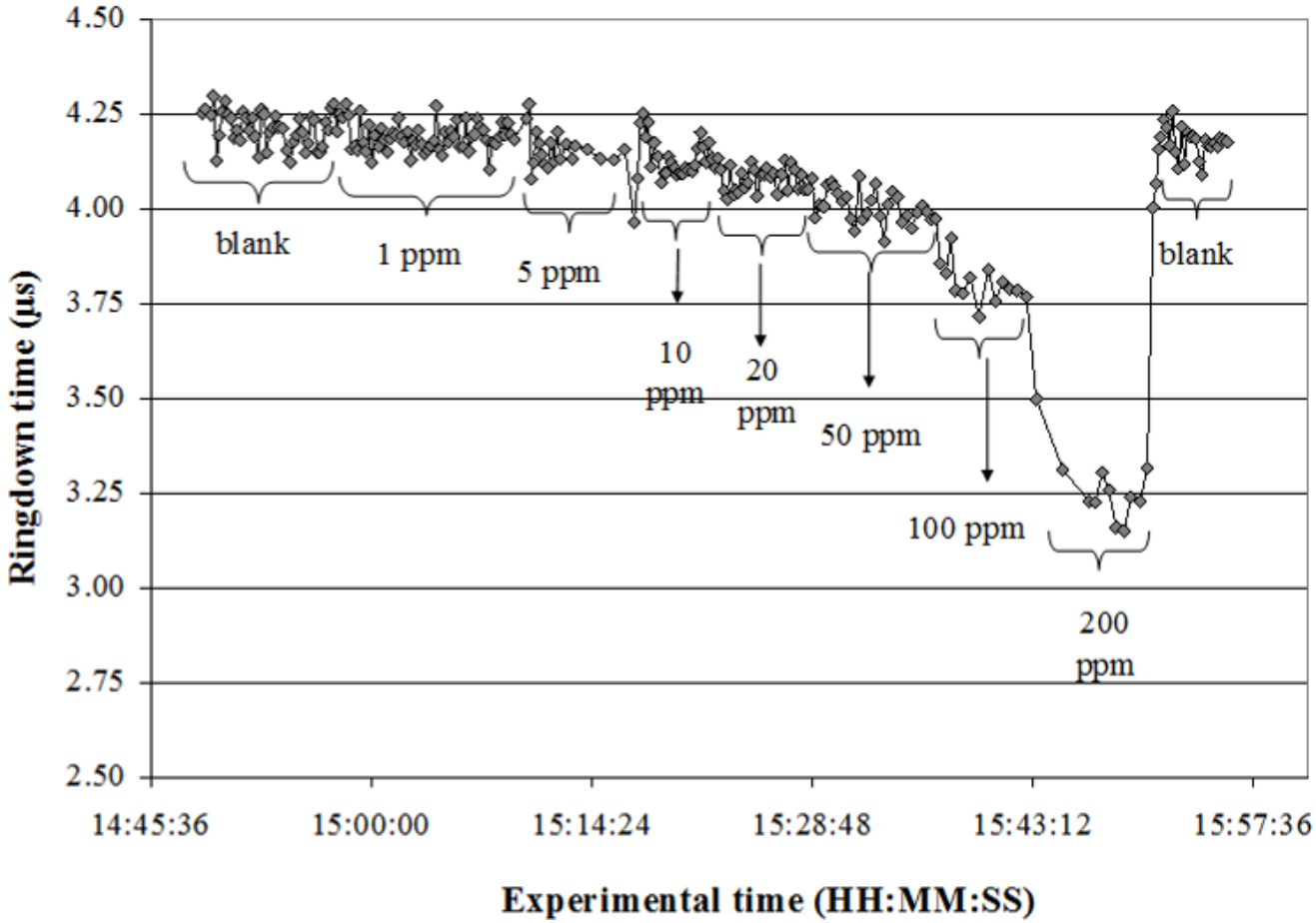

Figure 7.4 Change in ringdown time as a function of concentration of uranium introduced into the plasma using diode laser-ICP-CRDS.

The feasibility of detecting uranium using a UV diode laser in conjunction with ICP-CRDS is displayed. Sample solutions ranging from 1 to 200 ppm were examined.

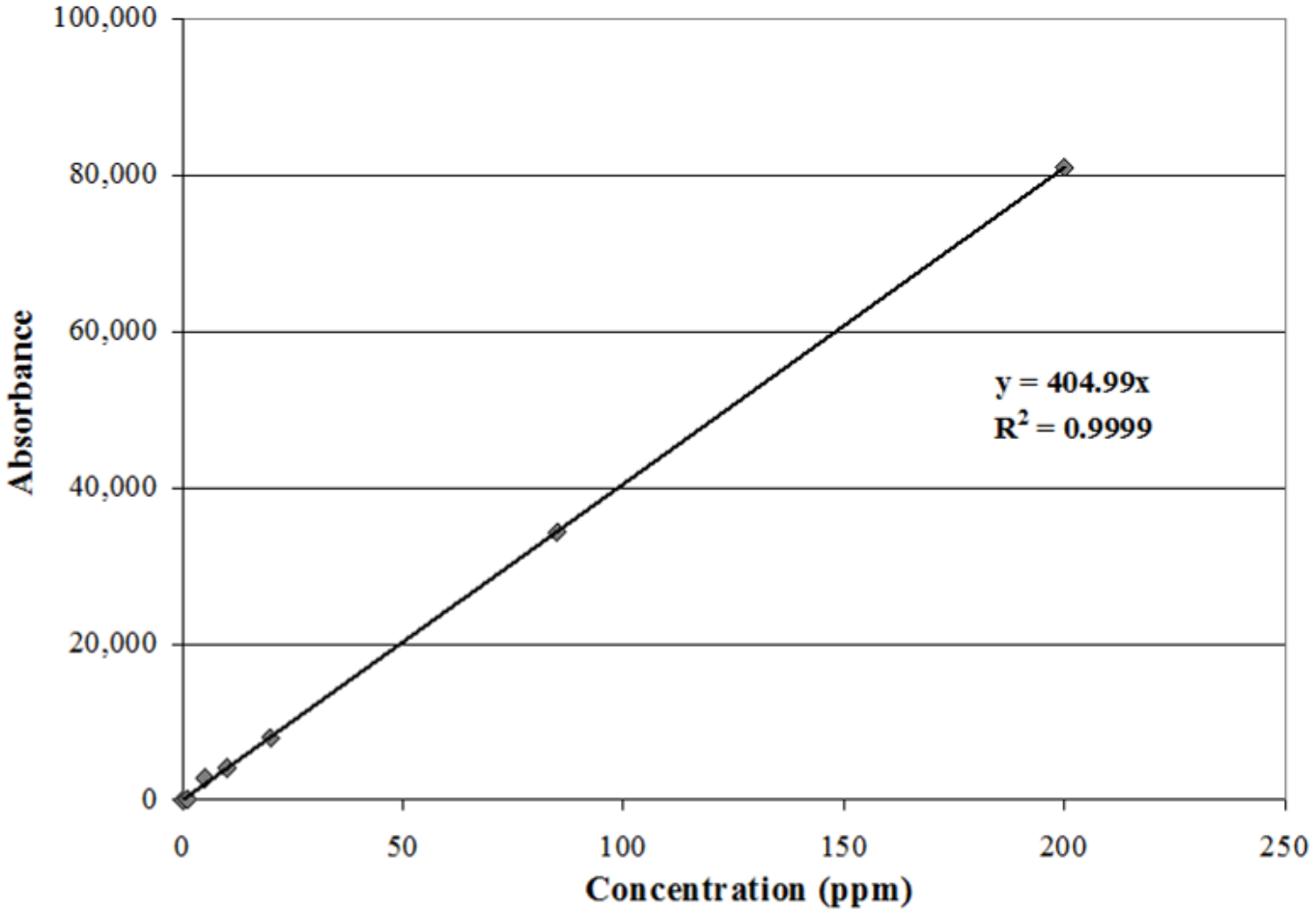

Figure 7.5 Preliminary calibration curve.

The feasibility of detecting uranium using diode laser-ICP-CRDS with a 250 W plasma is confirmed. Excellent linearity was observed for sample solutions ranging from 1 ppm to 200 ppm.

7.3.2 Diode Laser ICP-CRDS for Uranium Detection

Despite difficulties encountered with the triggering mechanism, single wavelength measurements of uranium were feasible; however, wavelength scans encompassing the uranium spectral transition profile were not possible utilizing the configuration shown in Figure 7.1. Once uranium was observed with the diode laser-ICP-CRDS, a quick calibration was conducted. As shown in Figure 7.4, a corresponding change in ringdown time was observed for different concentrations of uranium introduced into the ringdown cavity. When this data series was plotted in a calibration curve, as depicted in Figure 7.5, a very linear correlation (R^2 = 0.9999) was obtained. Each data point represented the average of 100 individual ringdown events. Based on this figure with 0.8 % baseline stability, the 3σ detection limit is 14.7 ppm for the input solution.

Once the ability to detect and measure uranium with this combined technique was proven, efforts turned to optimizing the system for enhanced uranium detection. It is well-known that atoms, ions, and radicals in a plasma are not homogeneously distributed throughout the entire plasma. Therefore, the position of the laser beam with respect to the plasma orientation is critical. The first parameter improved was the height of the laser beam above the surface of the plasma torch. Figure 7.6 illustrates the height dependence observed with a 250 W plasma and a 40 ppm uranium sample solution injected into the ringdown cavity. This plot displays the absorbance verses height of the laser in the plasma. Clearly, the vertical displacement distinctly affects the detection limits, and the optimized height was determined to be ~ 3.5 mm above the torch surface. The second parameter investigated was the lateral position. Lateral scans conducted with

100 ppm and 200 ppm uranium solutions in a 250 W plasma are shown in Figure 7.7. As evident in the figure, the position in which the largest absorption was observed was ~ 9 mm, the approximate center of the plasma. Once the vertical and lateral positions were optimized, a second calibration plot was generated. As can be inferred from Figure 7.8, the detection limit (2.4 ppm for the input solution) has improved by an order of magnitude by optimizing the position of the laser in the plasma.

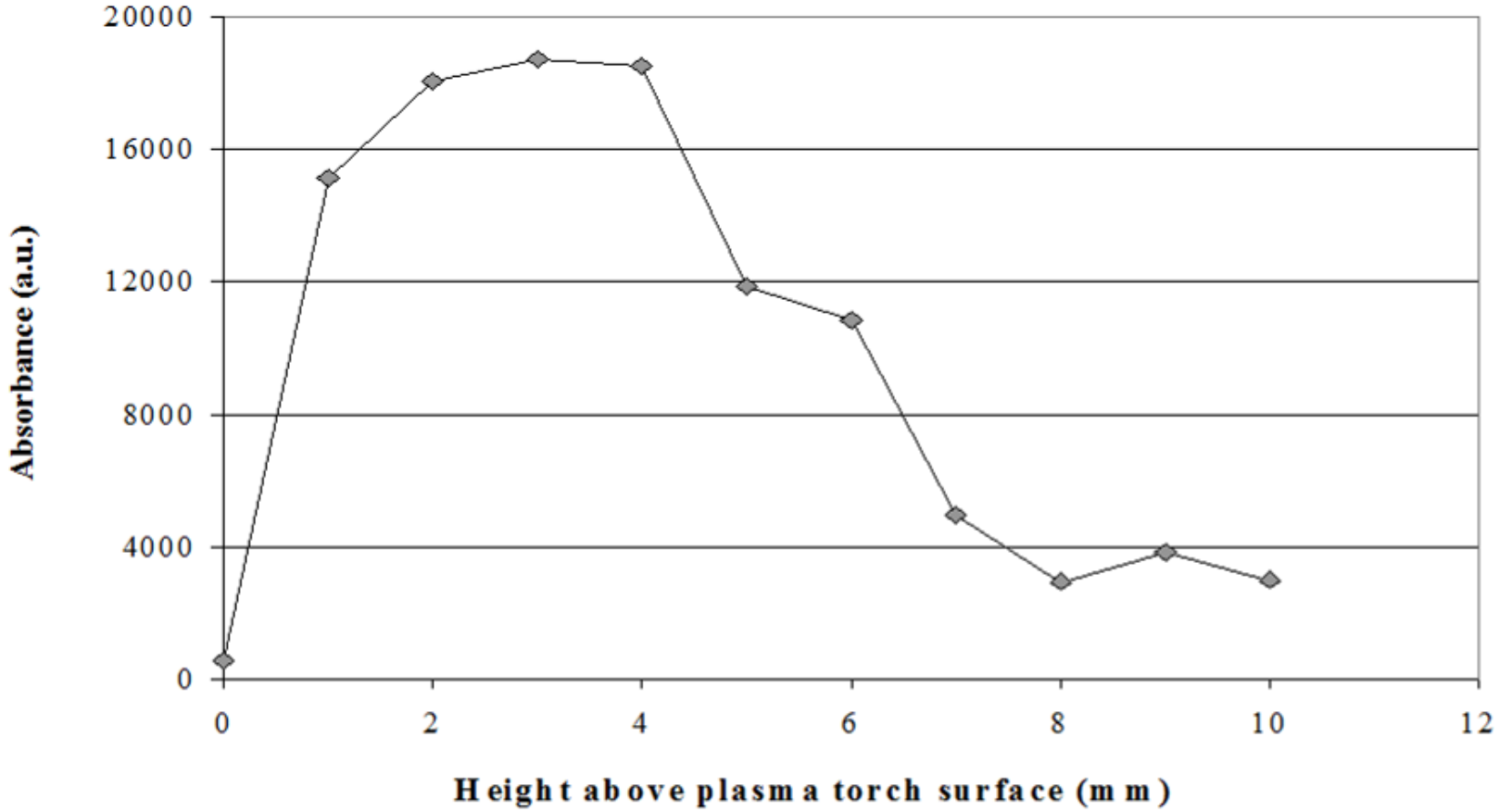

Figure 7.6 Change in absorbance as a function of the height of the laser above the plasma torch surface using diode laser-ICP-CRDS.

The ICP was operating at 250 W, and the flow rates were 15/0.1/1 mL/min for the outer, intermediate, and sample injection flows, respectively. A 40 ppm sample solution was utilized. The optimum height under the given plasma operating conditions is approximately 3 mm above the torch surface.

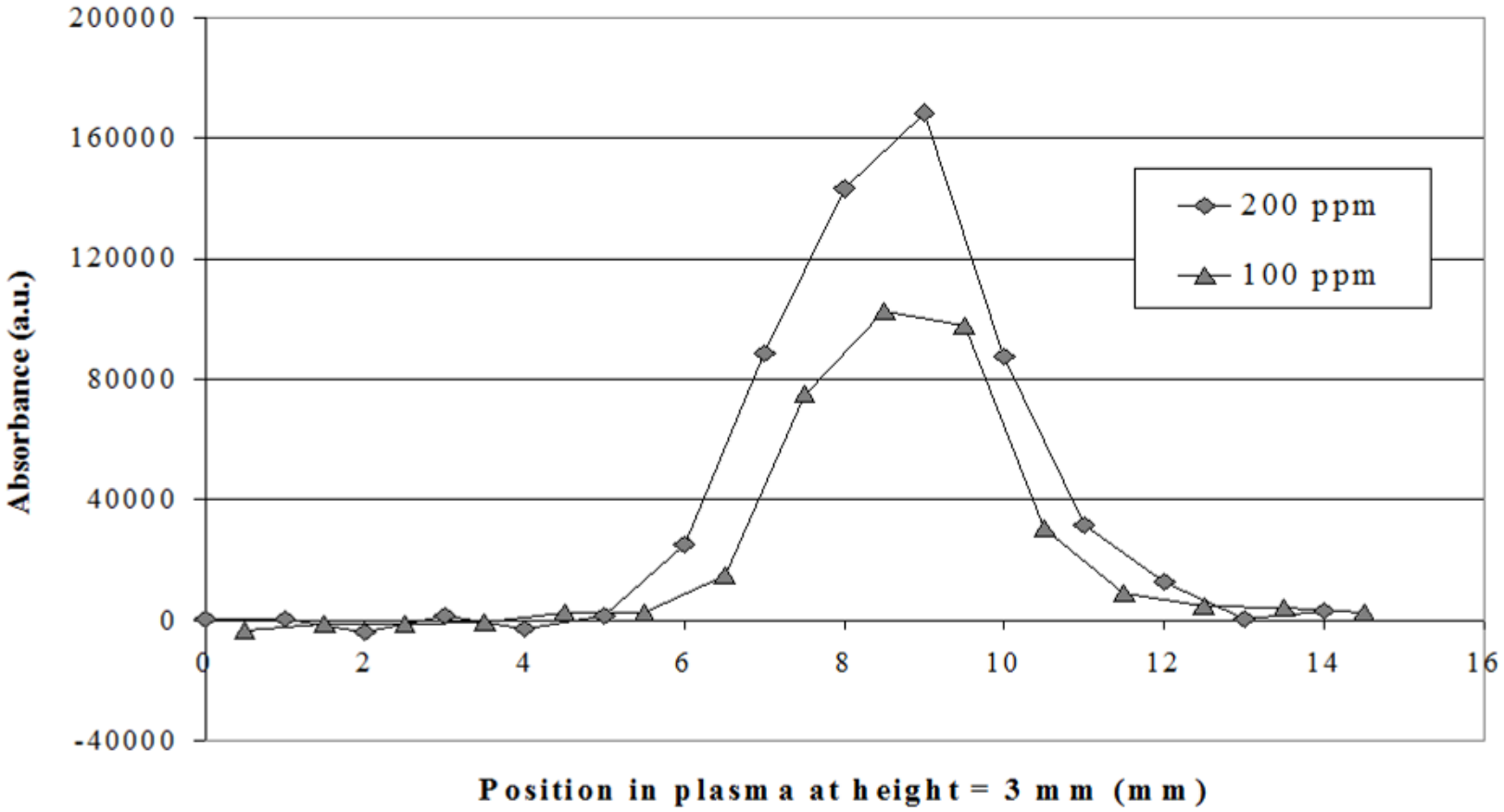

Figure 7.7 Absorption vs lateral position in the plasma at h = 3 mm.

With the laser beam approximately 3 mm above the torch surface, later scans across the plasma were conducted with 100 and 200 ppm U solutions. Reproducibility was observed. The starting position was shifted 0.5 mm in order to better observe the maximum position, which is determined to be approximately 8.5 mm. This value is located in approximately the center of the ICP.

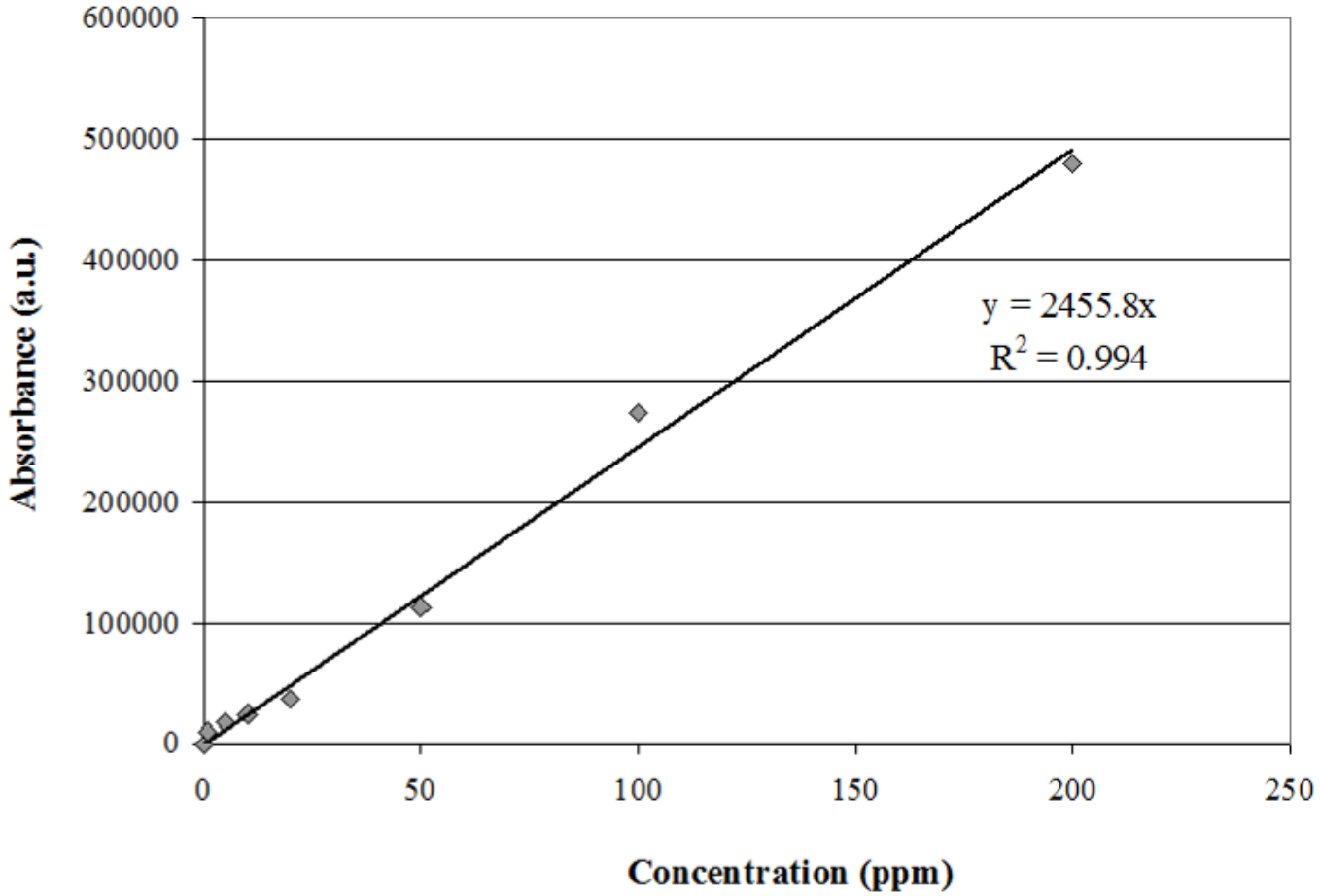

Figure 7.8 Calibration curve for uranium generated under optimized conditions with diode laser-ICP-CRDS.

Optimizing the plasma power and gas flow rates as well as the wavelength and position of the beam, laterally and vertically, produced an almost 6-fold enhancement in detection sensitivity.

7.3.3 ICP-CRDS vs LIF

In order to compare the detection sensitivities for ICP-CRDS and laser induced fluorescence (LIF) of uranium at 409 nm, LIF studies with the blue diode laser using the ICP as the atomization source were briefly explored. The experimental configuration utilized in these studies is shown in Figure 7.9. Multiple studies were conducted – with and without the diode present in the presence and absence of both the blank solution as well as the uranium solutions at multiple wavelength intervals on the 0.5 m Acton-SpectraPro spectrometer, which operated in ~ 20 nm increments. The monochromator was incorporated into the setup in order to simultaneously monitor the plasma for the presence of uranium. The laser parameters were set to reproduce the values used in the blue diode-ICP-CRDS studies. Unfortunately, the internal reference He/Ne of the Burleigh wavemeter expired. This prevented the system from accurately measuring the wavelengths of interest because the unit could not be internally calibrated. While the same parameters were employed, the exact wavelength of the diode could not be completely confirmed. The beam was directed through the spectrometer, and the readout indicated that the wavelength was 407.414 nm. However, it was not determined if this was the peak of the broad laser output with the specific laser parameters utilized or the optimized 409.0135 nm peak. Therefore, the ability to implement a blue diode for LIF measurements of uranium could not be completely ruled out.

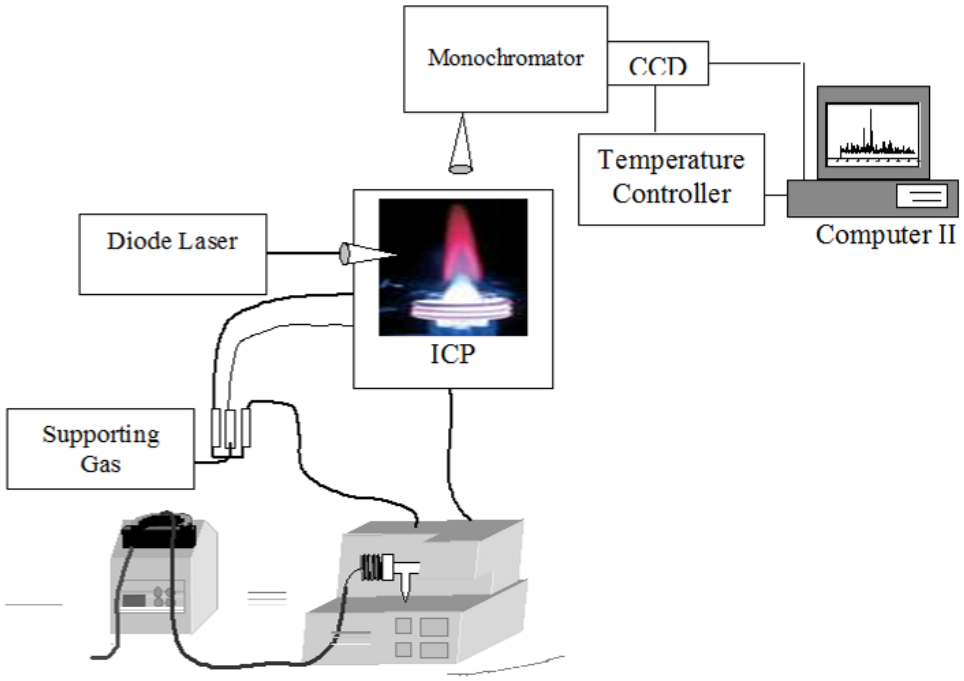

Figure 7.9 Experimental setup utilized in LIF-ICP analysis of U.

The liquid samples were pumped via a persistaltic pump to an ultrasonic nebulizer. The vapor sample was then carried to the plasma torch through a series of molecular sieves. The emission spectra were recorded on the monochromator and displayed on a PC.

In total, the feasibility of detection uranium using diode laser-ICP-CRDS was successfully explored. Difficulty maintaining wavelength stability after extended use as well as an inability to bypass the intrinsic voltage change induced by the triggering mechanism prevented further progress with this particular diode. As is evident from the research presented in this chapter, the potential to implement diode laser-ICP-CRDS for uranium measurements has been proven. Upon optimization of the plasma parameters, namely, plasma power and flow rates, and the position of the laser beam in the plasma, in terms of height and lateral position, uranium was successfully observed, demonstrating the feasibility of implementing a diode laser in conjunction with plasma-CRDS for uranium detection.

CHAPTER VIII

TRACE DETECTION OF VOLATILE ORGANIC COMPOUNDS

USING NIR-CRDS

8.1 Introduction

The research presented in this chapter is an extension of the experimental CRDS system developed for and presented in my master's thesis, A Novel Diode Laser Cavity Ringdown Spectroscopy System for Trace Volatile Organic Compound Detection (May 2002).[82] The primary objective of that work was to construct a ringdown system, utilizing NIR-diode lasers (DL), to demonstrate the feasibility of using DL-CRDS to accurately and reproducibly detect and measure trace concentrations of specific VOCs. Utilizing the ringdown system designed for the proof-of-concept exploration, absolute absorption cross-sections were determined for three aromatic VOCs at select wavelengths, and the performance of the system was evaluated while employing two types of diode lasers in the experimental CRDS system. Inferences pertaining to the factors affecting the sensitivity and detection limits as a function of wavelength as well as peak position of the aromatic VOCs' NIR absorption spectra, relative to benzene, were made.

In the research presented in this chapter, absorption cross-sections of the C-H stretching overtones of benzene, chlorobenzene, 1,2-dichlorobenzene, toluene, and acetone in the NIR (5970 to 6135 cm^{-1}) spectral region have been measured using CW-CRDS. The wavelength-dependent absorption cross-sections were obtained with the

Newport, Inc. External Cavity Tunable Diode Laser (ECDL) utilized in the proof-of-concept work. Low-pressure samples (0.001 to 2.0 Torr) were introduced into an evacuated cavity. The experimental, room temperature, absorption cross-sections obtained for these five volatile organic compounds (VOCs) were found to vary in intensity from approximately 1.2 x 10^{-22} to 6.9 x 10^{-21} cm^{-1} as a function of wavelength and molecular structure. Due to the presence of electron-withdrawing or electron-donating substituents on the benzene ring, spectral shifts in the absorption spectra, relative to benzene, were observed for the aromatic VOCs.

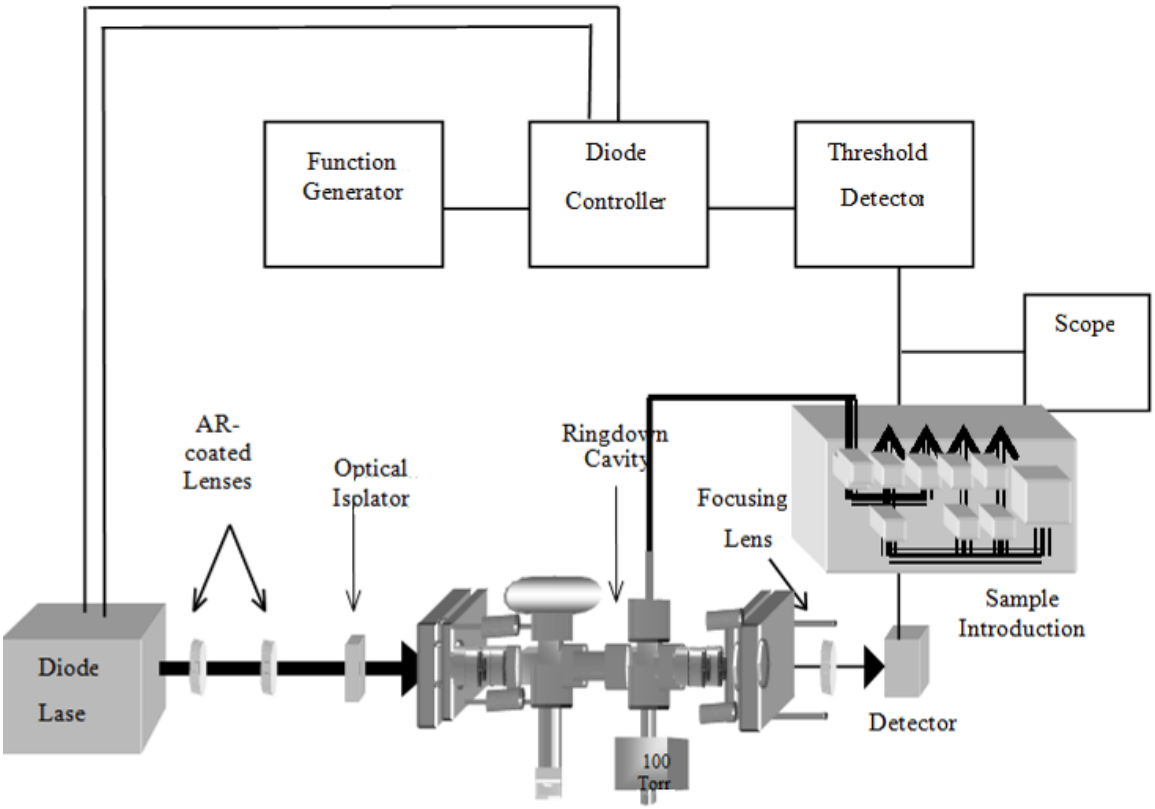

Figure 8.1 Experimental configuration used in conjunction with the external cavity tunable diode laser (ECDL) for VOC studies.

8.2 Experimental Setup

A detailed explanation of the experimental configuration and optical parameters utilized in this research is given in the aforementioned M.S. thesis.[82] The system described in that document incorporating the ECDL was used in this research without further modification. Therefore, the experimental and optical set-ups will be briefly described, with emphasis being placed on the novelty of the triggering mechanism. The major components of the experimental configuration, shown in Figure 8.1, include the laser source, the ringdown cavity and additional optical components, the triggering mechanism and corresponding detection electronics, and sample introduction. Laser light from the CW diode laser was mode-matched to the cavity's TEM_{00} modes, which resulted in an intensity build-up in the optical cavity corresponding to the excitation of a single type of cavity mode. Once sufficient build-up occurred, the threshold electronics were triggered, and the ringdown waveforms associated with these modes were recorded using the digital oscilloscope. The ringdown waveforms were transferred to a computer via a GPIB interface using "in-house" Lab Windows/CVI software.

8.2.1 Optical Considerations

This research utilized the output of an external cavity tunable diode laser (ECDL) (Newport Model 2010 A). The ECDL was designed to achieve tunable single-mode operation over a wide range of wavelengths. A typical operating range for the ECDL at 100 mA was 1595 - 1690 nm, and the linewidth was < 1 MHz. The ECDL utilized a Littman/Metcalf configuration to ensure wavelength adjustment with a minimum occurrence of mode hops. In order to minimize mode hops due to interference from the back-reflection of the laser from the first ringdown mirror, an optical isolator was positioned between the laser diode and the ringdown cavity. The optical isolator was a

Faraday rotator, which caused the back-reflection off the first high reflectivity mirror to be rotated 180° from the input beam, thus, eliminating feedback to the diode. The working range of the optical isolator was 1520 - 1660 nm. The 56.2 cm ringdown cavity, which was incorporated into the sample chamber for the room temperature vapor phase studies, consisted of two 1 m radius Newport ultra high reflectivity mirrors, which were manufactured for > 99.99 % reflectance over the wavelength range 1457 - 1659 nm. In order to accurately align the optical cavity, the high reflectivity mirrors were mounted in Newport model 600A-3 precision optical mounts, which offered micrometer adjustment capability. Once the optical cavity alignment had been optimized, the narrow linewidth laser was used to preferentially excite one type of cavity mode in order to produce very stable, reproducible baseline signals. For example, the longitudinal mode spacing of a 56.2 cm cavity is 267 MHz (0.0089 cm^{-1}) and the linewidth of the ECDL was < 1 MHz; therefore, by precisely mode-matching the input beam to the cavity's TEM_{00} modes and preferentially exciting these modes, extremely stable baseline measurements were readily obtained. Utilizing the output of the ECDL mode-matched to the TEM_{00} modes, single shot baseline stabilities were on the order of 0.20 %. Figure 8.2 depicts a typical baseline stability scan recorded when system is triggering only on the TEM_{00} mode.

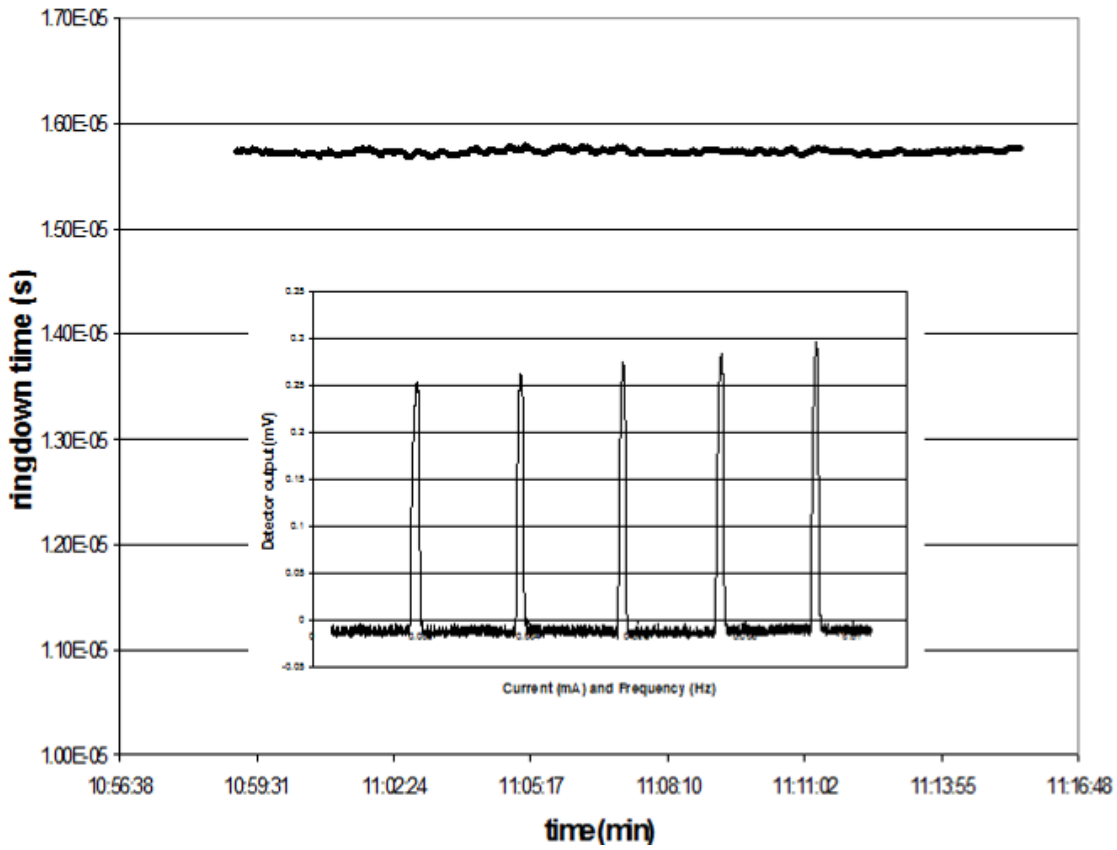

Figure 8.2 Baseline stability scan obtained for single-mode excitation.

This scan generates a 0.2 % stability. The inset is an example of the single-mode excitation.

8.2.2 Triggering Mechanism and Data Analysis

One critical aspect encountered when implementing continuous wave diode laser cavity ringdown spectroscopy (CW-CRDS) is the ability to rapidly block or divert the laser light from the ringdown cavity to allow the time constant of the decay to be detected and measured. In lieu of incorporating an acousto-optic modulator (AOM) to rapidly divert the beam from the optical cavity[155] or a signal combiner[82, 156] to modulate the frequency and current in unison to generate a rapid shut off of the laser as was employed with the DFB laser in the thesis, this approach incorporated a different type of frequency modulation. With the ECDL, the current and the frequency were independent of one

another. The current modulation was controlled by a Stanford Research System (SRS) delay/pulse generator, and the frequency modulation was controlled by a PZT transducer attached to the back-side of the tuning mirror in the laser cavity. A Hewlett Packard 15 MHz function/arbitrary waveform generator controlled the PZT modulation. The threshold level was set by the pulse generator, and the function generator supplied a 100 mV peak-to-peak (p-p) ramp at 100 Hz. The mode patterns and ringdown events were detected with a germanium photodiode detector, manufactured by Thorlabs, and the detector output was sent to the SRS delay/pulse generator and then displayed on a Tektronics TDS 430A digital oscilloscope. Once sufficient intensity build-up in the ringdown cavity had been achieved and the threshold trigger level was reached, the threshold electronics were triggered. The pulse generator rapidly decreased the current, while the function generator maintained the frequency; therefore, the intensity of the laser entering the ringdown cavity was significantly reduced, causing the laser to be effectively turned off. The waveform associated with the cavity mode excited was transferred from the oscilloscope via GPIB to a PC where the ringdown waveform was displayed and the ringdown time was calculated.

The ringdown waveforms were imported into a commercially available curve fitting program, SigmaPlot. Utilizing a three-parameter, single-decay exponential function: $y = y_0 + ae^{-\frac{x}{b}}$, the ringdown time was calculated. From this equation, the ringdown time is equivalent to b. Evaluation of the data using this more precise mathematical function than employed previously yielded remarkable accuracy and reproducibility. Each data point generated in this research was obtained from individual ringdown events; no averaging was employed prior to the data being imported into SigmaPlot. The ringdown time for each single-shot waveform was calculated and then

the ringdown times for each individual concentration at each individual wavelength were then used to generate a calibration curve for each sample species at every individual wavelength explored. At every wavelength studied, 8 – 10 individual waveforms were saved for both the baseline measurement as well as the measurements for various concentrations of sample introduced into the ringdown cavity. Once the average ringdown time for each concentration and its corresponding background was determined, a calibration curve was generated. From the calibration curve, the absorption cross-section for the sample species being explored at each wavelength could be readily determined.

8.2.3 Physical Parameters

The ringdown cavity was mounted on a stainless steel vacuum chamber that hosted two pressure gauges, a gas inlet, and a pump valve. For all of the research conducted after the proof-of-concept studies, one pressure gauge was an ion gauge, supplied by Kurt J. Lester, Co., which was used to ensure stable baseline pressures in the ringdown cavity before each sample was introduced, and the other was an MKS 0.1 Torr Baratron, which measured the pressure of the sample introduced into the ringdown cavity. The chamber was evacuated by a mechanical pump and a diffusion pump placed in series. In order to reduce the probability of pump oil contamination by the organics, a liquid nitrogen trap was placed between the pump valve and the pumps. The ringdown cavity was pumped down to 10^{-5} Torr for each baseline measurement prior to every individual measurement. An all-metal sample introduction system was constructed. The valve-tubing connections were welded together with Swagelok stainless steel welding joints. Vibrations induced from the mechanical and diffusion pumps as well as from the

operation of the pump valve were effectively dampened by inserting a flexible metal bellows tube between the vacuum chamber and the pumping scheme and by stabilizing the individual flanges with in-house fabricated mounts. Additionally, the cart housing the pumps was heavily weighted down to reduce vibrations after it was discovered that extra weight on the cart dampened the vibrations to a level which resulted in an extremely stable frequency-comb pattern on the oscilloscope.

8.2.4 Sample Introduction

In order to introduce relatively pure, vapor-phase VOCs into the ringdown cavity in a cost-effective manner, the freeze/thaw/pump technique was implemented. Approximately 5 mL of the liquid sample was placed in a 25 mL Schlenk tube, which was subsequently submerged in liquid nitrogen. When the organic was frozen, the headspace in the tube was evacuated to remove any impurities. The sample was then thawed, and the process was repeated for several cycles. Table 8.1 lists the suppliers and purity levels of the solvents prior to implementing the freeze/thaw/pump technique explored in this research. Upon the last thaw, the vapor phase sample was metered into the evacuated ringdown cavity where the pressure was directly measured and the corresponding ringdown event was recorded.

8.3 Results and Discussion

As previously mentioned and discussed in the thesis, the first overtone absorption spectra of the C-H asymmetric stretch of benzene and the benzene derivatives were investigated around ~ 6000 cm^{-1} (1667 nm). During the course of the thesis, the absorption cross-sections at three wavelengths on the absorption profile of these compounds around 1650 nm were determined. These were compared to the available

literature and were found to be in good agreement. Preliminary absorption scans of this asymmetric stretch were attempted; however, the ECDL experienced significant instability when operating in the wavelength scan mode. Therefore, to examine the difference between multiple VOC absorption spectra in this region with readily available, compact, room temperature diode lasers, much effort was put into determining the absorption cross-sections at various locations along the absorption profile, "filling in" the spectra of these three VOCs as well as incorporating 1,2-dichlorobenzene and acetone.

During the course of this research, the only available absorption cross-section data on the VOCs chosen for this study was benzene. The experimental peak wavelength obtained with the ECDL for benzene is ~ 1665 nm, and the absorption cross-section at this wavelength is 6.14×10^{-21} cm^2. When compared to the absorption cross-section at the peak of the absorption feature obtained by Reddy *et al*,[157] a relative ratio of 1.27 is calculated. These authors suggested that their data over-estimated the absorption cross-sections for this overtone by as much as a factor of 2 - 3 due to systematic errors. The data presented herein follows the same trend as theirs, suggesting their cross-sections are only over-estimated by roughly 25 %. As can be seen in Figure 8.3, the experimental and literature values correlated nicely.

Once the feasibility of mapping the absorption spectrum with this approach was confirmed, the procedure was implemented for chlorobenzene, 1,2-dichlorobenzene, toluene, and acetone. The individual spectra are depicted in Figures 8.4 - 8.7. The cavity ringdown spectroscopic technique provides sufficient sensitivity to readily measure absorption cross-sections as low as 1.1×10^{-22} cm^2. A compilation of the spectra, portrayed in Figure 8.4, illustrates the wavelength shifts observed for the chlorinated and methylated substituents. The main differences between the benzene and

chlorobenzene absorption spectra and, therefore, cross-section values, are due to the presence of the electron-withdrawing group, an effect discussed by Nakagaki and Hanayaki for chlorinated benzenes[158] and by Bassi *et al.*[159] for partially F-substituted benzenes. Using benzene as a standard compound, Nakagaki and Hanayaki have determined that chlorination of benzene induces a blue shift in the C-H stretching overtone spectra. The peak of the chlorobenzene absorption spectra occurs around 1659.5 nm (~ 6026 cm^{-1}), and the blue shift of the chlorobenzene spectra, relative to the first overtone of benzene, can also be clearly observed. In direct contrast to chlorobenzene, where a highly electron-withdrawing substituent is present and causes a blue shift from the "standard" benzene absorption spectrum, the absorption spectrum of the toluene overtones are red shifted, due to the presence of an electron-donating substituent. The peak of the toluene absorption spectra is found at slightly higher wavelengths, indicating a slight red shift in the absorption spectra of the first C-H overtone of toluene from that of benzene.

The research presented in this chapter was part of an on-going project to develop portable diode laser-CRDS systems for process gas monitoring, continuous emission monitoring of volatile organic species and atmospheric constituents, and biomedical applications. Detection limits for these compounds were determined to be in the 10's to 100's of ppb and are expected to improve by at least an order of magnitude with the implementation of higher reflectivity mirrors and mirrors specifically coated for this particular wavelength range.

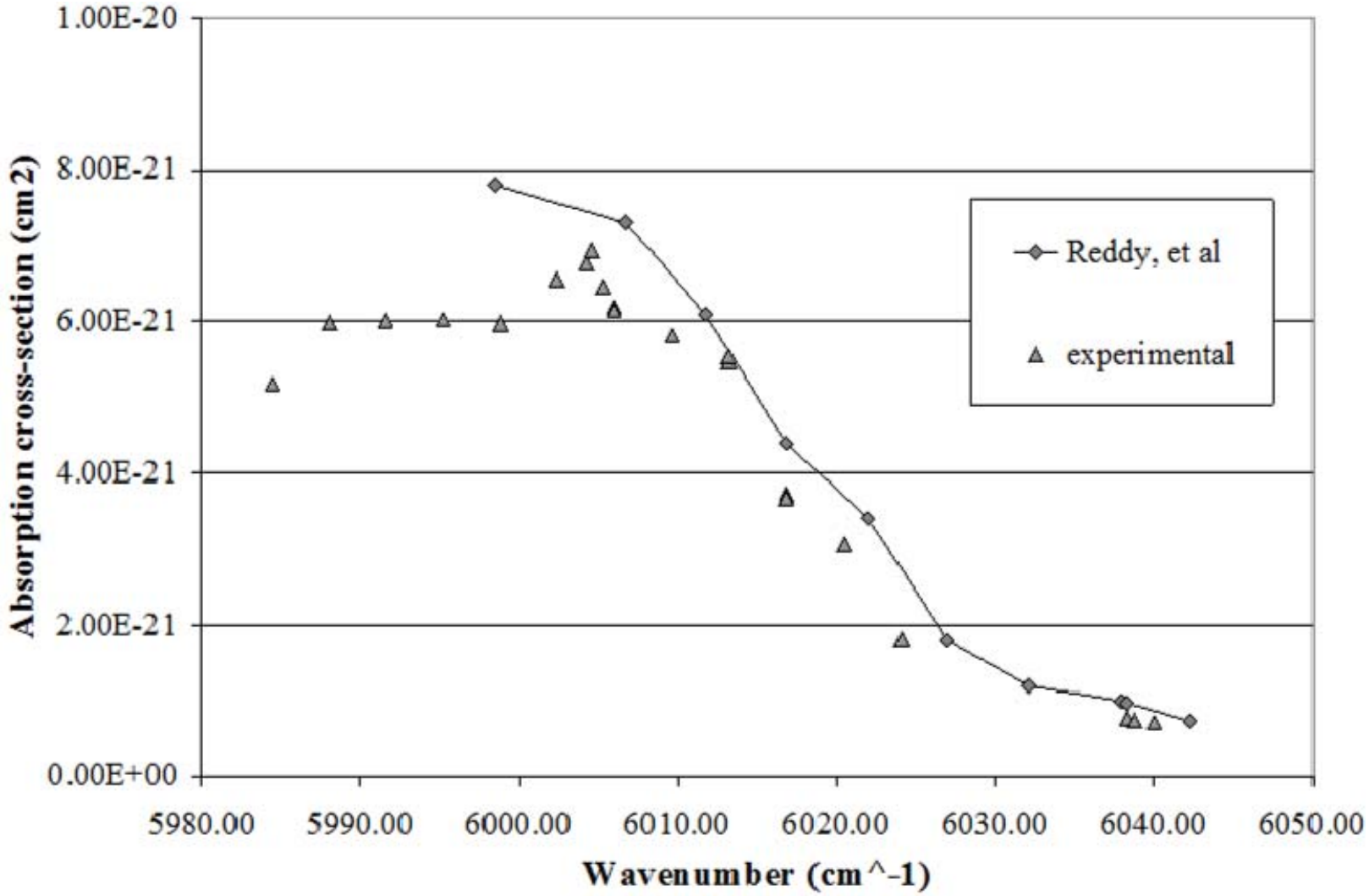

Figure 8.3 Comparison of experimental and literature absorption cross-sections for benzene.

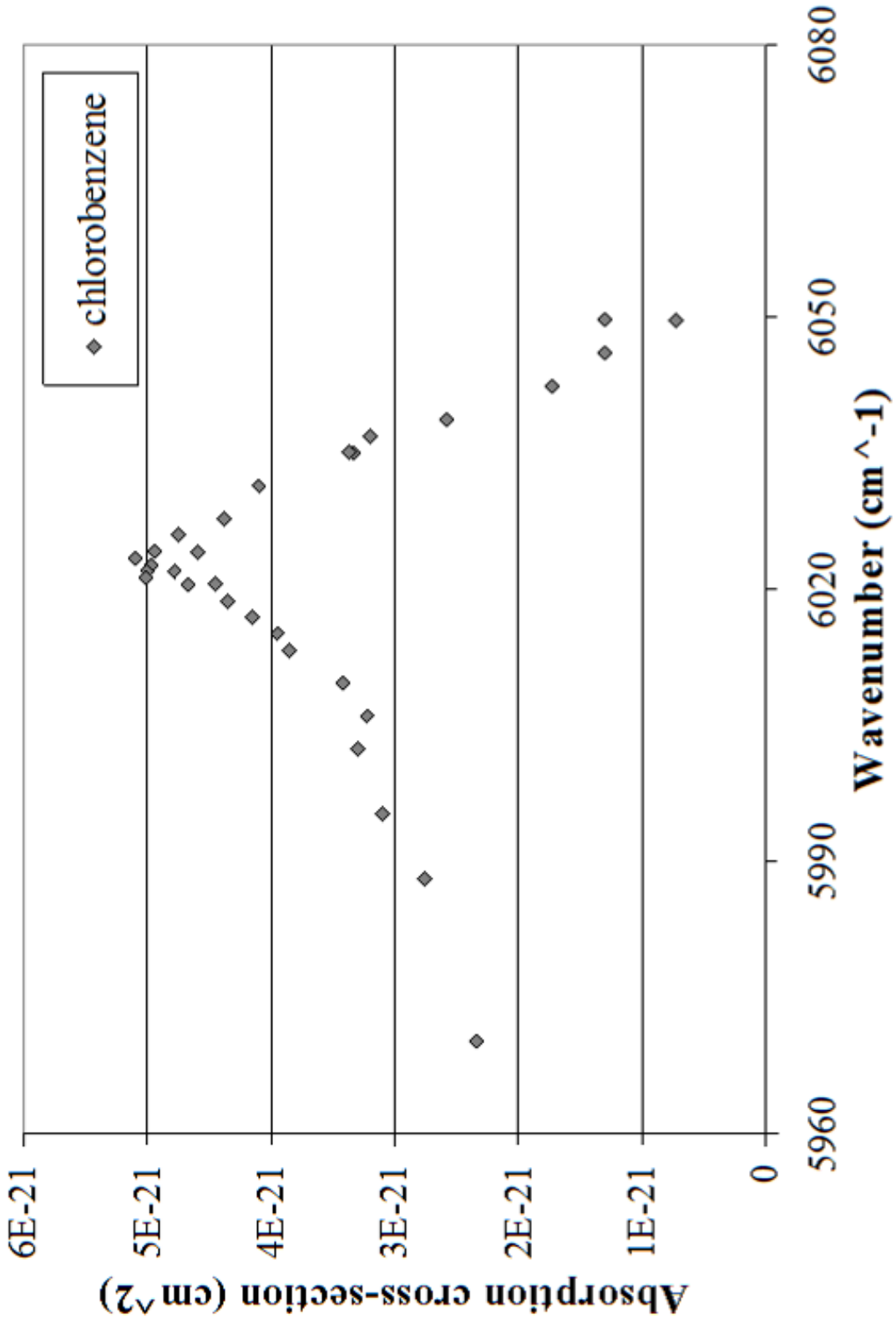

Figure 8.4 Experimental absorption cross-sections for chlorobenzene.

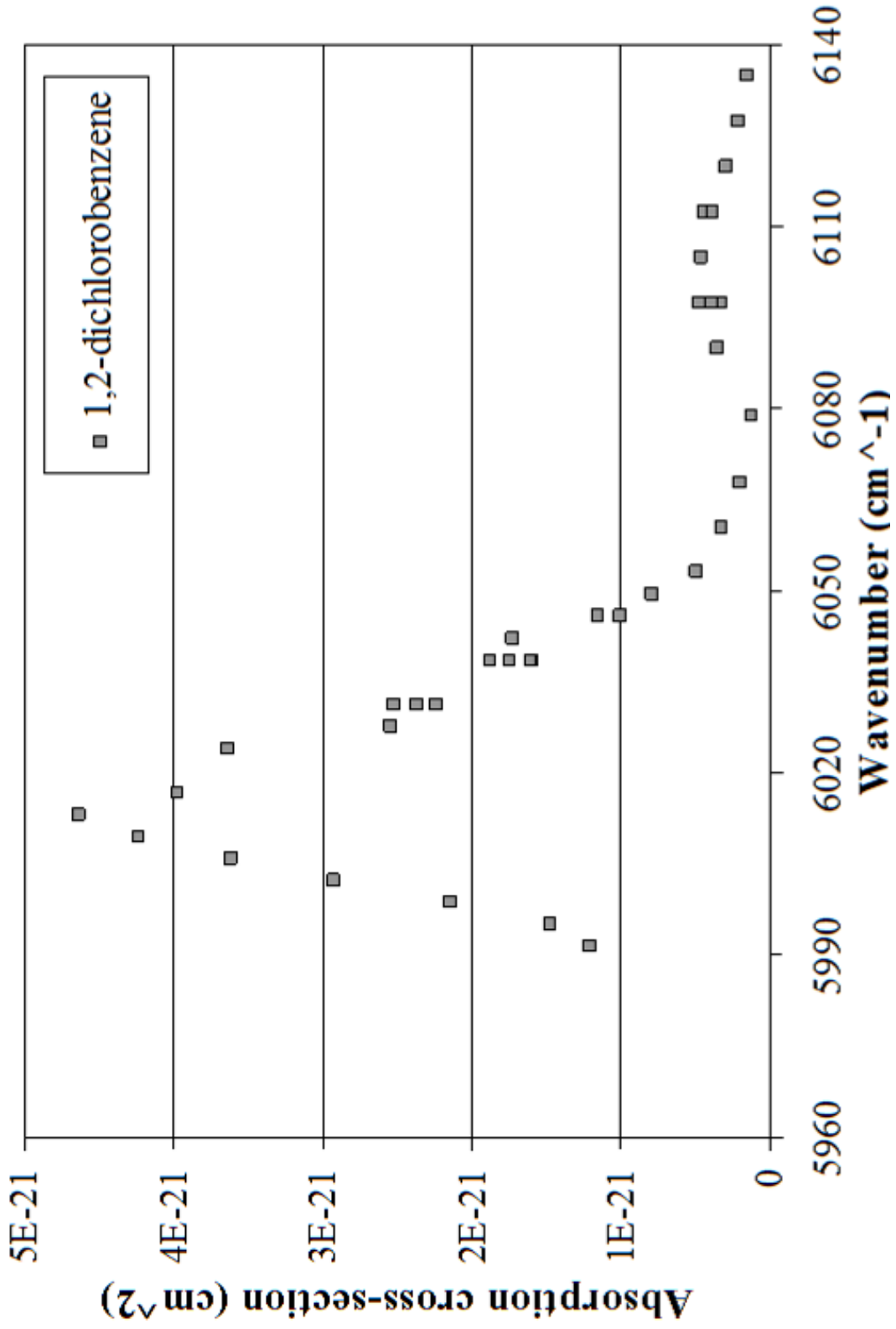

Figure 8.5 Experimental absorption cross-sections for 1,2-dichlorobenzene.

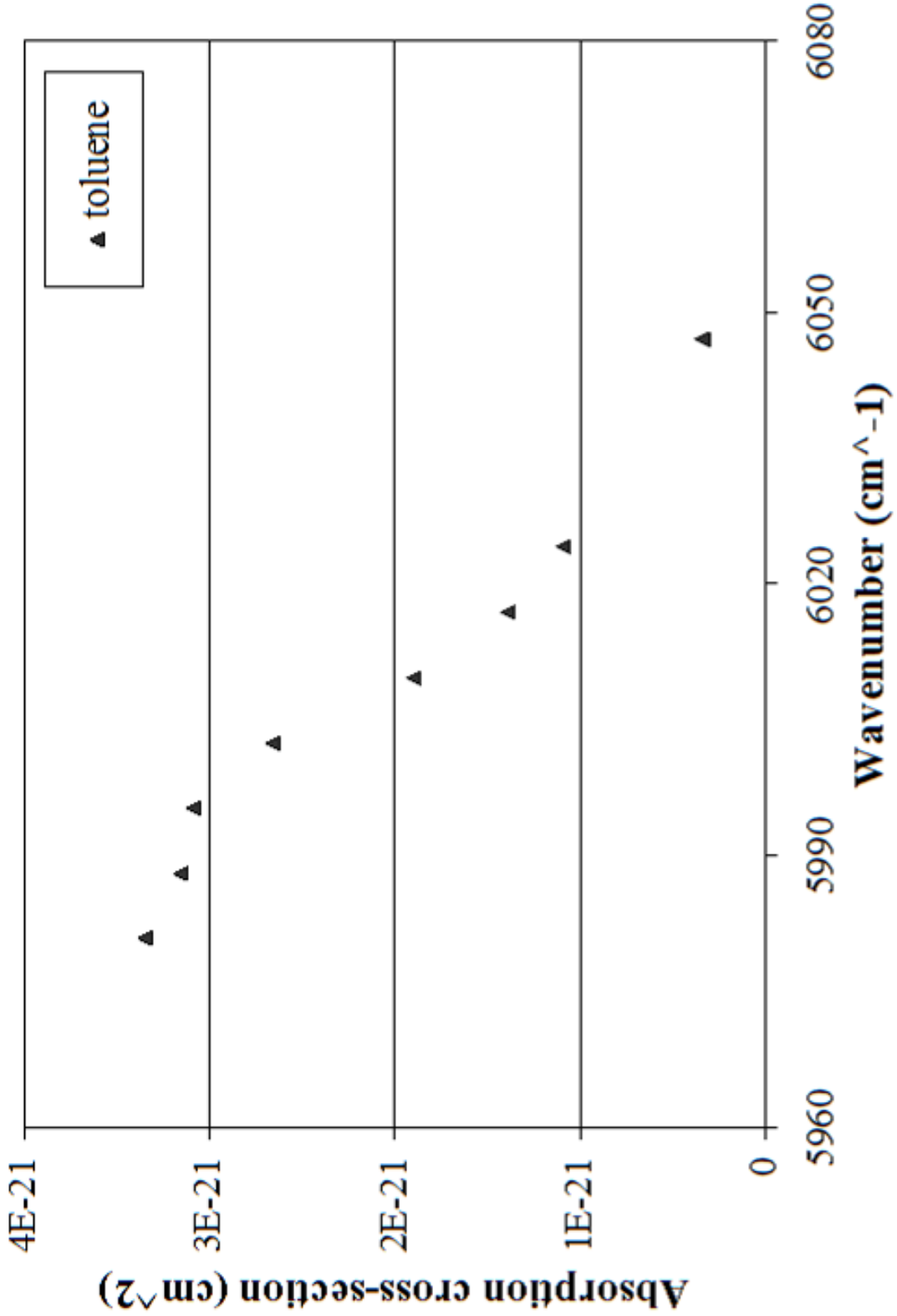

Figure 8.6 Experimental absorption cross-sections for toluene.

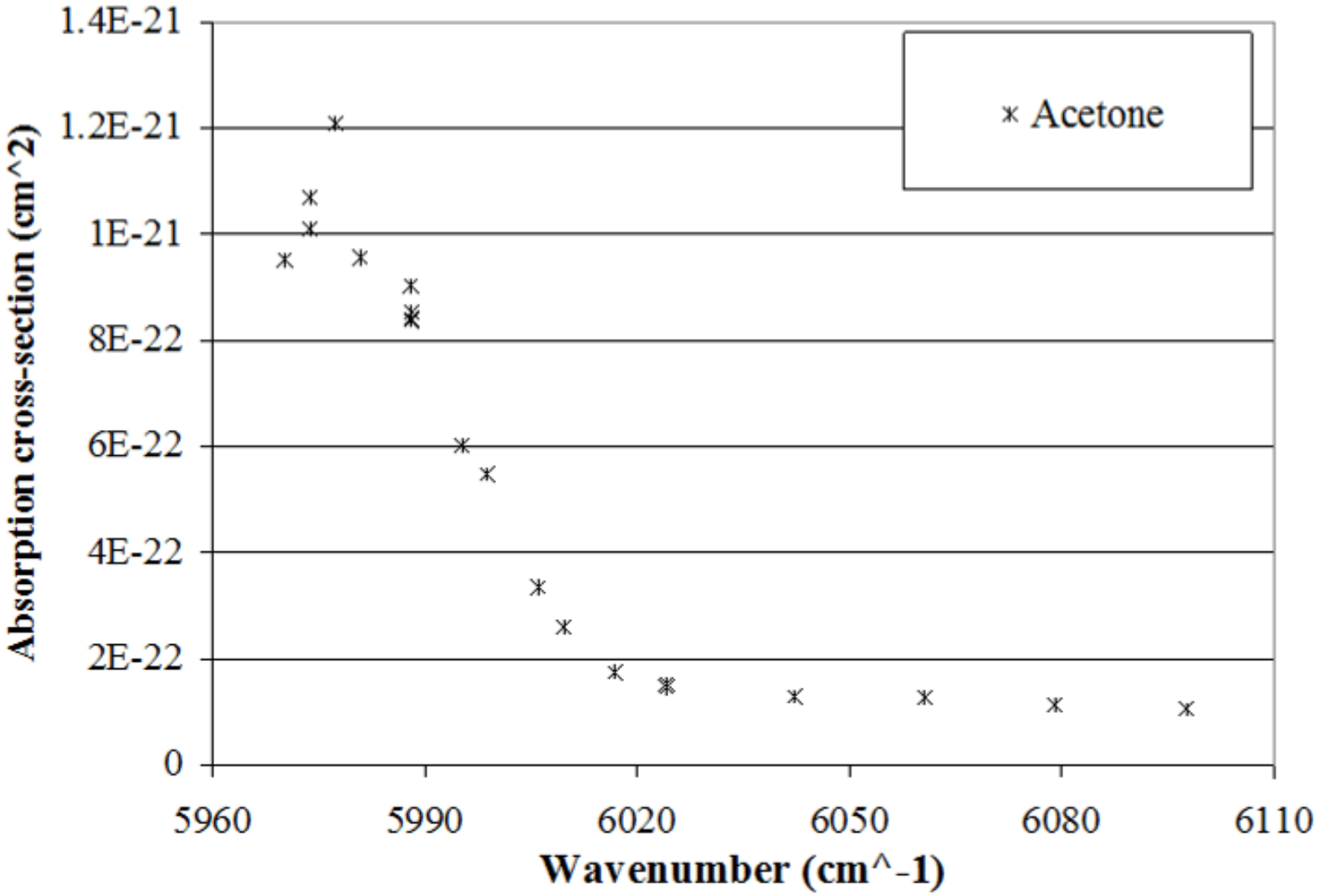

Figure 8.7 Experimental absorption cross-sections for acetone.

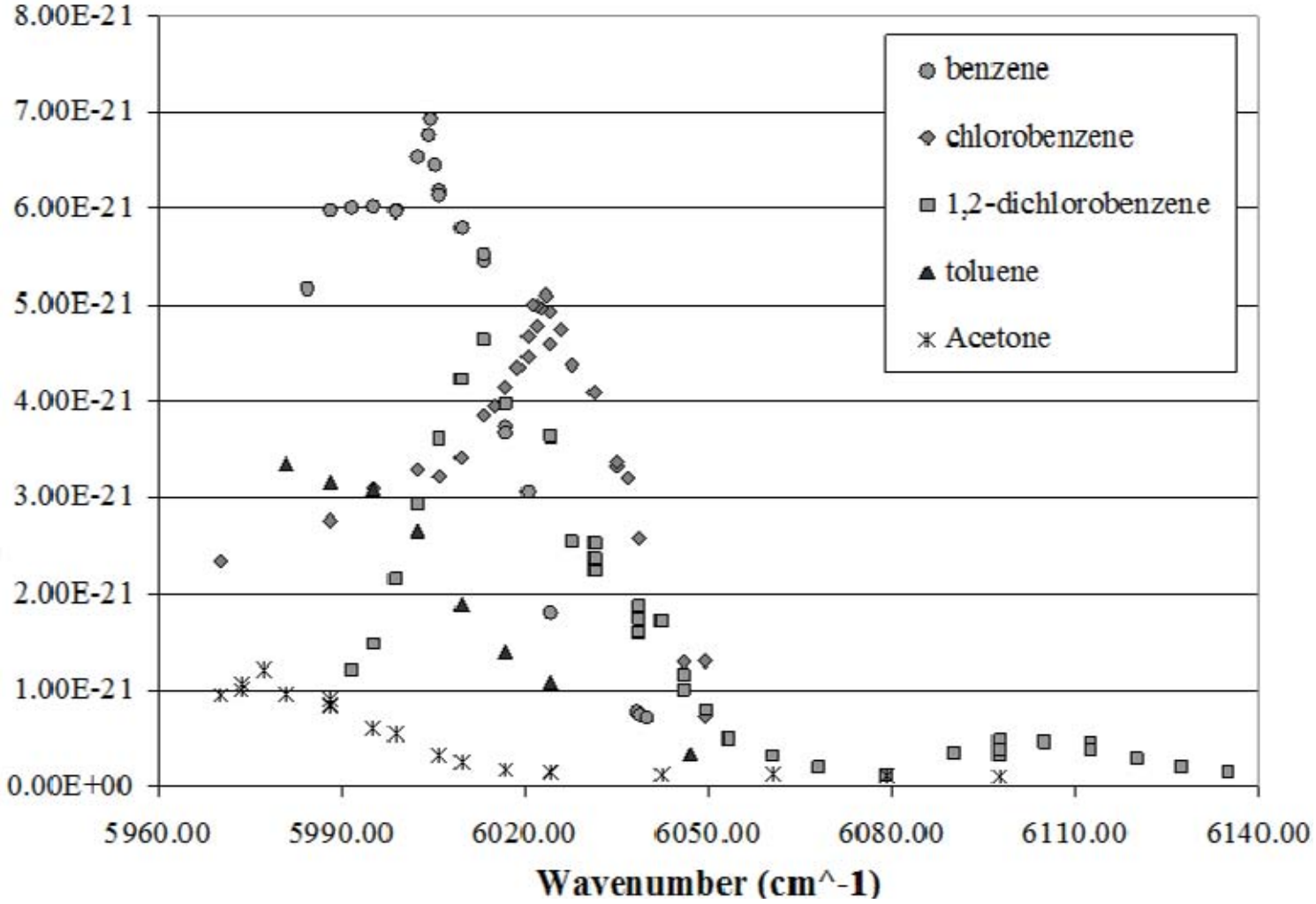

Figure 8.8 Compilation of the experimental absorption cross-sections for the VOCs studied in this research.

CHAPTER IX

SUMMARY AND DIRECTION OF FUTURE RESEARCH

9.1 Summary

9.1.1 Mercury

Mercury is a naturally occurring, environmental contaminant which is present in trace amounts in water, soil, and the atmosphere. Regardless of the chemical state, bound to inorganic or organic compounds or in its elemental state, mercury and mercury-containing compounds exhibit neurotoxic properties; therefore, mercury released into the environment has become a serious concern. Monitoring and remediation of mercury-contaminated sources requires an effective tool, which can provide on-site and real-time information regarding the presence and concentration of mercury. Toward that end, this research incorporated the highly sensitive cavity ringdown spectroscopic technique for the detection of Hg with the long-term goal of this project to develop a real-time, *in situ*, field-deployable plasma-CRDS spectrometer for measuring and monitoring trace environmental contaminants, such as mercury.

During the course of this research, the cavity ringdown technique has been applied to the measurement of elemental mercury in plasmas as well as ambient environments with high detection sensitivities. The first series of studies incorporated a candle-shaped MIP, which operated at low-temperature, low-powers, and low-flow rates. The experimental detection limit for this system is 221 ppt for the mercury vapor and 9 ppb for the input solution to generate that concentration with the given system. However,

very low detection limits were thwarted by the presence of an OH absorption peak generated by the plasma. In order to improve the detection limits and move towards a more compact atomization source, a copper surfatron microwave cavity with various plasma discharge tube configurations was incorporated into the ringdown system. The discharge tubes were individually examined for stability and capability to enhance Hg detection. Two tube configurations proved to generate acceptable Hg-MIP-CRDS data; and, using these configurations, the detection limits for the system improved by a factor of 10 as compared to the candle-shaped MIP. With these tube-shaped plasmas, the background OH peak was drastically reduced/eliminated and the Hg absorption peak at 253.6519 nm was readily obtained. With the minimum step rate of the laser system, low powers and low flow rates for the plasmas, which produced lower temperature plasmas, the fine structure of the 253.6519 nm mercury transition was observed.

The mercury research then tested the feasibility of directly detecting mercury naturally evaporating from contaminated soils and solutions using the CRDS technique. Solutions and soils which were contaminated with various concentrations of Hg were placed under the ringdown cavity, and Hg vapor was readily observed with the CRDS system. The results from this preliminary study have not only proven the feasibility of directly detecting Hg with no chemical treatment, no pre-concentration, no heating, etc., but improved on the detection limits. Experimental detection limits for this system, incorporating two different laser systems, was consistently 10's of ppt, and the estimated theoretical detection limit was 0.6 ppt. Additionally, the fine structure of the Hg 253.65 nm transition was observed with this approach. The capability of Hg isotopic measurements with a field-portable analyzer would be greatly beneficial in mercury monitoring and control processes.

9.1.2 Uranium

In an effort to move towards a field-deployable plasma-CRDS spectrometer for real time, *in situ* measurements of uranium, the potential of effectively generating uranium atoms and ions with a low-power, low-flow rate microwave-induced plasma was evaluated. At the time of this research, uranium measurements obtained while utilizing a low power, compact MIP had not been heavily explored, and, of the literature values available, the uranium measurements were obtained while utilizing a high-power MIP. Therefore, the capability and efficiency of generating uranium atoms and ions with a low-power MIP source prior to evaluation with the combined plasma-CRDS approach for uranium detection had to be investigated.

Upon successful atomization of uranium from solutions, efforts turned to optimizing the plasma parameters in order to collect spectra. Uranium emission spectra covering 320 – 430 nm were obtained, labeled, and compared to the available literature values. The effects of power, flow rates, height of the collected spectra, and concentration of sample injected into the plasma were taken into consideration. Calibration curves were generated and the detection limits were determined to be ~0.4 ppm.

The next step towards designing a portable spectrometer involved re-examining the laser source previously used. In the early plasma-CRDS studies of uranium, a large Nd:YAG-pumped dye laser system was used. In order to drastically reduce the size and cost of the light source, the feasibility of measuring U incorporating diode laser-plasma-CRDS was explored. The preliminary studies clearly show the ability to detect U vapor in a plasma with the diode laser used as the light source. Experimental parameters, such

as laser position in the plasma, lateral and vertical, and triggering mechanisms were studied. Sub-ppm detection limits were obtained in the preliminary studies.

9.1.3 Volatile Organic Compounds

Real-time quantification of emission by-products, pollutants, atmospheric constituents, and reaction intermediates is an important aspect of many environmental efforts. Volatile organic compounds (VOC), a principal component in atmospheric reactions that form ozone and other photochemical oxidants, are prevalent in the Earth's atmosphere. In addition to increasing ozone in the troposphere, many VOCs are classified as hazardous air pollutants; and to varying degrees, almost all VOCs are toxic and/or carcinogenic. Due to the impact on tropospheric reactions induced by the presence of VOCs, as well as the more recent correlations between human health diagnostics and the observed concentration of specific VOCs, sensitive, real-time detection of VOCs would serve as a valuable research tool for a wide range of applications, such as atmospheric and combustion studies, as well as medical diagnostics. Toward that aim, a continuous wave cavity ringdown spectroscopy system (CW-CRDS) was constructed, and the overall sensitivity of this system was evaluated by utilizing the absorption of the asymmetric C-H stretch overtones of several VOCs, including benzene, chlorobenzene, 1,2-dichlorobenzene, toluene, and acetone.

The energy necessary to excite the first overtone of benzene and its substituted derivatives is approximately 6000 cm^{-1} (or 1667 nm); and this region of the electromagnetic spectrum can be efficiently accessed with commercially available diode lasers, thus allowing the first vibrational C-H stretch overtone of many organic compounds to be examined with readily available, relatively low cost diode lasers. In the

research presented, absorption cross-sections of the C-H stretching overtones of benzene, chlorobenzene, 1,2-dichlorobenzene, toluene, and acetone in the NIR (5970 to 6135 cm^{-1}) spectral region have been measured using CW-CRDS. Detection limits for the molecules were all in the low ppb's.

9.2 Direction of Future Research

The results presented herein are very encouraging for a wide range of applications. The proof-of-concept explorations were very promising, and the in-depth analyses will provide the foundation for many research efforts to come. In order to generate a field-deployable, plasma-CRDS spectrometer, new plasma designs will not only be needed but will also have to be evaluated on a case-by-case basis. An additional step will be miniaturizing the existing systems and working towards more compact, portable units to be deployed in the field which still offer the desired sensitivities. In order to successfully obtain that goal, different atomization sources, lasers, optics, and detection electronics will need to be evaluated and optimized for each element and molecule to be studied.

REFERENCES CITED

[1] O'Keefe, A.; Deacon, D. A. G. *Rev. Sci. Instrum*. 1988, *59*, 2544.

[2] Pipino, A. C. R.; Hudgens, J. W.; Hule, R. E. *Rev. Sci. Instrum*. 1997, *68*, 2978.

[3] Brown, R. S.; Kozin, L.; Tong, Z.; Oleschuk, R. D.; Loock, H.-P. *J. Chem. Phys*. 2002, *117*, 10444.

[4] Wang, C.; Scherrer, S. T.; Hossain, D. *Appl. Spectrosc*. 2004, *58*, 784.

[5] Wang, C.; Koirala, S. P.; Scherrer, S. T.; Duan, Y.; Winstead, C. B. *Rev. Sci. Instrum*. 2004, *75*, 1305.

[6] Berden, G.; Peeters, R.; Meijer, G. *Int. Rev. Phys.Chem.* 2000 *19*(4), 565.

[7] Kiwanuka, S. S.; Clemens, T.; Kaminski, F. *Anal. Chem*. 2010 *82*(17), 7498.

[8] Hallock, A. J.; Berman, E. S. F.; Zare, R. N. *Appl. Spectrosc.* 2003 *57*(5), 571.

[9] Van der Sneppen, L.; Ariese, F.; Gooijer, C.; Ubachs, W. *Annu. Rev. Anal. Chem.* 2009 *2*(1), 13.

[10] Culbertson, B. J.; Foster, S. C. Cavity Ringdown Spectroscopy of Liquid Samples, SERMACS 2008.

[11] Busch, K. W.; Busch, M. A. (Eds.) ACS Symposium Series 720, Cavity-Ringdown Spectroscopy: An Ultratrace-Absorption Measurement Technique, Oxford University Press, 1999.

[12] Wang, C.; Miller, G. P.; Winstead, C. B., in *Cavity Ringdown Laser Absorption Spectroscopy*, a chapter in *Encyclopedia of Analytical Chemistry: Instrumentation and Applications*, R. A. Meyers, (Ed.), John Wiley & Sons, Ltd., Chichester, UK, 2008.

[13] Berden, G.; Engeln, R. (Eds.) Cavity Ring-Down Spectroscopy: Techniques and Applications John Wiley & Sons, Ltd., West Sussex, United Kingdown, 2009.

[14] Crock, J. G. 'Mercury', in Sparks, D. L.; Page, A. L.; Helmke, P. A.; Loeppert, R. H. (Eds) *Methods of Soil Analysis, Part 3: Chemical Methods, Soil Science of America*, Soil Sci. Soc. Amer. Book Series. 1996 *5*, 769.

[15] US Environmental Protection Agency, http://www.epa.gov/mercury/about.htm, accessed 10/13/11.

[16] Office of Research Facilities, http://orf.od.nih.gov/Environmental+Protection/Mercury+Free/MercuryHealthHazards.htm, accessed 10/13/11.

[17] US Geological Survey, http://www.usgs.gov/themes/factsheet/146-00/, accessed 10/13/11.

[18] Agency for Toxic Substances and Disease Registry, Accessed 10/20/11. http://www.atsdr.cdc.gov/toxfaqs/TF.asp?id=113&tid=24 .

[19] Natural Resources Defense Council, http://www.nrdc.org/health/effects/mercury/effects.asp, accessed 10/13/11.

[20] Buchanchenko, A. L. *Russian Chem. Rev.* 2009 *78*(4), 319.

[21] Adriano, D. C. *Trace Elements in Terrestrial Environments, 2nd Edition*, Springer: New York, 2001.

[22] Occupational Safety and Health Administration, www.osha.gov/SLTC/healthguidelines/mercuryvapor/recognition/html .

[23] National Institute for Occupational Safety and Health, www.cdc.gov/niosh/pel88/7439-79.html .

[24] Fairman; Hinds, M. W.; Nelms, S. M.; Penny, D. M.; Goodall, P. *J. Anal. At. Spectrom*. 2001 *16*, 1446.

[25] Mercader-Trejo, F.; de San Miguel, E. R.; de Gyves, J. *J. Anal. At. Spectrom*. 2005 *20*, 1212.

[26] Welz, B.; Schuber-Jacobs, M. *Fresenius' Z. Anal. Chem*. 1988 *33*, 324.

[27] Brown, R.; Gray, D. J.; Tye, D. *Water Air Soil Pollut*. 1995 *80*, 1237.

[28] Montaser, A. *Inductively Coupled Plasma Mass Spectrometry*, John Wiley & Sons, New York, NY, 1998.

[29] Szpunar, J. *Analyst* 2005, *130*, 442.

[30] Moldovan, M.; Krupp, E. M.; Holliday, A. E.; Donard, O. F. X. *J. Anal. At. Spectrom*. 2004 *19*, 815.

[31] Tanaka, H.; Kouuno, M.; Morita, H.; Okamoto, K.; Shimonura, S. *Anal. Sci*. 1992 *8*, 1047.

[32] Edner, H.; Sunesson, A.; Svanberg, S.; Uneus, L.; Wallin, S. *Appl. Opt*. 1986 *25*, 403.

[33] Platt, U.; Perner, D.; Patz, H. W. *J. Geophys. Res*. 1979 *84*, 6329.

[34] Edner, H.; Faris, G.; Sunesson, A.; Svanberg, S. *Appl. Opt*. 1989 *28*, 921.

[35] Alde´n, M.; Edner, H.; Svanberg, S. *Opt. Lett*. 1982 *7*, 221.

[36] Wang, C.; Scherrer, S. T.; Duan, Y.; Winstead, C. B. *J. Anal. At. Spectrom*. 2005 *20*, 638.

[37] Duan, Y.; Wang, C.; Scherrer, S. T.; Winstead, C. B. *Anal. Chem*. 2005 *77*(15), 4883.

[38] Tao, S.; Mazzotti, F. J.; Winstead, C. B.; Miller, G. P. *Analyst* 2000 *125*, 1021.

[39] Fain, X.; Moosmuller, H.; Obrist, D. *Atmos. Chem. Phys. Discuss*. 2009 *9*, 22143.

[40] Jongma, R. T.; Boogaarts, M. G. H.; Holleman, I.; Meijer G. *Rev. Sci. Instrum*. 1995 *66*(4), 2821.

[41] Spuler, S.; Linne, M.; Sappey, A.; Snyder, S. *Appl. Opt*. 2000 *39*(15), 2480.

[42] Wang, W.; Hammond, R. H.; Feijer, M. M.; Ahn, C. H.; Beasley, M. R.; Levenson, M. N.; Bortz, M. L. *Appl. Phys. Lett.* 1995 *67*, 1375.

[43] For example, CETAC Technologies, Inc., www.cetac.com/mercury_analyzers/ .

[44] Teledyne, www.teledyneleemanlabs.com/products/mercury/index.asp .

[45] Duan, Y.; Wang, C.; Winstead, C. B. *Anal. Chem*. 2003 *75*, 2105.

[46] Koirala, S. P., M.S. Thesis: Plasma cavity ringdown spectroscopy-A powerful technique for elemental measurements and plasma diagnostics, Department of Physics and Astronomy at Mississippi State University, December 2003.

[47] Wang, C.; Sahay, P,; Scherrer, S. T. *Phys. Lett. A* (Accepted, 2011).

[48] Uranium. *The Columbia Electronic Encyclopedia, Sixth Edition*. Accessed 10/22/11, http://www.answers.com/topic/uranium.

[49] C. R. Hammond (2000). *The Elements, in Handbook of Chemistry and Physics 81st Edition*. CRC Press. Boca Raton, FL, 2000.

[50] Miner, W. N.; Schonfeld, F. W. (1968). "Plutonium". Hampel, C. A. Ed. *The Encyclopedia of the Chemical Elements*. New York (NY): Reinhold Book Corp. pp. 540–546.

[51] Hoffman, D. C.; Lawrence, F. O.; Mewherter, J. L.; ROURKE, F. M. *Nature* 1971 *234*, 132.

[52] "Neptunium (revised)." Chemical Elements: From Carbon to Krypton. 2006. Accessed 10/26/11, http://www.encyclopedia.com/doc/1G2-3427000069.html.

[53] Cotton, F. A.; Wilkinson, G. *Advanced Organic Chemistry, 5th Edition*. John Wiley & Sons, Inc.: New York, 1988; Chapter 21.

[54] Goltz, D. M.; Gregoire, D. C.; Byrne, J. P.; Chakrabarti, C. L. *Specctrochim. Acta B* 1995 *50*, 803.

[55] Date, A. R.; Gray, A. A. Inductively Coupled Plasma Mass Spectrometry, Chapman & Hall, New York, NY, 1989.

[56] Goodall, P.S.; Johnson, S.G. *J. Anal. Atom. Spectrom*. 1996 *11*, 57.

[57] Vera, J.A.; Murray, G.M.; Weeks, S.J.; Edelson, M.C. *Spectrochim. Acta* 1991 *46B*, 1689.

[58] Smith, B. W.; Quentmeier, A.; Bolshov, M.; Niemax, K. *Spectrochim. Acta B* 1999 *54*, 943.

[59] Novovie, I.; Nikolic, V.; Markovic, D. M. *J. Anal. Chem*. 2007 *62*(9), 837.

[60] Winge, R. K.; Petterson, V. J.; Fassel, V. A. *Appl. Spectrosc*. 1979 *33*, 206.

[61] Boumans, P. W. J. M; Vrakking J. J. A. M. *Spectrochim. Acta B* 1987 *42*, 553.

[62] Miller, G. P.; Winstead, C. B. *J. Anal. At. Spectrom*. 1997 *12*, 907.

[63] Wang, C.; Mazzotti, F. J.; Miller, G. P.; Winstead, C. B. *Appl. Spectrosc*. 2003 *57*, 1167.

[64] Jin, X.; Duan, Y.; Olivares, J. A. *Spectrochim. Acta B* 1997 *52*, 131.

[65] Duan, Y.; Scherrer, S. T.; Koirala, S. P.; Wang, C.; Winstead, C. B. *Anal. Chim. Acta* 2005 *532*, 47.

[66] Nesdore, P. *Gases & Instrumentation* 2011 30.

[67] '*Tiger Optics Launches New Continuous Cleanroom Analyzer*,' in *Sensors* 2008.

[68] Wang, C.; Mbi, A. *Meas. Sci. Technol.* 2007 *18,* 2731.

[69] Todd, M. W.; Provencal, R. A.; Owano, T. G.; Paldus, B. A.; Kachanov, A.; Vodopyanov, L. L.; Hunter, M.; Coy, S. L.; Steinfeld, J. I.; Arnold, J. T. *Appl Phys. B* 2002 *75*, 367.

[70] Ramos, C.; Dagdigian, P. J. *Appl. Opt.* 2007 *46*(26), 6526.

[71] Pipino, A. C. R.; Silin, V. *Chem. Phys. Lett.* 2005 *404*(4), 361.

[72] Atkinson, D. B. *The Analyst* 2003 *128*, 117.

[73] Vasudev, R.; Usachev; A.; Dunsford, W. R. *Environ. Sci. Technol*. 1999 *33*(11), 1936.

[74] Brown, S. S. *Chem. Rev.* 2003 *103*(12), 5219.

[75] Hallock, A. J.; Berman, E. S. F.; and Zare, R. N. *Appl. Spectrosc*. 2003 *57*, 571.

[76] Persijn, S.; Harren, F.; van der Veen, A. *Appl. Phys. B* 2010 *100*, 383.

[77] Parkes, A. M.; Fawcett, B. L.; Austin, R. E.; Nakamichi, S.; Shallcross, D. E.; Orr-Ewing, A. J. *Analyst* 2003 *128*(Advanced Article).

[78] For example, Wang, C. *J. Anal. At. Spectro.* 2007 *22*, 1347.

[79] Peeters, R.; Berden, G.; Meijer, G. *Appl. Phys. B* 2001 *73*, 65.

[80] Bean, B. D.; Mollner, A. K.; Nizkorodov, S.; Okumura, M.; Sander, S. P.; Peterson, K. A.; Francisco, J. S. *J. Phys. Chem. A*. 2003 *107*, 6974.

[81] Robichaud, D. J.; Yeung, L. Y.; Long, D. A.; Okumura, M.; Havey, D. K.; Hodges, J. T.; Miller, C. E.; Brown, L. R. *J. Phys. Chem. A* 2009 *113*, 13089.

[82] Scherrer, S. T. M.S. Thesis: A novel diode laser cavity ringdown spectroscopy system for trace volatile organic compound detection, Department of Chemistry, Mississippi State University, May 2002.

[83] Tam, W. S.; Leonov, I.; Xu, Y. *Rev. Sci. Instrum.* 2006 *77*, 063117.

[84] http://www.picarro.com/gas_analyzers .

[85] Brumfield, B. R.; Stewart, J. T.; Widicus Weaver, S. L.; Escarra, M. D.; Howard, S. S.; Gmachl, C. F.; McCall, B.J. *Rev. Sci. Instrum.* 2010 *81*, 063103.

[86] Van der Sneppen; Wiskerke, A. E.; Ariese, F.; Gooijer, C.; Ubachs, W. *Anal. Chim. Acta* 2006 *558*, 2.

[87] Bechtel, K. L.; Zare, R. N.; Kachanov, A. A.; Sanders, S. S.; Paldus, B. A. *Anal. Chem*. 2005 *77*, 1177.

[88] Van der Sneppen; Wiskerke, A. E.; Ariese, F.; Gooijer, C. *Appl. Spectrosc*. 2006 *60*, 931.

[89] Richman, B. A.; Kachanov, A. A.; Paldus, B. A. *Opt. Express* 2005 *13*(9), 3376.

[90] Mürtz, M.; Dahnke, H.; Horstjann, M.; Kleine, D.; Thelen, S.; Hering, P. *Spectrochim. Acta, Part A*, 2006 *63*, 963.

[91] Crosson, E. R.; Ricci, K. N.; Richman, B. A.; Chilese, F. C.; Owano, T. G.; Provencal, R. A.; Todd, M. W.; Glasser, J.; Kachanov, A. A.; Paldus, B. A.; Spense, T. G.; Zare, R. N. *Anal. Chem.-Anal. Chem.* 2002 *74*(9), 2003.

[92] Wang, C.; Scherrer, S. T. *Opt. Lett*. 2004 *29*, 352.

[93] Wang, C.; Scherrer, S. T. *Appl. Opt*. 2004 *43*, 6458.

[94] Tarsa, P. B.; Wist, A. D.; Rabinowitz, P.; Lehmann, K. K. *Appl.Phys. Lett*. 2004 *85*, 4523.

[95] Kirkbright, G. F.; Sargent, M. *Atomic Absorption and Fluorescence Spectroscopy*, Academic Press: London, 1974.

[96] Siegman, A. E. *Laser*, University Science Books: Mill Valley, CA, 1986.

[97] Montaser, A. *Inductively Coupled Plasma Mass Spectrometry*, John Wiley & Sons: New York, NY, 1998.

[98] Griem, Hans. *Principles of plasma spectroscopy*. Cambridge University Press: New York, 1997.

[99] Breene, R. G. *The Shift and Shape of Spectral Lines*, Pergamon Press: Oxford, 1961.

[100] Laux, C. O.; Spence, T. G.; Kruger, C. H.; Zare, R. N. *Plasma Sources Sci. Technol*. 2003 *12*, 125.

[101] Yang, P. Y.; Barnes, R. M. *Spectrochim. Acta, Part B* 1989 *44*, 561.

[102] Fried, A.; Richter, D.; *Infrared absorption spectroscopy,* in *Analytical Techniques for Atmospheric Measurements*. Blackwell Publishing, 2006.

[103] Zalicki, P.; Zare, R. N. *J. Chem. Phys.* 1995 *102*, 2708.

[104] Mazurenka, M.; Orr-Ewing, A. J.; Peverall, R.; Ritchie, G. A. D. *Ann. Rep. Prog. Chem., Sect. C: Phys. Chem.* 2005 *101*, 100.

[105] Paul, J. B.; Lapson, L.; Anderson, J. G. *Applied Optics* 2001 *40*(27), 4904.

[106] Vallance, C. *New J. Chem*. 2005 *29*, 867.

[107] Svelto, O. *Principles of Lasers*, Plenum Press: New York, 1989.

[108] O'Shea, D. C.; Callen, W. R.; Rhodes, W. T. *Introduction to Lasers and Their Applications*, Addison-Wesley, Reading, 1978.

[109] Moisan, M.; Zakrzewski, Z. *J. Phys. D: Appl. Phys.* 1991 *24*, 1025.

[110] Scherer, J. J.; Voelkel, D.; Rakestraw, D. J.; Paul, J. B.; Collier, C. P.; Saykally, R. J.; O'Keefe, A. *Chem. Phys. Lett.* 1995 *245*, 273.

[111] Ball, S. M.; Jones, R. L. *Chem. Rev*. 2003 *103*(12), 5239.

[112] Huang, H.; Lehmann, K. K. *Appl. Opt.* 2009 *49*, 1378.

[113] Lehmann, K. K.; Huang, H. *Optimal signal processing in cavity ring-down spectroscopy*, in *Frontiers of Molecular Spectroscopy*. Laane, J. Ed. Elsevier, 2008, Chapter 18.

[114] Huang, H. Ph.D. Dissertation: Noise studies in CW cavity ring-down spectroscopy and its application in trace gas detection. Department of Chemistry, University of Virginia, 2009.

[115] Han, F. X.; Patterson, W. D.; Xia, Y.; Sridhar, B. B. M.; Su, Y. *Water, Air, and Soil Pollution*, 2006 *170*, 161.

[116] Allibone, J.; Fatmain, E.; Walker, P.J. *J. Anal. At. Spectrom.* 1999 *14*, 235.

[117] Fatemian, E.; Allibone, J.; Walker, P. J. *Analyst* 1999 *124*(8), 1233.

[118] Wang, C.; Winstead, C. B.; Duan, Y.; Scherrer, S. T.; Koirala, S. P.; Jang, P.-R.; Miller, G. P.; Mazzotti, F. J. *Plasma cavity ringdown spectrometer for elemental and isotopic measurements: past, present, and future,* presented at *ACS,* 2004.

[119] Harrison, G. R. *MIT Wavelength Tables*, *Vol. 2*, The MIT Press, Cambridge, MA, 1969.

[120] *NIST Atomic Spectra Database* (Ver. 4.1.0), [Online]. National Institute of Standards and Technology, Gaithersburg, MD; accessed 10/28/11; http://physics.nist.gov/cgi-bin/ASD/lines1.pl .

[121] Nishimura, Y.; Fujimoto, T. *Appl. Phys. B* 1985 *38*, 91.

[122] Carter, C. C. 'A Cavity Ringdown Spectroscopy Mercury Coninuous Emission Monitor,' submitted in the 7/1 – 9/30/2002 Quarterly Technical Progress Report for the U. S. Department of Energy.

[123] Schweitzer, Jr., G. W. *J. Opt. Soc. Amer.* 1963 *53*(9), 1055.

[124] Duan, Y.; Hou, M.; Du, Z.; Jin, Q. *Appl. Spectrosc.* 1993 *47*(11), 1871.

[125] Duan, Y.; Su, Y.; Jin, Z.; Abeln, S. P. *Anal. Chem.* 2000 *72*(7), 1672.

[126] Zamzow, D. S.;, Bajic, S. J.; Eckels, D. E.; Baldwin, D. P.; Winterrowd, C.; Keeney, R. *Rev. Sci. Instrum*. 2003 *74*, 3774.

[127] Ayers, J. D.; Apodaca, R. L.; Simpson, W. R.; Baer, D. S. *Appl. Opt*. 2005 *44*(33), 7239.

[128] Cotton, F. A.; Wilkinson, G. *Advanced Organic Chemistry, 5th Edition*. John Wiley & Sons, Inc.: New York, 1988; Chapter 16.

[129] Rom, W.N. (Ed.) *Environmental & Occupational Medicine*. 2nd *Edition*, Little Brown and Company: Boston, 1992.

[130] Pirrone, N.; Cinnirella, S.; Feng, X.; Finkelman, R. B. ; Friedli, H. R.; Leaner, J.; Mason, R.; Mukherjee, A. B.; Stracher, B. G.; Streets, D. G.; Telmer, K. *Atmos. Chem. Phys. Discuss.* 2010 *10*, 4719.

[131] Brown, A. S.; Brown, R. J. C.; Corns, W. T.; Stockwell, P. B. *The Analyst* 2008 *133*, 946.

[132] Brown, A. S.; Brown, R. J. C.; Dexter, M. A.; Corns, W. T.; Stockwell, P. B. *Royal Soc. of Chem.* 2010 *2*, 954.

[133] Dumarey, R.; Brown, R. J. C.; Corns, W. T.; Brown, A. S.; Stockwell, P. B. *Accred. Qual. Assur.* 2010 *15*(7), 409.

[134] Dumarey, R.; Dams, R. *Microchim Acta* 1984 *84*, 191.

[135] Dumarey, R.; Heindryckx, R.; Dams, R. *Anal. Chim. Acta* 1980 *118*, 381.

[136] Monts, D.; Su, Y.; Han, F.; Sridhar, B. B. M.; Waggoner, C. A.; Plodinec, M. J. *The 10th International Conference on Environmental Remediation and Radioactive Waste Management,* September 4-8, 2005, Scotland, ICEM05-1174.

[137] Rogers, R. D. *Soil Sci. Soc. Am. J.* 1979 *43*, 289.

[138] Han, F. X.; Patterson, W. D.; Xia, Y.; Sridhar, B. B. M.; Su, Y. *Water, Air, and Soil Pollution* 2006 *170*, 161.

[139] Obrist, D.; Johnson, D. W.; Lindberg, S.; Luo, Y. *American Geophysical Union*, Fall Meeting 2008.

[140] Gustin, M. S.; Stamenkovic, J. *Biogeochemistry* 2005 *76*, 215.

[141] Lindberg, S. E.; Jackson, d. R.; Huckabee, J. W.; Janzen, S. A.; Levin, M. J.; Lund, J. R. *J. Environ. Qual* 1979 *8*, 572.

[142] Gustin, M. S.; Taylor, G. E., Jr.; Maxey, R. A. *J. Geophys. Res.* 1997 *102*, 3891.

[143] Zhang, H.; Lindeberg, S. E.; Marsik, F. J.; Keeler, G. J. *Water Air Soil Pollut.* 2001 *136*, 151.

[144] Gustin, M. S.; Biester, H.; Kim, C. *Atmos. Environ.* 2002 *36*, 3241.

[145] Engle, M. A.; Gustin, M. S.; Zhang, H. *Atmos. Environ.* 2001 *35*, 3987.

[146] Engle, M. A.; Gustin, M. S.; Lindberg, S. E.; Gerler, A. W. *Mater. Geoenviron.* 2004 *51*, 1546.

[147] Rasmussen, P. E.; Edwards, G. c.; Kemp, J. R.; Fitzgerald-Hubble, C. R.; Schroeder, W. H. 'Towards an improved natural sources inventory for mercury,' in *Proceedings on the Metals in the Enviroment: An International Symposium*, 1998.

[148] Lindberg, S. E.; Zhang, H.; Gustin, M.; Vette, A.; Owens, J.; Marsik, F.; Casimir, A.; Ebinghaus, r.; Edwards, G.; Fitzgerald, C.; Kemp, J.; Kock, H. H.; London, J.; Majewski, M.; Poissant, L.; Pilote, M.; Rasmussen, P.; Schaedlich, F.; Schneeberger, D.; Sommar, J.; Turner, R.; Walshlager, D.; Xiao, Z. *J. Geophys. Res.* 1999 *104*(D17), 21879.

[149] Frescholtz, T. F.; Gustin, M. S. *Water Air Soil Pollut.* 2004 *155*, 223.

[150] Nacht, D. M.; Gustin, M. S. *Water Air Soil Pollut.* 2004 *151*, 179.

[151] Designed and fabricated by John Cambre at the Institute for Clean Energy Technology.

[152] Luque, J. LIFBASE, Version 2.0.130, 2003.

[153] Winge, R. K.; Fassel, V. A.; Peterson, V. J.; Floyd, M. A. *Inductively Coupled Plasma-Atomic Emission Spectroscopy – An Atlas of Spectral Information,* Elsevier Science Publishers, The Netherlands, 1993.

[154] Williams, R. M.; Thompson, J. S.; Stewart, T. L.; Tweedy, B.J. *FY04 SWIR CRDS Summary Report*, Pacific Northwest National Laboratory, Prepared for the U.S. Department of Energy.

[155] Brumfield, B. E.; Stewart, J. T.; McCall, B. J. *J. Molec. Spec.* 2011 *266*, 57.

[156] Cias, P.; Wang, C.; Dibble, T. S. *Appl. Spectrosc.* 2007 *61*(2), 230.

[157] Reddy, K. V.; Heller, D. F.; Berry, M. J. *J. Chem. Phys.* 1982 *76*(6), 2814.

[158] Nakagaki, R.; Hanazaki, I. *Spectrochim. Acta A* 1984 *40*(1), 57.

[159] Bassi, D.; Corbo, C.; Lubich, L.; Oss, S. ; Scotoni, M. *J. Chem. Phys.* 1997 *107*(4), 1106.